

**OFFICE OF CIVILIAN RADIOACTIVE WASTE MANAGEMENT
ANALYSIS/MODEL COVER SHEET**
Complete Only Applicable Items

1. QA: QA
Page: 1 of 194

<p>2. <input checked="" type="checkbox"/> Analysis Check all that apply</p> <table border="1" style="width:100%; border-collapse: collapse;"> <tr> <td style="width:20%;">Type of Analysis</td> <td> <input type="checkbox"/> Engineering <input type="checkbox"/> Performance Assessment <input checked="" type="checkbox"/> Scientific </td> </tr> <tr> <td>Intended Use of Analysis</td> <td> <input type="checkbox"/> Input to Calculation <input checked="" type="checkbox"/> Input to another Analysis or Model <input checked="" type="checkbox"/> Input to Technical Document </td> </tr> <tr> <td colspan="2">Describe use: Provides analyses of <i>in situ</i> field testing data for use in AMRs related to seepage into drifts and the UZ PMR in relation to understanding of seepage & flow processes.</td> </tr> </table>	Type of Analysis	<input type="checkbox"/> Engineering <input type="checkbox"/> Performance Assessment <input checked="" type="checkbox"/> Scientific	Intended Use of Analysis	<input type="checkbox"/> Input to Calculation <input checked="" type="checkbox"/> Input to another Analysis or Model <input checked="" type="checkbox"/> Input to Technical Document	Describe use: Provides analyses of <i>in situ</i> field testing data for use in AMRs related to seepage into drifts and the UZ PMR in relation to understanding of seepage & flow processes.		<p>3. <input type="checkbox"/> Model Check all that apply</p> <table border="1" style="width:100%; border-collapse: collapse;"> <tr> <td style="width:20%;">Type of Model</td> <td> <input type="checkbox"/> Conceptual Model <input type="checkbox"/> Abstraction Model <input type="checkbox"/> Mathematical Model <input type="checkbox"/> System Model <input type="checkbox"/> Process Model </td> </tr> <tr> <td>Intended Use of Model</td> <td> <input type="checkbox"/> Input to Calculation <input type="checkbox"/> Input to another Model or Analysis <input type="checkbox"/> Input to Technical Document </td> </tr> <tr> <td colspan="2">Describe use:</td> </tr> </table>	Type of Model	<input type="checkbox"/> Conceptual Model <input type="checkbox"/> Abstraction Model <input type="checkbox"/> Mathematical Model <input type="checkbox"/> System Model <input type="checkbox"/> Process Model	Intended Use of Model	<input type="checkbox"/> Input to Calculation <input type="checkbox"/> Input to another Model or Analysis <input type="checkbox"/> Input to Technical Document	Describe use:	
Type of Analysis	<input type="checkbox"/> Engineering <input type="checkbox"/> Performance Assessment <input checked="" type="checkbox"/> Scientific												
Intended Use of Analysis	<input type="checkbox"/> Input to Calculation <input checked="" type="checkbox"/> Input to another Analysis or Model <input checked="" type="checkbox"/> Input to Technical Document												
Describe use: Provides analyses of <i>in situ</i> field testing data for use in AMRs related to seepage into drifts and the UZ PMR in relation to understanding of seepage & flow processes.													
Type of Model	<input type="checkbox"/> Conceptual Model <input type="checkbox"/> Abstraction Model <input type="checkbox"/> Mathematical Model <input type="checkbox"/> System Model <input type="checkbox"/> Process Model												
Intended Use of Model	<input type="checkbox"/> Input to Calculation <input type="checkbox"/> Input to another Model or Analysis <input type="checkbox"/> Input to Technical Document												
Describe use:													

4. Title:
In Situ Field Testing of Processes

5. Document Identifier (including Rev. No. and Change No., if applicable):
ANL-NBS-HS-000005 Rev 00

<p>6. Total Attachments: 8</p>	<p>7. Attachment Numbers - No. of Pages in Each:</p> <p>I-23 II-4 III-3 IV-3 V-4 VI-5 VII-4 VIII-2</p>
---	--

	Printed Name	Signature	Date
8. Originator	J.S.Y. Wang	<i>Joseph S.Y. Wang</i>	3-17-2000
9. Checker	P. Persoff	<i>Peter Persoff</i>	3/13/00
10. Lead/Supervisor	G.S. Bodvarsson	<i>Bo Bodvarsson</i>	3/13/00
11. Responsible Manager	G.S. Bodvarsson	<i>Bo Bodvarsson</i>	3/13/00

12. Remarks:
Block 8: Other contributing authors include P.J. Cook, R.C. Trautz, Q. Hu, and R. Salve.
Editorial changes to pages 3 and 5, Table of Contents per 4/21/00
Editorial change to page 11, Figures per 4/21/00

**OFFICE OF CIVILIAN RADIOACTIVE WASTE MANAGEMENT
ANALYSIS/MODEL REVISION RECORD**

Complete Only Applicable Items

1. Page: 2 of 194

2. Analysis or Model Title:

In Situ Field Testing of Processes

3. Document Identifier (including Rev. No. and Change No., if applicable):

ANL-NBS-HS-000005 Rev 00

4. Revision/Change No.

5. Description of Revision/Change

REV00

Initial Issue

CONTENTS

	Page
ACRONYMS	15
I. PURPOSE	17
1.1 OBJECTIVES AND PROCESSES ANALYZED BY THE AMBIENT FIELD TESTING ACTIVITIES	17
1.2 LOCATIONS OF TEST SITES IN THE EXPLORATORY STUDIES FACILITY	18
1.3 CONSTRAINTS, CAVEATS, AND LIMITATIONS	21
2. QUALITY ASSURANCE	23
3. COMPUTER SOFTWARE AND MODEL USAGE	25
4. INPUTS	27
4.1 DATA AND PARAMETERS	27
4.2 CRITERIA	29
4.3 CODES AND STANDARDS	29
5. ASSUMPTIONS USED IN AMBIENT FIELD TESTING ANALYSES	31
5.1 ASSUMPTIONS USED IN BOREHOLE AIR-PERMEABILITY CALCULATIONS	32
5.2 ASSUMPTIONS USED IN ANALYZING AND INTERPRETING THE NICHE LIQUID-RELEASE AND SEEPAGE TEST DATA	33
5.2.1 Assumptions Used in Estimating Saturated Hydraulic Conductivity Using Air Permeability	33
5.2.2 Assumptions Used in Deriving the Capillary Strength of the Fractures Based on a Philip's Capillary Barrier Solution	34
5.2.3 Assumptions Used in Deriving the Estimated Volumetric Water Content for the Fractures Based on Braester's Wetted Profile Solution	34
5.3 APPROXIMATIONS USED IN TRACER-MIGRATION DELINEATION AT NICHE 3650 <i>35</i>	35 <i>JEH 4/21/00</i>
5.4 APPROXIMATIONS USED IN ANALYSES OF TRACER PENETRATION AND WATER IMBIBITION INTO WELDED TUFF MATRIX	35
5.5 APPROXIMATIONS USED IN CROSS-HOLE CONNECTIVITY ANALYSES	36
5.6 APPROXIMATIONS USED IN ANALYSES OF FRACTURE FLOW IN FRACTURE-MATRIX TEST BED AT ALCOVE 6	36
5.7 APPROXIMATIONS USED IN ANALYSES OF FLOW THROUGH THE FAULT AND MATRIX IN THE TEST BED AT ALCOVE 4	37
5.8 APPROXIMATIONS USED IN WATER-POTENTIAL MEASUREMENTS IN NICHES	37
5.9 APPROXIMATIONS USED IN MONITORING CONSTRUCTION-WATER MIGRATION	37
5.10 APPROXIMATIONS USED IN VENTILATION-INDUCED MOISTURE REMOVAL RATE	38

CONTENTS (Continued)

	Page
6. ANALYSES OF AMBIENT FIELD TESTING DATA	39
6.1 AIR-PERMEABILITY DISTRIBUTIONS AND EXCAVATION-INDUCED ENHANCEMENTS	43
6.1.1 Niche Test Site and Borehole Configuration	43
6.1.2 Air-Permeability Spatial Distribution and Statistical Analysis	47
6.2 ANALYSIS AND INTERPRETATION OF THE NICHE LIQUID-RELEASE AND SEEPAGE-TEST DATA	61
6.2.1 Review of Data Obtained from Liquid-Release and Seepage Tests Conducted at Niches	61
6.2.2 Seepage Threshold and Fracture Characteristic Curve	66
6.3 ANALYSES OF TRACER-MIGRATION DELINEATION AT NICHE 3650	79
6.3.1 Tracer Distribution from the Last Liquid-Release Test	79
6.3.2 Delineation of Tracer Distributions from Previous Liquid-Release Tests	82
6.4 ANALYSES OF TRACER PENETRATION AND WATER IMBIBITION INTO WELDED TUFF MATRIX	93
6.4.1 Penetration of Dyes into Rocks from the Niches	93
6.4.2 Retardation and Tracer Front Movement	100
6.5 CROSS-HOLE ANALYSES OF AIR INJECTION TESTS	107
6.5.1 Cross-Hole Responses in Welded Tuff	107
6.5.2 Permeability Distributions and Cross-Hole Responses in Nonwelded Tuff	112
6.6 ANALYSES OF FRACTURE FLOW IN FRACTURE-MATRIX TEST BED AT ALCOVE 6	117
6.6.1 Liquid-Release Tests in Low- and High-Permeability Zones	117
6.6.2 Observations of Wetting Front Migration and Fracture Flow	120
6.7 ANALYSES OF FLOW THROUGH THE FAULT AND MATRIX IN THE TEST BED AT ALCOVE 4	132
6.7.1 Flow Tests in Paintbrush Tuff Unit Layers and Fault	132
6.7.2 Observations of Fault Flow and Matrix Flow	137
6.8 COMPILATION OF WATER-POTENTIAL MEASUREMENTS IN NICHEs	144
6.8.1 Location and Timing of Water-Potential Measurements at Niches	144
6.8.2 Observations of Dryout in Niche Boreholes	147
6.9 OBSERVATIONS OF CONSTRUCTION-WATER MIGRATION	152
6.9.1 Equipment Set-Up for Construction-Water Monitoring	152
6.9.2 Wetting Front Detection and Monitoring Below the Cross Drift	155
6.10 STATUS OF ANALYSES OF ESF CONSTRUCTION EFFECTS	165
6.10.1 Summary of Construction-Induced Effects	165
6.10.2 Moisture Conditions and Perturbations Observed in Drifts	169
7. SUMMARY AND CONCLUSIONS OF AMBIENT FIELD TESTING ANALYSES	173
7.1 SUMMARY OF AIR-PERMEABILITY DISTRIBUTION AND EXCAVATION- INDUCED ENHANCEMENT IN NICHEs	176

CONTENTS (Continued)

	Page
7.2 CONCLUSIONS OF LIQUID-RELEASE AND SEEPAGE TESTS IN NICHE	176
7.2.1 Pre-Excavation Liquid-Release Testing and Niche Excavation Activities	176
7.2.2 Post-Excavation Seepage Tests at Niche 3650	177
7.2.3 Constraints, Caveats, and Limitations of the Niche Seepage Test Results	178
7.3 CONCLUSIONS OF TRACER-MIGRATION DELINATION AT NICHE 3650	178
7.4 SUMMARY AND CONCLUSIONS ON TRACER PENETRATION AND WATER IMBIBITION INTO WELDED TUFF MATRIX	179
7.5 SUMMARY OF SINGLE-HOLE PERMEABILITY DISTRIBUTIONS AND CROSS HOLE CONNECTIVITY ANALYSES	180
7.6 CONCLUSIONS OF FRACTURE FLOW IN FRACTURE-MATRIX TEST BED AT ALCOVE 6	180
7.7 CONCLUSIONS OF FLOW THROUGH THE FAULT AND MATRIX IN THE TEST BED AT ALCOVE 4	182
7.8 CONCLUSIONS OF WATER-POTENTIAL MEASUREMENTS IN THE NICHEs	182
7.9 CONCLUSIONS OF MONITORING THE CONSTRUCTION-WATER MIGRATION	183
7.9.1 Starter Tunnel	183
7.9.2 Monitoring of Cross-Over Point	184
7.10 CONCLUSIONS OF ANALYSES OF CONSTRUCTION EFFECTS	184
8. INPUTS AND REFERENCES	185
8.1 DOCUMENTS CITED	185
8.2 CODES, STANDARDS, REGULATIONS, AND PROCEDURES	187
8.3 SOURCE DATA, LISTED BY DATA TRACKING NUMBER	188
8.4 OUTPUT DATA, LISTED BY DATA TRACKING NUMBER	189
8.5 SUPPORTING DOCUMENTS	190
9. ATTACHMENTS	193
ATTACHMENT I - DOCUMENT INPUT REFERENCE SHEET	
ATTACHMENT II - AUTOMATED AIR INJECTION SYSTEM	
ATTACHMENT III - COMPARISON OF LIQUID AND AIR-DERIVED SATURATED HYDRAULIC CONDUCTIVITIES	
ATTACHMENT IV - WATER CONTENT PROFILE EVALUATION	
ATTACHMENT V - TRACER MEASUREMENTS OF NICHE CORES	
ATTACHMENT VI - LABORATORY MEASUREMENTS OF RETARDATION AND FRONT SEPARATION	
ATTACHMENT VII - FIELD EQUIPMENT FOR CONTROLLED WATER RELEASE, WETTING FRONT DETECTION AND SEEPAGE COLLECTION	
ATTACHMENT VIII - MEASUREMENT OF WATER POTENTIAL \$ USING PSYCHROMETERS	

*jeH
4/22/00*

INTENTIONALLY LEFT BLANK

FIGURES

	Page
1. Schematic Illustration of Alcove and Niche Locations in the Exploratory Studies Facility at Yucca Mountain.....	19
2. Schematic Illustration of Cross Drift.....	20
3. Schematic Illustration of East-West Distribution of Hydrogeologic Units Intersected by the Potential Repository Horizon (Ttptmn, Ttptll, and Ttptln).....	20
4. Schematic Illustration of Flow Tests in the Exploratory Studies Facility at Yucca Mountain.....	40
5. Schematic Illustration of the Cross-Over Point of Cross Drift with the Main Drift.....	41
6. Schematic Illustration of Location Map for Niches 3107, 3566, 3650, and 4788.....	44
7. Schematic Illustration of the End View of Borehole Clusters at Niche Sites.....	46
8. Schematic Illustration of the Plan View of Borehole Clusters at Niche Sites.....	47
9. Pre-Excavation Air-Permeability Profiles along Axial Boreholes at Niche 3566.....	50
10. Post-Excavation Air-Permeability Profiles along Radial Boreholes at Niche 3566.....	51
11. Pre- and Post-Excavation Air-Permeability Profiles along Upper Boreholes at Niche 3650.....	52
12. Pre-Excavation Air-Permeability Profiles along Middle and Bottom Boreholes at Niche 3650.....	53
13. Pre- and Post-Excavation Air-Permeability Profiles along Upper Boreholes at Niche 3107.....	54
14. Pre-Excavation Air-Permeability Profiles along Middle and Bottom Boreholes at Niche 3107.....	55
15. Pre- and Post-Excavation Air-Permeability Profiles along Upper Boreholes at Niche 4788.....	56
16. Pre-Excavation Air-Permeability Profiles along Middle and Bottom Boreholes at Niche 4788.....	57
17. Mass of Water Released Versus Aspect Ratio.....	63

FIGURES (Continued)

	Page
18. Schematic Illustration of Seepage Capture System and Test Intervals at Niche 3650.....	65
19. Relative Humidity Inside Niche 3107.....	66
20. Liquid-Release Flux Versus Seepage Percentage.....	67
21. Seepage Threshold Fluxes.....	69
22. Water Retention Curves for High-Angle Fractures and Fracture Networks.....	78
23. Sampling Borehole Array: (a) Schematic Plan View with Liquid-Release/Dye-Application History, and (b) Three-Dimensional View from Inside the Niche..	81
24. Dye Detection along Borehole 7: (a) FD&C Blue No. 1, and (b) Sulpho Rhodamine B.....	84
25. Dye Detection of: (a) Pyranine Along Borehole 11, and (b) Acid Yellow 7 along Borehole 2.....	85
26. Three-Dimensional View of FD&C Blue No. 1 Detection Related to the Release Intervals Above the Niche.....	86
27. Three-Dimensional View of Sulpho Rhodamine B Detection Related to the Release Intervals above the Niche.....	87
28. Three-Dimensional View of Pyranine Detection Related to the Release Interval above the Niche.....	88
29. Three-Dimensional View of Acid Yellow 7 Detection Related to the Release Interval Above the Niche.....	89
30. Three-Dimensional View of Amino G Acid Detection Related to the Release Interval above the Niche.....	90
31. Three-Dimensional View of FD&C Yellow No. 6 Detection Related to the Release Intervals above the Niche.....	91
32. Photograph for Illustration of Sampling Location of Rock Stained by FD&C Blue No. 1 during Niche Excavation at Niche 4788.....	94
33. Rock Sample Stained by Sulpho Rhodamine B Collected from Niche 3650.....	95

FIGURES (Continued)

	Page
34. Sulpho Rhodamine B Penetration Profiles into Rock Matrix from the Fracture Surface.....	95
35. Tracer Penetration Profile into Rock Matrix from the Fracture Surface: (a) FD&C Blue No.1 at Niche 3650, (b) FD&C Blue No.1 at Niche 4788.....	99
36. Comparison of Tracer Concentration Profiles in a Low-Initial-Saturation Core: (a) Bromide, (b) FD&C Blue No. 1, (c) Sulpho Rhodamine.....	102
37. Comparison of Tracer Concentration Profiles in a High-Initial-Saturation Core: (a) Bromide, (b) FD&C Blue No. 1, (c) Sulpho Rhodamine B.	103
38. Cross-Hole Responses for the Borehole Cluster in Niche 4788.....	109
39. Single-Hole Air-Permeability Profiles along Boreholes in Alcove 6.....	110
40. Cross-Hole Responses for the Borehole Cluster in Alcove 6.....	111
41. Schematic Illustration of Alcove 4 Test Bed.....	112
42. Single-Hole Air-Permeability Profiles along Boreholes in Alcove 4.....	114
43. Cross-Hole Responses for Borehole Cluster at Alcove 4 PTn Test Bed with All Response Pressure (Resp.) Ratios below 0.2 Included.....	115
44. Cross-Hole Responses for Borehole Cluster at Alcove 4 PTn Test Bed with Small Response Pressure (Resp.) Ratios Filtered.	116
45. Schematic Illustration of (a) Plan view of Location and (b) Vertical View of Layout of Test Bed at Alcove 6 in the ESF at Yucca Mountain.....	118
46. Water Intake Rates Observed in the Low Permeability Zone.....	121
47. Water Intake Rates Observed in the High Permeability Zone.....	121
48. Changes in Electrical Resistance and Water Potential Detected during Liquid Injection into the Low Permeability Zone.....	123
49. Changes in Electrical Resistance and Water Potential Detected during Liquid Release into the High Permeability Zone.....	125
50. Seepage into Slot: (a) Percentage of Injected Water Recovered and (b) Seepage Rates for Various Release Rates.....	127

FIGURES (Continued)

	Page
51. Seepage into Collection Trays in the Slot: (a) Tray Configuration and (b) Percentages of Injected Water Recovered for Different Trays.	129
52. Volume of Water Recovered in the Slot after Liquid Injection into the High Permeability Zone was Stopped.....	130
53. Tracer Concentrations in Seepage Water Following Injection into the High Permeability Zone.....	131
54. Geological Sketch for the North Face of Alcove 4 in the ESF at Yucca Mountain. Also included are location of boreholes and the slot.....	133
55. Schematic Illustration of Three-Dimensional View of the Boreholes, Slot, and Lithological Unit Contacts in the Alcove 4 Test Bed.....	135
56. Intake Rates along the 0.3-m Zone Located on the Fault in Borehole 12.....	138
57. Wetting Front Arrival in Borehole 11 Following Liquid Released into the Fault in Borehole 12.....	139
58. Changes in Electrical Resistance in Borehole 11 in Response to Liquid Released into the Fault in Borehole 12.....	140
59. Changes in Electrical Resistance in Borehole 2 in Response to Liquid Released into the Fault in Borehole 12.....	141
60. Intake Rates along a 0.3-m Zone in the Matrix Located 2.44–2.74 m from the Collar in Borehole 5.....	142
61. Changes in Electrical Resistance in Borehole 6 in Response to Liquid Released in Borehole 5.....	143
62. Schematic Illustration of the Location of Psychrometers in Niche 3566 (a) in Pre-Excavation, (b) in Post-Excavation Conditions.....	145
63. Schematic Illustration of Location of Psychrometers in Niche 3650.....	146
64. Schematic Illustration of Location of Psychrometers in Niche 3107 (Pre-Excavation).....	147
65. Pre-Excavation Water Potential Measured along Borehole U in Niche 3566.....	150
66. Water Potential Measured along Borehole UM in Niche 3107.....	151

FIGURES (Continued)

	Page
67. Schematic Illustration of the Location of Wetting Monitoring Borehole at the Starter Tunnel of the Cross Drift	152
68. Schematic Illustration of the Borehole Wetting Front Monitoring System with Psychrometers and Electrical/Resistivity Probes.....	153
69. Schematic Illustration of SeAsor Arrays for Wetting Front Monitoring	154
70. Changes in Water Potential Observed along the Wetting Front Monitoring Borehole at the Starter Tunnel of Cross Drift	160
71. Changes in Electrical Resistance Observed along the Wetting Front Monitoring Borehole at the Starter Tunnel of the Cross Drift	161
72. Comparison of Performance of Electrical Resistivity Probe and Psychrometer	163
73. Example of Time Domain Reflectometry Probe Data at the Cross-Over Point in the ESF Main Drift	164
74. Relative Humidity Temporal Variations in the Cross Drift	172
75. Relative Humidity Spatial Variations along the Cross Drift	172

INTENTIONALLY LEFT BLANK

TABLES

		Page
1.	Software and Routines.....	25
2.	Input Data and Data Tracking Numbers.....	28
3.	Assumptions.....	31
4.	Scientific Notebooks.....	42
5.	Statistical Analyses of Air-Permeability Along Boreholes Above Niches.....	59
6.	Comparison of Geometric Means and Standard Deviations of Niches and Alcoves in the Exploratory Studies Facility at Yucca Mountain.....	60
7.	Seepage Threshold Fluxes (K_o^*).....	68
8.	Alpha (α) Values for the Fractures.....	72
9.	Estimated Changes in Volumetric Content ($\Delta\theta$) of the Fractures.....	74
10.	Estimated Water Potential (ψ) for the Fractures.....	77
11.	Compilation of Tracer Detection Versus Borehole Location.....	83
12.	Compilation of Information About the Dyed Rock.....	96
13.	Tracer Release Tests and Measured Seepage Concentrations at Niche 3650.....	96
14.	Compilation of C/C_0 Value for Rock Drilling Taken at 0–1 mm Interval.....	98
15.	Measured Properties for Core Samples.....	104
16.	Amount of Water and Types of Tracers Released into the Injection Borehole.....	120
17.	Summary of Liquid-Injection Tests in the High Permeability Zone.....	126
18.	Summary of Liquid Releases into the Fault Zone in Borehole 12.....	136
19.	Water-Potential Measurements in Niche 3566.....	148
20.	Water-Potential Measurements in Niche 3650.....	149
21.	Water-Potential Measurements in Niche 3107.....	149
22.	Psychrometers Response to Excavation at the Starter Tunnel of the Cross Drift.....	156

TABLES (Continued)

	Page
23. Electrical Resistivity Probe Responses to Excavation at the Starter Tunnel of the Cross Drift	157
24. Moisture-Monitoring Stations in the Exploratory Studies Facility.....	166
25. Water-Potential Measurements in the Exploratory Studies Facility.....	168
26. Saturation Measurements in the Exploratory Studies Facility.....	169

ACRONYMS

1-D	one-dimensional
2-D	two-dimensional
3-D	three-dimensional
ACC	Accession Number
AMR	Analysis/Model Report
AP	Administrative Procedure (DOE)
B	Bottom borehole
BST	Borehole Sensor Tray
CDCS	Cross Drift Construction Station
CRWMS	Civilian Radioactive Waste Management System
CS	Construction Station (ESF main loop)
DOE	Department of Energy
DTN	Data Tracking Number
ECM	Effective Continuum Method
ECRB	Enhanced Characterization of Repository Block
ERP	Electrical Resistivity Probe
ESF	Exploratory Studies Facility
FD&C	Food, Dye and Cosmetics
FY	Fiscal Year
HPZ	High Permeability Zone
LA	License Application
LANL	Los Alamos National Laboratory
LBNL	Lawrence Berkeley National Laboratory
LPZ	Low Permeability Zone
M	Middle borehole
M&O	Management and Operating Contractor
M&TE	Measuring and Test Equipment
ML	Middle Left borehole
MFC	Mass Flow Controller
MR	Middle Right borehole
OCRWM	Office of Civilian Radioactive Waste Management

ACRONYMS (Continued)

PA	Performance Assessment
PMR	Process Model Report
PTn	Paintbrush non-welded hydrogeologic unit
PVC	Polyvinyl Chloride
Q	Qualified
QA	Quality Assurance
QAP	Administrative Procedure (M&O)
QARD	Quality Assurance Requirements and Description
QIP	Quality Implementing Procedure
RIS	Records Information System
SR	Site Recommendation
SLPM	Standard Liter Per Minute
TBM	Tunnel Boring Machine
TBV	To Be Verified
TCO	Test Coordination Office
TCw	Tiva Canyon welded hydrogeologic unit
TDMS	Technical Data Management System
TDR	Time Domain Reflectometry
Tpbt2	Upper pre-Pah Canyon bedded tuff
Tpp	Pah Canyon tuff unit
Tptpll	Lower lithophysal Topopah Spring welded tuff unit
Tptpln	Lower nonlithophysal Topopah Spring welded tuff unit
Tptpmn	Middle nonlithophysal Topopah Spring welded tuff unit
Tptpul	Upper lithophysal Topopah Spring welded tuff unit
TSPA	Total System Performance Assessment
TSw	Topopah Spring welded hydrogeologic unit
U	Upper borehole
UL	Upper Left borehole
UM	Upper Middle borehole
UR	Upper Right borehole
USGS	United States Geological Survey
UV/Vis	Ultraviolet and Visible
UZ	Unsaturated Zone
YAP	Administrative Procedure (YMP)
YMP	Yucca Mountain Site Characterization Project

1. PURPOSE

The purpose of this Analysis/Model Report (AMR) is to document the data and subsequent analyses from the ambient field testing activities performed in the Exploratory Studies Facility (ESF). This is in accordance with the *AMR Development Plan for U0015 In-Situ Field Testing of Processes, Rev. 00* (CRWMS 1999a). These activities were performed to investigate *in situ* flow and transport processes. The evaluations provide the necessary framework to: (1) refine and confirm the conceptual model of matrix and fracture processes in the unsaturated zone (UZ) and (2) analyze the impact of excavation on the UZ flow and transport processes. This AMR supports the AMR on the development of conceptual and numerical models for UZ flow and transport, and the UZ Flow and Transport Process Model Report (PMR). This AMR also provides documentation for the milestone data submittal SPB148M4–*Seepage Data Feed to UZ Drift-Scale Flow Model for Total System Performance Assessment (TSPA) for Site Recommendation (SR)*. (Data Tracking Number (DTN): LB990601233124.001, DTN: LB990601233124.002, and DTN: LB990601233124.003 submitted to Technical Database Management System (TDMS)).

In general, the results discussed in this AMR are from studies conducted in a combination or a subset of the following three approaches: (1) air-injection tests, (2) liquid-release tests, and (3) moisture monitoring using in-drift sensors or in-borehole sensors to evaluate the impact of excavation, ventilation, and construction-water usage on the surrounding rocks. The liquid-release tests and air-injection tests provide an evaluation of *in situ* fracture flow and the competing processes of matrix imbibition. For the seepage testing data provided in this AMR, only the findings from this testing that are not covered in the AMR on the seepage calibration model will be included. The modeling AMR provides inputs to the AMR on seepage models for performance assessment (PA).

1.1 OBJECTIVES AND PROCESSES ANALYZED BY THE AMBIENT FIELD TESTING ACTIVITIES

ESF field-test findings and their implications for drift seepage, fracture flow, matrix imbibition, and moisture evolution can be used to address PA uncertainties and potential repository design issues. In TSPA for the Viability Assessment uncertainty analyses, the fraction of waste packages contacted by seepage water is the most important parameter in determining peak dose rates in 10,000, 100,000, and 1,000,000-year periods (DOE 1998a, Section 4.3.2, Figure 4-34, pp. 4-73 through 4-74). The significance of uncertainties in seepage fraction to TSPA is categorized as high (DOE 1998a, Section 6.4, Table 6-1, p. 6-12; DOE 1998b, Section 2.2.4.1, Table 2-2, p. 2-20). The UZ flow and transport model and the drift-scale model need field data for partitioning UZ flux into a fast fracture-flow component and a slow matrix-flow component in the potential repository within the Topopah Spring welded tuff unit (TSw) and throughout the UZ. This partitioning is controlled by the fracture-matrix interaction. The damping of infiltration pulses and diversion by the Paintbrush nonwelded tuff unit (PTn) above the TSw are potential mechanisms for infiltration and percolation flux redistribution. In the vicinity of the potential repository, perturbations by drift excavation, air ventilation, and water usage can change hydrologic regime in the UZ. Retardation by rock mass and dispersion through fractures are processes affecting the migration of tracers and the dilution of potential radionuclides below the

drifts to the water table. Some of these processes and related uncertainties, issues, and concerns are addressed by the ambient testing program at test sites in the ESF.

1.2 LOCATIONS OF TEST SITES IN THE EXPLORATORY STUDIES FACILITY

The ESF provides underground access to tuff units at and above the potential repository level. *In situ* testing and monitoring studies are being conducted to directly assess and evaluate the potential waste emplacement environment and the UZ natural barriers to radionuclide transport at Yucca Mountain. This AMR summarizes the progress and status of ambient studies of UZ flow conducted in 1997–1999 at various test sites along the ESF¹, as illustrated in Figure 1. The new Cross Drift over the potential repository block provides access to different subunits of TSw for Enhanced Characterization of Repository Block (ECRB), as illustrated in Figures 2 and 3.

Figure 1 illustrates the locations of four alcoves (Alcoves 1, 2, 3, and 4) along the North Ramp, and three alcoves (Alcoves 5, 6, and 7) and four niches (Niches 3566, 3650, 3107, and 4788) along the Main Drift of the ESF. The numerical identification for each niche denotes the distance in meters from the North Portal. The Cross Drift branches out from the North Ramp, crosses over the Main Drift near Niche 3107, and reaches the western boundary of the potential repository block, as illustrated in Figure 2. Two niches with fracture-matrix test beds and three alcoves are planned for excavation in the Cross Drift. Figure 3 illustrates the potential repository units along the Cross Drift to access lower tuff units. The Cross Drift goes through all three potential repository stratigraphic units: the Topopah Spring middle nonlithophysal (Ttpmn), lower lithophysal (Ttpll), and lower nonlithophysal (Ttpln) units (stratigraphic nomenclature of Buesch et al. 1996, Table 2, pp. 5-8). Most of the emplacement drifts will be in the lower tuff units. The lower units could have distinctly different tuff characteristics with unknown effects on seepage fraction and fracture-matrix flow partition. A systematic study with transient air injection and pulse liquid release along boreholes into the crown of the Cross Drift is on-going to supplement the niche and alcove tests. The Cross Drift entrance is in the TSw upper lithophysal (Ttpul) unit.

¹ As of the date of this AMR, as-built surveys had not been performed and/or the qualified survey data had not been released for use to determine the final location of the some of alcoves and niches shown in Figures 1, 2, and 3. Therefore, the approximate locations of the test sites are illustrated for information only. This AMR does not directly rely on any of the location information.

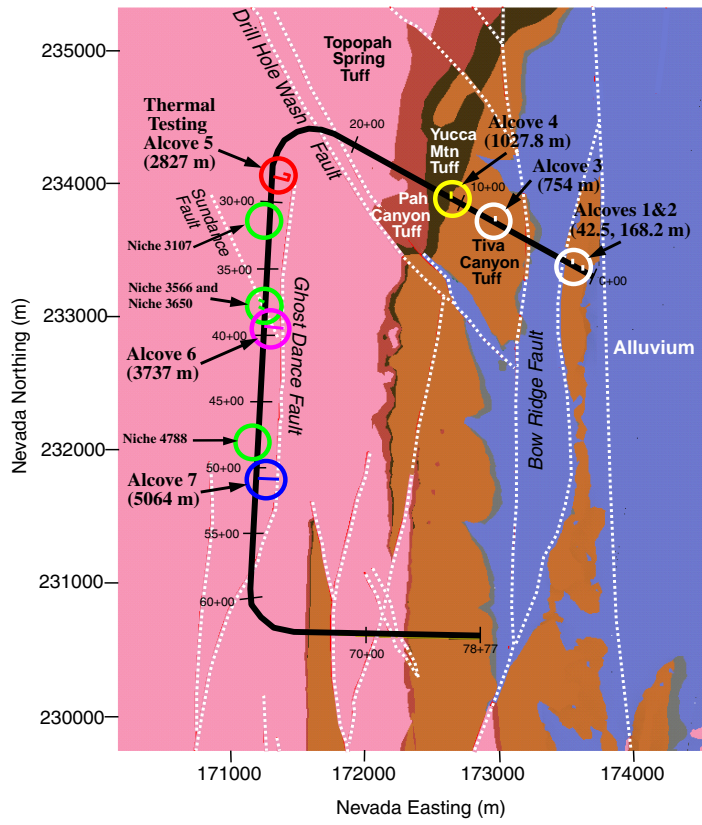


Figure 1. Schematic Illustration of Alcove and Niche Locations in the Exploratory Studies Facility at Yucca Mountain.

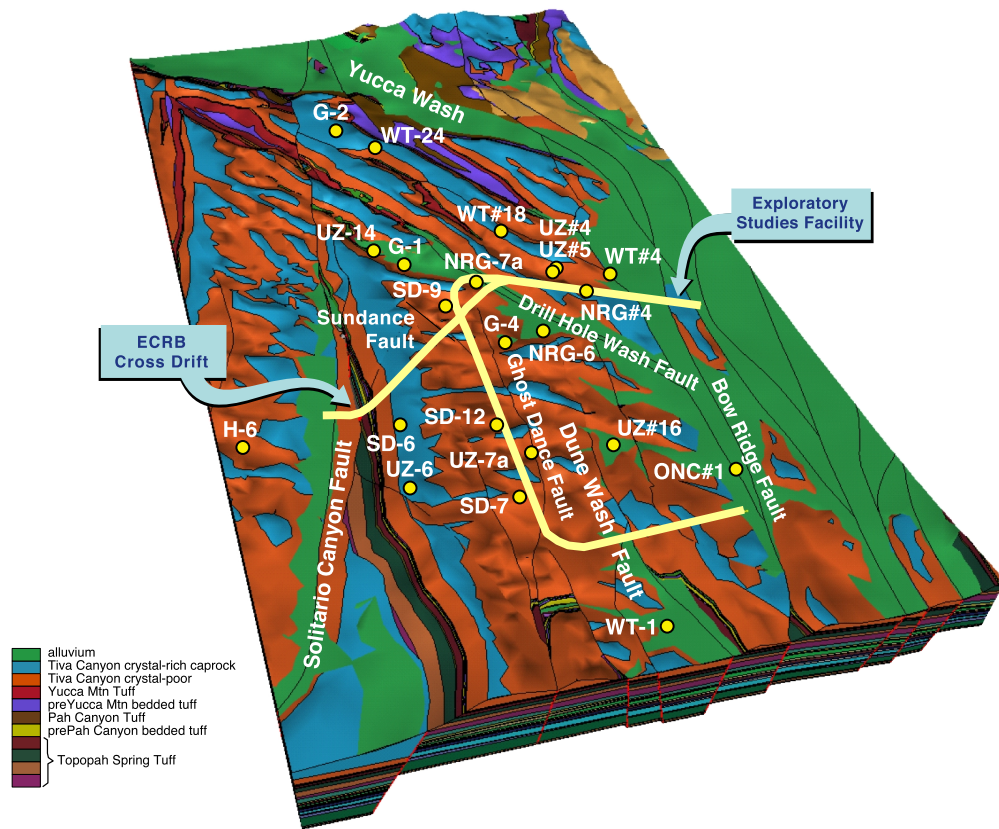


Figure 2. Schematic Illustration of Cross Drift. The new drift branches out from the North Ramp of the Exploratory Studies Facility, crosses over the Main Drift, and accesses the western fault boundary of the potential repository block at Yucca Mountain.

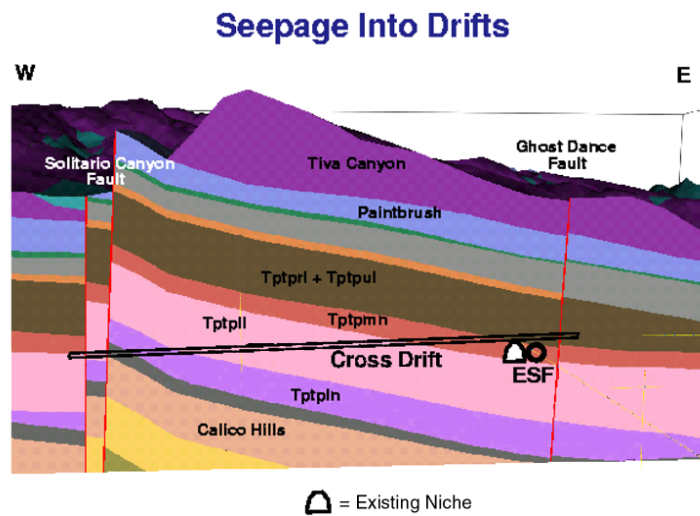


Figure 3. Schematic Illustration of East-West Distribution of Hydrogeologic Units Intersected by the Potential Repository Horizon (Tptpmn, Tptpll, and Tptpln).

1.3 CONSTRAINTS, CAVEATS, AND LIMITATIONS

The field-testing activities and the associated analyses are subject to the constraints and limitations of spatial locations and temporal durations for tests conducted in the underground ESF. With existing alcoves and niches located at and above the horizon of the Ttpmn unit, the test results and analyses provide information for upper tuff units. Most of the active flow tests were conducted within a few hours to a few days because of limits of accessibility to the test beds in the evenings and weekends. Depending on the system characteristics, the establishment of steady-state conditions may require longer tests. These constraints, caveats, and limitations are addressed in the analyses, if applicable.

INTENTIONALLY LEFT BLANK

2. QUALITY ASSURANCE

The activities documented in this Analysis/Model Report (AMR) were evaluated in accordance with QAP-2-0, *Conduct of Activities*, and were determined to be subject to the requirements of the U.S. DOE Office of Civilian Radioactive Waste Management (OCRWM) *Quality Assurance Requirements and Description* (QARD) (DOE 1998c). This evaluation is documented in CRWMS 1999a, b; and Wemheuer 1999 (*Activity Evaluation for Work Package WP 1401213UMI*).

This AMR was developed in accordance with AP-3.10Q, Rev. 1, ICN 0, *Analyses and Models*. Other applicable DOE Administrative Procedures (APs) and YMP-LBNL Quality Implementing Procedures (QIPs) are identified in the *AMR Development Plan for U0015 In-Situ Field Testing of Processes* (CRWMS 1999a).

INTENTIONALLY LEFT BLANK

3. COMPUTER SOFTWARE AND MODEL USAGE

Standard spreadsheet and plotting programs were used in the analyses performed on the ESF field test data. Earthvision (STN: 30035-2 V4.0, Version 4.0) was obtained from configuration management and used to plot tracer distributions (see Table 1). For data collection, only software acquired as an integral part of the Measuring and Test Equipment (M&TE) and controlled by YAP-12.3Q, *Control of M&TE and Calibration Standards*, and routines qualified per AP-SI.1Q, *Software Management* (see Table 1) were utilized.

Table 1. Software and Routines

Software	Software Tracking Number (STN)			Computer Usage
Earthvision V4.0	30035-2 V4.0			UNIX–plot tracer distribution
Routine	LBNL Scientific Notebook ID	Pages	Accession Number (ACC)	Computer Usage
Perm Formula 1 ft Zone.vi V.1.0 (It runs in Labview 4.1)	YMP-LBNL-JSW-PJC-6.2	p. 93	MOL.19991018.0188	PC–calculate air permeability
Mettler Double Scale 1.vi V.1.0 (and associated Labview sub vi)	YMP-LBNL-JSW-6a	pp. 17-30	MOL.19991018.0189	PC–acquire weight data of seepage with Mettler balances
	YMP-LBNL-JSW-6b	pp. 14-150		
	YMP-LBNL-JSW-6c	pp. 41-50		
	YMP-LBNL-RCT-1	pp. 62-73		

No models were used for the analyses performed in this AMR.

INTENTIONALLY LEFT BLANK

4. INPUTS

Field data collected from the ESF that characterize ambient and testing conditions include the following:

- Pneumatic pressure and air-permeability data from alcoves 4 and 6
- Pneumatic pressure and air-permeability data (pre- and post-excavation) for ESF niches
- Laboratory dye measurements and sorptivity data
- Seepage and liquid-release data
- Water-potential data from niche walls and boreholes
- Fracture aperture and frequency data

4.1 DATA AND PARAMETERS

The properties resulting from the analyses of the above field data include air-permeability distribution, fracture network connectivity, fracture flow-path distribution, seepage percentage, seepage threshold, fracture characteristic curve, formation intake rate, wetting-front travel time, fracture porosity, fracture volume, fracture flow fraction, tracer distribution, matrix imbibition, retardation factor, fault and matrix flow, water-potential distribution, construction-water migration, relative humidity, and moisture conditions.

The input data used in this AMR are summarized in [Table 2](#). The Q-status of these data are provided in [Attachment I](#) and the DIRS database.

Reports documenting past experimental work related to ambient field testing at Yucca Mountain are listed in Section 8.5, Supporting Bibliography. This bibliography is for information only, and this AMR does not directly rely on any of the listed documents.

Table 2. Input Data and Data Tracking Numbers

Data Description	DTN
Geological map of Alcove 4	GS960908314224.020
Relative humidity, temperature, and pressure in ESF monitoring stations	LB960800831224.001
Moisture data report from October 1996 to January 1997	LB970300831224.001
Moisture-monitoring data collected at ESF sensor stations, before and after the completion of the ESF	LB970801233124.001
Moisture-monitoring data at moisture stations	LB970901233124.002
Water-potential measurements in Niches 3566 and 3650	LB980001233124.001
Air-permeability data from air-injection testing in niches	LB980001233124.002
Liquid-release testing in Niches 3650, 3107, and 4788	LB980001233124.004
Data collected from niche at construction station 3650: VA Supporting Data	LB980101233124.001
Post-excavation permeability data collected from Niche 3650 of the ESF	LB980101233124.002
Pneumatic pressure and air permeability data from Niches 3107 and 4788 in the ESF	LB980901233124.101
Laboratory dye measurements and sorptivity data	LB980901233124.002
Liquid-release and tracer testing data from Niches 3566, 3650, 3107, and 4788	LB980901233124.003
Pneumatic pressure and air permeability data from Alcove 6 in the ESF	LB980901233124.004
Pneumatic pressure and air-permeability data from Alcove 4 in the ESF	LB980901233124.009
Borehole monitoring at the single borehole in the ECRB and ECRB crossover point in the ESF	LB980901233124.014
Air-injection data from Niche 3107 of the ESF	LB980912332245.001
Pneumatic pressure data from Niches 3 and 4 (3107 and 4788) in the ESF	LB990601233124.001
Liquid-release test data	LB990601233124.002
Tracer data	LB990601233124.003

4.2 CRITERIA

At this time, no specific criteria (e.g., System Description Documents) have been identified as applying to this analysis activity in project requirements documents. However, this AMR provides information required in specific subparts of the proposed U.S. Nuclear Regulatory Commission rule 10 CFR 63 (see Federal Register for February 22, 1999, 64 FR 8640). It supports the site characterization of Yucca Mountain (Subpart B, Section 15), the compilation of information regarding the hydrology of the site in support of the License Application (Subpart B, Section 21(c)(1) (ii)), and the definition of hydrologic parameters used in performance assessment (Section 114(1)).

The DOE interim guidance (Dyer 1999), requiring the use of specified subparts of the proposed NRC high-level waste rule, 10 CFR Part 63 (64 FR 8640), was released after completion of the work documented in this AMR; it has no impact on this work activity.

4.3 CODES AND STANDARDS

No specific formally established standards have been identified as applying to this analysis.

INTENTIONALLY LEFT BLANK

5. ASSUMPTIONS USED IN AMBIENT FIELD TESTING ANALYSES

This AMR on field testing of processes presents data collected in the ESF at Yucca Mountain. The first group of four testing activities contributes to the drift seepage study to characterize fracture systems at niche sites, to determine seepage thresholds, and to evaluate tracer distributions. The second group of three activities involves flow and transport tests in two slotted test beds. The third group of three activities concerns the effects induced by ventilation and construction-water usage along underground drifts.

The assumptions used in analyses of field-testing data are documented in this section. Depending on the status of the testing activities, the list of assumptions varies among different activities. Each of the ten activities is discussed in its own subsection. Each subsection in Section 5 on assumptions is related to the corresponding subsections in Section 6 on analyses and in Section 7 on conclusions. (i.e., Sections 5.1, 6.1, and 7.1 are on Activity 1, 5.2, 6.2, and 7.2 on Activity 2, etc.) The assumption subsection contents range from specific discussion of the equation used in data analysis to general comment on the uncertainties, approximations, and approaches used in interpreting the test results. Some cross references to the main text in Section 6 on analyses are presented, especially for activities entering the stage of intensive interaction between data collection and test interpretation. The specific assumptions used in analyzing the test results are assigned ordering numbers for cross referencing, with the main descriptions summarized in [Table 3](#). Approximations and approaches are summarized in bulleted lists.

Table 3. Assumptions

Ordering Number	Summary Description	Application Context	Justification or Evaluation Section	Assumption Used Section
1	Air as ideal gas	Air-permeability calculation formula	5.1	6.1.2.1 6.1.2.2
2	Flow around finite line source			
3	Air-flow through fractures, Darcy's law			
4	Saturated liquid permeability equal to air permeability	Saturated hydraulic conductivity estimation	Attachment III	6.2.2.1
5	Gravity-driven liquid-flow, Darcy's law			
6	Steady-downward flow through homogeneous, isotropic, infinite porous medium	Philip's capillary barrier solution	6.2.2.2	6.2.2.2
7	One-dimensional flow	Braester's wetted profile solution	Attachment IV	6.2.2.3
8	Downward translation of wetted profile at constant velocity			

5.1 ASSUMPTIONS USED IN BOREHOLE AIR-PERMEABILITY CALCULATIONS

In air-permeability tests, permeability values were obtained from pressure changes and flow rates using an analytic formula (modified Hvorslev's solution given in Section 6.1.2.1) derived from the following assumptions.

Assumption 1: Air behaves as an ideal gas.

This assumption is very nearly true at the ambient temperatures and pressures used in the air-permeability tests. It is our current judgement that no justification or evaluation of this assumption is required for the ambient field testing conditions. This assumption is used in the equation presented in Section 6.1.2.1.

Assumption 2: Finite line source is used to represent a borehole injection interval.

This assumption is applied to the borehole injection interval where all air flow is assumed to be in the radial direction, and none in the axial direction. This is in general a good assumption if the length of injection is longer than its radius. In the air-permeability tests, the length of injection zone was 0.3048 m and the radius of the borehole was 0.0381 m. The injection zone is a long, thin cylinder. Flows along axial directions were blocked by packers, and occurrences of packer leaks were monitored by pressures in adjacent borehole intervals, as described in [Attachment II](#).

Although the fractured tuff of the niches is not a homogenous or infinite medium, the equation provides a consistent method of obtaining a permeability value for an equivalent homogeneous case and enables comparison of the test results for various injection locations which is the focus of these tests. Because the heterogeneity of the surrounding medium is not known *a priori*, the permeabilities calculated by analytic formula are estimates of effective values around the injection borehole intervals. The results of the air-permeability tests are used to characterize the heterogeneity of the medium of niche sites and test beds. The main test results using this assumption are presented in Sections 6.1.2.1 and 6.1.2.2 for the niches.

Assumption 3: Air flows are mainly through fractures and are governed by Darcy's law.

For the ambient conditions with unsaturated states in fractured tuff at Yucca Mountain, the liquid is mainly confined to the matrix from capillarity considerations, and the gas flows mainly through the fractures, which have higher permeability values than the tuff matrix. Darcy's law for laminar flows is used to relate flux to pressure and gravitational gradients. Additional effects due to turbulent flow and gas-slip flow phenomena (Klinkenberg 1941) are assumed to be negligible. It is our current judgement that no justification or evaluation of this assumption of Darcy's law for air flows in fractures is required for the ambient field testing conditions. The analytic equation is used in Section 6.1.2.2. Small effects potentially associated with movement of residual water within the fractures are discussed in [Attachment II](#).

5.2 ASSUMPTIONS USED IN ANALYZING AND INTERPRETING THE NICHE LIQUID-RELEASE AND SEEPAGE TEST DATA

In liquid tests for seepage quantification, the saturated conductivities are estimated from air permeability values, the fracture capillarities are estimated from the seepage threshold fluxes, and the water potentials are estimated for the flow paths from the liquid-release interval to the niche ceiling. The following assumptions are used to derive the seepage parameters.

5.2.1 Assumptions Used in Estimating Saturated Hydraulic Conductivity Using Air Permeability

Permeability is an intrinsic parameter characterizing the resistance to flow by the rock medium. For laboratory test conditions with well defined uni-directional flow path through a core specimen, the permeability value is independent to the fluid used in the measurement. In the field conditions associated with localized injections, the flow path followed by the air is different from the flow path followed by the liquid. The following assumptions, together with detailed evaluation in [Attachment III](#), addresses the relationship between air permeability and liquid permeability in the niche seepage tests.

Assumption 4: Saturated liquid permeability is equal to air permeability.

For locally saturated conditions such as in the immediate vicinity of a liquid-filled borehole interval, the saturated permeability to liquid flow is assumed to be equal to the permeability measured in air-injection tests. The saturated liquid flux is estimated from the air-permeability value and the wetted area of the borehole, as described in [Attachment III](#).

The estimations of saturated liquid permeability are evaluated in [Attachment III](#) from available data collected in the niche studies. The evaluation compares the estimated flux values with measured flux values for cases with evidence that the borehole intervals tested are in saturated conditions with return flows observed. With liquid flow mainly through fractures below the borehole interval due to gravity drainage and air flow into fractures all around the borehole interval driven by pressure gradient, the liquid permeability and air permeability represent the effective values of different fracture flow paths. The evaluation of the difference between liquid permeability and air permeability is documented in [Attachment III](#). The evaluation requires also the following assumption.

Assumption 5: Gravity-driven flow is the primary flow mechanism in fractures with weak capillarity and liquid fracture flows are governed by Darcy's law.

Under unsaturated conditions, capillary forces and gravity are driving mechanisms for flow. Since the capillary strength is inversely related to the pore sizes and fracture apertures, it is a reasonable assumption to neglect fracture capillarity and use the gravity gradient to estimate the flux. The small fracture capillarity is evaluated in Section 6.2.2.2. It is our current judgment that no justification or evaluation of using Darcy's law for fracture flows is required for the ambient field testing conditions. The assumption is used in [Attachment III](#) and in Section 6.2.2.1 where seepage threshold fluxes are compared with estimated hydraulic conductivities.

5.2.2 Assumptions Used in Deriving the Capillary Strength of the Fractures Based on a Philip's Capillary Barrier Solution

Philip et al. (1989) developed an analytical solution describing under what conditions water will flow from an unsaturated porous medium into a buried cylindrical cavity. The solution is used in Section 6.2.2.2 to compute the sorptive number, α , a hydraulic parameter that is related to the strength of the capillary forces exerted by the porous medium. Philip et al. (1989, pp. 16–18) assumed the following in the analysis:

Assumption 6: Steady-downward flow of water through a homogeneous, isotropic unsaturated porous medium is assumed. Far from the cavity, the flow velocity is spatially uniform. The flow region is infinite in extent.

Philip et al. (1989, Section 1.5, p. 17) note, however, that the requirement for homogeneity is relatively weak. Analytic solutions are generally derived in most cases with simplified descriptions and assumptions about the flow domain in the surrounding medium. The results derived from an analytic solution represent effective values. The description, evaluation, and justification of Philip's capillary barrier solution are presented in Section 6.2.2.2.

5.2.3 Assumptions Used in Deriving the Estimated Volumetric Water Content for the Fractures Based on Braester's Wetted Profile Solution

Braester (1973) derived a time-dependent solution for the average volumetric water content distribution in a porous medium that results from the water release from a surface source of constant flux. This solution is described and used to estimate the volumetric water content of the fractures in Section 6.2.2.3. In addition to using Darcy's law for an unsaturated fractured medium, similar to Assumptions 3 and 5 described above, the following assumptions were used by Braester (1973) to derive the solution.

Assumption 7: A one-dimensional (1-D) formulation of Richard's equation, which includes both gravity and capillary-driven components of flow, is used to describe flow through an unsaturated porous medium.

The 1-D flow approximation can be evaluated and justified by (1) the weak fracture capillarity values described in Section 6.2.2.2, (2) by the roughly 1-D flow paths observed during niche excavation described in Section 6.2.1.2, and (3) by the limited spatial spread of seepage fluxes observed during post-excavation seepage tests described in Section 6.2.1.3.1. The evaluation of this assumption is addressed further in [Attachment IV](#).

Assumption 8: The downward translation of a wetted profile is at constant velocity.

The average value of the water content at the infiltrating surface over time is assumed by Braester (1973, p. 688) to be equal to the average value of water content over the wetted depth. This approximation becomes valid if the solution of water content takes the form of a downward translation of the entire wetted profile at constant velocity. This would generally occur after the capillary forces near the source have diminished and the volumetric water content at the soil surface reaches its steady-state limit, with the gravity gradient driving the liquid flux. The times

needed to reach steady state and the evaluations of this assumption of downward translation of wetted profiles at constant velocity are addressed further in [Attachment IV](#).

The following approximations are also used in Section 6.2.2.3 with Braester's solution to estimate water content.

- Residual water content in fractures is negligible. This approximation is reasonable for fracture flow paths, which are likely to be dry under ambient conditions, with liquid mainly residing in the matrix.
- A linearized solution is used to provide a reasonable approximation of the water content at the infiltrating surface and the advance of the wetting front. The evaluations of the solutions by Braester's solution are discussed in Section 6.2.2.3.

5.3 APPROXIMATIONS USED IN TRACER-MIGRATION DELINEATION AT NICHE 3650

Tracer measurements were conducted on cores collected at Niche 3650. Twelve boreholes were drilled around the last liquid-release point. The core analyses delineated the spatial distributions of the specific tracers released in the last liquid-release event as well as tracers used in previous tests in the fractured rock mass above the niche ceiling. The following approximations were used in the analysis and interpretation of tracer results.

- Iodine and various dye tracers were used in the liquid-release tests and were analyzed on samples along the boreholes. Iodine was treated as a nonreactive conservative tracer. Dyes were used to trace the main flow paths through the fractures.
- Higher ratios of detected tracer concentration to the background concentration indicated the stronger presence of tracers. The ratio representation was used to minimize the dependence of test results on measurement sensitivity and tracer purity associated with different dyes and chemicals.
- Locations of subsamples were estimated from information of the rock sample packets. The spatial resolutions were poor, especially for fragmented samples.
- The absence of tracers in the twelve surrounding boreholes was used to indicate the localization of liquid released in the central borehole.

5.4 APPROXIMATIONS USED IN ANALYSES OF TRACER PENETRATION AND WATER IMBIBITION INTO WELDED TUFF MATRIX

Tracer-stained rock samples were collected during niche excavation for laboratory analyses. Clean rock samples collected from the same stratigraphic unit were used to evaluate the relative extents of dye penetration, tracer penetration, and water imbibition. The following approximations were used in the analysis and interpretation of test results.

- Dye-stained rock samples collected during niche excavations were associated with liquid-release tests conducted before niche excavations.
- Initial concentrations were derived from weights of tracers divided by water volumes.
- Rock powders from drilling into field samples and lab cores to different depths were used in determining tracer profiles.
- Visual observations on cores were used to determine water penetration.

5.5 APPROXIMATIONS USED IN CROSS-HOLE CONNECTIVITY ANALYSES

The cross-hole data were acquired at the same time as the single-hole data (as described in Section 5.1), by logging the steady-state pressure response in all the noninjected (observation) zones while performing an injection. Observation response pressure is a function of the injection pressure, the connectivity between zones, and the distance between zones. In practice it is not well understood, in the fractured rock, how to normalize response to distance. Attempts at dividing pressure response by any function of distance result in the apparent connectivity being skewed to the more distant zones. Distance is thus not included in the approximation used in cross-hole analyses. The approximation uses the simple ratio of observation response pressure to injection pressure. If a test is performed at low pressures at twice the injection pressure change, the response change should also be twice. The ratio is

$$\frac{\Delta P_{res}}{\Delta P_{inj}}$$

where

ΔP_{res} is the steady-state pressure rise above ambient at the observation location, and

ΔP_{inj} is the steady-state pressure rise in the injection zone.

The ratio provides a measure of how well a response zone is connected to an injection zone in relation to that response zone's connections to the rest of the site. The value enables all the observation responses from all injections at a site to be directly compared, so that they can all be viewed on a single three-dimensional (3-D) diagram instead of individual diagrams for each tested injection zone.

5.6 APPROXIMATIONS USED IN ANALYSES OF FRACTURE FLOW IN FRACTURE-MATRIX TEST BED AT ALCOVE 6

Flow tests were conducted in a test bed at Alcove 6 in the ESF within the Tptpmn unit. The test bed has a slot excavated below a cluster of boreholes. Wetting front detectors in monitoring boreholes and seepage collection trays in the slot were developed to evaluate the evolution of flow field in response to liquid releases and injections into localized zones along an injection

borehole. The following approximations were used in the interpretation and analysis of test results.

- Wetting front arrivals were indicated by decreases in electrical resistance of probes in contact with the borehole walls and by increases in water potentials measured by psychrometers.
- Seepage arrivals in the slot within minutes to hours after liquid injections were interpreted to be associated with fracture flow paths.
- Drainage into the slot after termination of injection for each test was interpreted to be a measure of the volume of the fracture flow paths.

5.7 APPROXIMATIONS USED IN ANALYSES OF FLOW THROUGH THE FAULT AND MATRIX IN THE TEST BED AT ALCOVE 4

Flow tests were conducted in a test bed at Alcove 4 in the ESF within the PTn unit. The test bed has a series of horizontal boreholes underlain by a single slot. Water was injected into isolated zones within some of these boreholes, and the resulting water plume was then monitored as it migrated past adjacent boreholes. The following approximations were used in the interpretation and analysis of the test results.

- Wetting front arrivals were indicated by decreases in electrical resistance of probes in contact with the borehole walls and increases in water potentials measured by psychrometers.
- Fast travel times, observed following injection of water in the borehole through the fault, were interpreted to be associated with flow through the fault.

5.8 APPROXIMATIONS USED IN WATER-POTENTIAL MEASUREMENTS IN NICHES

Potential measurements were measured in boreholes with psychrometers, with the following approximation:

- Psychrometers in the boreholes were in approximate equilibrium with the moisture in the borehole interval.

5.9 APPROXIMATIONS USED IN MONITORING CONSTRUCTION-WATER MIGRATION

Construction-water migrations were monitored at the starter tunnel of the Cross Drift and at the cross-over point in the Main Drift, with the following indications:

- Construction-water arrivals at a borehole below the invert were indicated by decreases in electrical resistance of probes in contact with the borehole walls and increases in water potential measured by psychrometers.
- Construction-water arrivals to the Main Drift below the Cross Drift would be indicated by wetting of the drift walls and seepage into a water-collection system.

5.10 APPROXIMATIONS USED IN VENTILATION-INDUCED MOISTURE REMOVAL RATE

Moisture data collected by moisture-monitoring stations can be used to estimate the moisture removal rate, if the ventilation rate is known or estimated. The pertinent estimations involve the following approximations:

- Vapor density is determined by the relative humidity multiplied by the saturated vapor density. The saturated vapor density can be determined by the temperature from a standard steam table.
- Equivalent evaporation rate can be calculated with vapor-density differences multiplied by the ventilation flow rate and divided by the total drift wall area between two stations.

6. ANALYSES OF AMBIENT FIELD TESTING DATA

This section of AMR U0015 describes the field testing results of processes in the ESF at Yucca Mountain. The field activities include drift seepage tests in four niches, fracture-matrix interaction tests in Alcove 6, Paintbrush flow tests in Alcove 4, potential monitoring, construction-water migration, and moisture-monitoring studies in the ESF Main Drift and in the ECRB Cross Drift.

Sections 6.1 and 6.5 present the test site characteristics of niches and alcoves from pneumatic air-permeability test results. Section 6.2 shows that drift-seepage thresholds exist and that seepage threshold data can be interpreted with capillary barrier theory. It also presents liquid-flow path data for niche sites. Sections 6.3 and 6.4 present laboratory measurement results for tracer migration and matrix imbibition for welded tuff samples from the ESF. Section 6.6 presents the results of two series of fracture-matrix interaction tests to quantify the partition of flux into fast and slow components. Section 6.7 presents the results for flow tests in the Paintbrush nonwelded tuff (PTn) test bed. Sections 6.8–6.10 summarize data collected on ambient water-potential distribution, construction-water migration, and moisture conditions.

The tests performed in niches and alcoves along the ESF are illustrated in [Figure 4](#). Seepage into drifts at the potential repository level is related to water percolating down from the ground surface. Drift seepage tests at the niche sites quantify the seepage from liquid pulses released above the niches. Percolation flux has a fast fracture-flow component and a slow matrix-flow component. This partitioning of flow is evaluated at the fracture-matrix test bed in Alcove 6. The heterogeneous hydrogeologic setting with alternating tuff layers determines the percolation distribution throughout the UZ with input from infiltration at the surface boundary. The mechanism of redistributing near-surface fracture flow by the porous PTn, especially the flow-damping process by the PTn unit, is studied in a test bed in Alcove 4 that consisted of layered, altered and bedded tuffs that were transected by fractures and a fault. Wetter climate conditions increase the infiltration, as quantified in an artificial infiltration test in Alcove 1 and in moisture monitoring at depth in Alcove 7. The seepage threshold data from Niche 3650 are inputs to an AMR on seepage calibration model. The Alcove 1 data are inputs to an AMR on model validation.

[Figure 4](#) lists major TSPA issues (DOE 1998a) related to UZ flow processes of seepage, percolation, and infiltration. The tests illustrated in [Figure 4](#) focus on different issues to quantify the functional relationships among these processes. Seepage is hypothesized to be smaller than the percolation flux resulting from capillarity-induced drift diversion, while percolation may be smaller than the infiltration because of lateral diversion of water along tuff interfaces to bounding faults. All tests use tracers to assist the characterization of plume migration.

[Figure 5](#) illustrates the Cross Drift to ESF Main Drift seepage collection system to study the migration of water and tracer flow from one drift to another drift. The cross-over point is located in the northern part of the ESF, as illustrated in [Figures 1 and 2](#). In 1998, the seepage monitoring system was used to monitor the migration of construction water from the Cross Drift. Niche 3107, currently used for the drift seepage study, will be part of the drift-to-drift study as a monitoring station. The existing horizontal boreholes at Niche 3107 will be used for wetting

front monitoring for liquid released from a new alcove excavated horizontally from the Cross Drift and directly above the niche.

Each testing activity has unique findings to contribute to the assessment of unsaturated flow and transport processes at Yucca Mountain. The progress and analyses of field-test results are presented in the following ten subsections for ten testing activities. Key scientific notebooks (with relevant page numbers) used for recording the ESF Field Testing activities and analyses described in this AMR are listed in Table 4.

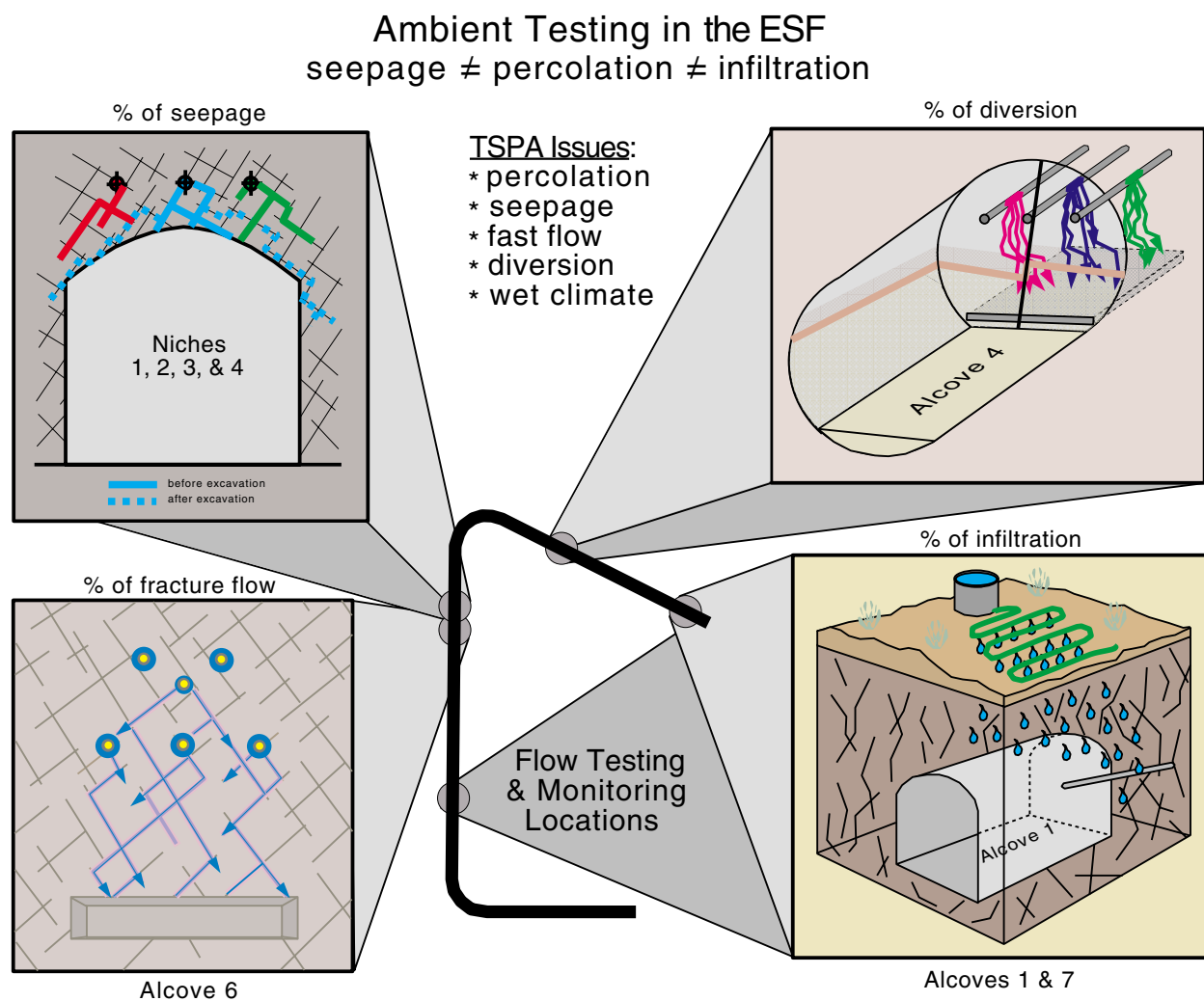


Figure 4. Schematic Illustration of Flow Tests in the Exploratory Studies Facility at Yucca Mountain. The tests evaluate functional relationships between unsaturated zone processes to resolve TSPA issues.

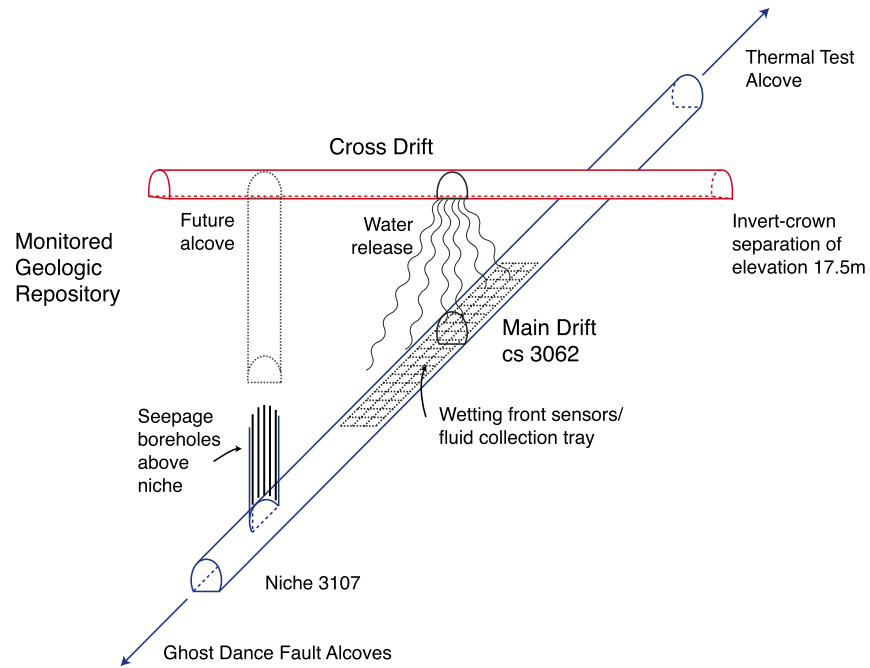


Figure 5. Schematic Illustration of the Cross-Over Point of Cross Drift with the Main Drift. Wetting front sensors and fluid collection trays monitored the construction-water migration. Both the Cross Drift and the Main Drift, together with the future alcove and niche boreholes are horizontal.

Table 4. Scientific Notebooks

LBL Scientific Notebook ID	M&O Scientific Notebook ID	Pages	Accession Number (ACC)
YMP-LBNL-JSW-6	SN-LBNL-SCI-065-V1	pp. 1-156	MOL.19991013.0459
YMP-LBNL-JSW-6a	SN-LBNL-SCI-066-V1	pp. 1-156	MOL.19991013.0460
YMP-LBNL-JSW-6b	SN-LBNL-SCI-121-V1	pp. 1-156	MOL.19991013.0461
YMP-LBNL-JSW-6c	SN-LBNL-SCI-122-V1	pp. 1-156	MOL.19991013.0462
YMP-LBNL-JSW-QH-1	SN-LBNL-SCI-089-V1	pp. 1-156	MOL.19991013.0463
YMP-LBNL-JSW-QH-1A	SN-LBNL-SCI-090-V1	pp. 20-22, 37-48, 54, 68-82, 86-99, 103-126	MOL.19991013.0464
YMP-LBNL-JSW-QH-1B	SN-LBNL-SCI-091-V1	pp. 9, 27, 35, 40, 42, 48-73, 77, 81-94, 107-110, 115, 118-119, 123-142, 149, 154-155	MOL.19991013.0465
YMP-LBNL-JSW-QH-1C	SN-LBNL-SCI-092-V1	pp. 13, 16-25, 39-41, 51-102, 105-112, 116, 128-133, 139-140, 143-145	MOL.19991013.0466
YMP-LBNL-JSW-QH-1D	SN-LBNL-SCI-093-V1	pp. 3-151	MOL.19991013.0467
YMP-LBNL-JSW-QH-1E	SN-LBNL-SCI-154-V1	pp. 3-16	MOL.19991013.0468
YMP-LBNL-JSW-PJC-6.2	SN-LBNL-SCI-078-V1	pp. 1-99	MOL.19991013.0469
YMP-LBNL-JSW-RS-1	SN-LBNL-SCI-102-V1	pp. 1-115	MOL.19991013.0470
YMP-LBNL-JSW-RS-1a	SN-LBNL-SCI-104-V1	pp. 1-39	MOL.19991013.0471
YMP-LBNL-JSW-RS-2	SN-LBNL-SCI-105-V1	pp. 1-7	MOL.19991013.0472
YMP-LBNL-JW-1.2	SN-LBNL-SCI-048-V1	pp. 103-152	MOL.19991025.0235
YMP-LBNL-JW-1.2A	SN-LBNL-SCI-133-V1	pp. 1-43	MOL.19991013.0473
YMP-LBNL-JSW-JJH-1	SN-LBNL-SCI-088-V1	pp. 1-68	MOL.19991013.0474
YMP-LBNL-JSW-CMO-1	SN-LBNL-SCI-042-V1	pp. 1-59	MOL.19991013.0475
YMP-LBNL-JSW-4.3	SN-LBNL-SCI-116-V1	pp. 1-24, 61-67, 74-81	MOL.19991018.0187
YMP-LBNL-JSW-JS-1	SN-LBNL-SCI-150-V1	pp. 18, 148	MOL.19991013.0476
YMP-LBNL-RCT-1	SN-LBNL-SCI-113-V1	pp. 62-73, 88-150	MOL.19991013.0477
YMP-LBNL-RCT-2	SN-LBNL-SCI-156-V1	pp. 27-34	MOL.19991013.0478

6.1 AIR-PERMEABILITY DISTRIBUTIONS AND EXCAVATION-INDUCED ENHANCEMENTS

Pneumatic air-permeability tests were undertaken at various locations in the ESF to characterize the potential fluid flow paths in the rock. The potential repository host rock consists predominantly of unsaturated, fractured welded tuff. As assumed in Section 5.1, air flows are mainly through the fractures. Air-permeability tests are utilized to study the fracture heterogeneity. Air-permeability tests can characterize fractured systems efficiently. Once the injections stop, the pressure field returns to its ambient conditions within minutes under most field-test conditions.

To determine potential flow paths in the test sites, packer assemblies were used to isolate intervals in clusters of boreholes drilled into the fractured rock to perform pneumatic testing. In these tests, air is injected into specific intervals at constant mass flux while pressure responses are monitored in other intervals. The objectives for pneumatic testing include profiling the air permeability of boreholes along their length, investigating the effects of nearby excavation on the permeability of a rock mass, and enabling a site-to-site comparison of air-permeability statistics and related scale effects. Two basic types of data are readily available from pneumatic testing and are used to satisfy these testing objectives: (1) single-hole air permeability profiles, which are used for hole-to-hole and site-to-site comparisons, and (2) cross-hole pressure-response data, which enable a determination of connectivity through fracture networks between locations at a given site. This section focuses on the permeability profiles for boreholes in four niche sites. Permeability profiles before niche excavation are compared with profiles measured after niche excavation. Section 6.5 focuses on cross-hole data analyses.

6.1.1 Niche Test Site and Borehole Configuration

A number of tunnels, known as alcoves, and also room-size excavations, called niches, have been excavated at sites along the ESF. Extensive cross-hole air permeability measurements have been made in borehole clusters at four of the niches and at two of the alcoves within the ESF tunnel, as part of a program to select locations for liquid-release tests. The air permeability along each borehole in a cluster serves as a guide to the selection of the liquid-release intervals.

6.1.1.1 Site Selection

The niche sites were selected for study based on fracture and hydrologic data collected in the ESF, as illustrated in [Figure 6](#). Four niches were excavated along the Main Drift of the ESF. The first niche site is located at Construction Station (CS) 35+66 (hereafter referred to as Niche 3566) in a brecciated zone between the Sundance fault and a cooling joint where a preferential flow path is believed to be present (based on elevated $^{36}\text{Cl}/\text{Cl}$ ratios described in the AMR on geochemistry data). Niche 3566 is sealed with a bulkhead to permit long-term monitoring of *in situ* conditions. The second niche site is located at CS 36+50 (Niche 3650) in a competent rock mass with lower fracture density than Niche 3566. The third niche is located at CS 31+07 (Niche 3107) in close proximity to the cross-over point located at CS 30+62. Future plans include constructing a test alcove (Alcove 8) from the Cross Drift to a position immediately above Niche 3107 so that a large-scale seepage test can be conducted at this location. The fourth niche site is

located at CS 47+88 (Niche 4788) and is located in a 950-m-long exposure of the middle nonlithophysal zone referred to by Buesch and Spengler (1998, p. 19) as the intensely fractured zone. Each of the existing niches described above consist of a short drift, or mined opening, constructed on the west side of the ESF main drift within the middle nonlithophysal zone of the Topopah Spring welded unit.

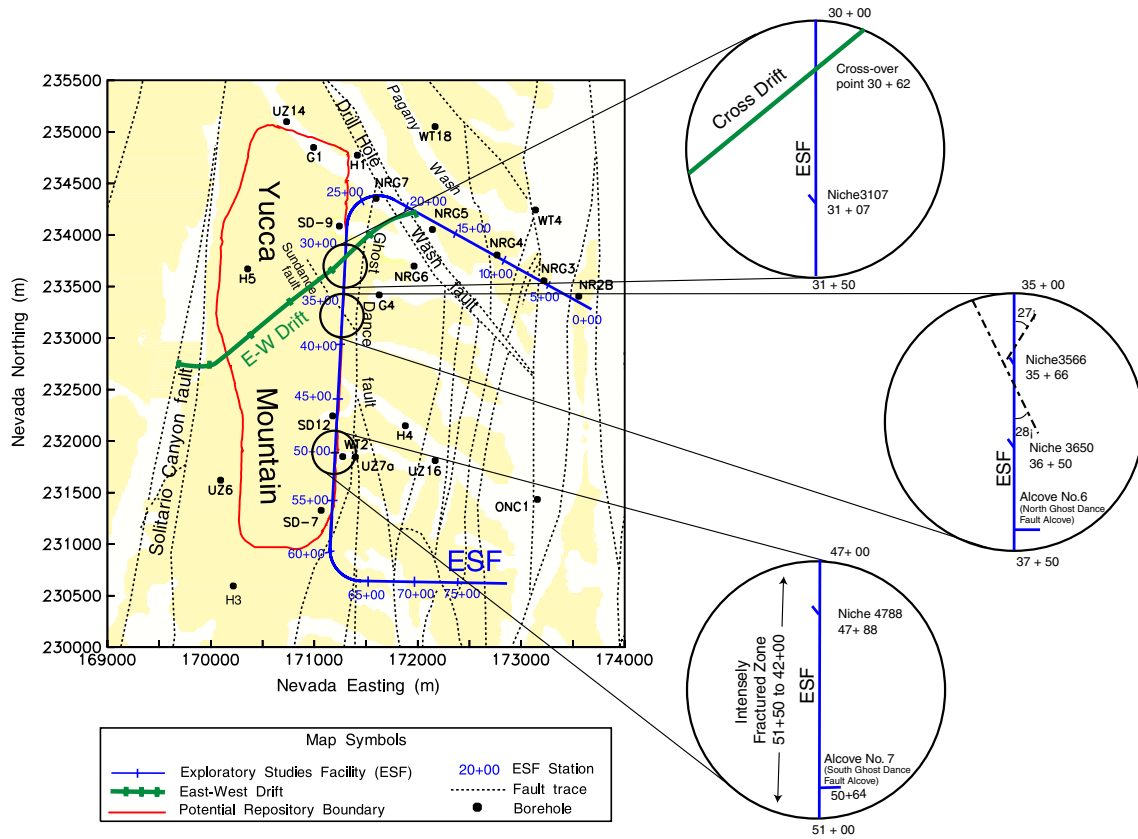


Figure 6. Schematic Illustration of Location Map for Niches 3107, 3566, 3650, and 4788.

6.1.1.2 Borehole Configuration

Three boreholes were installed at Niche 3566, and seven boreholes per niche were drilled at each of Niches 3650, 3107, and 4788 prior to excavation to gain access to the rock for testing and monitoring purposes. [Figure 7](#) shows the schematics of borehole clusters tested at the niche sites. At the niches, boreholes were drilled before excavation into both the rock to be excavated and the surrounding rock. Both types of boreholes were tested before niche excavation, and the surrounding boreholes were retested after excavation, allowing a study of excavation effects on the permeability of the surrounding rock. All boreholes shown in [Figure 7](#) are parallel to the niche axis as illustrated in [Figure 8](#). [Figures 7a and 8a](#) show that three boreholes were originally installed at Niche 3566 along the same vertical plane coincident with the center of the niche.² The three boreholes were assigned the designation U, M, and B, corresponding to the upper, middle, and bottom borehole, respectively. Boreholes M and B were subsequently removed when the rock was mined out creating the niche, and borehole U still remains. [Figures 7b and 8b](#) show the location of the seven boreholes installed at Niche 3650. Three of the boreholes, designated UL, UM, and UR (upper left, upper middle, and upper right), were installed approximately one meter apart and 0.65 m above the crown of the niche in the same horizontal plane. The remaining boreholes (ML, MR, BL, and BR) were drilled within the limits of the proposed niche and were subsequently mined out when the niche was constructed as planned.

[Figures 7c and 8c](#) show the final configuration of the seven boreholes installed at Niche 3107. The original intent was to install the middle boreholes ML and MR beyond the limits of the proposed excavation to monitor the movement of moisture around the niche during subsequent testing. Unfortunately, the middle boreholes were not installed at the correct elevation above Niche 3107 and were partially mined away during construction.

[Figures 7d and 8d](#) show the final configuration of the seven boreholes installed at Niche 4788. A misinterpretation of a survey mark, along with bad ground conditions (i.e., falling rock or collapsing ground conditions) at Niche 4788, also resulted in the partial loss of borehole ML at this site. The original plan was to install the U and M series boreholes outside the excavation.

After the excavation of Niche 3566, a special set of horizontal boreholes was drilled from within the niche into the walls and end of the niche in a radial pattern. A similar scheme was used at Niche 3107 after its excavation.

² As of the date of this AMR, as-built surveys had not been performed and/or the qualified survey data had not been released for use to determine the final configuration of the niche opening and location of the boreholes shown in [Figures 7 and 8](#). The figures were generated using field measurements recorded in scientific notebooks (YMP-LBNL-JSW-6, YMP-LBNL-JSW-6A, YMP-LBNL-JSW-6B, YMP-LBNL-JSW-6C, and YMP-LBNL-RCT-1) and/or using pre-built plans for niche construction. Therefore, [Figure 7](#) shows the idealized shape of the niche and approximate locations of the boreholes.

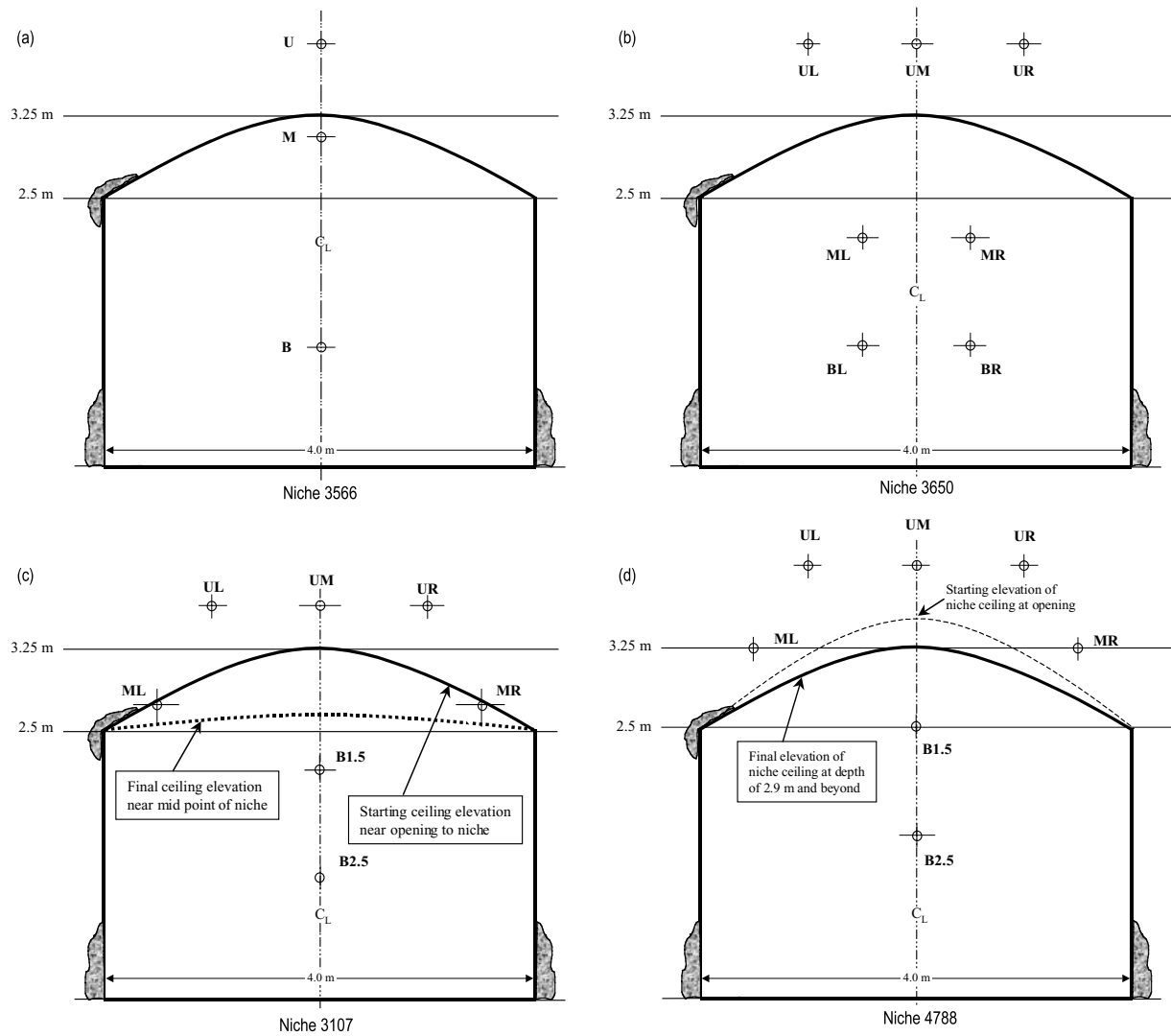


Figure 7. Schematic Illustration of the End View of Borehole Clusters at Niche Sites. The niche faces are on the west wall of the Main Drift of the Exploratory Studies Facility.

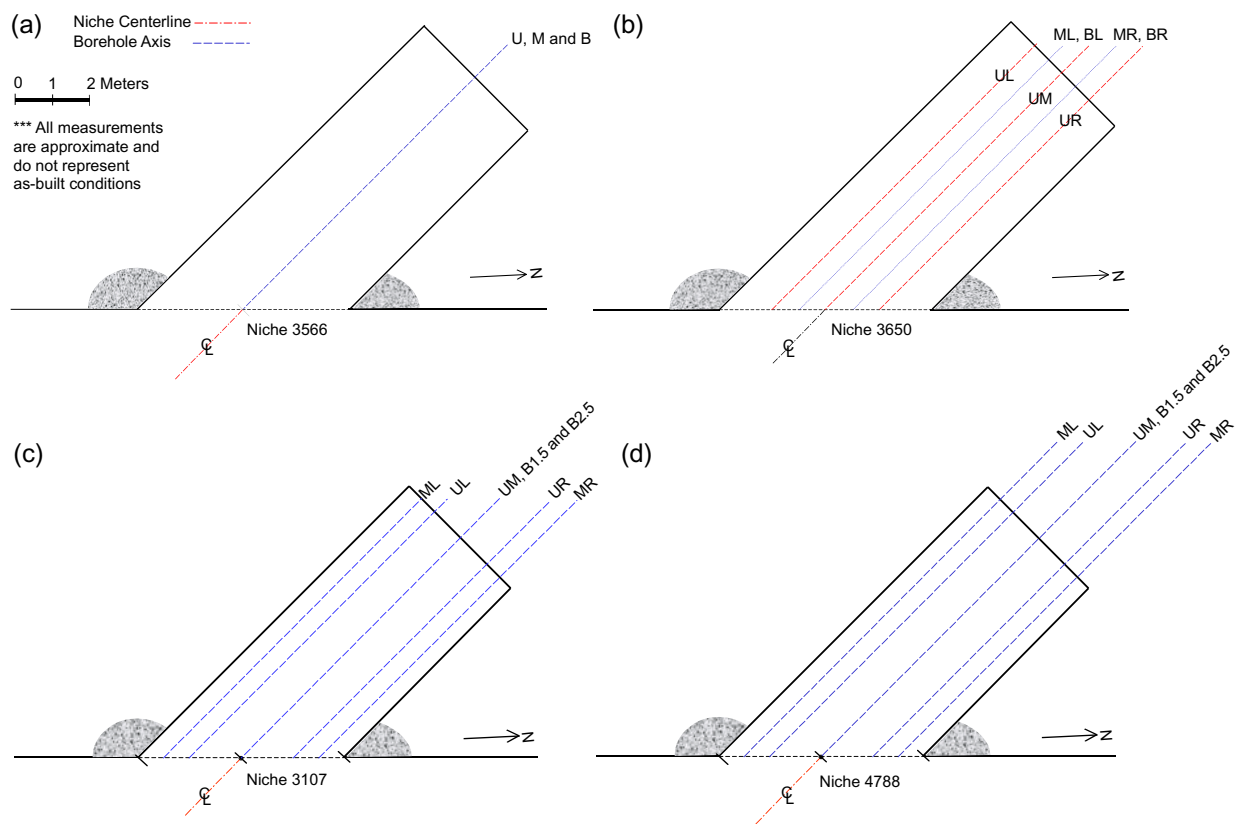


Figure 8. Schematic Illustration of the Plan View of Borehole Clusters at Niche Sites. The boreholes shown are oriented horizontally in the northwestern direction parallel to the niche axis.

6.1.2 Air-Permeability Spatial Distribution and Statistical Analysis

To date, an estimated 3,500 separate air injections have been undertaken in the *in situ* studies in the ESF. Nearly a quarter-million pressure-response curves have been logged in the studies. The number of tests lends itself to visualization and statistical comparison of the flow connections and the distributions of permeability in the rock mass. The specially designed equipment for pneumatic testing is described in Attachment II. With the equipment, it is feasible to conduct tests for site-to-site and borehole-to-borehole comparisons.

6.1.2.1 Data Reduction and Air-Permeability Determination

Data in the field were acquired in the form of voltage output from the various instruments and converted in real time or post-test time to physical units using each instrument's calibration data. At Niches 3107 and 4788, data acquisition was fully automated, so that log entries for each individual injection test could be done by computer and correlation with the data files linked. Each of these tests was given three minutes to reach steady state. Based on previous experience with the other tests, the maximum flow rate that did not cause the interval pressure to exceed the packer leak-by pressure was chosen for the purposes of the permeability calculations.

Because each injection test was repeated to accommodate two different observation packer configurations, there are two tests for each injection location from which to choose flow and

pressure data for the single-hole results. When graphed, the two are usually indistinguishable. Preference should be given to the lower of the two if there is a significant difference to further safeguard against packer leak-by effects.

Reported data consist of the acquisition filename, test location, time, date, channel or interval number, flow rate, start pressure, and steady-state pressure. The derived steady-state single-hole permeability can be obtained using the expression described below, with Assumptions 1, 2 and 3 discussed in Section 5.1.

In air-permeability tests to characterize the fracture heterogeneity of the test sites, permeability values are obtained from pressure changes and flow rates using the following modified Hvorslev's formula (LeCain 1995, Equation (15), p. 10):

$$k = \frac{P_{sc} Q_{sc} \mu \ln\left(\frac{L}{r_w}\right) T_f}{\pi L (P_2^2 - P_1^2) T_{sc}} \quad (\text{Eq. 1})^3$$

k	permeability, m ²
P_{sc}	standard pressure, Pa
Q_{sc}	flow-rate at standard conditions, m ³ /s
μ	dynamic viscosity of air, Pa-s
L	length of zone, m
r_w	radius of bore, m
T_f	temperature of formation, °K
P_2	injection zone pressure at steady-state, Pa
P_1	ambient pressure, Pa
T_{sc}	standard temperature, °K

For the purpose of calculation, standard pressure is 1.013E+05 Pa (one atmosphere). The dynamic viscosity of air used is 1.78E-05 Pa-s. Temperature contributions to Equation 1 are negligible with $T_f \sim T_{sc}$ for ambient temperature testing conditions.

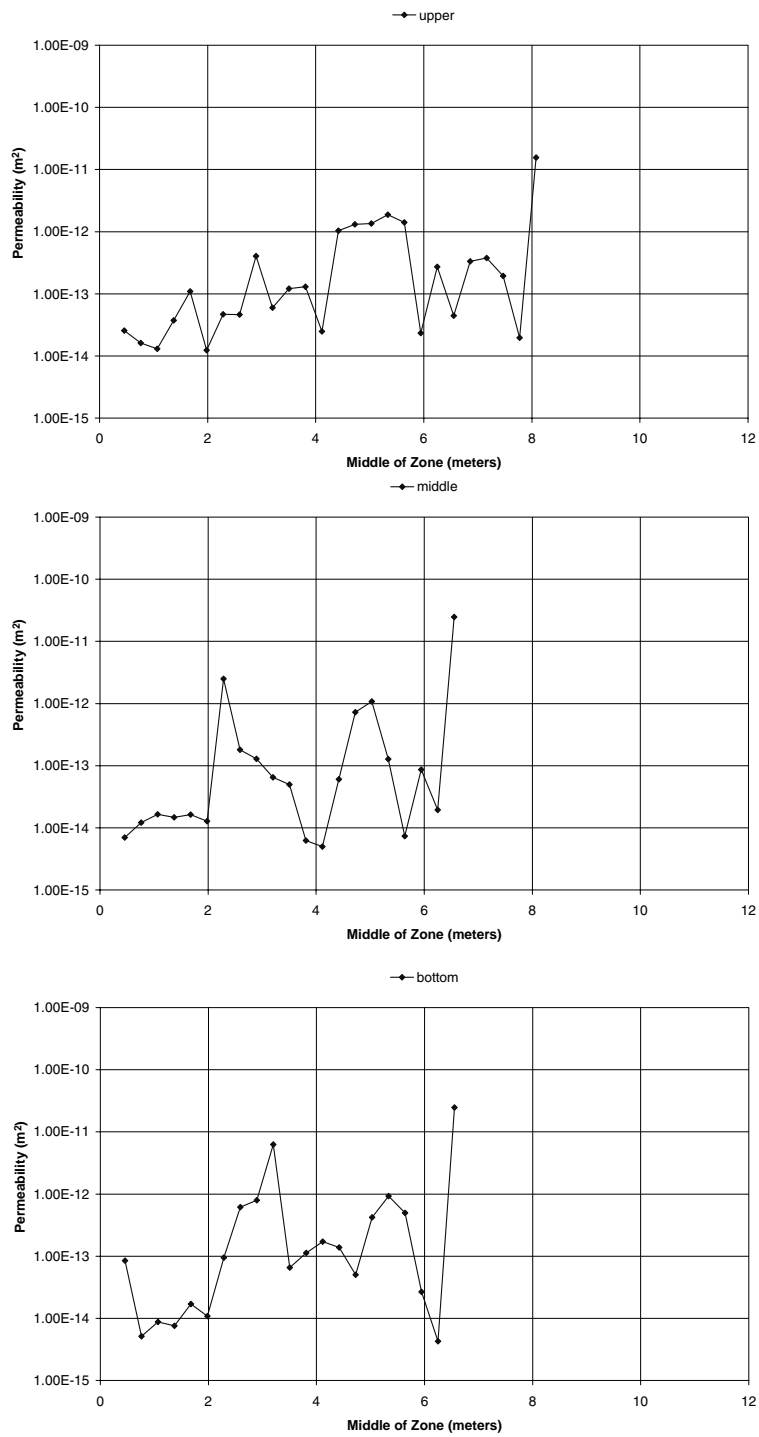
³ The solution is derived for the steady state ellipsoidal flow field around a finite line source. If the length L in the natural logarithm term in Equation 1 is replaced by an external radius R_e , this formula is identical to the cylindrical flow solution with an ambient constant pressure boundary at the external radius (Muskat 1982, p. 734). This replacement is used in Section 6.2.2.1 to estimate the saturated hydraulic conductivity for post-excavation liquid flow paths from the borehole interval to the niche ceiling.

6.1.2.2 Pre- and Post-Excavation Permeability Profiles

All boreholes at niches as illustrated in [Figures 7 and 8](#) are nominally 10 m long and 0.0762 m in diameter. The boreholes were drilled dry with compressed air to remove drill cuttings. The packer interval length and the test interval length are 0.3 m. The details of packer assembly and testing operation are described in [Attachment II](#).

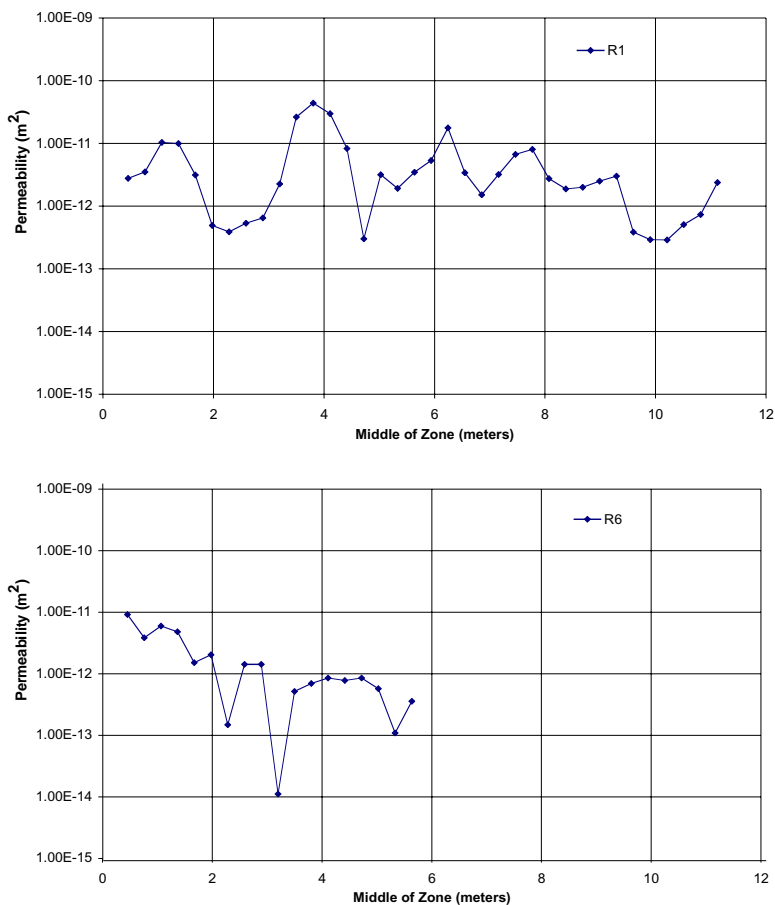
Permeability values along boreholes for four niches are presented in eight figures, with two figures for each niche. [Figure 9](#) illustrates three Niche 3566 permeability profiles along the upper, middle, and bottom boreholes, which are parallel to the niche axis. In [Figure 9](#) and subsequent figures of permeability profiles, the permeability value from each test interval is plotted against the location of the middle of the test interval (zone). The air-permeability tests were conducted before niche excavation. Niche 3566, the first niche excavated in the ESF, is located in the vicinity of the Sundance fault. The last data point in each permeability profile was the estimated value from tests conducted beyond the last packer interval. All three boreholes penetrated brecciated zones in the last one-third of the boreholes, with broken rock pieces preventing packer penetration. A wet feature in a brecciated zone was observed at the end of this niche right after completion of dry excavation (Wang et al. 1999, Figure 4, p. 331). The width of the wet feature is comparable to the borehole-interval length of 0.3 m, used in the air-permeability tests (this Section) and liquid-release seepage tests (Section 6.2).

After niche excavation, six additional horizontal boreholes were drilled from the inside of the niche, fanning out radially in different directions. The permeability profiles for two radial boreholes on the left side of the niche are illustrated in [Figure 10](#). These boreholes also penetrated brecciated zones. On average, the permeability values along the radial boreholes are higher than the average values in the three axial boreholes. However, the comparison is based on measurements in boreholes at different locations in the same niche site.



DTN: LB980001233124.002

Figure 9. Pre-Excavation Air-Permeability Profiles along Axial Boreholes at Niche 3566.

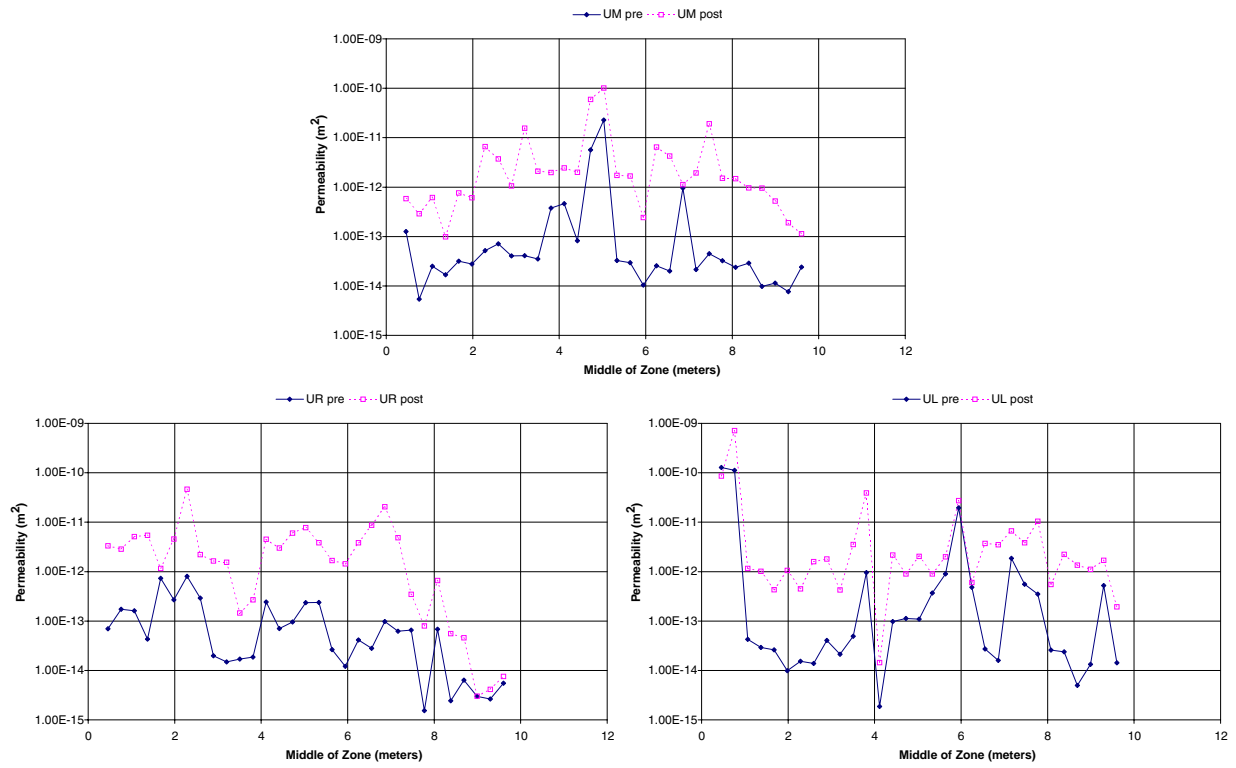


DTN: LB980001233124.002

Figure 10. Post-Excavation Air-Permeability Profiles along Radial Boreholes at Niche 3566.

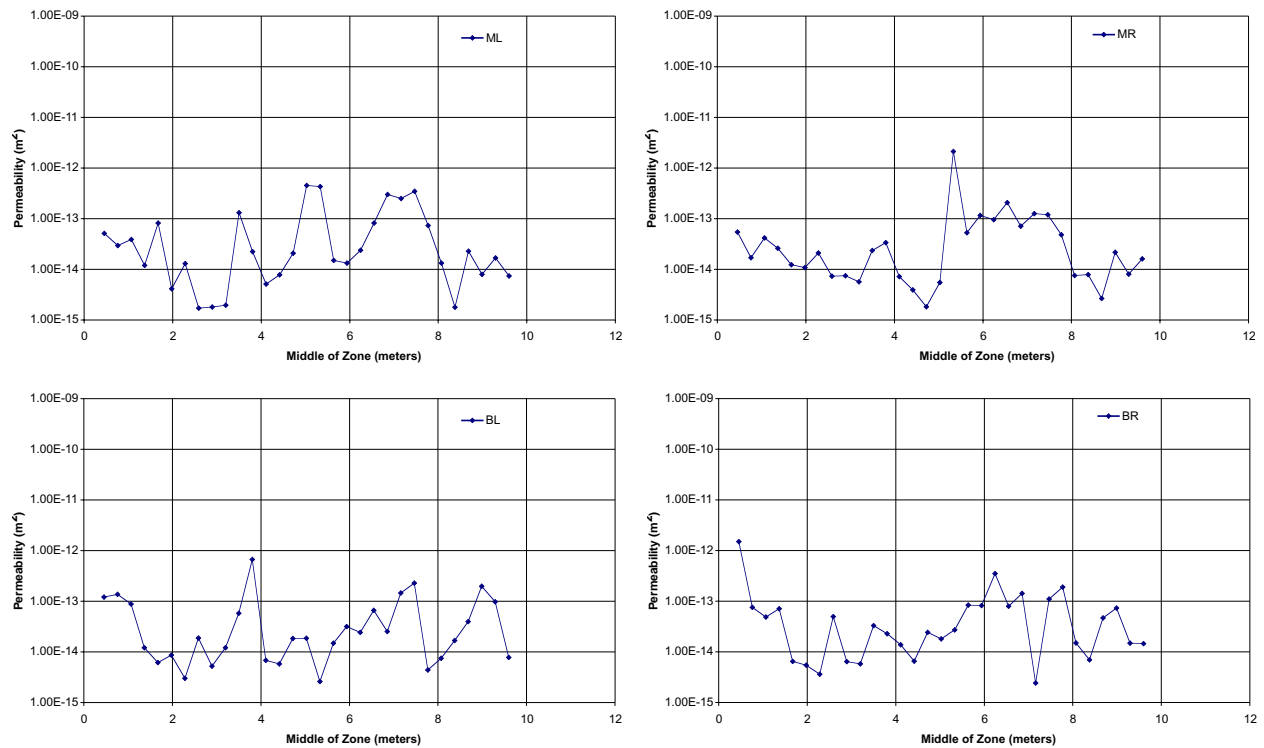
Figure 11 illustrates the permeability profiles along three upper boreholes at Niche 3650. Both pre-excavation values and post-excavation values are presented. The comparisons in Figure 11 were based on air-injection tests conducted at the same borehole intervals above the niche. The permeability increases could be interpreted as the opening of pre-existing fractures induced by stress releases associated with niche excavation (Wang and Elsworth 1999, pp. 752–756). The niches were excavated using an Alpine Miner, a mechanical device with a rotary head cutting the rocks below the upper-level boreholes, as illustrated in Figure 7.

Intervals with high pre-excavation permeability recorded the smallest post-excavation permeability changes. In addition to the main mechanical effects, some of the permeability increases could be related to the intersection of previously dead-end or long fractures with the new free surface. For borehole intervals near the end beyond the extent of niche excavation, the permeability values are less altered. Figure 12 illustrates the pre-excavation permeability profiles of the other four boreholes. The middle- and bottom-level boreholes were available for air-injection testing only before niche excavation, since they were subsequently removed by excavation.



DTN: LB980001233124.002

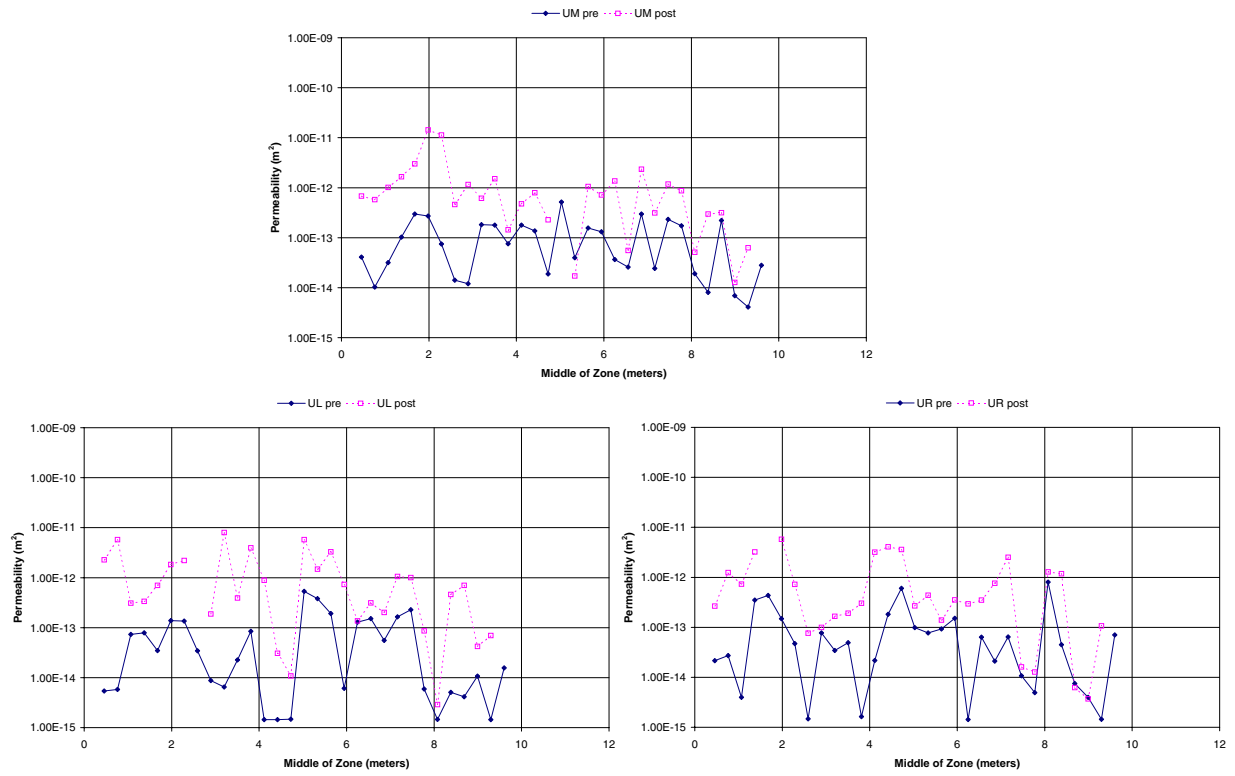
Figure 11. Pre- and Post-Excavation Air-Permeability Profiles along Upper Boreholes at Niche 3650.



DTN: LB980001233124.002

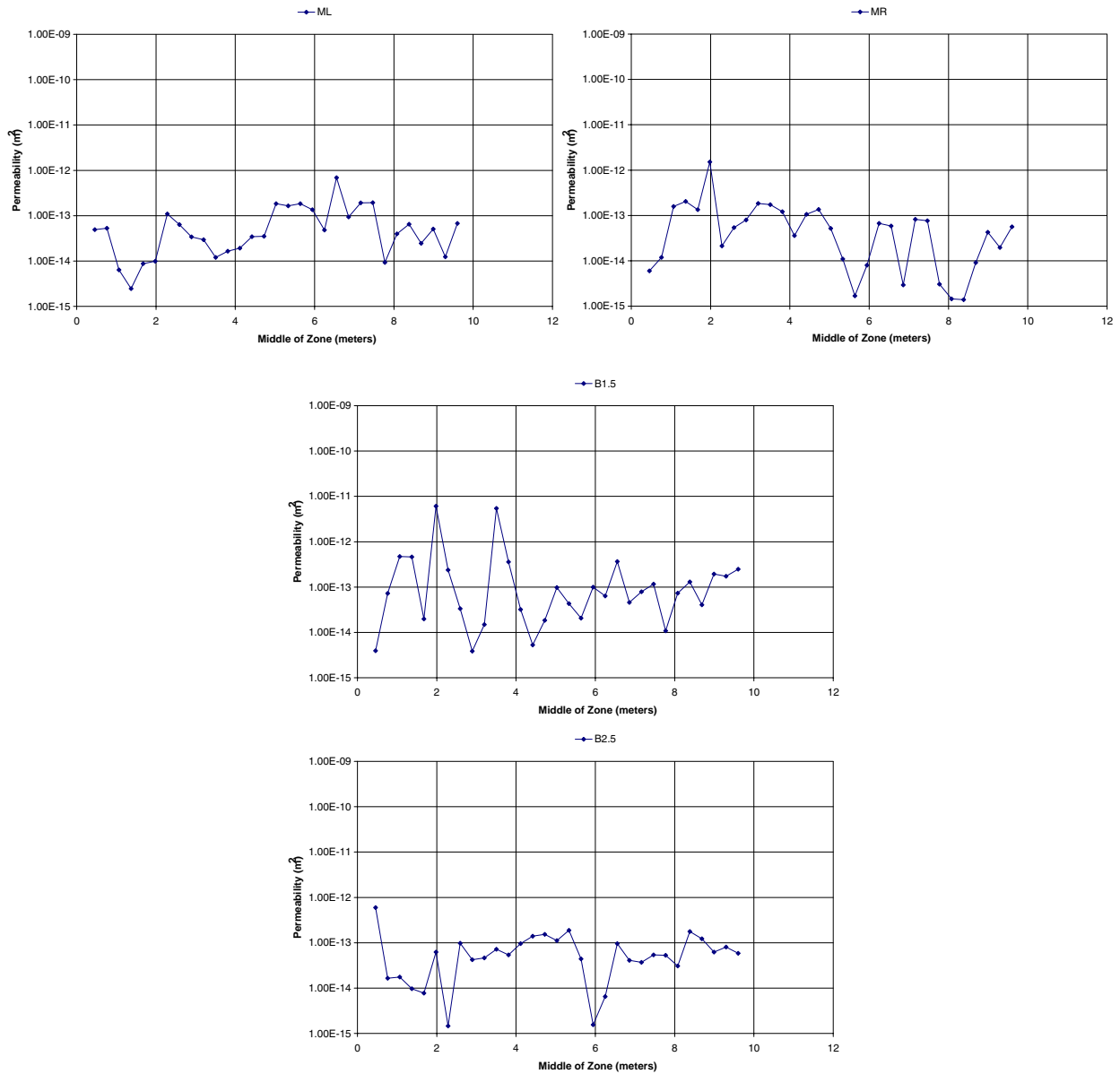
Figure 12. Pre-Excavation Air-Permeability Profiles along Middle and Bottom Boreholes at Niche 3650.

To compare with Niche 3650, the corresponding results of the permeability profiles are presented in Figures 13 and 14 for Niche 3107 and in Figures 15 and 16 for Niche 4788. Figures 13 and 15, similar to Figure 11, are for the upper boreholes, with both pre-excavation and post-excavation values presented for the evaluation of excavation-induced enhancements in permeabilities. Figures 14 and 16 are pre-excavation permeability profiles for the middle- and lower-level boreholes of Niches 3107 and 4788. The borehole layouts for these two niches are modified from the layout in Niche 3650, as illustrated in Figure 7.



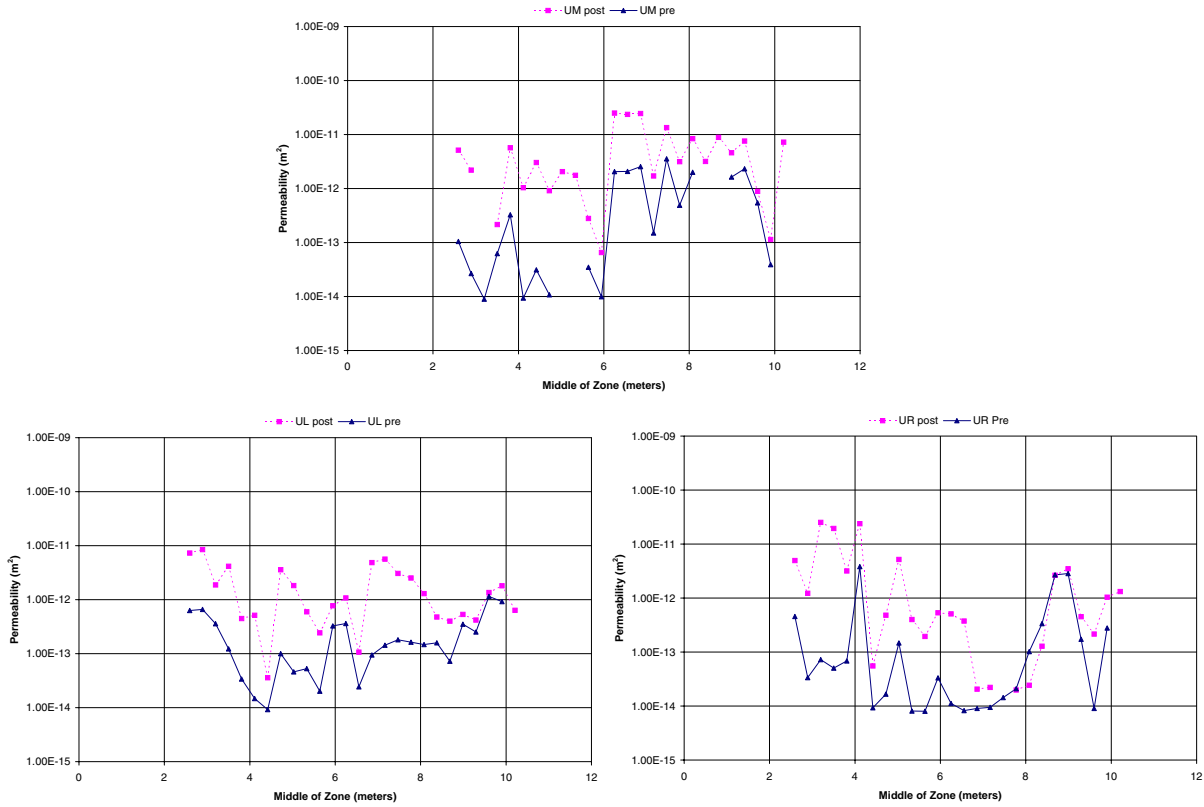
DTNs: LB980901233124.101 for pre-excavation data, LB990601233124.001 for post-excavation data

Figure 13. Pre- and Post-Excavation Air-Permeability Profiles along Upper Boreholes at Niche 3107.



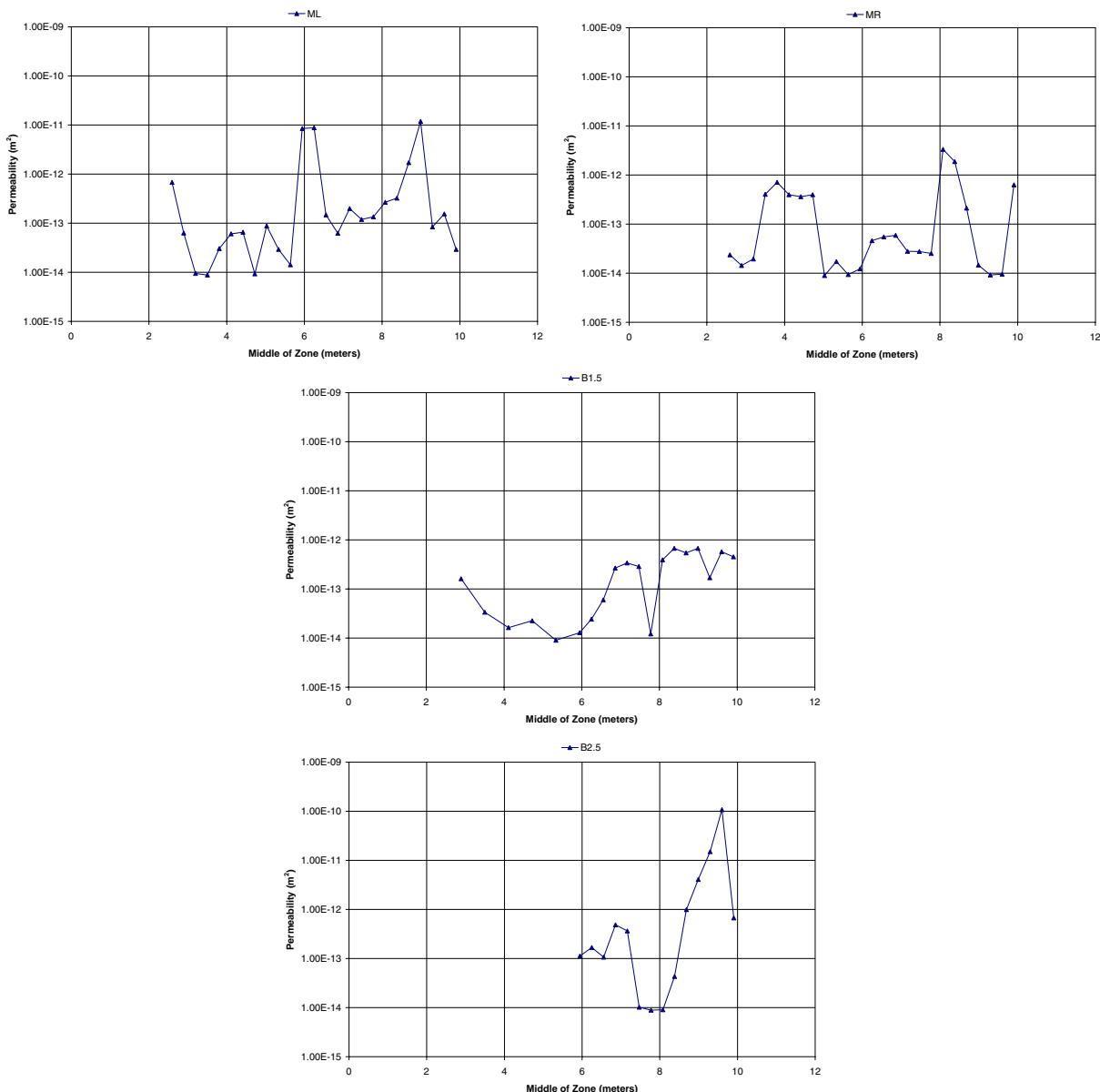
DTN: LB980901233124.101

Figure 14. Pre-Excavation Air-Permeability Profiles along Middle and Bottom Boreholes at Niche 3107.



DTNs: LB980901233124.101 for pre-excitation data, LB990601233124.001 for post-excitation data

Figure 15. Pre- and Post-Excavation Air-Permeability Profiles along Upper Boreholes at Niche 4788.



DTN: LB980901233124.101

Figure 16. Pre-Excavation Air-Permeability Profiles along Middle and Bottom Boreholes at Niche 4788.

6.1.2.3 Statistical Comparison of Air-Permeability Distributions

Table 5 summarizes the average values, standard deviations, and ranges of variations for the boreholes and for niche sites. In addition to permeability values, the ratios of post-excavation to pre-excavation permeabilities are also analyzed. (The ratios are calculated from the permeability values for each interval before the statistical analyses.) Arithmetic means, geometric means, and standard deviations are presented. Drift-scale variations along boreholes and among different boreholes within the same niche test site are larger than differences among different sites.

The permeability values from the middle and bottom boreholes are included in the averaging results presented in [Table 6](#). Pre-excavation means and standard deviations were derived from averaging over all seven boreholes in each niche cluster. The middle- and lower-level boreholes supplement the upper boreholes to characterize the 3-D space in the niche test beds and locate flow paths under pre-excavation conditions. After excavation with only upper boreholes in a horizontal plane left, the air-permeability tests can characterize only the zones above the niche ceilings. The post-excavation analyses in [Tables 5 and 6](#) are over the upper boreholes for assessing the excavation-induced impacts.

[Table 6](#) summarizes the geometric means and standard deviations of all clusters of boreholes tested in the ESF. Each niche has a distinct air-permeability character. The spatial variabilities are significant in the borehole-interval scale of 0.3 m before averaging over 10-m scale along the boreholes and 100-m³ volume over the borehole clusters (3 or 7 boreholes). Niches 3107 and 3566 each have a “radial” entry in the table, which indicates boreholes that are drilled from inside the niches after construction. Permeability values from these boreholes for Niche 3107 (profiles not shown) vary little from those of the pre-excavation boreholes, indicative of the uniformity of the formation around Niche 3107. For Niche 3566, however, the radial boreholes that were tested ran through the brecciated zone within the niche wall and so exhibited higher permeability than that for the pre-excavation boreholes. (The entries in [Table 6](#) for Alcove 4 and Alcove 6 are included for completeness and will be discussed in [Section 6.5](#).)

Table 5. Statistical Analyses of Air-Permeability Along Boreholes Above Niches.

	Niche 3650			Niche 3107			Niche 4788		
	Pre-Excavation	Post-Excavation	Post/Pre Ratio*	Pre-Excavation	Post-Excavation	Post/Pre Ratio*	Pre-Excavation	Post-Excavation	Post/Pre Ratio*
Geometric Mean									
UL	1.17E-13	2.09E-12	17.88	2.22E-14	4.55E-13	20.51	1.30E-13	1.07E-12	8.40
UM	5.25E-14	1.64E-12	31.19	5.81E-14	4.82E-13	8.72	1.81E-13	2.56E-12	11.09
UR	4.27E-14	1.01E-12	23.56	3.32E-14	2.64E-13	8.94	5.91E-14	6.27E-13	9.70
All 3	6.40E-14	1.51E-12	23.60	3.50E-14	3.87E-13	11.69	1.00E-13	1.20E-12	9.90
Arithmetic Mean									
UL	8.59E-12	2.98E-11	47.06	8.12E-14	1.46E-12	135.48	2.56E-13	2.07E-12	14.82
UM	1.01E-12	7.78E-12	72.98	1.14E-13	1.55E-12	21.36	8.59E-13	6.19E-12	26.43
UR	1.27E-13	4.59E-12	53.62	1.14E-13	1.04E-12	30.95	4.49E-13	3.79E-12	46.78
All 3	3.24E-12	1.40E-11	57.89	1.03E-13	1.35E-12	62.60	5.02E-13	3.99E-12	30.09
Minimum Value									
UL	1.86E-15	1.45E-14	0.67	1.44E-15	2.90E-15	1.06	9.16E-15	3.57E-14	1.18
UM	5.40E-15	9.88E-14	1.19	4.10E-15	1.24E-14	0.43	8.99E-15	6.56E-14	1.64
UR	1.53E-15	3.02E-15	1.01	1.43E-15	3.72E-15	0.63	8.01E-15	1.98E-14	0.24
All 3	1.53E-15	3.02E-15	0.67	1.43E-15	2.90E-15	0.43	8.01E-15	1.98E-14	0.24
Maximum Value									
UL	1.27E-10	7.15E-10	271.15	5.32E-13	7.99E-12	1229.23	1.15E-12	8.44E-12	51.54
UM	2.28E-11	1.01E-10	427.91	5.15E-13	1.40E-11	153.02	3.56E-12	2.50E-11	110.52
UR	8.07E-13	4.66E-11	310.67	8.06E-13	5.80E-12	184.13	3.83E-12	2.51E-11	386.90
All 3	1.27E-10	7.15E-10	427.91	8.06E-13	1.40E-11	1229.23	3.83E-12	2.51E-11	386.90
Log Range									
UL	4.83	4.69	2.61	2.57	3.44	3.06	2.10	2.37	1.64
UM	3.63	3.01	2.56	2.10	3.05	2.55	2.60	2.58	1.83
UR	2.72	4.19	2.49	2.75	3.19	2.47	2.68	3.10	3.21
All 3	4.92	5.38	2.80	2.75	3.68	3.45	2.68	3.10	3.21
Std. Dev. of Log									
UL	1.18	0.84	0.69	0.81	0.83	0.83	0.56	0.57	0.50
UM	0.80	0.70	0.62	0.57	0.71	0.61	0.95	0.70	0.58
UR	0.73	1.05	0.66	0.79	0.90	0.74	0.85	0.94	0.85
All 3	0.93	0.88	0.66	0.74	0.82	0.75	0.79	0.78	0.66

Input:

Niche 3650 DTN: LB980001233124.002

Niche 3107 Pre-Excavation DTN: LB980901233124.101, Post Excavation DTN: LB990601233124.001

Niche 4788 Pre-Excavation DTN: LB980901233124.101, Post-Excavation DTN: LB990601233124.001

Output:

DTN: LB990901233124.004

NOTE: *The post/pre ratio is the ratio of post-excitation to pre-excitation permeabilities. This ratio was calculated for each interval in each borehole. Values reported are the statistical measures (maximum, minimum, mean, etc.) of all post/pre ratios calculated for each borehole. For example, mean of (post/pre) ratio is not the same as the ratio of mean(post)/mean(pre).

Table 6. Comparison of Geometric Means and Standard Deviations of Niches and Alcoves in the Exploratory Studies Facility at Yucca Mountain.

Borehole Cluster	Type of Site	log(k) (m ²)	
		Mean	Standard Deviation
Niche 3566 Pre-Excavation	Intersects brecciated zone	-13.0	0.92
Niche 3566 Radial	Predominantly within brecciated zone	-11.8	0.66
Niche 3650 Pre-Excavation	Moderately fractured welded tuff	-13.4	0.81
Niche 3650 Post-Excavation	Post-excavation welded tuff	-11.8	0.88
Niche 3107 Pre-Excavation	Moderately fractured welded tuff	-13.4	0.70
Niche 3107 Post-Excavation	Post-excavation welded tuff	-12.4	0.82
Niche 3107 Radial	Moderately fractured welded tuff	-13.8	0.92
Niche 4788 Pre-Excavation	Highly fractured welded tuff	-13.0	0.85
Niche 4788 Post-Excavation	Post-excavation welded tuff	-11.9	0.78
Alcove 4	Discretely faulted and fractured non-welded tuff	-13.0	0.93
Alcove 6	Highly Fractured Post-construction welded tuff	-11.9	0.67

Input:

DTNs: LB980001233124.002, LB980901233124.101, LB990601233124.001, LB980901233124.004, LB980901233124.009, LB980912332245.001

Output:

DTN: LB990901233124.004

6.2 ANALYSIS AND INTERPRETATION OF THE NICHE LIQUID-RELEASE AND SEEPAGE-TEST DATA

The ESF Drift Seepage Test and Niche Moisture Study was proposed to characterize the seepage process and to further our understanding of how seepage could impact the design and performance of the potential repository. Specific objectives of the study include:

- Measure *in situ* hydrologic properties of the potential repository host rock for use in the AMR on Seepage Calibration Model and the AMR on Seepage Model for Performance Assessment;
- Provide a database containing liquid-release and seepage data that can be used to evaluate seepage and other related UZ processes;
- Evaluate drift-scale seepage processes to quantify the extent to which seepage is excluded from entering an underground cavity;
- Determine the seepage threshold below which percolating water will not seep into a drift.
- The drift seepage tests were conducted by releasing a finite pulse of water above the cavity to simulate the arrival of an episodic percolation event through fast-flow pathways at the potential repository horizon.

The objectives of the study are realized through a combination of field experiments, including air injection, liquid-release and seepage tests. The information compiled in this AMR is an integrated summary of the work performed to date and provides a reference that other researchers can cite. The intent of this section is to produce a concise summary of the work performed to date. Assumptions used in the analyses are described in Section 5.2.

6.2.1 Review of Data Obtained from Liquid-Release and Seepage Tests Conducted at Niches

This section provides a general overview of the tests, including field activities performed prior to, during, and after the niches were excavated.

6.2.1.1 Pre-Excavation Liquid-Release Test Data

Hundreds of air-injection tests were conducted in the boreholes at the four niche sites prior to excavation. The test results were used to determine the distribution of single-hole air permeabilities within the rock mass (refer to Section 6.1 in this AMR). These data were then used to select test intervals for subsequent liquid-release tests. The intervals selected for liquid-release testing exhibited a wide range of air permeabilities, including both high and low values.

Liquid-release tests were conducted in the same boreholes as the air-injection tests by pumping water containing colored or fluorescent dyes at a constant rate into various 0.3-m-long test

intervals. A finite amount of dye-spiked water, typically 1 liter, was introduced into each test interval at a low flow rate to minimize buildup of fluid pressure in the test interval. Various colored and fluorescent tracers were used during the study to document the flow path traveled by the wetting front. Hereafter, the term “water” will be used to describe the test fluid, which may or may not have contained tracer.

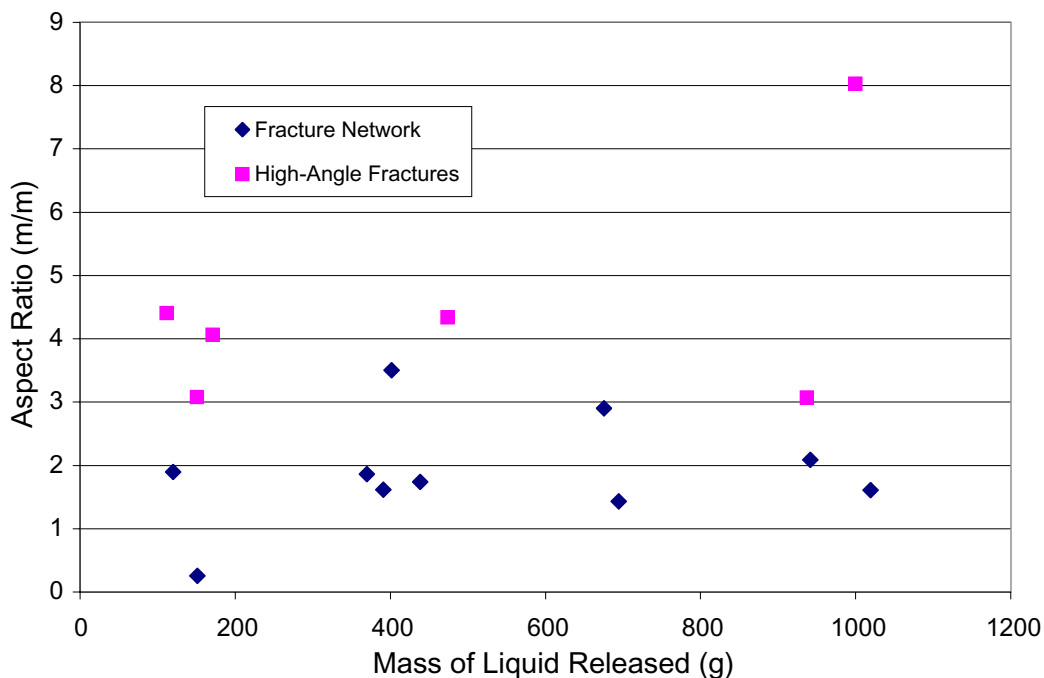
Pre-excavation liquid-release tests were performed during early June and early August 1997, in boreholes installed prior to the excavation of Niches 3566 and 3650, respectively. Pre-excavation liquid-release tests were also performed at Niches 3107 and 4788, starting in late April and late June 1998, respectively. The data from these pre-excavation tests, including the mass of water released, pumping rates and times, liquid-release rates, etc., were tabulated and entered into the TDMS, and assigned DTN: LB980001233124.004 for Niches 3566 and 3650 and DTN: LB980901233124.003 for Niches 3107 and 4788.

6.2.1.2 Niche Excavation Activities

The niches were excavated dry using an Alpine Miner, a mechanical device, to observe and photograph the distribution of fractures and dye within the welded tuff. As reported in DTN: LB980001233124.004 (data reports s99468_006 and s99468_019), dye was observed along individual fractures as well as along intersecting fractures to depths ranging from 0 to 2.6 m below the liquid-release points at the Niches 3566 and 3650 sites. Likewise, dye was observed at a maximum depth of about 1.2 m below the release point at Niche 3107 and about 1.8 m at Niche 4788, as reported in DTN: LB980901233124.003 s98293_014. (In this AMR, TDMS DTN and data report table name are both identified if many files are in a given DTN.) Flow of water through a relatively undisturbed fracture-matrix system was documented in this manner.

During the mining operation, two types of flow paths were observed in the field based on the observed pattern of dye, including: (1) flow through individual or small groups of high-angle fractures; and (2) flow through several interconnected low- and high-angle fractures creating a fracture network.

In general, the maximum distance that the wetting front traveled from the point of injection to the furthest point of observation increased with the mass of water injected. The data did not show that the type of flow (i.e., network or vertical fracture flow) had any significant influence on the maximum travel distance. However, examination of [Figure 17](#), which illustrates the ratio of depth traveled to lateral distance traveled (aspect ratio) versus mass of water injected, shows an important trend. Although the data are sparse, the aspect ratio is consistently higher for the high-angle fracture flow group than for the fracture-network data.



DTNs: LB980001233124.004, LB980901233124.003

Figure 17. Mass of Water Released Versus Aspect Ratio.

6.2.1.3 Post-Excavation Seepage Tests

A series of short duration seepage tests were performed at Niche 3650 and are in progress at Niche 3107 to characterize seepage into an underground opening. In general, the tests are used to quantify the amount of water seeping into the drift from a localized source of water of known duration and intensity. The tests are also used to establish the seepage threshold flux (K_o^*), defined as the largest flux of water that can be introduced into the test borehole without resulting in seepage into the niche.

The seepage tests are conducted after the niches are excavated by pumping water into select test intervals in boreholes UL, UM, and UR located above each niche. The distance from boreholes to niche ceiling is nominally 0.65 m. The tests are performed by sealing a short interval of borehole using an inflatable packer system, similar to the system used in air-injection test as described in [Attachment II](#). Any water that migrates from the borehole to the niche ceiling and drips into the opening is captured and weighed.

For each packer interval, a liquid return (overflow) line prevents pressure build up of excess pressure. If the liquid injection rate is high and return flow is observed, the liquid-release rate is determined by the difference between injection flow rate and return flow rate. For low rate tests without overflowing, its liquid-release rate is given by the injection-flow rate.

6.2.1.3.1 Niche 3650

Forty liquid-release tests were performed on 16 test intervals positioned above Niche 3650 beginning in late 1997 and ending in early 1998. Water migrated through the rock and seeped

into the niche in 10 out of the 16 zones tested. The seepage threshold flux was determined for the 10 zones that seeped. The seepage and liquid-release data were tabulated and entered into the TDMS, where it was assigned DTN: LB980001233124.004.

The mass of water released to the formation was computed by mass balance. In turn, the liquid release-rate (Q_s) for each test was computed by dividing the mass released by the respective duration of each test; thus, these values represent time-averaged rates. The rate at which water was released to the formation ranged from 0.007 to 2.892 g/s for all of the tests, and the mass released ranged from 274.5 to 5597.5 g per test as summarized in DTN: LB980001233124.004 s99468_007.

When water appeared at the niche ceiling during a test and dripped into the opening, it was collected in the capture system and weighed. Figure 18 shows the approximate location of the capture system and test intervals relative to the niche boundaries, and the sequence of dyes and number of tests performed on each test interval. Most of the water was typically captured in only one or two 0.305×0.305 m cells located directly beneath the test interval. The wetting front typically arrived at the niche ceiling directly below the test zone. In the immediate vicinity at the intersection of the niche ceiling and the conducting fractures, the relative humidity could be high from local evaporation. However, the localized humid conditions were not met everywhere within the niche and/or the ESF Main Drift.

The mass of water captured ranged from 0.0 to 568.6 g per test as reported in DTN: LB980001233124.004 s99468_007. The seepage percentage, defined as the mass of water that dripped into the capture system divided by the mass of water released to the rock, is as shown below:

$$\text{Seepage Percentage} = 100 \times \frac{\text{"Mass Captured (g)"}}{\text{"Mass Released (g)"}} \quad (\text{Eq. 2})$$

The seepage percentage ranged from 0% for zones that did not seep to 56.2% for a predominantly gravity-driven flow through a highly saturated fracture (DTN: LB980001233124.004 s99468_007).

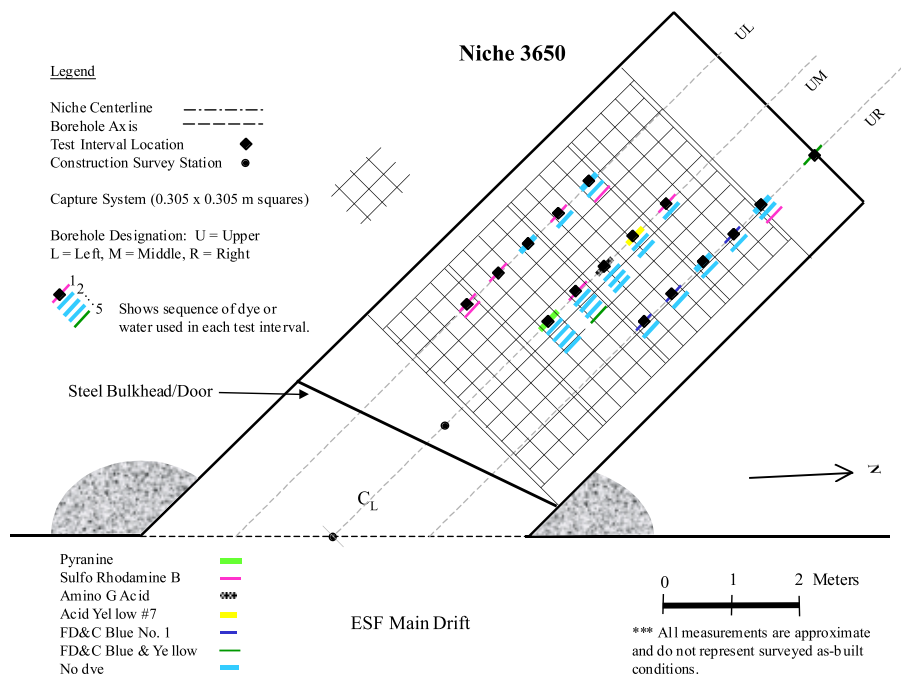


Figure 18. Schematic Illustration of Seepage Capture System and Test Intervals at Niche 3650.

6.2.1.3.2 Niche 3107

Seven seepage tests were performed in 1999 at Niche 3107 to determine the amount of water that will seep into the opening when the air within the niche is maintained at a high relative humidity. Post-closure potential repository conditions such as these are expected to exist after forced ventilation of the waste-emplacement drifts ceases and the waste and surrounding rock cool to ambient conditions. The relative humidity within Niche 3107 is being raised artificially to an average of 93%, as shown in Figure 19, to reduce seepage water losses caused by evaporation. Additional seepage tests are in progress under high relative humidity conditions.

It was observed during the early stages of testing at Niche 3650 that the seepage percentage for two of the tests were significantly different even though the tests were conducted at nearly the same liquid-release rate. The large difference in seepage percentage was attributed to the effect of wetting history; that is, residual water remaining in the fractures from the first test influenced the amount of seepage that occurred during the second test. Therefore, a second objective of the Niche 3107 testing program is to study the effect of wetting history on seepage and seepage rates (seepage-memory effect).

The seepage, liquid-release, and relative humidity data collected to date were tabulated and entered into the TDMS, and assigned DTN: LB990601233124.002.

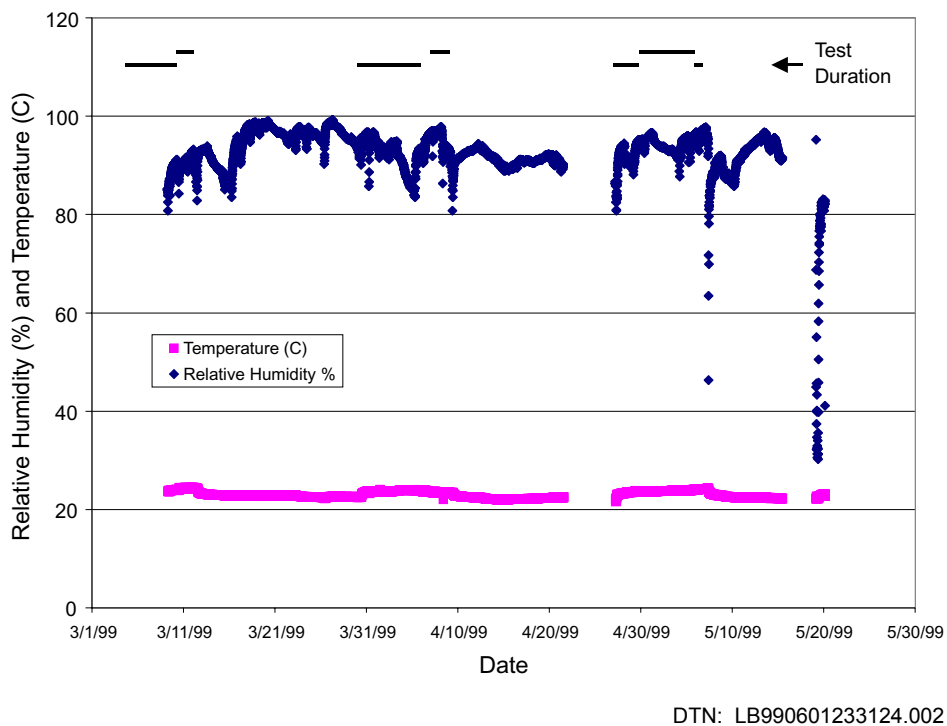


Figure 19. Relative Humidity Inside Niche 3107.

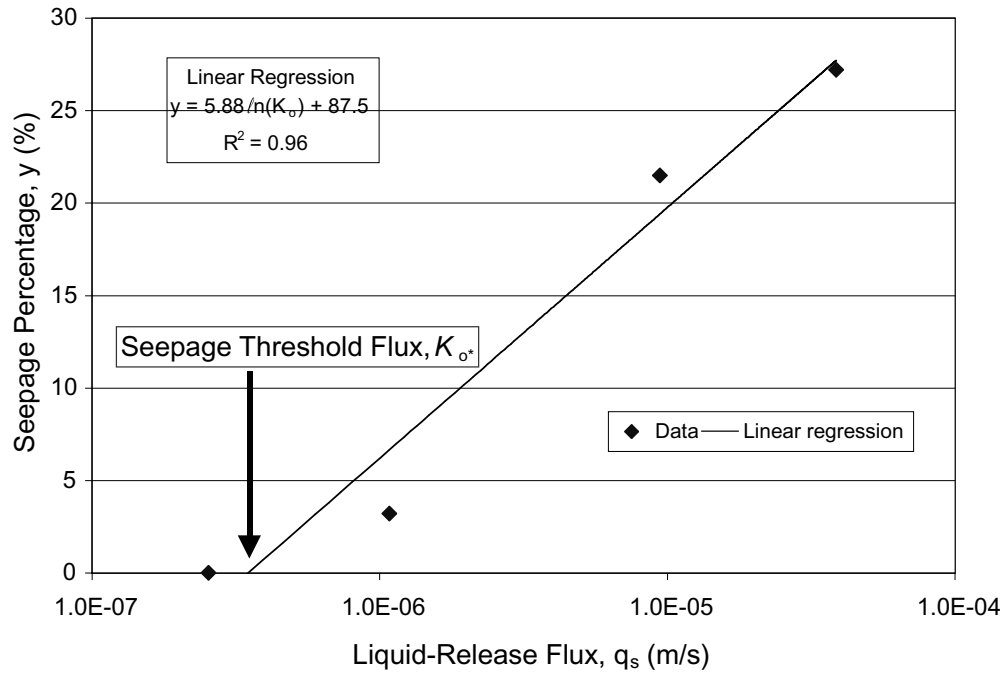
6.2.2 Seepage Threshold and Fracture Characteristic Curve

The bulk of the seepage data collected and interpreted in this AMR was obtained from tests conducted at Niche 3650. These data are analyzed in detail in this section.

6.2.2.1 Post-Excavation Liquid-Release and Seepage Threshold Fluxes

For a given test interval, seepage tests were initially conducted at high liquid-release rates (injection rates into borehole interval without excessive pressure buildup). Subsequent tests were performed at lower liquid-release rates to determine whether a threshold could be defined where seepage into the cavity would no longer occur.

Figure 20 shows a plot of the seepage percentages observed during four tests conducted at different q_s in borehole UM at the same depth of 5.49–5.79 m from the borehole collar. A linear regression was performed on the four data points to compute the equation for the trendline and the R-squared values (R^2) reported in Figure 20 and tabulated in Table 7. This exercise was repeated for the remaining test intervals to produce the regression data reported in Table 7 for all the zones that seeped. The R-squared values were computed separately for each interval and are listed for those intervals where three or more data points are available.



DTN: LB980001233124.004

Figure 20. Liquid-Release Flux Versus Seepage Percentage. The Seepage tests were conducted for the interval 5.49-5.79 m from the collar for the upper middle borehole at Niche 3560.

Table 7. Seepage Threshold Fluxes (K_o^*).

Borehole	Test Interval (m)	Regression Equation	Data Points (n)	R ² - Value	Seepage Threshold Flux (m/s) (K_o^*)	Saturated Hydraulic Conductivity (m/s) (K_i)*
UL	7.01-7.32	$y = 0.6833 \ln(K_o) + 8.5742$	2	NA	3.55E-06	8.98E-05
	7.62-7.92	$y = 5.7394 \ln(K_o) + 92.627$	3	0.979	9.80E-08	1.51E-04
UM	4.27-4.57	$y = 5.2757 \ln(K_o) + 79.443$	4	0.921	2.89E-07	2.62E-05
	4.88-5.18	$y = 2.304 \ln(K_o) + 31.767$	3	0.975	1.03E-06	2.52E-03
	5.49-5.79	$y = 5.8876 \ln(K_o) + 87.528$	4	0.963	3.50E-07	2.16E-05
UR	4.27-4.57	$y = 0.314 \ln(K_o) + 4.3283$	2	NA	1.03E-06	4.08E-05
	4.88-5.18	$y = 0.3165 \ln(K_o) + 4.3751$	2	NA	9.92E-07	9.87E-05
	5.49-5.79	$y = 28.419 \ln(K_o) + 351.09$	2	NA	4.31E-06	1.71E-05
	6.10-6.40	$y = 4.2169 \ln(K_o) + 79.596$	2	NA	6.35E-09	3.01E-05
	6.71-7.01	$y = 10.574 \ln(K_o) + 165.28$	3	0.974	1.63E-07	2.28E-04
All Data	Various	$y = 3.7696 \ln(K_o) + 59.976$	30	0.187	1.23E-07	

DTN: LB980001233124.004 s99468_011

NOTES: NA - not applicable

y = predicted seepage percentage

 K_o = net downward liquid-release flux from regression model

* K_i was derived from air permeability (k) values using the distance from the test interval to the niche ceiling equal to 0.65 meters. These values are slightly different from the k values reported in DTN: LB980001233124.002 s98131_002 which use the test interval length equal to 0.30 meters in the computation of k.

Table 7 also summarizes the seepage threshold flux (K_o^*), defined as the liquid-release flux below which water will not seep into the drift (i.e., see K_o^* defined on Figure 20). The K_o^* values were determined using the regression equations provided in Table 7 by setting the seepage percentage, y, equal to 0, then solving for $K_o = K_o^*$. Here the symbol K_o is used to denote the liquid-release flux used in the regression model to distinguish it from the liquid-release flux computed using the field data (q_s). The seepage threshold flux may be interpreted as follows:

- If the liquid-release flux exceeds the seepage threshold flux ($K_o > K_o^*$) for the given interval, then water will seep into the drift.
- If the liquid-release flux is less than the seepage threshold flux ($K_o < K_o^*$), then water will not enter the cavity.

Figure 21 shows a log-log plot of K_{o^*} versus the saturated hydraulic conductivity (K_l) for the 10 test zones where seepage occurred. The air permeabilities obtained from the post-excavation gas-injection tests were converted into equivalent saturated hydraulic conductivities (DTN: LB980001233124.004 s99468_010) as shown in Scientific Notebook YMP-LBNL-JSW-6c, pp. 34–38, to produce the values recorded in Table 7 and plotted in Figure 21.

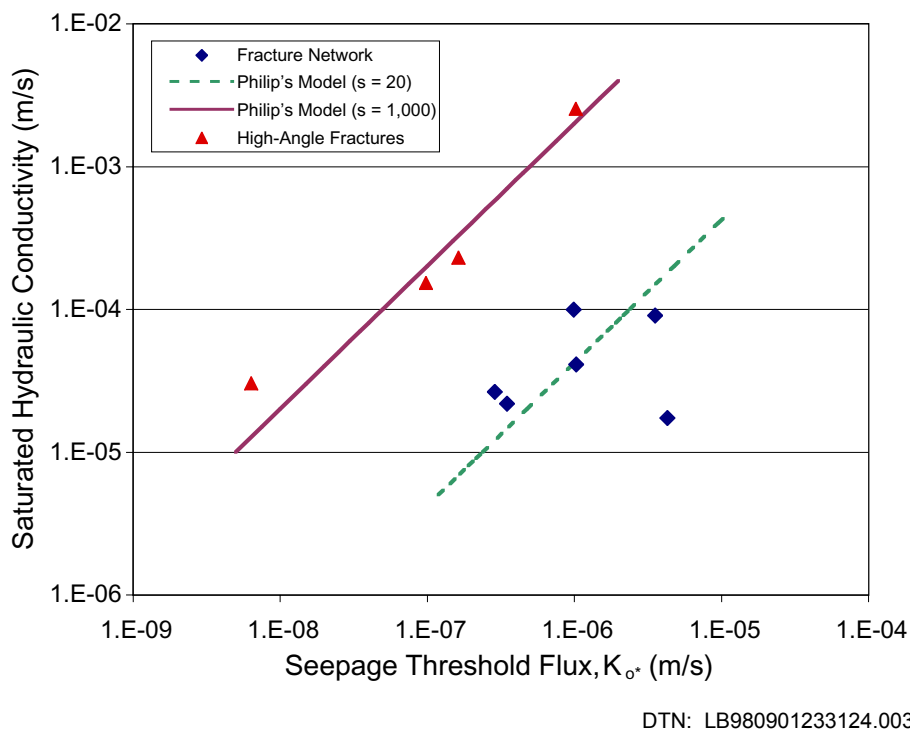


Figure 21. Seepage Threshold Fluxes.

The estimation of saturated hydraulic conductivity using air-permeability test data is evaluated in Attachment III.

6.2.2.2 Capillary Strength (α^{-1}) of the Fractures

Philip et al. (1989) recognized that buried cylindrical cavities are obstacles to flow preventing water from entering the cavity. Given Assumption 6 in Section 5.2.2, the following theoretical relation between K_{o^*} and K_l was provided by Philip et al. (1989, Section (3.4), p.19):

$$K_{o^*} = K_l [\vartheta_{max}(s)]^{-1} \tag{Eq. 3}$$

where s is the value of the dimensionless cavity length and ϑ_{max} is the maximum value of the dimensionless potential ϑ at the boundary of the cavity. Philip et al. (1989, Equation (56), p. 20) shows that ϑ_{max} occurs at the apex or crown of a cylindrical cavity. The dimensionless cavity length, s , is a measure of the relative importance of gravity and capillarity in determining flow. As $s \rightarrow 0$, capillarity dominates, whereas gravity dominates as $s \rightarrow \infty$.

An exponential functional relation between unsaturated hydraulic conductivity, $K(\psi)$, and water potential, ψ , is used:

$$K(\psi) = K_l e^{\alpha(\psi - \psi_e)} \quad (\text{Eq. 4})$$

Pullan (1990, p. 1221) notes that K_l should be set equal to the saturated hydraulic conductivity of the soil and $\psi_e = 0$. If the soil exhibits a significant air entry potential (i.e., the value of ψ at saturation for which $d\theta/d\psi \neq 0$, where θ is the volumetric water content of the medium), then K_l is the conductivity at the air entry value $\psi = \psi_e$.

This Gardner exponential functional relation is used by Philip et al. (1989, Equation (12), p. 18) and by Braester (1973, Equation (5), p. 688) to transform and linearize the unsaturated governing equations. Equation 4 is also used in Section 6.2.2.4 to estimate water potential.

Philip et al. (1989, Equation (14), p. 18) notes that the dimensionless cavity length s in Equation 3 is related to the exponential fitting parameter α (Equation 4) and a characteristic length of the cavity ℓ by the following expression:

$$s = 0.5\alpha\ell \quad (\text{Eq. 5})$$

When s is large, Philip et al. (1989, Section 6, pp. 23–25) demonstrate that a boundary layer adjoining the ceiling of the cavity surface will develop. This allows the steady flow equation to be replaced by a boundary layer equation that is readily solved. The asymptotic expansion of ϑ_{\max} for large values of s yields (Philip et al. 1989, Equation (84), p. 23):

$$\vartheta_{\max} = 2s + 2 - \frac{1}{s} + \frac{2}{s^2} - \dots \quad (\text{Eq. 6})$$

Philip et al. (1989, Table 1, Section 6, p. 25) note that when $s \geq 1$, the first three terms on the right-hand side of Equation 6 produce an adequate estimate that is within 12% or better of the exact value of ϑ_{\max} . The characteristic length of the cavity, ℓ , used in Equation 5 is assumed to be 2 meters, which is approximately equal to the equivalent radius of the niche.

Equation 3 and the first three terms in the series of Equation 6 were used to generate the two lines plotted on Figure 21. The s values were selected so the lines produced the best-fit possible by eye to the data set. Two lines were used instead of one because the data appear to be grouped into two distinct sets. We believe that the data appear to fit two lines with different s values because the seepage tests were performed on, and thus the data are derived from, two distinct fracture populations. As noted in Section 6.2.1.2 from observations during niche mining operation, fracture flow paths appear to be grouped into two general populations, including flow through individual or small groups of high-angle fractures and flow through interconnected fracture networks. Highly conductive individual or small groups of high-angle fractures that are free draining because of gravity-dominated flow exhibit a greater value of s than a network of

interconnected fractures influenced to a greater extent by lateral spreading of the wetting front and capillary-driven flow. Based on this information and the observations presented in the previous paragraph, we hypothesize that the data trending along the $s = 1,000$ line are characteristic of high-angle fractures, and the data trending along the $s = 20$ line are characteristic of interconnected fracture networks.

Using Equation 5, α takes on the following values for the different fracture populations:

$$\begin{aligned}\alpha_{\text{High-Angle Fractures}} &= \alpha_{s=1,000} = 1,000 \text{ m}^{-1} \\ \alpha_{\text{Fracture Networks}} &= \alpha_{s=20} = 20 \text{ m}^{-1}\end{aligned}\quad (\text{Eq. 7})$$

Philip (1985, Equation (2), p. 788) and White and Sully (1987, Equation (1), p. 1514) both recognized that α^{-1} is a K -weighted mean soil-water potential related to the macroscopic capillary length, λ_c , as follows:

$$\lambda_c = \alpha^{-1} = [K(\Psi_0) - K(\Psi_n)]^{-1} \int_{\Psi_n}^{\Psi_0} K(\Psi) d\Psi \quad (\text{Eq. 8})$$

$$\alpha^{-1} = \Delta K^{-1} \int_{\theta_n}^{\theta_0} D(\theta) d\theta \quad (\text{Eq. 9})$$

Here White and Sully (1987, p. 1514) define Ψ_0 and $\theta_0 = \theta(\Psi_0)$ as the water potential (Ψ) and volumetric water content (θ) at the water-supply surface (i.e., relative to the liquid-release interval), respectively, and Ψ_n and $\theta_n = \theta(\Psi_n)$ as the water potential and volumetric water content at antecedent conditions. $D(\theta) = K(\Psi) d\Psi/d\theta$ is the hydraulic diffusivity and $\Delta K = K(\Psi_0) - K(\Psi_n)$. White and Sully (1987) recognized that the macroscopic capillary length, λ_c , and hence α^{-1} , could be thought of as a “mean” height of capillary rise above a water table. Using the value of $1/\alpha$ from Equation 7, λ_c becomes:

$$\begin{aligned}\lambda_c (\text{high-angle fractures}) &= \alpha^{-1} = 0.001 \text{ m} \Rightarrow 9.8 \text{ Pa}; \\ \lambda_c (\text{fracture network}) &= \alpha^{-1} = 0.05 \text{ m} \Rightarrow 490 \text{ Pa}\end{aligned}\quad (\text{Eq. 10})$$

(The capillary height values are converted to the pressure values by multiplying $\rho_w g$.) Individual α values were computed for each test interval exhibiting seepage by adjusting the value of s in Equation 6, and hence the value of $\vartheta_{Max}(s)$, until the left-hand side of Equation 3, K_{o*} , was equal to the right-hand side, $K_l [\vartheta_{Max}(s)]^{-1}$. Values of K_{o*} and K_l were taken from Table 7. Table 8 summarizes the values of α and the geometric mean value of α for the fracture network and vertical-fracture populations. The geometric mean values are nearly equal to the α values obtained using the graphical technique described above. This correspondence is to be expected, however, since the α values obtained from the graphical technique also represent an average fit

of the data to the Philip et al. (1989) model, but with lower precision given the best fit was performed by eye.

Table 8. Alpha (α) Values for the Fractures.

Borehole and Test Interval (m) at Niche 3650	Seepage Threshold Flux (m/s) (K_o)	Saturated Hydraulic Conductivity m/s, (K_i)	Alpha (m^{-1})
Fracture Networks			
UR 4.88-5.18	9.92E-07	9.87E-05	48.8
UL 7.01-7.32	3.55E-06	8.98E-05	11.7
UR 4.27-4.57	1.03E-06	4.08E-05	18.8
UM 4.27-4.57	2.89E-07	2.62E-05	44.4
UM 5.49-5.79	3.50E-07	2.16E-05	29.9
UR 5.49-5.79	4.31E-06	1.71E-05	1.4
Geometric Mean			16.4
Individual or Small Groups of High-Angle Fractures			
UM 4.88-5.18	1.03E-06	2.52E-03	1225.5
UR 6.71-7.01	1.63E-07	2.28E-04	699.2
UL 7.62-7.92	9.80E-08	1.51E-04	771.9
UR 6.10-6.40	6.35E-09	3.01E-05	2373.7
Geometric Mean			1119.4

DTN: LB980901233124.003 s98293_004

6.2.2.3 Estimated Volumetric Water Content (θ) of the Fractures

Another useful piece of information that can be derived using the niche seepage data includes estimates of the volumetric water content (θ) of the fractures. Direct measurement of fracture θ in the field is difficult at best using conventional hydrologic techniques (e.g., using neutron moisture logs). Therefore, an alternative method of measuring average volumetric water contents indirectly using wetting-front arrival times observed at the niche ceiling during the seepage tests is described below. Assumptions used in the analyses are described in Section 5.2.3.

Braester (1973) derived a time-dependent analytical solution for the volumetric water-content distribution that results from a surface source of constant flux. He then compared the volumetric water-content profile at a given time predicted using his analytical solution to the output produced from a numerical model with the same soil type and properties. Although Braester (1973) determined that his analytical solution produced a relatively poor estimate of the actual θ -profile at a given time, he found that the depth of the wetting front could be accurately

determined using the following equation (Braester 1973, Equation (17), p. 690, symbolically replacing z_F , q_o , $\bar{\theta}_o$, and θ_i with z_p , q_s , θ_{ave} , and θ_i):

$$z_p = \frac{q_s t}{(\theta_{ave} - \theta_n)} \quad (\text{Eq. 11})$$

where z_p is the depth from the water-supply surface to the leading edge of the wetting front, t is the arrival time of the front at depth z_p , q_s is the constant flux of water supplied at the source, and θ_n is the antecedent (or residual) water content.

Using the arrival time for the wetting front observed at the niche ceiling (DTN: LB980001233124.004 s99468_016) and the q_s data (DTN: LB980001233124.004 s99468_005), it is possible to estimate the change in volumetric water content $\Delta\theta = \theta_{ave} - \theta_n$ for each seepage test by applying Equation 11. [Table 9](#) provides a summary of the estimated $\Delta\theta$ values that result when z_p is equal to 0.65 m (i.e., the distance from the borehole to the niche ceiling). With approximation described in Section 5.2.3 that the antecedent or residual moisture content θ_n is negligible compared to θ_{ave} , then $\Delta\theta$ becomes a measure of the average volumetric water content.

The water-content values shown in [Table 9](#) range from 0.09 to 2.4 percent. Surprisingly, this indicates that the saturated water contents or porosities of the fractures could be as high as 2.4%, which is greater than expected. In turn, these values could influence travel-time calculations computed for the unsaturated zone, since travel time is proportional to water content. Using larger water contents for the fractures would result in longer travel times.

Assumptions 7 and 8 in Section 5.2.3 are used to estimate water contents for the fractures. These two assumptions are evaluated in [Attachment IV](#).

Table 9. Estimated Changes in Volumetric Content ($\Delta\theta$) of the Fractures

Borehole at Niche 3650	Test Name	Date	Test Interval (m)	Arrival Time of Wetting Front at Ceiling ¹ (s)	Liquid Release Flux ² (m/s)	Distance to Ceiling (m)	Average Water Content Change ³ (m ³ /m ³)	Comment
Fracture Networks								
UR	Test #1 1-15-98	1/15/98	4.88-5.18	1790	3.55E-06	0.65	0.0098	
	Test #1 2-6-98	2/6/98	4.88-5.18	4395	9.92E-07	0.65	0.0067	Test conducted below seepage threshold
UL	Test #1 12-10-97	12/10/97	7.01-7.32	240	3.65E-05	0.65	0.0135	
	Test #1 1-6-98	1/6/98	7.01-7.32	3290	3.55E-06	0.65	0.0180	Test conducted below seepage threshold
UR	Test #1 1-14-98	1/14/98	4.27-4.57	3368	3.71E-06	0.65	0.0192	
	Test #1 2-5-98	2/5/98	4.27-4.57	9910	1.03E-06	0.65	0.0157	Test conducted below seepage threshold
UM	Test 5 Niche 3650	11/13/97	4.27-4.57	416	3.78E-05	0.65	0.0242	Flux slightly greater than K_f derived from air k value
	Test #1 12-3-97	12/3/97	4.27-4.57	1008	9.42E-06	0.65	0.0146	
	Test #2 12-3-97	12/3/97	4.27-4.57	514	9.47E-06	0.65	0.0075	Hysteresis
	Test #1 1-7-98	1/7/98	4.27-4.57	8811	8.82E-07	0.65	0.0120	
	Test #2 2-10-98	2/10/98	4.27-4.57	13375	3.09E-07	0.65	0.0063	Arrival estimated from video and below seepage threshold
UM	Test 4 Niche 3650	11/13/97	5.49-5.79	208	3.87E-05	0.65	0.0124	Flux slightly greater than K_f derived from air k value
	Test #2 12-4-97	12/4/97	5.49-5.79	420	9.43E-06	0.65	0.0061	
	Test #1 1-9-98	1/9/98	5.49-5.79	2750	1.08E-06	0.65	0.0046	
	Test #1 2-11-98	2/11/98	5.49-5.79	10130	2.55E-07	0.65	0.0040	
UR	Test #2 1-13-98	1/13/98	5.49-5.79	540	4.31E-06	0.65	0.0036	
	Test #2 2-10-98	2/10/98	5.49-5.79	230	6.85E-06	0.65	0.0024	saturated - return flow

DTN: ¹LB980001233124.004 s99468_014, ²LB980001233124.004 s99468_010, ³LB980901233124.003 s98293_003

Table 9. Estimated Changes in Volumetric Content ($\Delta\theta$) of the Fractures (Cont.)

Borehole at Niche 3650	Test Name	Date	Test Interval (m)	Arrival Time of Wetting Front at Ceiling ¹ (s)	Liquid Release Flux ² (m/s)	Distance to Ceiling (m)	Average Water Content Change ³ (m ³ /m ³)	Comment
Individual or small groups of High-Angle Fractures								
UM	Test 1 Niche 3650	11/12/97	4.88-5.18	180	5.41E-05	0.65	0.0150	
	Test #1 12-4-97	12/4/97	4.88-5.18	298	9.49E-06	0.65	0.0043	
	Test #2 12-5-97	12/5/97	4.88-5.18	952	2.70E-06	0.65	0.0040	Hysteresis
	Test #1 1-8-98	1/8/98	4.88-5.18	6060	8.75E-07	0.65	0.0082	Test conducted below seepage threshold
	Test #1 3-6-98	3/6/98	4.88-5.18	21690	2.48E-07	0.65	0.0083	Arrival estimated from video and below seepage threshold flux
UR	Test #1 1-13-98	1/13/98	6.71-7.01	416	3.68E-06	0.65	0.0024	
	Test #1 2-3-98	2/3/98	6.71-7.01	626	1.91E-06	0.65	0.0018	
	Test #1 3-5-98	3/5/98	6.71-7.01	4457	2.48E-07	0.65	0.0017	
UL	Test #2 1-6-98	1/6/98	7.62-7.92	690	9.49E-06	0.65	0.0101	
	Test #1 2-12-98	2/12/98	7.62-7.92	570	1.89E-06	0.65	0.0017	
	Test #1 3-4-98	3/4/98	7.62-7.92	2610	2.33E-07	0.65	0.0009	
UR	Test #2 1-14-98	1/14/98	6.10-6.40	960	3.57E-06	0.65	0.0053	
	Test #1 2-4-98	2/4/98	6.10-6.40	3755	1.07E-06	0.65	0.0062	

DTN: ¹LB980001233124.004 s99468_014, ²LB980001233124.004 s99468_010, ³LB980901233124.003 s98293_003

6.2.2.4 Estimated Water Potentials (ψ) of the Fractures

The direct measurement of water potentials is difficult to make in unsaturated fractures because hydrologic instruments are not readily adaptable to measuring such small features. Therefore, an indirect measure of the water potential (ψ) was formulated using the α -values computed in Section 6.2.2.2, the liquid-release fluxes, air-derived saturated hydraulic conductivities, employing Equation 4 with $q_s = K(\psi)$, and solving for ψ as shown below:

$$\psi = \frac{\ln(q_s / K_l)}{\alpha} \quad (\text{Eq. 12})$$

Using the values for q_s and K_l reported in DTN: LB980001233124.004 s99468_005 and s99468_011, respectively, and the α -values from Table 8, ψ was computed for several tests by employing Equation 12. A summary of the resulting ψ values is provided in Table 10.

Table 10. Estimated Water Potential (ψ) for the Fractures

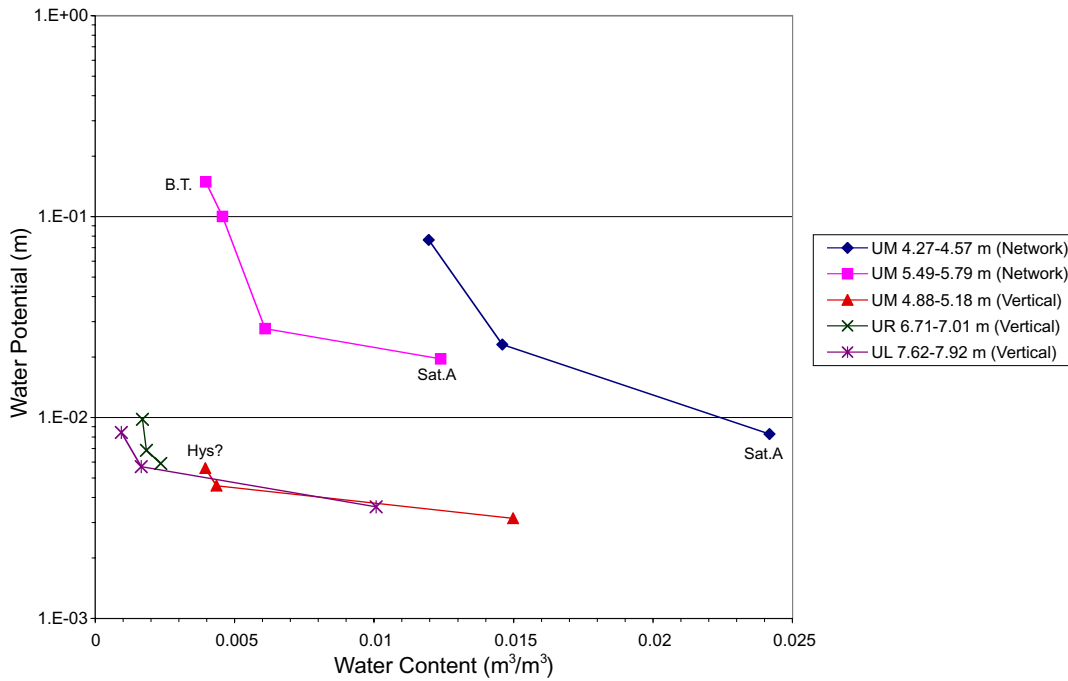
Borehole	Test Name	Date	Test Interval (m)	Absolute Value of the Water Potential (m)
Fracture Networks				
UR	Test #1 1-15-98	1/15/98	4.88-5.18	6.82E-02
	Test #1 2-6-98	2/6/98	4.88-5.18	9.43E-02
UL	Test #1 12-10-97	12/10/97	7.01-7.32	7.71E-02
	Test #1 1-6-98	1/6/98	7.01-7.32	2.76E-01
UR	Test #1 1-14-98	1/14/98	4.27-4.57	1.27E-01
	Test #1 2-5-98	2/5/98	4.27-4.57	1.95E-01
UM	Test 5 Niche 3650	11/13/97	4.27-4.57	8.26E-03
	Test #1 12-3-97	12/3/97	4.27-4.57	2.30E-02
	Test #2 12-3-97	12/3/97	4.27-4.57	2.29E-02
	Test #1 1-7-98	1/7/98	4.27-4.57	7.64E-02
	Test #2 2-10-98	2/10/98	4.27-4.57	1.00E-01
UM	Test 4 Niche 3650	11/13/97	5.49-5.79	1.95E-02
	Test #2 12-4-97	12/4/97	5.49-5.79	2.77E-02
	Test #1 1-9-98	1/9/98	5.49-5.79	1.00E-01
	Test #1 2-11-98	2/11/98	5.49-5.79	1.48E-01
UR	Test #2 1-13-98	1/13/98	5.49-5.79	1.02E+00
	Test #2 2-10-98	2/10/98	5.49-5.79	6.76E-01
Individual or small groups of Vertical Fractures				
UM	Test 1 Niche 3650	11/12/97	4.88-5.18	3.13E-03
	Test #1 12-4-97	12/4/97	4.88-5.18	4.56E-03
	Test #2 12-5-97	12/5/97	4.88-5.18	5.58E-03
	Test #1 1-8-98	1/8/98	4.88-5.18	6.50E-03
	Test #1 3-6-98	3/6/98	4.88-5.18	7.53E-03
UR	Test #1 1-13-98	1/13/98	6.71-7.01	5.90E-03
	Test #1 2-3-98	2/3/98	6.71-7.01	6.84E-03
	Test #1 3-5-98	3/5/98	6.71-7.01	9.76E-03
UL	Test #2 1-6-98	1/6/98	7.62-7.92	3.59E-03
	Test #1 2-12-98	2/12/98	7.62-7.92	5.68E-03
	Test #1 3-4-98	3/4/98	7.62-7.92	8.39E-03
UR	Test #2 1-14-98	1/14/98	6.10-6.40	8.98E-04
	Test #1 2-4-98	2/4/98	6.10-6.40	1.41E-03

DTN: LB980901233124.003 s98293_001

6.2.2.5 Fracture-Water Characteristic Curves

The volumetric water-content values from Section 6.2.2.3 and the water-potential values derived in Section 6.2.2.4 are plotted on Figure 22 to create a water-characteristic curve for high-angle and networked fractures. Only those test intervals where three or more tests were conducted are included in the figure. (Inclusion of zones having only two data points joined by a straight line contributes little to understanding of the functional relation between θ and ψ .) In addition, data points that were influenced by hysteresis or from tests conducted below the seepage threshold flux were excluded, unless noted.

Although Assumptions 6, 7 and 8 described in Sections 5.2.2 and 5.2.3 were used to derive these curves, it is interesting to note that the near-vertical fractures are grouped together, exhibiting similar water-retention characteristics. They also appear to drain very quickly, approaching a residual water content of perhaps 0.001 to 0.002 at water potentials as high as -0.01 m.



B.T. = Data point was measured at or below the seepage threshold flux and may be influenced by the capillary barrier. Hys? = This data point may be influenced by fracture hysteresis. Sat.A = The flux was equal to or slightly greater than the equivalent saturated hydraulic conductivity (determined using the air permeability data) for this data point.

DTN: LB980901233124.003

Figure 22. Water Retention Curves for High-Angle Fractures and Fracture Networks.

6.3 ANALYSES OF TRACER-MIGRATION DELINEATION AT NICHE 3650

At the drift-seepage test site Niche 3650 in the ESF, an array of twelve boreholes was drilled to collect core samples for tracer analyses. The core analyses delineated the extent of tracer migration from an episodic liquid-release event. The field studies and laboratory measurements are presented below.

6.3.1 Tracer Distribution from the Last Liquid-Release Test

6.3.1.1 Field Studies at Niche 3650

Figure 7a illustrates the location of seven 0.0762-m-diameter boreholes installed at Niche 3650, constructed on the western side of the ESF main drift within the Tptpmn unit. Three of the boreholes, designated UL, UM, and UR were installed approximately one meter apart and 0.65 m above the niche ceiling in the same horizontal plane.

Liquid-release tests were conducted prior to the niche excavation to evaluate how far a finite pulse of liquid would travel through unsaturated fractured rock. Water containing a colored dye was used to mark the wetted area, and flow paths resulting from each test. The niche was then excavated dry (using an Alpine Miner) to observe and photograph the distribution of fractures and dye within the welded tuff (Wang et al. 1999, pp. 329–332). After niche excavation, a series of short-duration seepage tests were performed to determine the amount of liquid that would seep into the mined opening (see Section 6.2 in this report).

Along the three upper boreholes, two dyes for Food, Drug & Cosmetics (FD&C) usage were released before niche excavation: FD&C Blue No. 1 and FD&C Red No. 40. Blue and red bars in Figure 23a on the upper-left side of test-interval locations represent the pre-excavation liquid-release tests. After niche excavation, liquid-injection tests with various tracers or without additional tracers were conducted at various depth intervals along the boreholes to measure seepage into the niche. Post-excavation tracers included FD&C Blue No. 1, Sulpho Rhodamine B, Pyranine, FD&C Yellow No. 6, Acid Yellow 7, and Amino G Acid. The post-excavation seepage test sequences are also summarized schematically on Figure 23a.

6.3.1.2 Last Tracer-Release Test

The last test (the focus of this section) was conducted at Niche 3650 six months after the seepage tests. During September 16-18, 1998, a liquid containing six tracers (iodide, bromide, FD&C Blue No.1, FD&C Yellow No. 5, 2,3-difluorobenzoic acid, and pentafluorobenzoic acid) was released into a highly permeable zone located in borehole UM 4.88–5.18 m from the borehole collar. Iodide, bromide, and fluorinated benzoic acids were used as nonreactive tracers, while dyes were applied as sorbing tracers. The released tracer concentrations were 4.60 g/l NaI, 4.60 g/l CaI₂, 4.60 g/l CaBr₂, 1.56 g/l FD&C Blue No.1, 1.76 g/l FD&C Yellow No. 5, 0.019 g/l 2,3-difluorobenzoic acid, and 0.018 g/l pentafluorobenzoic acid. The release rate was 0.013 g/sec, with a total released volume of about 1.52 liters. The wetting front was observed to reach the niche ceiling in a large fracture/breakout, but water did not drip into the niche.

Between September 23 and October 1, 1998, twelve sampling boreholes, nominally 1.5 m long, were drilled into the niche ceiling around and below the liquid-release interval to determine the extent of the tracer migration. Rock-core samples were collected during the drilling process for subsequent laboratory chemical analyses. Refer to pp. 99–107 and 123–124 of Scientific Notebook YMP-LBNL-JSW-6C for detailed description of this last test.

Figure 23b shows a schematic 3-D prospective view of the sampling borehole array. The cores from the boreholes were 4.47 cm in diameter and were divided into sections during coring with each section separately wrapped in Saran wrap. Each wrapped sample was placed inside a Lexan liner (with tapes wrapping both sides of the liner) and sealed in a Protec core packet. The depth interval for each section was noted on the packet, which was assigned a unique identifier number.

The tracer chemical information is shown in the scientific notebooks (YMP-LBNL-JSW-QH-1B, pp. 154–155; YMP-LBNL-JSW-QH-1D, p. 151). Tracer analysis results and discussions are presented as ratios, which is independent of the chemical purity. Attachment V describes core sample processing and aqueous tracer measurement for the analyses of tracer distribution.

No iodide concentrations above the background level were detected in the samples collected from the twelve boreholes drilled around the release interval. FD&C Yellow No. 5 was also not detected. Both iodide and FD&C Yellow No. 5 were tracers applied only during the last tracer-release episode and were not used in the early series of seepage tests at Niche 3650. Bromide was not detected above the background level. These results indicated that the sampling borehole array did not capture the tracer plume of the last release event. Liquid migration was most likely localized and very possibly confined within the 1.0 m × 1.6 m area directly below the liquid-release interval.

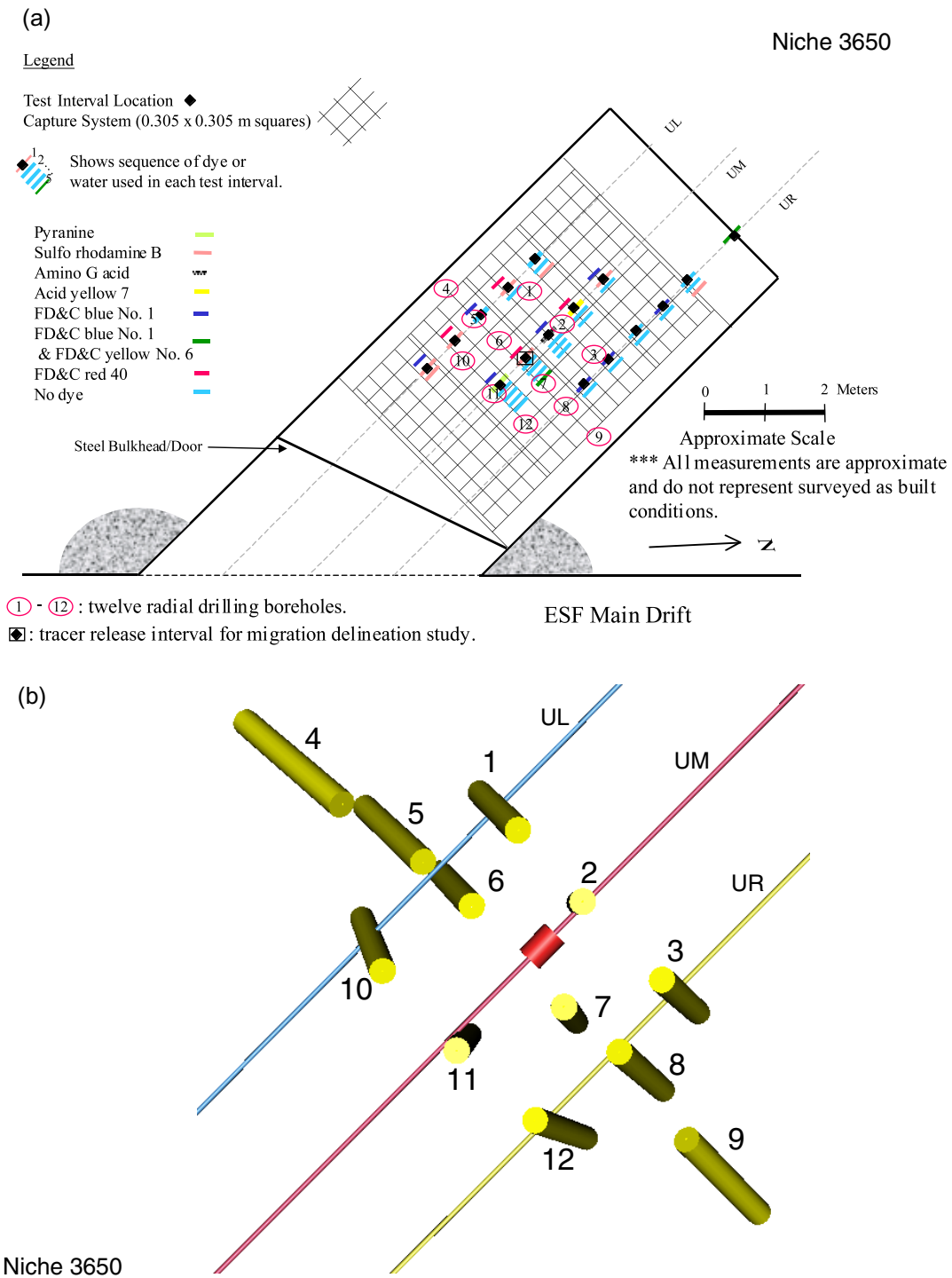


Figure 23. Sampling Borehole Array: (a) Schematic Plan View with Liquid-Release/Dye-Application History, and (b) Three-Dimensional View from inside the Niche. The red-colored cylinder denotes the release interval of the last tracer test.

6.3.2 Delineation of Tracer Distributions from Previous Liquid-Release Tests

In this section, the tracer distributions from all liquid release tests performed before the last test are evaluated. The previous tests were conducted at different borehole intervals with different flow rates to determine the seepage thresholds for individual borehole intervals. As illustrated the test sequences in [Figure 18](#) in Section 6.2.1.3.1 and in [Figure 23a](#) in this Section, some of the forty liquid release tests over 16 borehole intervals at Niche 3650 used dye tracers and some tests used water without dye. The distributions of these tracers are evaluated by the analyses of cores of the twelve boreholes drilled into the flow domains. The tracer distributions can be used to assess the extent of the spreading above the niche and provide data for evaluation of the seepage processes.

The tracer data are presented as detection ratios (dimensionless) of the detected tracer level to the background level, with a higher ratio indicating the stronger presence of the tracer in the particular depth interval of a borehole. The ratio representation provided sufficient information about spatial distributions of tracers from borehole samples, reconciled the difference in measurement detection sensitivities between ultraviolet and visible Spectrophotometer and Fluorescence Spectrophotometer, and eliminated the need to use and verify chemical purity information provided by manufacturers. Measured dye distributions were plotted in three dimensions using Earth Vision 4.0 software (Dynamic Graphics, Inc.).

6.3.2.1 Detection of Tracers

Several dyes from previous applications of seepage tests (Section 6.2.1.3.1) were detected within the borehole samples, as summarized in [Table 11](#). FD&C Blue No.1 was present at seven out of twelve boreholes, some of them with relatively high concentrations. Sulpho Rhodamine B was also detected within four borehole samples. Examples of measured dye concentration versus the depth interval from borehole collar are shown in [Figures 24 and 25](#). Overall, the dye distribution pattern was relatively spotty, reflecting the complex interplay of preferential flow paths and liquid application history, as summarized in [Figure 23a](#). Multiple tests with or without dye spiked were conducted to distribute dye tracers. All the previous liquid-release and seepage tests were conducted at least six months before the last liquid tests. The tracer distributions could associate with quasi-steady flow and transport field after the introduction of liquid pulses.

Table 11. Compilation of Tracer Detection Versus Borehole Location.

Borehole ID	FD&C Blue No. 1	Sulpho Rhodamine B	FD&C Yellow No. 6	Pyranine	Acid Yellow 7	Amino G Acid
1	-	+++	-	-	-	-
2	+++	-	-	-	+++++	+
3	+++	-	-	-	-	-
4	-	-	-	-	-	-
5	-	-	-	-	-	-
6	-	-	-	-	-	-
7	+++++	+++++	+++	-	-	-
8	+++	-	-	-	-	-
9	+	-	-	-	-	-
10	+++	+++++	-	+	-	-
11	+++++	+	-	+++	-	-
12	-	-	-	-	-	-

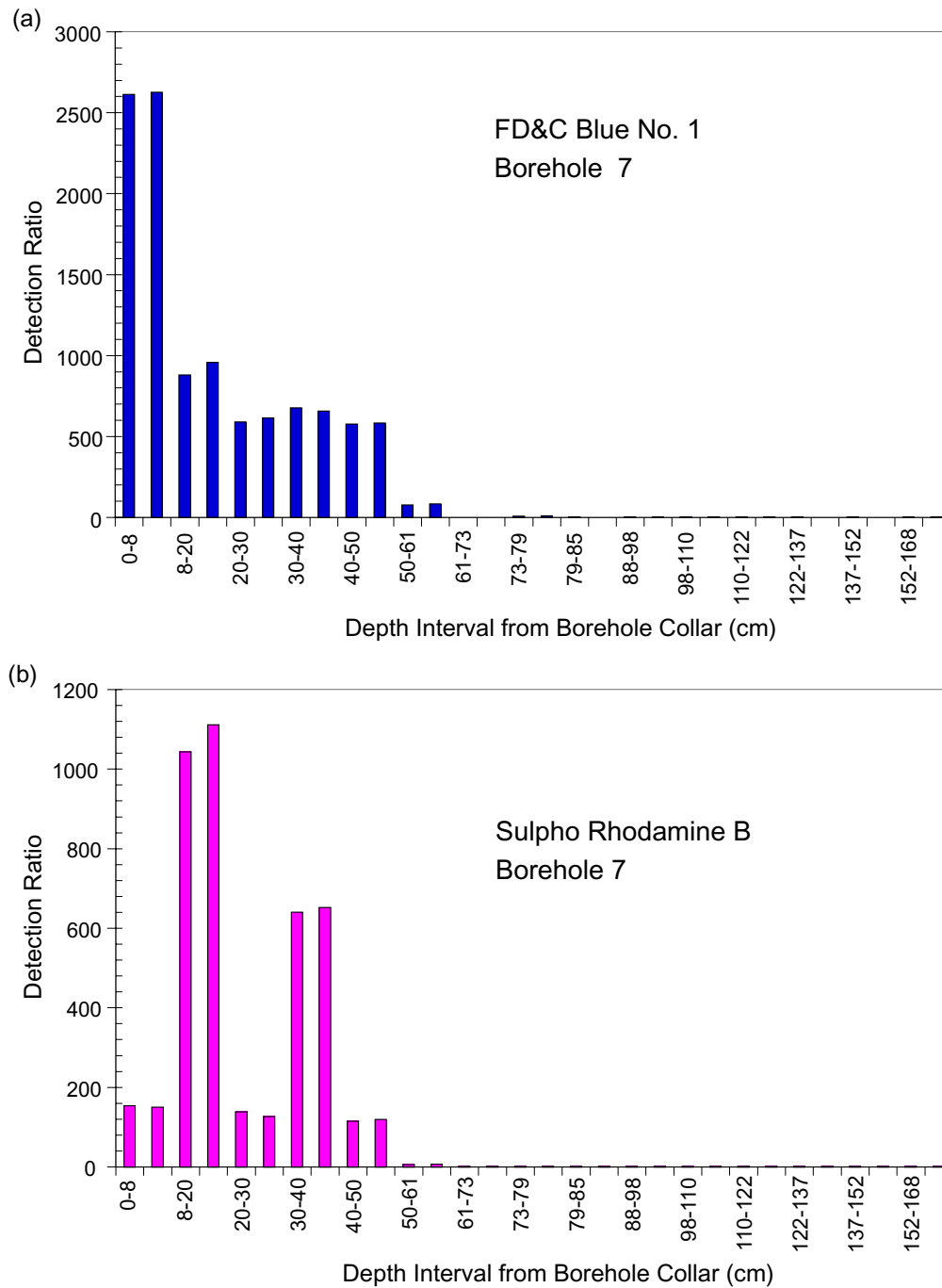
DTN: LB990601233124.003

NOTES: -: detection ratio < 3 (treated as nonpresent).

+: the highest detection ratio is between 3 - 100 within this particular borehole.

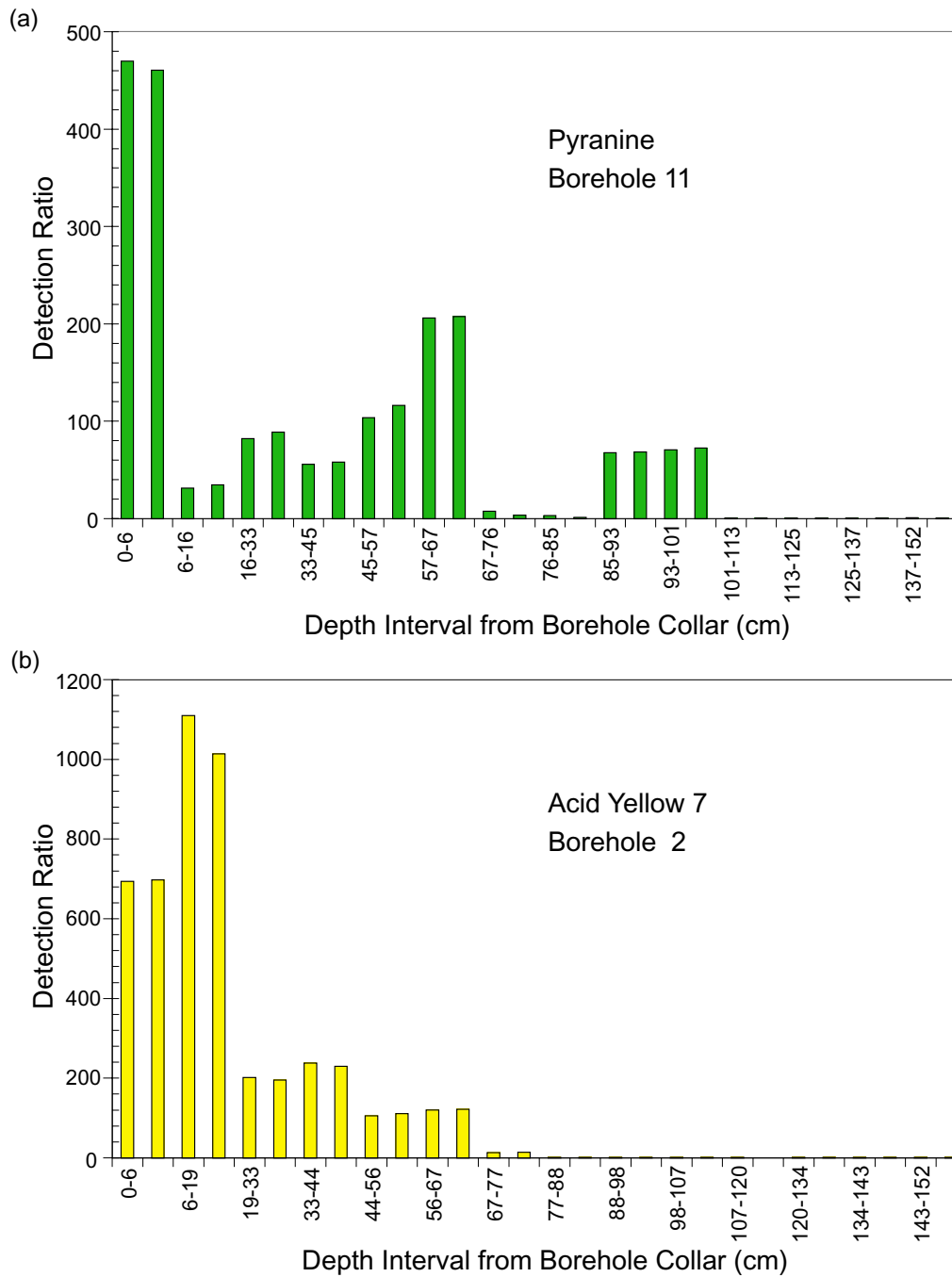
+++ : the highest detection ratio is between 100 - 1000 within this particular borehole.

+++++ : the highest detection ratio is >1000 within this particular borehole.



DTN: LB990601233124.003

Figure 24. Dye Detection along Borehole 7: (a) FD&C Blue No. 1, and (b) Sulpho Rhodamine B.



DTN: LB990601233124.003

Figure 25. Dye Detection of: (a) Pyranine Along Borehole 11, and (b) Acid Yellow 7 along Borehole 2.

6.3.2.2 Distribution of Dyes

FD&C Blue No. 1 was released in six intervals during pre-excitation liquid-release tests and in four intervals during post-excitation seepage tests (including one with a mixture of blue and yellow dyes). The blue dye distributions, together with release-interval locations, are illustrated in Figure 26. The figure legend shows the color gradients that corresponds to the detection ratios (dimensionless). Boreholes with tracer detected are represented by lines with large diameter. Boreholes without tracer detected are represented by lines with small diameter. The multiple releases and dilutions introduced a complex application history in relating individual tracer detection to its original release. Overall results suggested that most of the blue dyes were associated with nearby release intervals where tracer release tests were conducted.

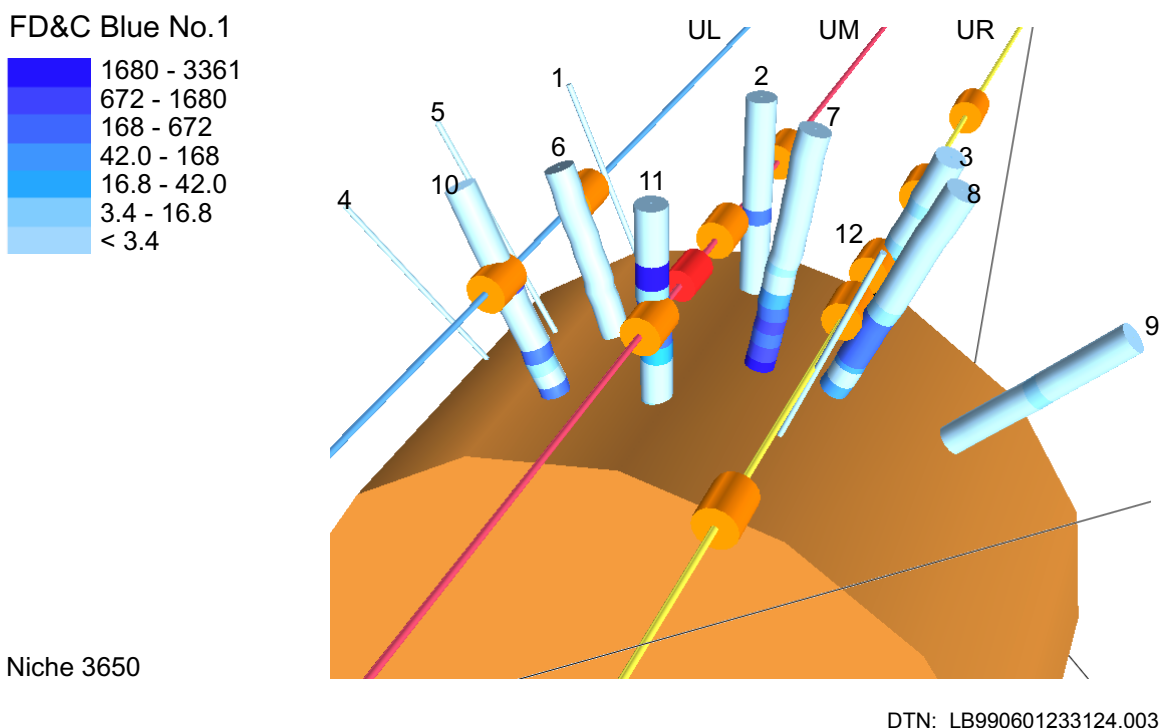


Figure 26. Three-Dimensional View of FD&C Blue No. 1 Detection Related to the Release Intervals Above the Niche. The red cylinder denotes the tracer release interval of last episode and the other orange cylinders for intervals of early release events. The sampling boreholes are individually identified. Detection ratios (dimensionless) are presented in the legend.

Figure 27 illustrates the results for Sulpho Rhodamine B. Similar to FD&C Blue No. 1, Sulpho Rhodamine B was used extensively in eight seepage tests along seven borehole intervals. Near borehole 7, Sulpho Rhodamine B was released once (in the interval UM 4.88–5.18 m), followed by three liquid releases with water without dyes, and one with the green dye (mixture of FD&C Blue No. 1 and FD&C Yellow No. 6). Presence of Sulpho Rhodamine B in borehole 7, and near the niche ceiling in borehole 8, most likely originated from this release episode. There is no detection of Sulpho Rhodamine B in boreholes 3, 9, and 12. This suggested that the Sulpho Rhodamine B was likely migrating downward, rather than spreading laterally, from the ensuing elution episode.

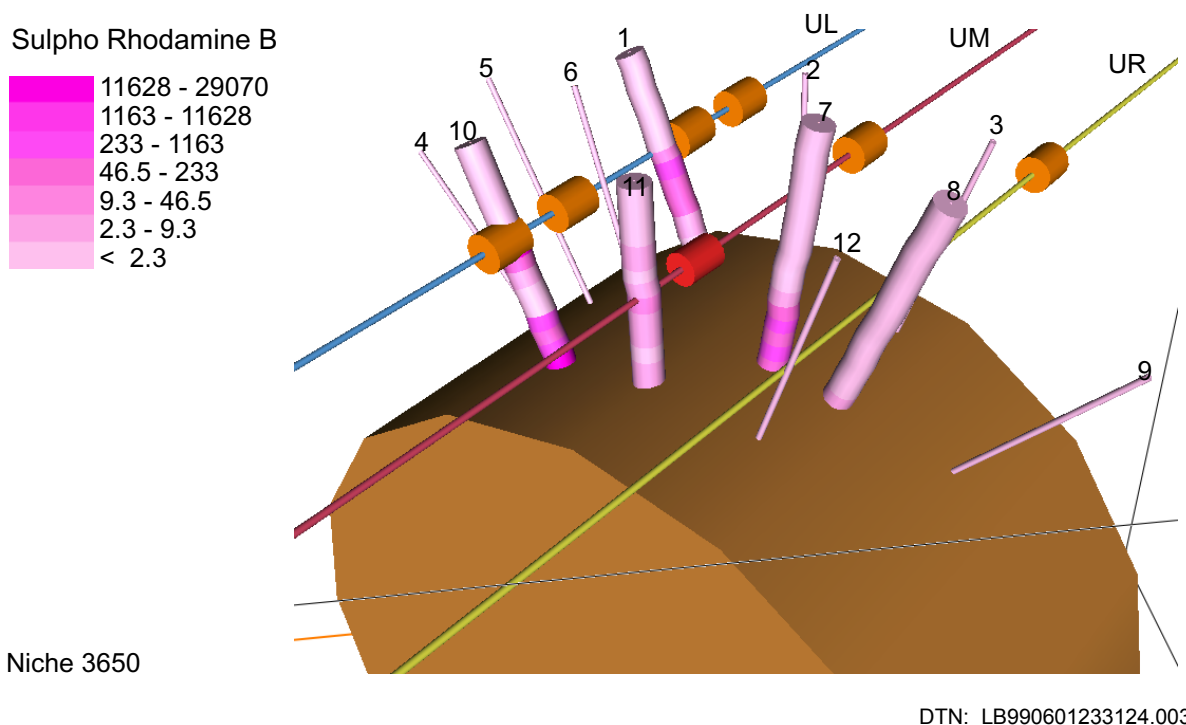


Figure 27. Three-Dimensional View of Sulpho Rhodamine B Detection Related to the Release Intervals above the Niche. The red cylinder denotes the tracer release interval of last episode and the other orange cylinders for intervals of early release events. The sampling boreholes are individually identified. Detection ratios (dimensionless) are presented in the legend.

The observations of localized tracer distribution and downward migration were more definitively confirmed by the results of four other dyes. Pyranine, Acid Yellow 7, and Amino G Acid have only been applied once at Niche 3650. FD&C Yellow No. 6 was used once at UM 4.88–5.18 m within the sampling borehole array, and another time at UL 7.62–7.92 m that was outside the borehole array (see Figure 23a). Pyranine, Acid Yellow 7, and Amino G Acid are fluorescent dyes. The low detection limits achievable with the Fluorescence Spectrophotometer enhance the efficiencies for the delineation of dye-stained flow paths within the sampling borehole array.

Pyranine was detected at the nearby boreholes 10 and 11, with its presence much lower at borehole 10 than that at borehole 11 (Table 11 and Figure 28). Borehole 11 is located almost exactly below the interval of UM 4.27–4.57 m where Pyranine has been released. Four episodes of water-only seepage tests were conducted following this Pyranine application. These liquid releases did not seem to enhance extensive lateral spreading. Overall, the lateral spreading of Pyranine was observed to be about 0.75 m to the left, resulting from these five release tests. Its presence at borehole 10 was only slightly above the background level.

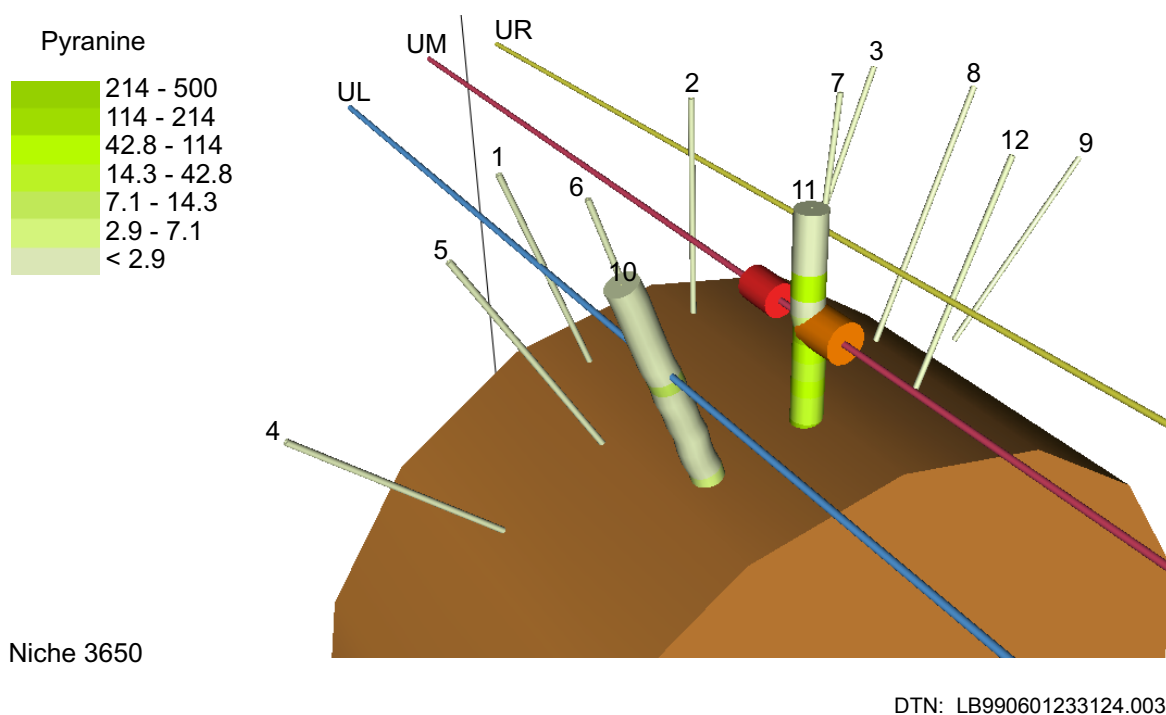


Figure 28. Three-Dimensional View of Pyranine Detection Related to the Release Interval above the Niche. The red cylinder denotes the tracer release interval of last episode and the other orange cylinder for interval of an early release event. The sampling boreholes are individually identified. Detection ratios (dimensionless) are presented in the legend.

Acid Yellow 7 was detected only at borehole 2, which was about 0.3 m from UM 6.10–6.40 m where it was released (Figure 29). Amino G Acid was also detected near the detection limit at borehole 2, which was about 0.3 m from UM 5.49–5.79 m where it was released (Figure 30). Note that although the UM 5.49–5.79 m release interval was encompassed within the sampling borehole array, no other sampling boreholes detected Amino G Acid.

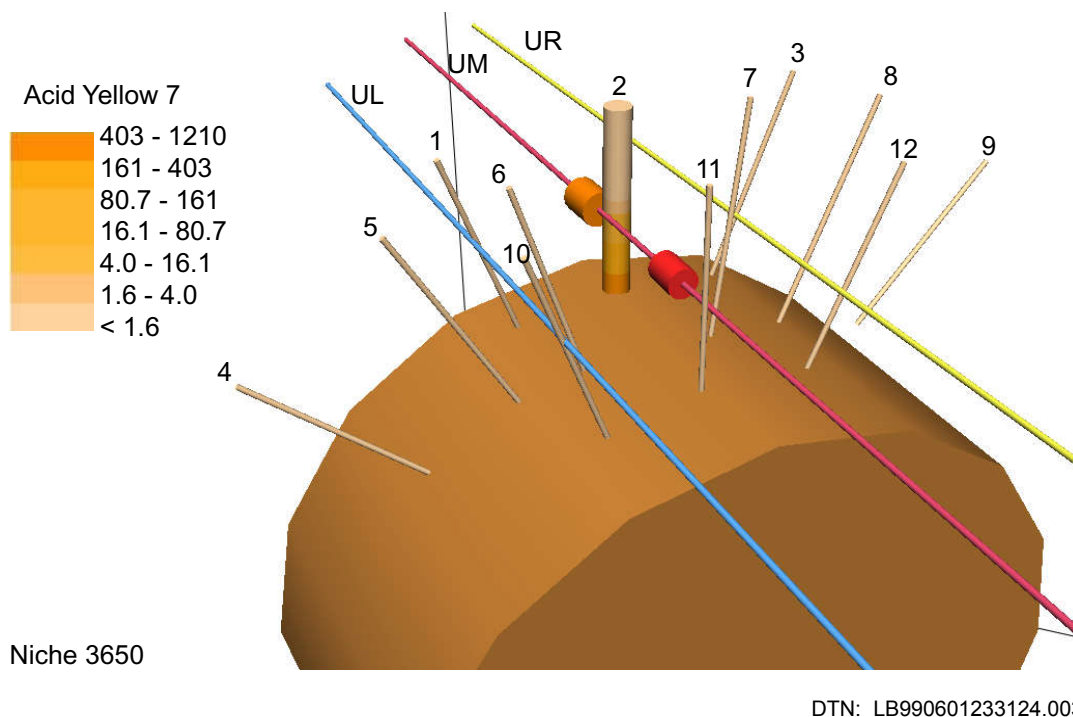
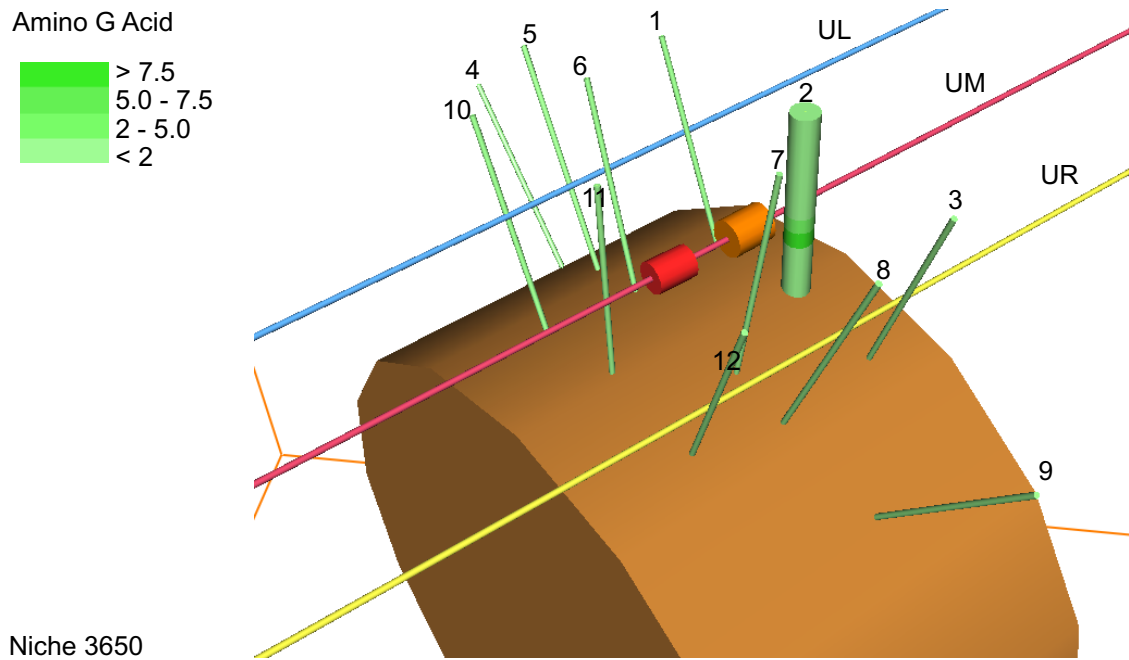


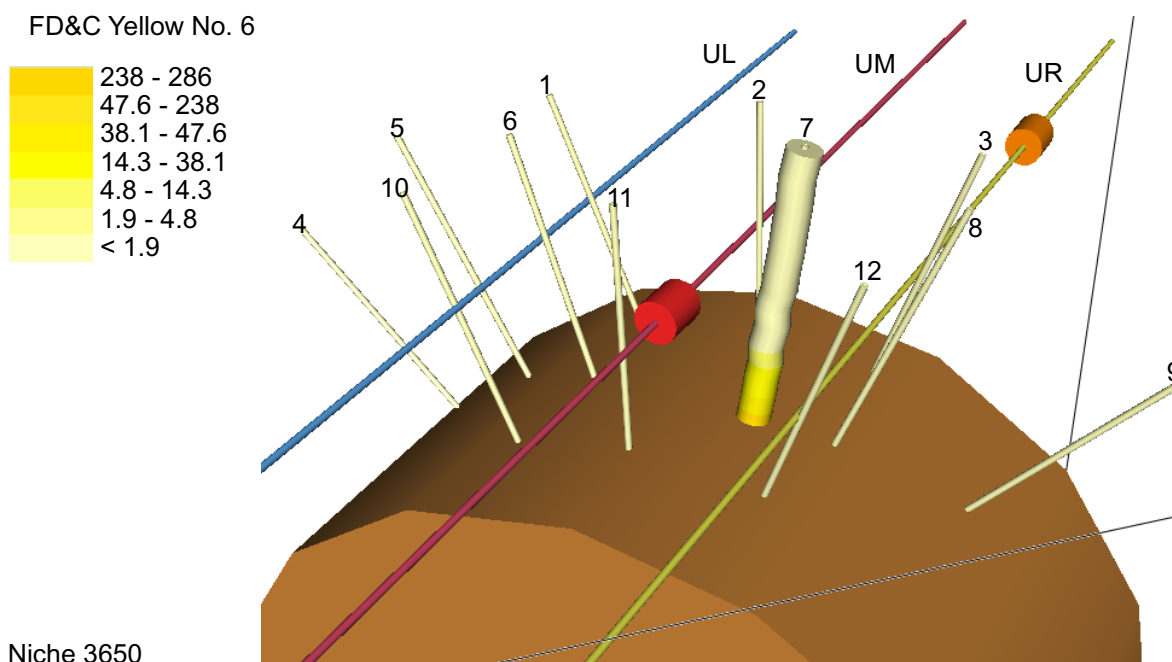
Figure 29. Three-Dimensional View of Acid Yellow 7 Detection Related to the Release Interval Above the Niche. The red cylinder denotes the tracer release interval of last episode and the other orange cylinder for intervals of early release event. The sampling boreholes are individually identified. Detection ratios (dimensionless) are presented in the legend.



DTN: LB990601233124.003

Figure 30. Three-Dimensional View of Amino G Acid Detection Related to the Release Interval above the Niche. The red cylinder denotes the tracer release interval of last episode and the other orange cylinder for interval of an early release event. The sampling boreholes are individually identified. Detection ratios (dimensionless) are presented in the legend.

The last dye distribution shown is associated with FD&C Yellow No. 6 (Figure 31). The dye was present to some high extent at borehole 7. Borehole 7 was about 0.5 m away on the right side from UM, 4.88–5.18 m where both FD&C Yellow No. 6 and FD&C Blue No. 1 were simultaneously released. This release episode was one of the lowest in concentration (0.013 g/s) while the released liquid volume was the largest (5597 g) among all the liquid-release tests conducted at Niche 3650 (see Section 6.2 of this report). Borehole 7 was located in the middle of the sampling borehole array. The sole presence of FD&C Yellow No. 6 in borehole 7 further demonstrated the localized characteristics of liquid flow with limited lateral spreading, even in this case with comparatively large release volume.



DTN: LB990601233124.003

Figure 31. Three-Dimensional View of FD&C Yellow No. 6 Detection Related to the Release Intervals above the Niche. The red cylinder denotes the tracer release interval of last episode and the other orange cylinders for intervals of early release events. (One of the two release intervals is the same as the last release event, represented by the red cylinder.) The sampling boreholes are individually identified. Detection ratios (dimensionless) are presented in the legend.

The dye distribution plots also indicated that some dyes might have migrated above the injection intervals, as illustrated in [Figure 26](#) for FD&C Blue No. 1, in [Figure 28](#) for Pyranine, and to a lesser degree in [Figure 27](#) for Sulpho Rhodamine B, in [Figure 29](#) for Acid Yellow 7, and in [Figure 30](#) for Amino G Acid. This is an interesting observation, indicating that fairly strong capillary forces may induce upward movements against gravity. However, the exact spatial extents of upward suction and tracer distribution need further verification. The locations of subsamples were derived from sample packets, and the spatial resolutions were poor, especially for fragmented core samples. The tracer subsample locations should be further checked against borehole logs (digital version if available) and core logs to improve the spatial resolution.

6.4 ANALYSES OF TRACER PENETRATION AND WATER IMBIBITION INTO WELDED TUFF MATRIX

The objectives of this study are to investigate water flow and tracer transport, focusing on the relative extents of fracture flow and fracture-matrix interaction, in the unsaturated, fractured tuff through a combination of field and laboratory experiments. Field work was conducted in the ESF niches with liquid containing tracers released at specified borehole intervals. Tracer-stained rock samples were collected during niche excavation for subsequent laboratory analyses. Clean rock samples, collected from the same stratigraphic unit, were machined into cylinders for laboratory studies of tracer penetration into the rock matrix under two initial water-saturation levels.

6.4.1 Penetration of Dyes into Rocks from the Niches

The niche test sites, borehole configurations, liquid-release tests, and tracers used in the field are described in Sections 6.2 and 6.3. Samples for laboratory analyses were collected from Niches 3650 and 4788. Laboratory tests under controlled conditions were conducted to compare the travel front behavior of moisture, nonreactive bromide, and sorbing dye tracers. Sample drilling and tracer profiling techniques were developed. The descriptions and evaluations of laboratory analyses are presented in [Attachment VI](#).

6.4.1.1 Field Observations

During the niche excavation, as described in Section 6.2.1.2, dye was observed along individual fractures and intersecting fractures to a maximum depth of 2.6 m below the liquid-release points at Niche 3650, and to a maximum of about 1.8 m at Niche 4788. In general, the dye remained relatively close to the release interval and did not spread laterally more than 0.5 m. [Figure 32](#) shows the picture of fracture network stained by FD&C Blue No. 1 at Niche 4788 and the sampling location where the dye-stained rock was collected for laboratory tracer profiling analysis. Results of post-niche excavation liquid-seepage tests at Niche 3650 further indicated the fast fracture flow with limited lateral spreading. The seepage water was captured below in cells directly beneath or immediately adjacent to the test interval.

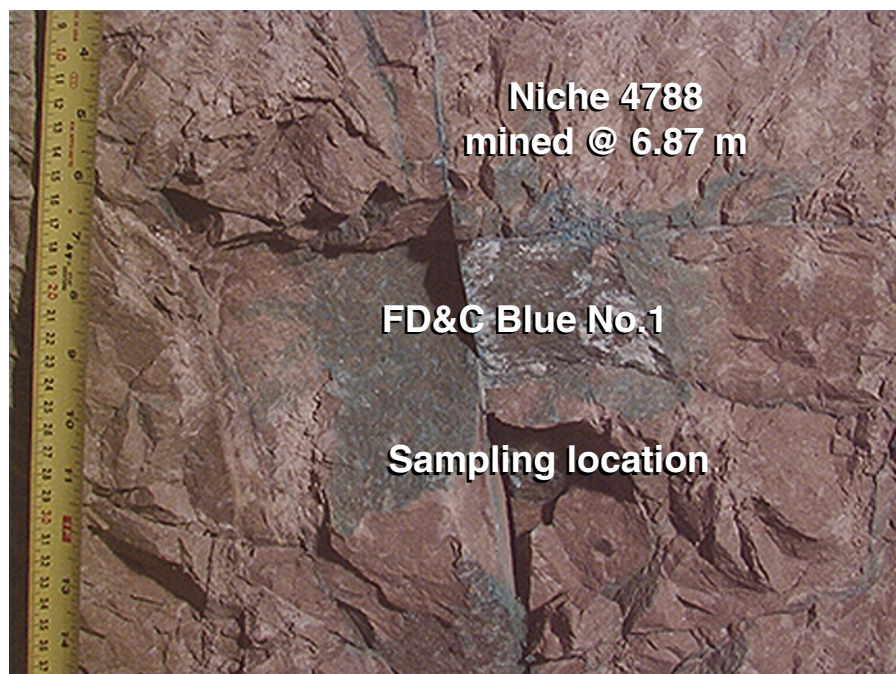


Figure 32. Photograph for Illustration of Sampling Location of Rock Stained by FD&C Blue No. 1 during Niche Excavation at Niche 4788. Refer to pp. 69–71 of Scientific Notebook YMP-LBNL-JSW-6C.

6.4.1.2 Dye Penetrations into Rocks

Visual inspection of dyed rocks collected from the field studies showed that the dye stained the fracture surfaces and the color decreased with the distance and disappeared within a few millimeters from the fracture surfaces. Figure 33 shows the rock sample stained with the Sulpho Rhodamine B from Niche 3650. The plot of Sulpho Rhodamine B detection ratio (dimensionless) versus depth from the fracture surface is shown in Figure 34. (Detection ratio is the division of the measured tracer level with the background level.) The depth on the x-axis denotes the mid-point of the drilling interval. For example, measured tracer concentration from a 1–2-mm drilling interval is shown at the 1.5 mm location from the sample surface. For three rock samples stained with either FD&C Blue No.1 or Sulpho Rhodamine B, each dye concentration decreased from the highest concentration to the background level in less than 6–7 mm. These results quantify the noticeable tracer matrix imbibitions from liquid flowing through the fractures.

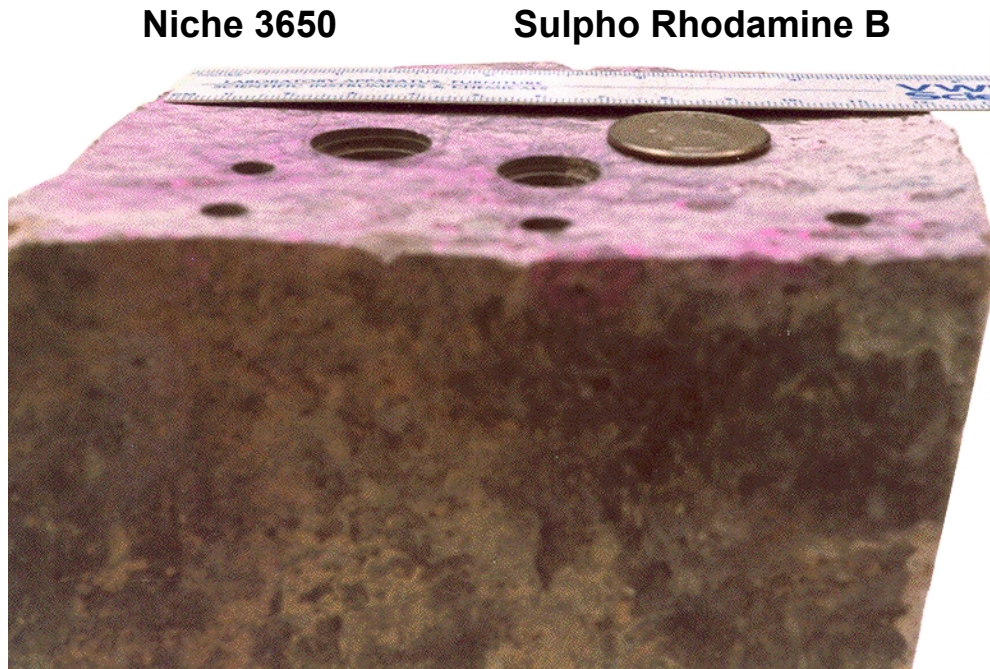
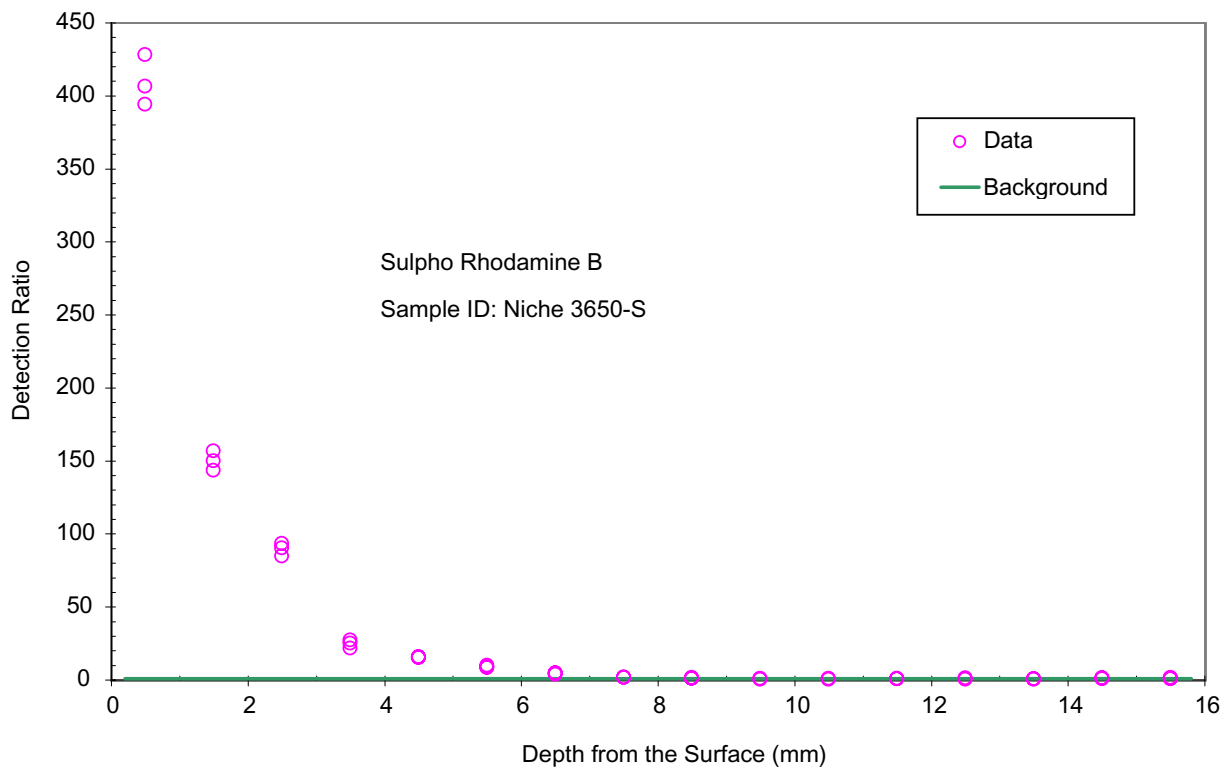


Figure 33. Rock Sample Stained by Sulpho Rhodamine B Collected from Niche 3650. A quarter coin is on the sample for size comparison. Also shown are the drilled holes for dye profiling.



DTN: LB990901233124.003

Figure 34. Sulpho Rhodamine B Penetration Profiles into Rock Matrix from the Fracture Surface.

Table 12 provides relevant information about the three dyed rock samples analyzed. The samples were collected 7–13 days after the dye-spiked water was released into the formation. Water flow in post-excavation seepage tests was shown to be very rapid, traversing 0.65 m in 4 minutes under the release rate of about 1.9 g/s (Table 13). It is therefore expected that the fluid-rock contact time is relatively short. Short travel times, together with high ratios of dye concentration in seepage water versus release water (in the far-right column of Table 13), indicated that the contacts between flowing water in the fractures and the adjacent tuff matrix were highly transient. The exact duration of contacts on the fracture surfaces could not be easily measured for transient fracture flows through the tuff rock mass.

Table 12. Compilation of Information About the Dyed Rock

Tracer	Test Date	Test Location ^c	Tracer Conc. (g/l)	Release Rate (g/s)	Release Duration (min)	Mass Released (g)	Sampling Date
Sulpho Rhodamine B ^a	8/8/97	ML 6.71 – 7.01 m	2.0	2.0	8.22	170.9	8/19/97
FD&C Blue No. 1 ^a	8/6/97	UM 6.71 – 7.01 m	7.7	1.9	8.20	438.7	8/19/97
FD&C Blue No. 1 ^b	7/2/98	UM 6.40 – 6.70 m	6.77	0.49	35.0	1019.7	7/9/98

Input: DTNs: LB980001233124.004, LB980901233124.003

NOTES: ^aTests conducted at Niche 3650 m location.

^bTest conducted at Niche 4788 m location.

^cUM: upper middle borehole; ML: middle left borehole. Depth measurement (in meters) is from the collar of the borehole to the test interval.

Table 13. Tracer Release Tests and Measured Seepage Concentrations at Niche 3650.

Tracer	Test Location ^a	Release Rate (g/s)	Mass Released (g)	Mass of Seepage Recovered (g)	Wetting Front Arrives at (min:sec) ^b	Ratio of Seepage vs. Release Conc. (%)
Sulpho Rhodamine B	UL 7.01 – 7.32 m	1.949	1005.5	16.0	4:00	95.6
FD&C Blue No. 1	UR 4.27 – 4.57 m	0.198	995.7	4.0	56:08	77.0
FD&C Blue No. 1	UR 4.88 – 5.18 m	0.190	1016.4	4.0	29:50	103.9

Input: DTN: LB980001233124.004

Output: DTN: LB990901233124.003

NOTES: ^aUL: upper left borehole; UR: upper right borehole. Depth measurement (in meters) is from the collar of the borehole to the test interval.

^bWetting front arrives relative to the start of water release to the formation.

6.4.1.3 Fraction of Fracture Flow

Fast fracture flow was demonstrated during the post-excavation seepage tests where dye-spiked water was released and collected, if present, at the collection system below the niche ceiling. The last column of [Table 13](#) shows the ratios of collected to released concentrations for FD&C Blue No. 1 and Sulpho Rhodamine B. The average seepage versus release concentration ratio is $92.2 \pm 13.8\%$ over three tests with dyes. The concentration ratio could be used to represent the extent of fracture flow associated with seepage flow, with the following considerations taken into account: The seepage solution is a composite sample, which could be diluted from the resident water, if any, in the flowing fractures. Also, note that the release concentrations were obtained from the known dye mass dissolved in the known liquid, and no liquid sample was collected for the released solution at Niche 3650 tests. This uncertainty could contribute to the unphysical ratio of 103.9% for one of the FD&C Blue No. 1 tests. Significant dilutions (about 1,000 times), needed to bring down the sample concentration within the linear standard curve needed for measurement, could also contribute to the uncertainty. More accurate ratios could be obtained if both the seepage and release solutions were measured simultaneously.

6.4.1.4 Concentration of Dye Tracer at Saturated Contact

For the dye-stained samples from the field, tracer concentrations were measured on powders by mill drillings. Tracer concentrations on the solid mass basis (C_g , mg/kg) were transformed to the tracer concentration on the liquid basis (C_v , mg/l) using the following relationship:

$$C_v = C_g \times (\rho_b / \theta) \quad (\text{Eq. 13})$$

where ρ_b is the bulk density (g/cm^3) and θ is the volumetric water content (cm^3/cm^3). With this conversion, measured tracer concentrations can be compared directly with concentration of released water. Measured bulk density (2.238 ± 0.029) and porosity ϕ (0.0877 ± 0.009) for 15 core samples were used in the calculations (DTN: LB990901233124.003).

The primary interest in the tracer concentration profiles is on the first several millimeters from the fracture surface. [Table 14](#) focuses on the results of the first sampling interval 0–1 mm from the fracture surfaces of different field samples as well as laboratory core samples (which will be discussed below). For three dye-stained samples from the field, two samples were associated with seepage tests at Niche 3650 with FD&C Blue #1 (Niche 3650-F sample ID) and with Sulpho Rhodamine B (Niche 3650-S sample ID). These tests with low volumetric concentration ratios C/C_0 (e.g., measured C_v divided by the released concentration C_0) of 17.2% and 23.3% for the first 1-mm intervals could be associated with fast transient flows through open fractures. Noticeable water and tracer imbibition into the surrounding matrix was observed even though the fracture flow could be fast. The average value over these two samples is $20.3 \pm 4.3\%$. The concentration profile is presented in [Figure 35a](#) for FD&C Blue No. 1 dye.

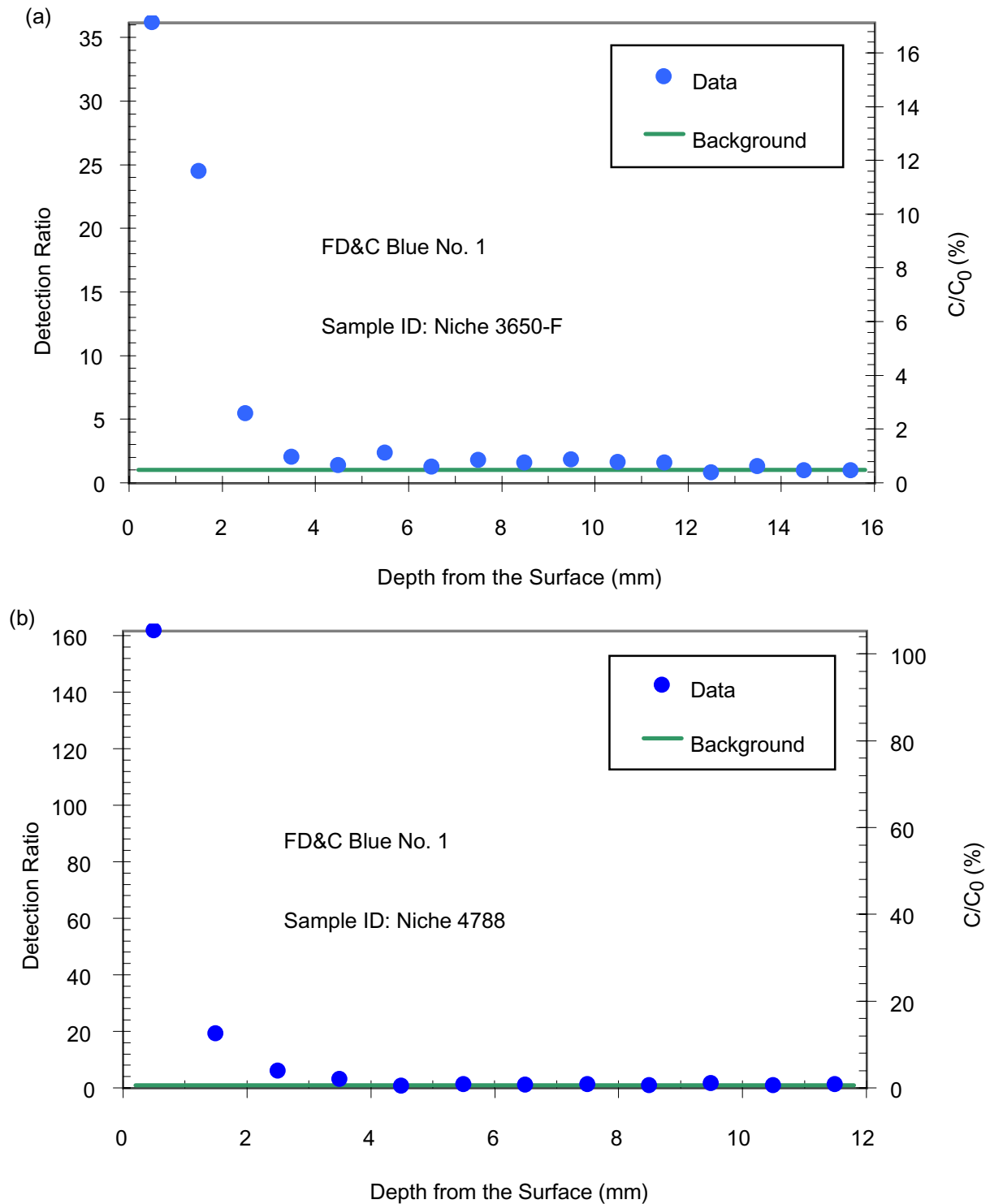
Table 14. Compilation of C/C_0 Value for Rock Drilling Taken at 0–1 mm Interval

Sample ID	Initial Saturation S_w (%)	Tracer	C/C_0 (%) ^a
Niche 3650-F	Not known	FD&C Blue No. 1	17.2±0.5
Niche 3650-S	Not known	Sulpho Rhodamine B	23.3±0.1
Niche 4788	Not known	FD&C Blue No. 1	105.5±0.6
Core D	12.5	Bromide	138.1±3.6
Core E	12.2	Bromide	135.1±3.7
Core F	15.2	Bromide	108.7±2.8
Core J	83.0	Bromide	91.4±2.1
Core H	75.8	Bromide	104.9±2.9
Core D	12.5	FD&C Blue No. 1	281.6±1.8
Core H	75.8	FD&C Blue No. 1	220.3±1.9
Core D	12.5	Sulpho Rhodamine B	272.2 ± 0.1
Core H	75.8	Sulpho Rhodamine B	271.7±0.1

DTN: LB990901233124.003

NOTE: ^a Average of data ± background (triplicate measurements)

The third data point of 105.5% ratio in Table 14 is associated with the sample shown in Figure 32. The sample was adjacent to a vertical fracture that apparently dead-ended near the sampling location. The full profile is illustrated in Figure 35b. For this sample, the fluid-rock contact time could have been longer, contributing to the higher concentration ratio at the first interval. The measured volumetric concentration ratio in the second (1–2 mm) interval drops drastically to 12.5%, which is similar to the other two rock samples. With longer contact time, stronger surface sorption of the dye might occur in this rock sample.



DTN: LB990901233124.003

Figure 35. Tracer Penetration Profile into Rock Matrix from the Fracture Surface: (a) FD&C Blue No.1 at Niche 3650, (b) FD&C Blue No.1 at Niche 4788.

6.4.2 Retardation and Tracer Front Movement

Laboratory tests were conducted to quantify the imbibition of water and the retardation of tracers and dyes into rock cores. In the laboratory, tests can be conducted under controlled conditions, with concentrations in rock samples and in the core reservoir measured simultaneously. The flow paths along cores are well-defined in comparison to the flow paths observed in the field. The laboratory test results can assist in interpreting data collected on dye-stained samples from the field tests.

There are two approaches presented for measuring the retardation factor: by front separation and by local "saturated" measurements at the core-reservoir contact. The consistency between these two approaches lends credence to the quantification of retardation factors on core samples.

6.4.2.1 Dye Retardation Factor Determined by Front Separation

Rock cores, 5.08 cm in diameter and 2.0 cm in length, were used for the imbibition experiments to examine tracer penetration into the unsaturated rock matrix. Cores were cut and machined from a clean sample block from the same stratigraphic unit as the niche locations where tracer release tests were conducted. Porosity, bulk-density and particle-density measurements were based on the core dry weight at a temperature of 60°C.

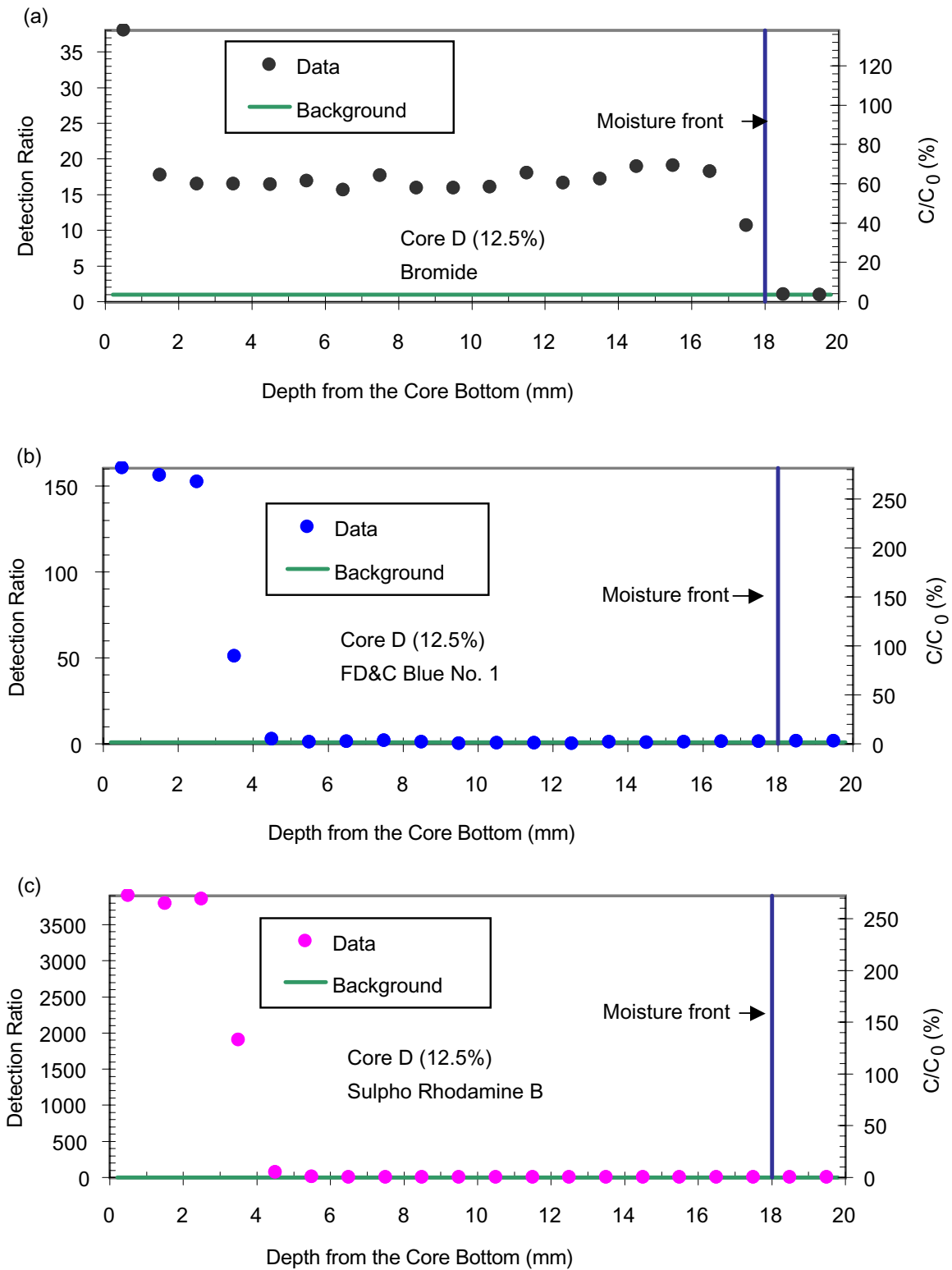
Partial saturation of cores was obtained by equilibrating cores within relative humidity chambers controlled by different saturated brines and/or water until they reached constant weights. Cores with two different levels of initial water saturation S_w , approximately 15% and 80%, were used in this work to investigate and compare tracer penetration behavior with respect to the saturation levels.

The core was hung inside a humidity-controlled chamber, with the core bottom submerged in a water reservoir containing tracers to a depth of about 1 mm. The core weight gain was continuously recorded by a data acquisition system. This study was designed to simulate the imbibition and penetration of tracers into the matrix from a continuously flowing fracture, modeled here as the core bottom. After a predetermined period of time (about 16–20 hrs), the core was lifted out of the reservoir, and the moisture front was visually examined. Rock sampling was immediately conducted as described below. The water contained about 10 g/l LiBr, 1 g/l FD&C Blue No. 1, and 1g/l Sulpho Rhodamine B. These tracers were selected to compare the behavior of nonreactive bromide with the dyes used in the field tracer work.

Figures 36 and 37 compare the concentration profile of nonreactive bromide with the concentration profiles of both FD&C Blue No.1 and Sulpho Rhodamine B, relative to the moisture fronts obtained from visual inspection. The dyes lag behind the bromide front, indicating dye sorption to the rock. FD&C Blue No.1 and Sulpho Rhodamine B were the most visible in the tuff among dyes tested. Sorption of these dyes on rock is expected from their complex chemical structure with various functional groups, even though they are negatively charged under normal pH conditions.

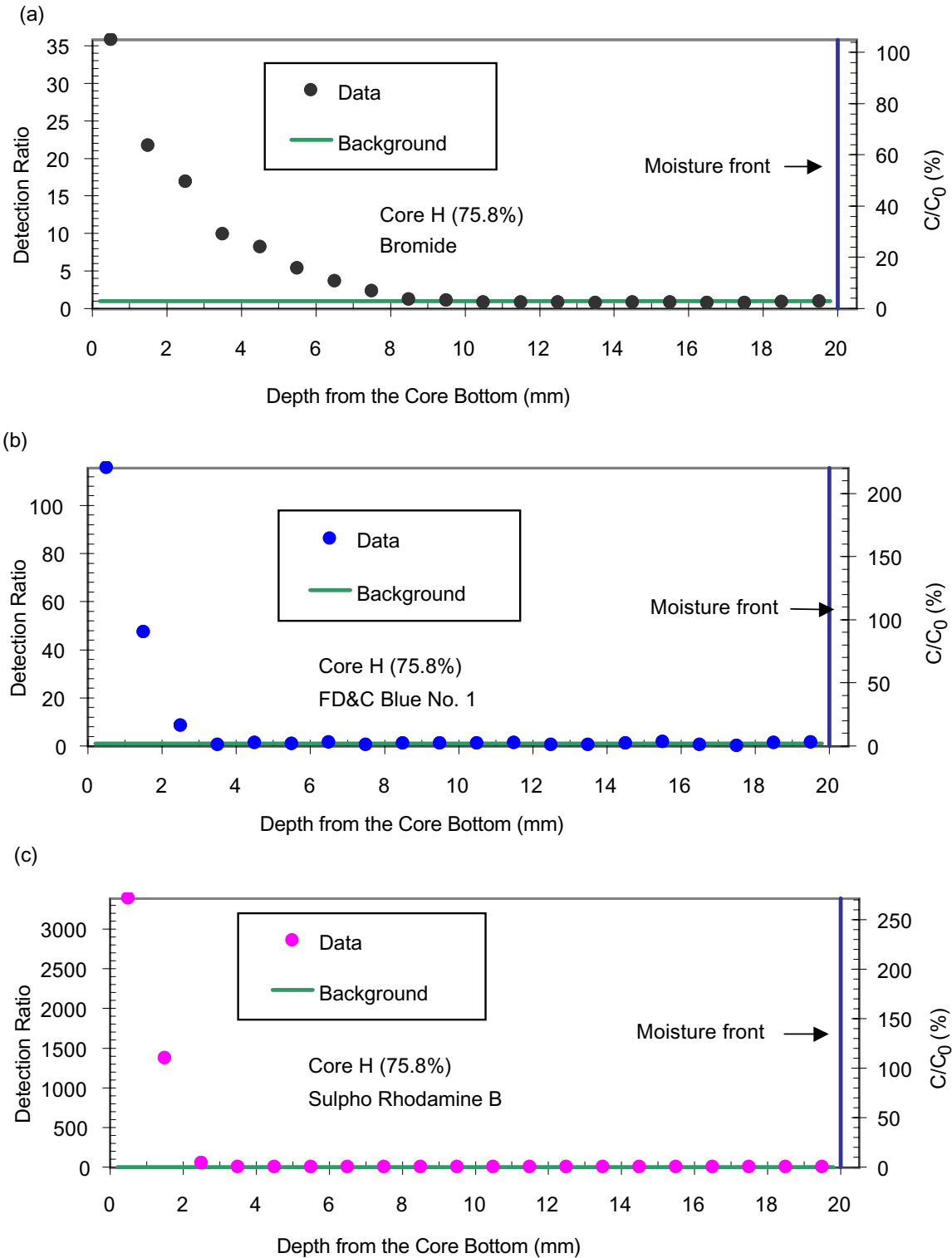
From the tracer profiles, the retardation factor R can be derived as the ratio of travel distance of nonreactive tracer divided by the travel distance of sorbing tracer. Bromide is assumed to be a

nonreactive tracer in tuff. In Figure 36 for Core D at low initial saturation, the bromide front is located at 17–18 mm from the core bottom ($d_{0.5} = 17.5$ mm, where $d_{0.5}$ is the depth at which the concentration is half of the maximum concentration in the profile). The first data point at the 0-1 mm interval was treated as an outlier and was excluded for bromide front determination. For both sorbing tracers FD&C Blue No. 1 and Sulpho Rhodamine B, $d_{0.5}$ is located at 3.5 mm (Figure 36). The retardation factor for both dyes is estimated to have the value 5 ($= 17.5$ mm/3.5 mm). Similarly, R is estimated to be 2.33 ($= 3.5$ mm / 1.5 mm) for both dyes in Core H with high initial S_w (Figure 37).



DTN: LB990901233124.003

Figure 36. Comparison of Tracer Concentration Profiles in a Low-Initial-Saturation Core: (a) Bromide, (b) FD&C Blue No. 1, (c) Sulpho Rhodamine B. Core D had initial saturation of 12.5% and was in contact with saturated boundary for 19.5 hours.



DTN: LB990901233124.003

Figure 37. Comparison of Tracer Concentration Profiles in a High-Initial-Saturation Core: (a) Bromide, (b) FD&C Blue No. 1, (c) Sulpho Rhodamine B. Core H had initial saturation of 75.8% and was in contact with saturated boundary for 17.9 hours.

The saturation dependence of the retardation factor is derived from the following functional relationship (Porro and Wierenga 1993, p. 193-194):

$$R = 1 + \rho_b \times K_d / \theta \quad (\text{Eq. 14})$$

where K_d (ml/g) is the sorption distribution factor representing the distribution of solutes between aqueous and solid phase, ρ_b is the bulk density (g/ml), and θ is the water content. This equation explicitly shows that solute retardation is inversely related to water content. If the effective θ value is estimated as the average of the initial water content and the final water content, the K_d value can be derived from the R -value. For the two core samples, the K_d value was calculated to be 0.089 ml/g for Core D and 0.047 ml/g for Core H. The bulk density and porosity values for each core were measured independently, with values listed in Table 15. These measured values in Table 15 were used in calculating K_d values from measured R values.

Table 15. Measured Properties for Core Samples

Sample ID	Porosity (cm ³ /cm ³)	Bulk density (g/cm ³)	Particle density (g/cm ³)
Core D	0.0888	2.248	2.466
Core E	0.0849	2.251	2.459
Core F	0.0890	2.239	2.457
Core H	0.0896	2.245	2.465
Core J	0.0823	2.266	2.469

DTN: LB990901233124.003

As an additional consistency check, we can reverse the calculations and derive the R values from the K_d values for a fully saturated condition. The $R_{100\%}$ at 100% is 3.25 for Core D and 2.17 for Core H from the inverse calculations. The average $R_{100\%}$ is 2.71 ± 0.76 for both FD&C Blue No. 1 and Sulpho Rhodamine B. Both K_d value and $R_{100\%}$ are constants independent of saturation. The simple checking verifies the functional relationship of Equation 14. For comparison, Andreini and Steenhuis (1990, p. 85, 98) found that the retardation factor for FD&C Blue No. 1 ranged from 1.5 to 7 in a fine, sandy loam soil.

6.4.2.2 Dye Retardation Factor Measured at Saturated Contact

Another way to evaluate the test data is to compare the saturated $R_{100\%}$ with the measured concentration ratios at the core contact boundary. The interval of 0–1 mm of a core was in contact with traced water in the laboratory tests and was therefore in nearly saturated conditions. The ratio C/C_0 is a direct measure of the retardation factor or the effects of sorbing tracer accumulation. For the two tests with each dye in Table 14, the averaged values for C/C_0 are 2.51 for FD&C Blue No. 1, 2.72 for Sulpho Rhodamine B, and 2.61 ± 0.28 over both dyes. These values can be compared to the $R_{100\%}$ value of 2.71 ± 0.76 . With the small number of samples (two cores, two tracers), the consistency with different approaches is encouraging. For comparison, the average of five tests with bromide in Table 14 is 1.16 ± 0.20 for this presumably nonreactive tracer.

It is important to state that the core measurements presented in this study can generate K_d values for intact rock under *in situ* partially saturated conditions. Most of the K_d values for sorbing solutes have been acquired by batch experiments using crushed rock, with the sizes chosen more or less arbitrarily and mainly for experimental convenience. The batch experiments were performed under saturated conditions with large water/rock ratios. There are concerns regarding the use of crushed-rock samples versus solid-rock samples in batch experiments on tuff rocks. The water/rock ratios used in the sorption experiments with crushed samples were large in comparison with the water/rock ratios likely to exist in the UZ. The laboratory approach with core analyses presented here could be adopted to generate more representative K_d values for radionuclide transport in the UZ.

6.4.2.3 Partitioning of Fracture Flow and Matrix Imbibition in Fast Flow Paths

The laboratory-tested core samples in contact with dye water were shown to accumulate high concentrations in the first 1-mm interval, with the average concentration ratio C/C_0 (%) of $261 \pm 28\%$ from the last four entries in Table 14. The first two entries in the table, as discussed in Sections 6.4.1.2 and 6.4.1.3, were associated with two field samples stained by relative fast flows activated by the pulsed releases used in seepage tests. The average concentration ratio of $20.3 \pm 4.3\%$ was much lower than the corresponding laboratory core values. The dilution factor of 7.7% ($= 20.3\%/261\%$) represents the percentage of tracer water imbibed into the first 1-mm interval of the matrix adjacent to the flowing fracture. An independent estimate of the fracture flow percentage was presented in Section 6.4.1.3. The average seepage versus release concentration ratio of $92.2 \pm 13.8\%$ was derived from averaging over three seepage tests with releases of dye-traced water. The concentration ratio could be used to represent the extent of fracture flow associated with seepage flow. The bulk of the released water seeping into the niche was likely associated with fast fracture flows of short contact duration with the adjacent matrix water. The approximately 92% fracture-flow estimate from seepage water, sampled during drift seepage testing in niches, is consistent with the approximately 8% estimate of tuff medium in the fracture-matrix contact, based on laboratory analyses of rock samples collected during niche excavation. The 92% fracture-flow and 8% matrix-imbibition estimates, from independent field and laboratory analyses, provide the critical data on flow partitioning between fracture and matrix under the seepage test conditions at Yucca Mountain potential repository horizon.

6.4.2.4 Travel Front Separation

As a nonreactive tracer, bromide is frequently used for flow tracking. The bromide front is comparable to the moisture front in the rock core at the initial water saturation of 12.5%, as illustrated in [Figure 36a](#). On the contrary, the bromide front lags significantly behind the moisture front at the higher initial water saturation of 75.8%, as shown in [Figure 37a](#). Note that the core top was wet when the experiment was ended, although the moisture front was shown at the 20 mm location at [Figure 36b](#). This observation of nonreactive solute front lagging behind the moisture front agrees with the findings in moist soils (Warrick et al. 1971, pp. 1216, 1221; Ghuman and Prihar 1980, pp. 17, 19; Porro and Wierenga 1993, pp. 193, 196). Warrick et al. (1971, pp. 1216–1225) first reported that the advance of a solute front was highly dependent on the soil moisture content during infiltration. During infiltration, no solute was found in the advancing wetting front where soil moisture contents were increasing, although the initially infiltrating water contained nonreactive tracer. The importance of this front separation, observed under a transient flow condition, might be more pronounced for low porosity materials under high moisture saturation, such as tuff at Yucca Mountain. Under these circumstances, a relatively small amount of invading solution can push the initial water further into the matrix.

For the imbibition experiment in Core D with low initial water saturation, the bromide front is sharp, with the strong capillary force driving the advection-controlled transport. Whereas for the Core H with high initial water saturation, the bromide front is quite diffuse since dispersion and dilution become important processes (on account of weaker capillarity) compared to advective flow. Sharp and diffused front separations between bromide nonreactive tracer front and moisture front, as well as between sorbing tracer front and bromide front, would provide the data for elucidating the flow and transport in unsaturated, fractured tuff.

6.5 CROSS-HOLE ANALYSES OF AIR INJECTION TESTS

This section continues the pneumatic air-permeability test analyses first presented in Section 6.1. Section 6.1 focuses on the air-permeability variations along boreholes in four niches. The permeability profiles provide initial inputs to liquid-release-test interval selection, as described in Section 6.2. The permeability profiles were also used in a seepage calibration study documented in the AMR on seepage calibration in defining the heterogeneity permeability structure used in modeling.

This section focuses on analyses of cross-hole data for fracture-network connectivity. The fracture-network connectivity is one of the most important characteristics in evaluating flow paths from the inlets to the outlets of a given regime. The larger the system, the more elusive it is to determine the dominant flow paths. Air flow paths elucidated in this section are used to characterize test beds for liquid-flow test design and analysis, as described in the following Sections 6.6 and 6.7 for two slotted test beds in the ESF.

Cross-hole tests used the same pneumatic testing equipment described in [Attachment II](#). Up to seven identical packer strings were fabricated and installed in the boreholes to sample a rock volume in the niches and in the test beds. The packer can isolate 0.3-m intervals along its length. Each interval can become either an observation zone used to monitor pressure or the injection zone where air is introduced under pressure during the test. The automation system controls the permutations through pre-assigned sequences of injection tests in all borehole intervals in the borehole cluster.

The cross-hole data is acquired at the same time as the single-hole data, by logging the steady-state pressure response in all observation zones while performing an injection. As described in Section 5.5, the observation response pressure is divided by the injection pressure to provide a measure of how well a response zone is connected to an injection zone in relation to that response zone's connections to the rest of the site. The normalization with injection pressure enables all the observation responses from all injections at a site to be directly compared. The cross-hole connections can all be viewed on a single 3-D diagram instead of individual diagrams for each tested injection zone.

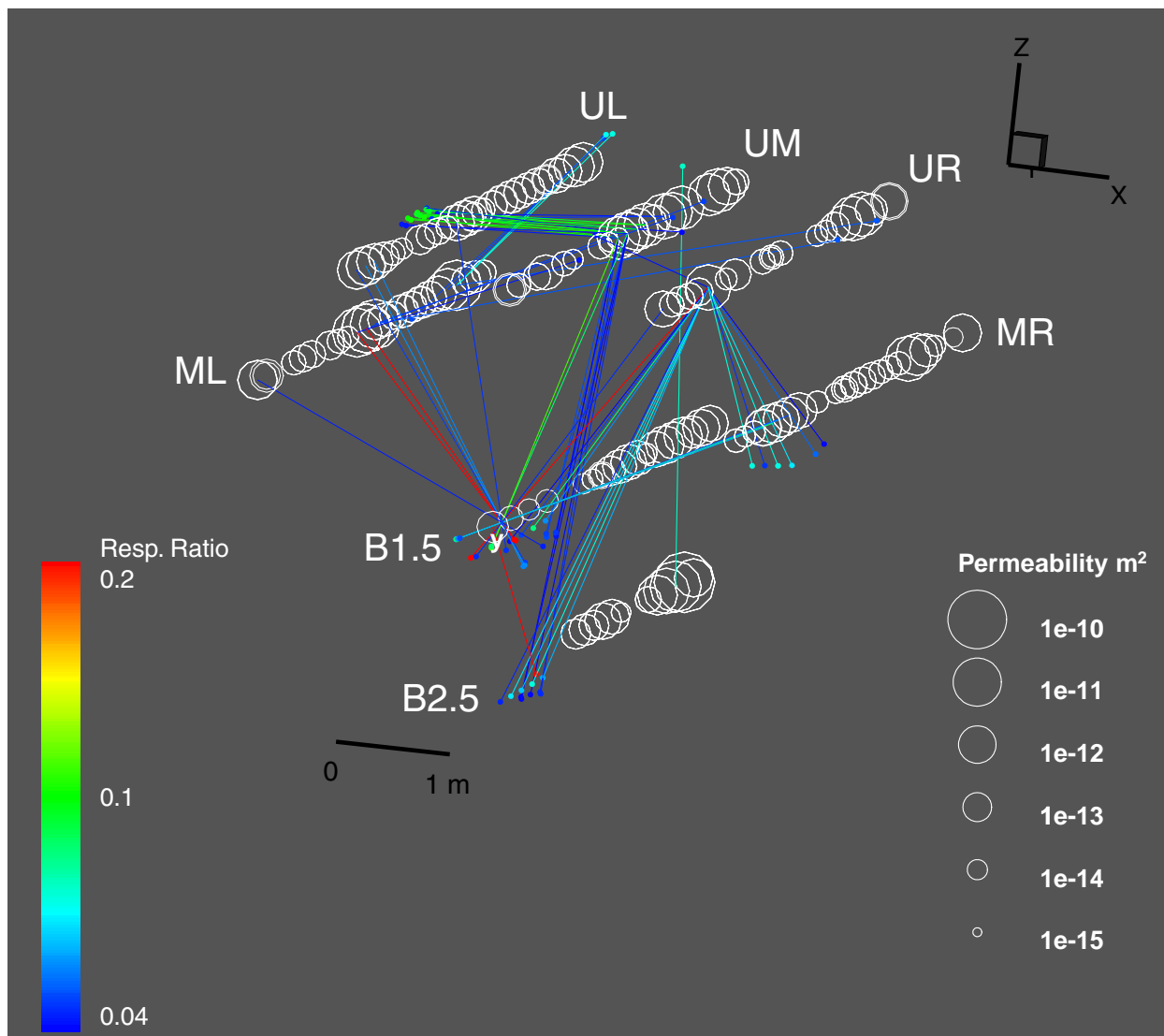
The four niches and Alcove 6 are located within the TSw unit in the potential repository horizon. The Alcove 4 test site is in the PTn unit along the North Ramp of the ESF. Both the fractured TSw and the predominately porous PTn were evaluated by the pneumatic air-permeability tests.

6.5.1 Cross-Hole Responses in Welded Tuff

In Section 6.1.2, the single-hole permeability profiles were presented for four niches as the bases for selecting liquid-release intervals for drift seepage testing. The first example of cross-hole analysis in fractured rock is on Niche 4788, located in an intensely fractured zone. The cross-hole analysis for Niche 4788 is illustrated in [Figure 38](#). The single-hole permeability values (presented in Section 6.1 as profile plots in [Figures 15 and 16](#)) are represented by circles in the cross-hole plot, with each circle centered along the test interval within each of the boreholes. The size of the circles scales with the single-hole permeability at each interval. Grayscale pins are shown with their points at the centers of the circles of the injection zones and

heads intersecting through the centers of other circles at the observation zones. Direction of flow is towards the pinhead, and the grayscale indicates the normalized response ratio (Resp. Ratio in the figure) from zero to one.

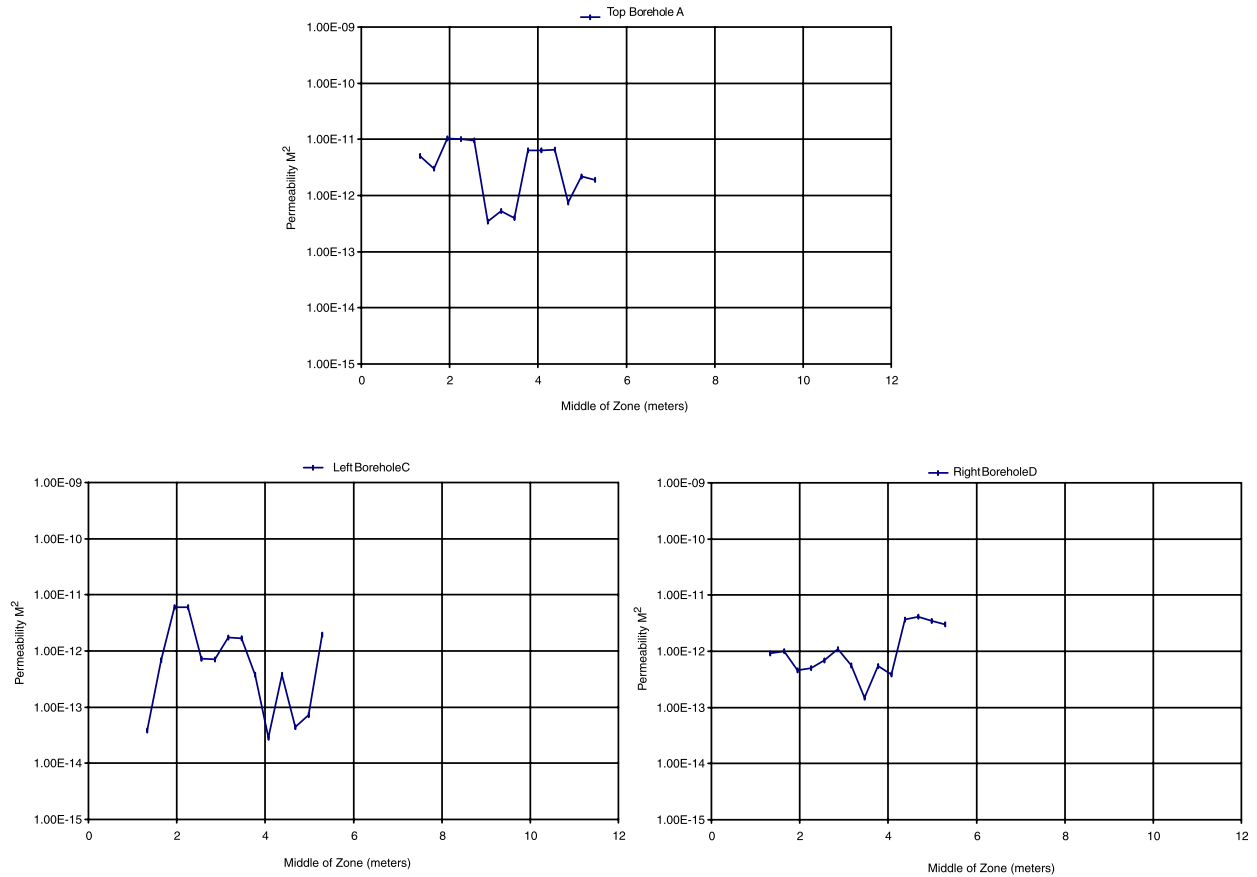
Figure 38 for Niche 4788 is fairly representative of a fractured site, showing discrete connections. It should be noted that very few of the connections have an opposite counterpart; the connections are predominantly one-way. This observation by no means indicates that flow is limited to one direction between points in the rock, but rather that the influence of local connections on the pressure response is strong. The pressure at a response zone discretely connected to the injection zone (and no other zone) will yield a large response. However, if the original injection zone in the reversed injection-observation combination is also well connected to the fracture network or a free surface, then it will not respond strongly to an injection in the original observation zone.



DTN: LB990901233124.004

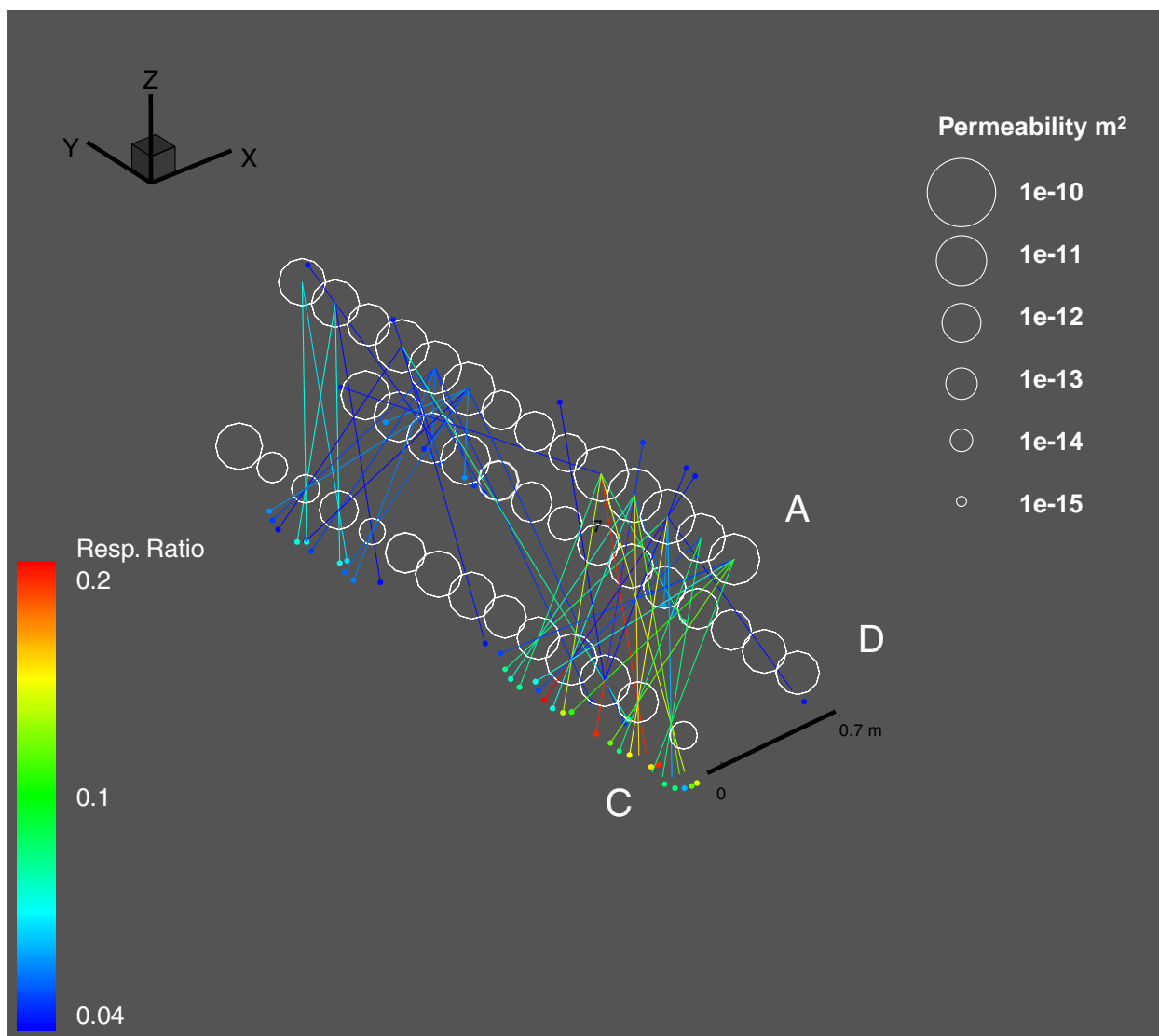
Figure 38. Cross-Hole Responses for the Borehole Cluster in Niche 4788.

The fracture-matrix interaction test site in Alcove 6 of the ESF is in rock that is fractured, with discrete, subvertical fractures and relatively few subhorizontal fractures. The single-hole permeability profiles for three boreholes tested in Alcove 6 are illustrated in Figure 39. Borehole A was used for a series of liquid-release tests, as described in Section 6.6. Boreholes C and D were used for wetting-front monitoring. Boreholes C and D are located 0.7 m and 0.6 m below Borehole A, respectively, and 0.7 m apart. The cross-hole responses for this triangular cluster of boreholes are illustrated in Figure 40. Both Figures 39 and 40 corresponded to the first series of tests conducted in the region between 1.3 m and 5.3 m from the borehole collars. Another series of tests was conducted with a straddle packer system (two-packer string to isolate one zone for liquid releases) right before liquid-release tests along the injection borehole.



DTN: LB980901233124.004

Figure 39. Single-Hole Air-Permeability Profiles along Boreholes in Alcove 6.



DTN: LB990901233124.004

Figure 40. Cross-Hole Responses for the Borehole Cluster in Alcove 6.

Both Figure 38 for Niche 4788 and Figure 40 for Alcove 6 represent cross-hole responses in fractured rock. The ratios of pressure response in the observation borehole interval to pressure in the injection borehole interval ("Resp." in figure scales) were displayed in the figures for the maximum value of 0.2 (or 20%). Niche 4788, in an intensely fractured zone, has wider range (or larger standard deviation, as shown in Table 6) of distribution in permeability than the variations over a smaller scale at Alcove 6. Both fracture sites contain discrete and well-defined flow paths between boreholes.

During liquid-release tests in the welded tuff (Section 6.2 on niche seepage tests and Section 6.6 on fracture flow tests), it was observed, in some cases, that liquid flux at certain zones was not always commensurate with the air-permeability values at these zones (see Attachment III). Besides the capillary mechanism (that water will prefer smaller aperture fractures), another

possible explanation for this observation is that liquid tries to flow downward following gravity and is thus more sensitive to the directionality of permeability than is air. Directionality of flow is not available from single-hole data and requires cross-hole data analyses.

6.5.2 Permeability Distributions and Cross-Hole Responses in Nonwelded Tuff

The Alcove 4 test bed is located in the PTn unit. The test bed contains several nonwelded and bedded subunits, including a pinkish-colored argillic layer. The test bed contains a fault plane as illustrated in Figure 41. Section 6.7 describes in more detail the borehole configuration and specifications. In this section, the focus is on the cluster of seven boreholes. Boreholes 1, 4, 11, and 12 intersected the projected fault plane in the front part of the test block, while boreholes 2, 15, and 16 penetrated other features in the test block, with potential fault zone influences (if any) confined near the ends of the boreholes. If the fault is perfectly planar, the last three holes would not be intercepted by the fault.

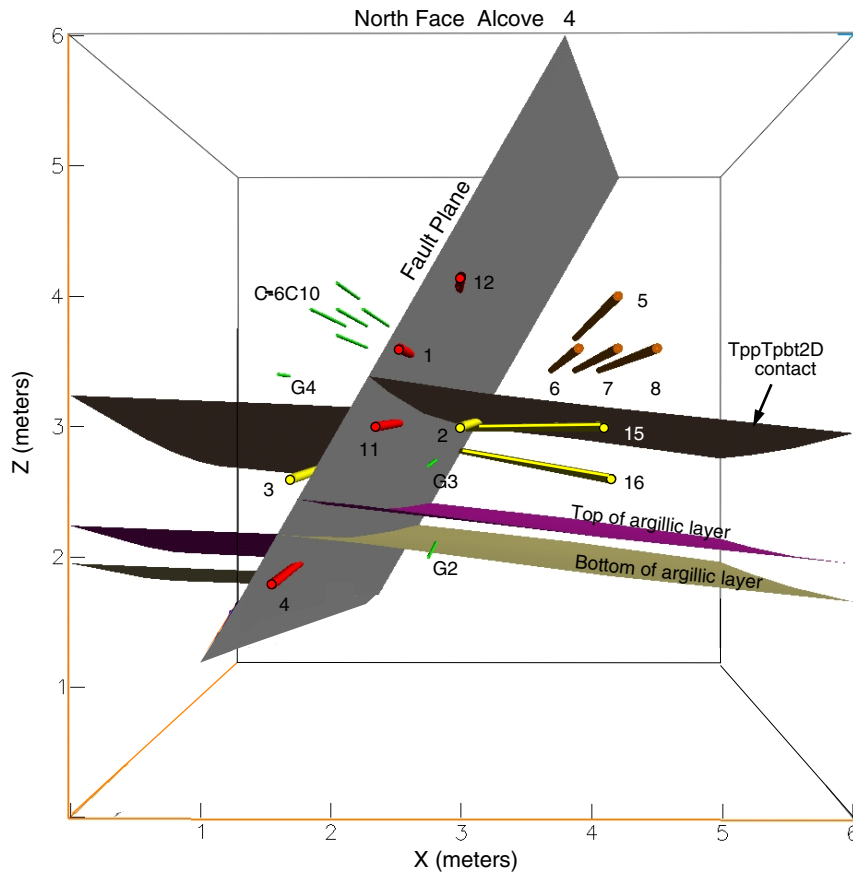
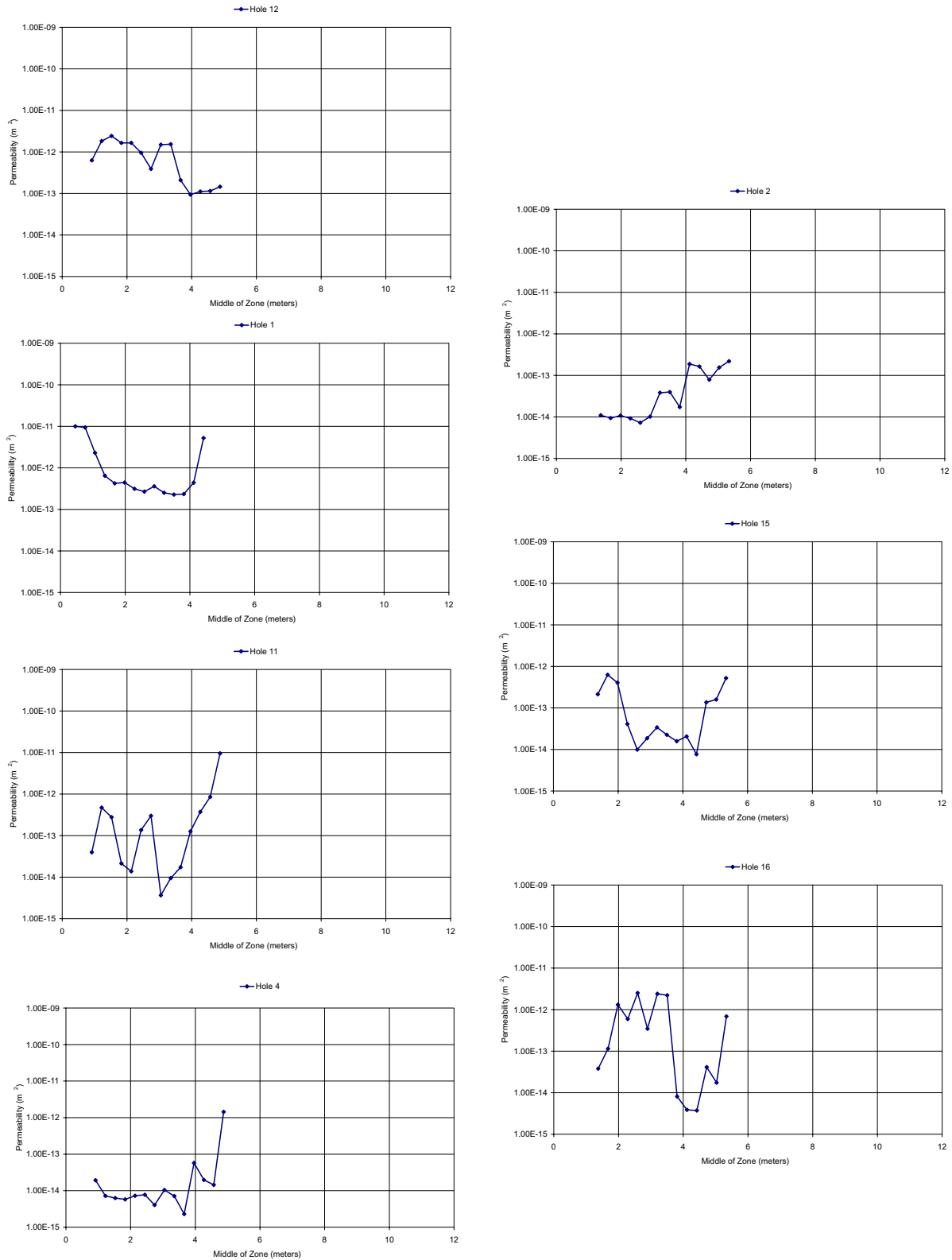


Figure 41. Schematic Illustration of Alcove 4 Test Bed.

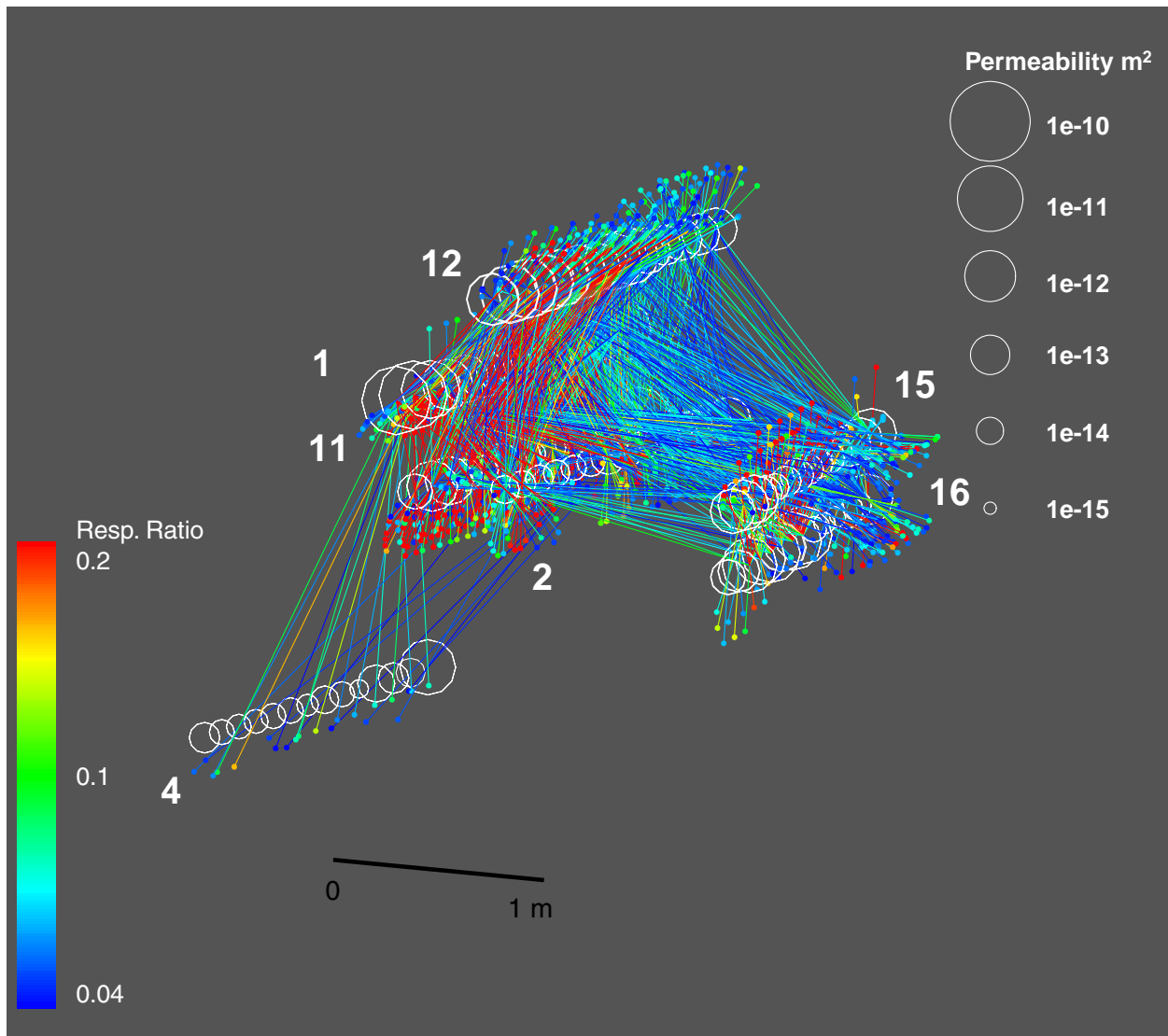
Figure 42 illustrates the single-borehole air-permeability profiles along the boreholes. Layer variations and the influence of faults could contribute to the widely distributed set of permeabilities over a broad range, both along individual boreholes and among different boreholes. With the exception of borehole 12, the other six boreholes penetrate a high-permeability zone near the end of the boreholes. Among all the borehole clusters tested in the ESF up to date, the Alcove 4 PTn cluster shows the largest standard deviation of any of the sites (see Table 6 in Section 6.1.2.3). Even the cluster at the intensely fractured site at Niche 4788 has lower standard deviation of log permeability (0.85) than the value at Alcove 4 (0.93). The mean permeabilities of these two distinctly different sites (in lithological, geological, and fracture characteristics) are incidentally nearly identical. In comparison, the standard deviation for Alcove 6 cluster was 0.67, and mean was nearly one order of magnitude higher.

Figure 43 shows the connections for Alcove 4 at the same shading scale used in welded tuff plots (Figures 38 and 40). The number of connections is much higher for this nonwelded tuff site. To better display the stronger connections, Figure 44 portrays the data at Alcove 4 on a more appropriate scale and trims off the weaker connections. The salient features of the site now become apparent. Strong vertical connections are apparent between the upper and middle boreholes, but very little connectivity exists between the middle borehole and the lower-left borehole, despite similar flow rates and distances. The argillic layer exists between these locations and the slot provides a nearly impermeable barrier. The single strong connection running from left to right is most likely associated with a high-permeability zone identified by the single-hole profiles. The high-permeability zone could be associated with the fault intersecting the boreholes near the end. Interceptions were not identified in pre-test design in Figure 42. The connections were identified by cross-hole analyses of pneumatic air-permeability test data.



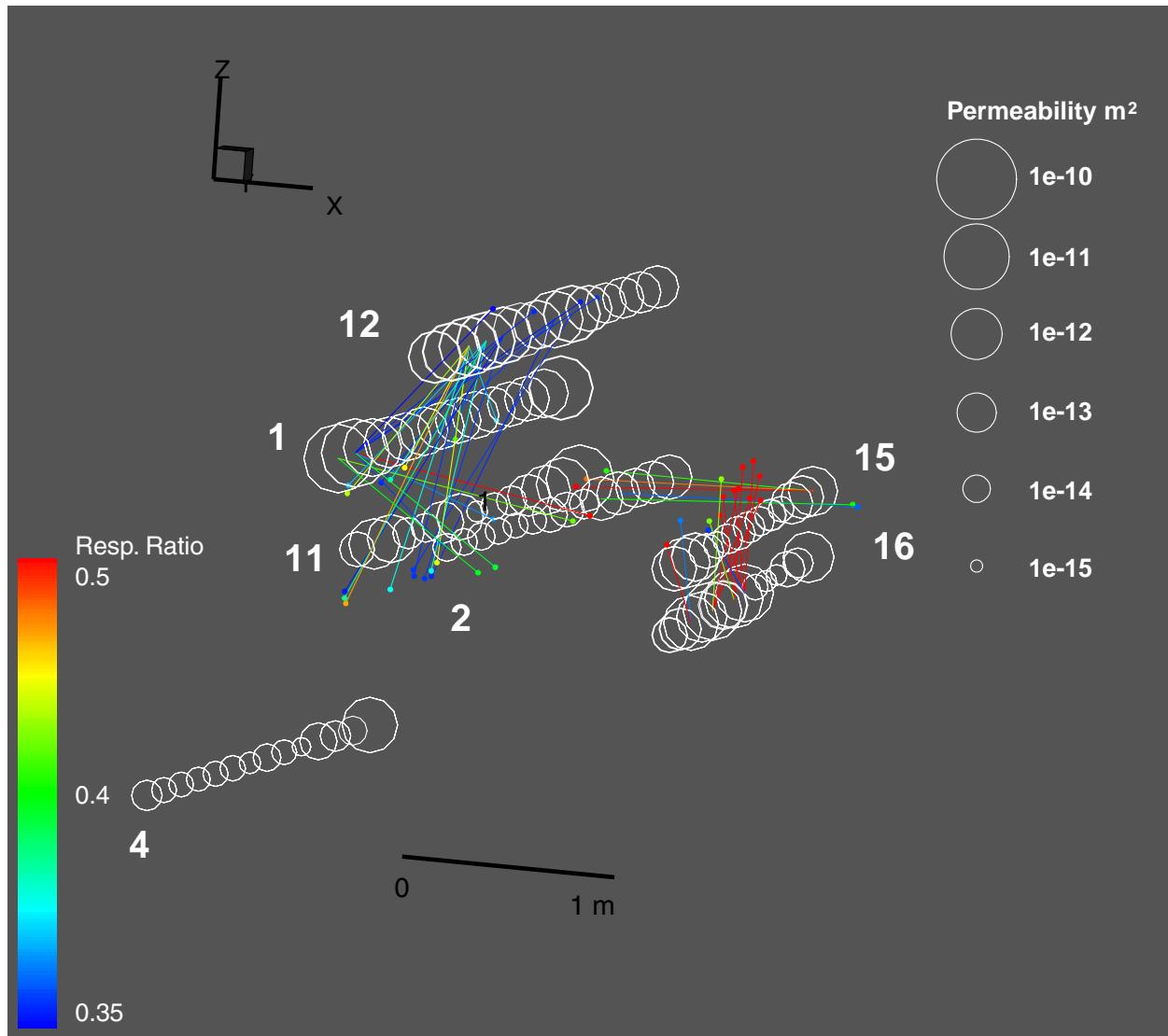
DTN: LB990901233124.004

Figure 42. Single-Hole Air-Permeability Profiles along Boreholes in Alcove 4.



DTN: LB990901233124.004

Figure 43. Cross-Hole Responses for Borehole Cluster at Alcove 4 PTn Test Bed with All Response Pressure (Resp.) Ratios below 0.2 Included.



DTN: LB990901233124.004

Figure 44. Cross-Hole Responses for Borehole Cluster at Alcove 4 PTn Test Bed with Small Response Pressure (Resp.) Ratios Filtered.

6.6 ANALYSES OF FRACTURE FLOW IN FRACTURE-MATRIX TEST BED AT ALCOVE 6

Wetting-front movement, flow-field evolution, and drainage of fracture flow paths were evaluated in a test bed with a slot excavated below a cluster of boreholes. The slotted test bed is located within the Topopah Spring welded tuff (TSw) at Alcove 6 in the ESF at Yucca Mountain, Nevada. Hydraulic parameters such as formation intake rates, flow velocities, seepage rates, and fracture volumes were measured under controlled boundary conditions, using techniques developed specifically for *in situ* testing of flow in fractured rock. The test bed configuration and field instrumentation are described before the results are presented.

6.6.1 Liquid-Release Tests in Low- and High-Permeability Zones

Field tests were conducted at Alcove 6 over a period of six weeks starting in late July 1998. These included multiple releases of tracer-laced water in one high-permeability zone (HPZ) and one low-permeability zone (LPZ) along an injection borehole. The permeabilities of these zones were determined from air-permeability measurements conducted over 0.3-m sections along the borehole, using a straddle packer that also was used for liquid releases. The HPZ had an air-permeability value of $6.7 \times 10^{-12} \text{ m}^2$, and the LPZ had an air-permeability value of $2.7 \times 10^{-13} \text{ m}^2$ (Scientific Notebooks YMP-LBNL-JSW-RS-1, pp. 48–49, YMP-LBNL-JSW-PJC-6.2, pp. 51–53). During and following liquid-release events, changes in saturation and water potential in the fractured rock were measured in three monitoring boreholes, with changes continuously recorded by an automated data acquisition system. The water that seeped into the excavated slot below the injection zone was collected, quantified for volumes and rates, and analyzed for tracers.

6.6.1.1 The Test Bed

The test bed was located at Alcove 6 in the ESF (Figure 45a), lying within the middle nonlithophysal portion of the TSw. The rock was visibly fractured with predominantly vertical fractures and a few subhorizontal fractures. The relatively wide fracture spacing (on the order of tens of centimeters) facilitated the choice of injection zones, allowing discrete fractures and well-characterized fracture networks to be isolated by packers for localized flow testing.

A horizontal slot and a series of horizontal boreholes are the distinct features of the test bed (Figure 45b). The slot, located below the test bed, was excavated by an over-coring method. The excavation sequence required first the drilling of parallel pilot holes, 0.10 m in diameter, over 4 m in length with a 0.22-m spacing, normal to the alcove wall. The pilot holes were then over-cored by a 0.3-m drill-bit to excavate the 2.0-m-wide, 4.0-m-deep and 0.3-m-high slot located approximately 0.8 m above the alcove floor. Three I-beam supports were installed along the length of the slot for support. Four horizontal boreholes, 0.1 m in diameter and 6.0 m in length, were drilled perpendicular to the alcove wall above the slot. Boreholes A and B were located 1.6 m above the slot ceiling, while boreholes C and D were 0.9 m and 1.0 m above the slot ceiling, respectively, and 0.7 m apart (Figure 45b).

Borehole A was used for fluid injection while boreholes B, C, and D were monitored for changes in moisture conditions. The slot was used to collect water seeping from the fractured rocks

above. A flexible plastic curtain 3.0 m wide and 0.9 m high was installed to cover the slot face and to minimize air movement between the alcove and the slot.

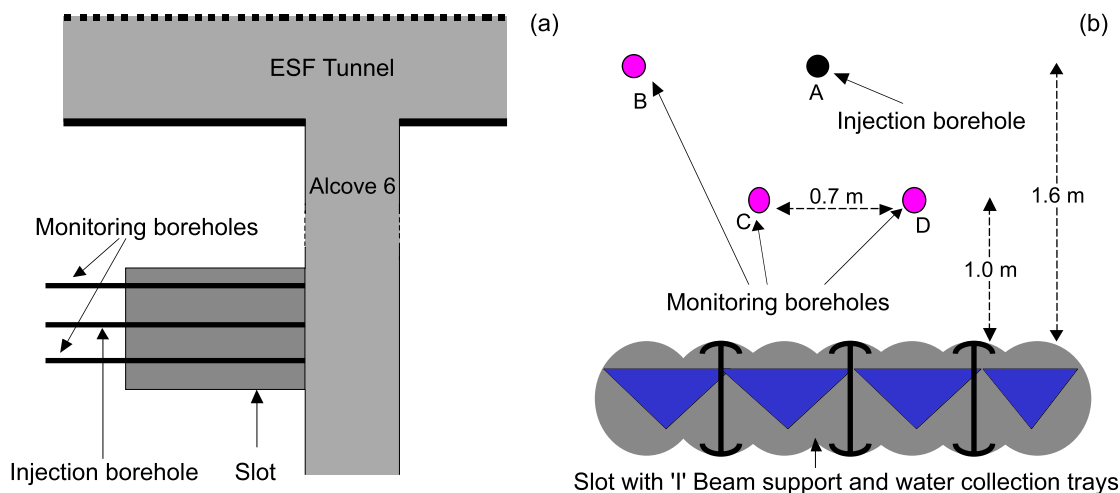


Figure 45. Schematic Illustration of (a) Plan view of Location and (b) Vertical View of Layout of Test Bed at Alcove 6 in the ESF at Yucca Mountain. Figures are not drawn to scale.

6.6.1.2 Instrumentation

There were three distinct components to the flow investigation: (1) controlled release of water into isolated zones, (2) borehole monitoring for changes in saturation and water potential, and (3) collection of seepage from the slot ceiling. The key features of new instruments developed for this field investigation are presented in [Attachment VII](#).

6.6.1.3 Liquid-Release Experiments

Air-permeability measurements were done along 0.3-m sections of the injection borehole as described in Sections 6.1 and 6.4. The HPZ is located 2.3–2.6 m from the borehole collar and the LPZ is 0.75–1.05 m from the collar. In both HPZ and LPZ, a series of constant-head tests were conducted to determine the temporal changes in the rate at which the formation could take in water. In the HPZ, a second series of tests was conducted with different injection rates. Tests conducted in this field investigation are summarized in [Table 16](#). The seepage rates into the slot were monitored.

All the water used in the ESF was spiked with lithium bromide for mining-related activities and for most of the scientific investigations. Additional tracers were added to the water injected into the LPZ and during the first set of experiments in the HPZ ([Table 16](#)). During the tests, water that seeped into the slot was periodically sampled and analyzed for tracer concentrations.

Water was released into the LPZ three times over a period of two weeks, starting on July 23, 1998 ([Table 16](#)). For the first release, water was injected at a constant pump rate of approximately 56 ml/min. At 66 minutes, water was observed in the overflow line, indicating that water was being injected at a rate higher than the intake capacity of the zone. At this time, the flow rate on the pump was immediately reduced to approximately 6.0 ml/min. Within 22

minutes, return flow ceased, and water was injected continuously at this rate for the next 4 hours and 23 minutes. Based on the actual flow rate determined from transducers located at the bottom of the water reservoir (see [Attachment VII-2](#)), a total of 6.3 liters of water was injected into the zone, of which 0.7 liters was recovered as return flow. The other 5.6 liters was released into the formation. Average net release rate into the formation rate was approximately 17 ml/min.

For the second liquid release in the LPZ, the constant-head injection system was used. The constant-head chamber was located adjacent to the injection borehole such that the head of water was 0.07 meters in the injection zone. This constant head was maintained for 4 hours in the injection zone, while the water level in the reservoir was continuously monitored. At the end of this constant-head period, water supply to the injection zone was discontinued, resulting in a falling-head boundary condition inside the injection zone. A total of 1.4 liters of water was introduced into the LPZ from both the constant-head and falling-head periods.

The final release into the LPZ was initiated on July 29, 1998 when water was introduced into the formation under a constant head (of 0.07 m) that was maintained for 43 hours, after which the ponded water in the injection zone continued to percolate into the formation under a falling-head condition. During the test, 1.0 liters of water were released under the constant-head boundary while 1.2 liters were released under the falling head.

Summing up all three tests in the LPZ, 9.2 liters of water were released to the formation under a combination of constant and falling-head boundary conditions at the point of injection.

Water was injected into the HPZ during two groups of tests over a period of two weeks ([Table 16](#)). The first group of four tests was conducted during August 4–6, 1998 and the second group of four tests were conducted during August 25–28, 1998. The first two tests (Tests HPZ-1 and HPZ-2) in the first group were constant-head tests (of head 0.07 m) that served to establish the intake rates at which the injection zone could release water to the formation. The HPZ-1 constant-head test rate was ~ 119 ml/min. The HPZ-2 constant-head test rate was ~98 ml/min. After HPZ-2 test, tests were conducted at constant flow rates. During the third test (Test HPZ-3) conducted on the next day, water was injected at approximately half the intake rates observed with the constant head system (i.e., ~ 53 ml/min). During the fourth test (Test HPZ-4) on August 6, 1998, water was injected at a constant rate of ~ 5 ml/min over 12 hours. During the second group of tests (Tests HPZ-5 through HPZ-8) over a period of four days starting on August 25, 1998, the injection rate was sequentially reduced from ~ 69, ~ 38, ~ 29 and finally to ~ 14 ml/min.

Table 16. Amount of Water and Types of Tracers Released into the Injection Borehole

Date	Test #	Injection type	Infiltration rate (ml/min)	Volume of water injected (l)	Additional Tracer *
7/23/98	LPZ-1	Constant rate	~16	5.6	Sodium Bromide 2,3,6 Trifluorobenzoic acid
7/24/98	LPZ-2	Constant head	~1.2	0.3	2,4,5 Trifluorobenzoic acid
7/24-25/98	LPZ-2	Falling head		1.1	2,4,5 Trifluorobenzoic acid
7/29-30/98	LPZ-3	Constant head	~0.5	0.4	3,5 Difluorobenzoic acid
7/30-31/98	LPZ-3	Constant head	~0.5	0.6	3,5 Difluorobenzoic acid
7/31-8/4/98	LPZ-3	Falling head		1.2	3,5 Difluorobenzoic acid
8/4/98	HPZ-1	Constant head	~119	16.3	Potassium Fluoride Pentafluorobenzoic acid
8/4/98	HPZ-2	Constant head	~98	17.3	2,3,4 Trifluorobenzoic acid
8/5/98	HPZ-3	Constant rate	~53	17.5	3,4 Difluorobenzoic acid
8/6/98	HPZ-4	Constant rate	~5	3.4	2,3,4,5 Tetrafluorobenzoic acid
8/25/98	HPZ-5	Constant rate	~69	18.4	
8/26/98	HPZ-6	Constant rate	~38	18.4	
8/27/98	HPZ-7	Constant rate	~29	18.2	
8/28/98	HPZ-8	Constant rate	~14	9.4	

DTN: LB990901233124.002

NOTES: LPZ located 0.75-1.05 m from borehole collar

HPZ located 2.30-2.60 m from borehole collar

* All injected water was tagged with lithium bromide

6.6.2 Observations of Wetting Front Migration and Fracture Flow

Water released in the injection borehole flowed through the fractured rock and, in the case of the HPZ, some of the water seeped into the slot located 1.6 m below. Liquid-release rates in the injected zone were measured, saturation and water-potential changes were observed along monitoring boreholes, and seepage water into the slot was collected.

6.6.2.1 Liquid-Release Rates

Measurements of liquid-release rates in the LPZ in this test bed in fractured welded tuff exhibited a response similar to that observed for (unfractured) porous media. The initially high rates asymptotically approached low steady-state values of ~ 0.35 ml/min (Figure 46a). Near continuity was observed in the decreasing liquid-release rates even with a five-day gap between liquid releases into the formation (Figure 46b).

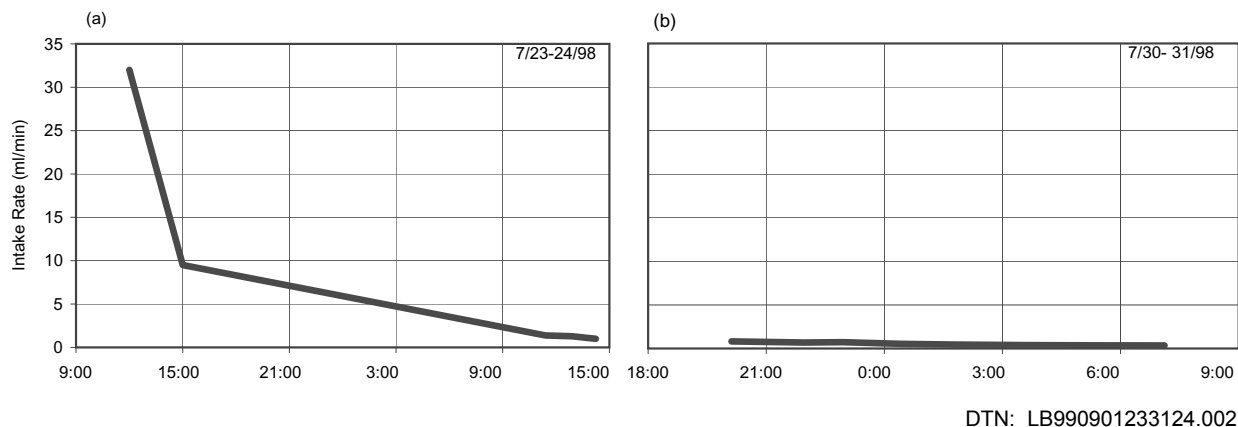


Figure 46. Water Intake Rates Observed in the Low Permeability Zone.

For the first two constant-head tests conducted in the HPZ, the rates of liquid release varied significantly during and between tests (Figure 47). In the first test, the liquid-release rate continued to climb for the first sixty minutes and then remained steady for the next 15 minutes before briefly increasing sharply. For the remainder of the test it continued to fluctuate between 70 and 160 ml/min. In the second test, the liquid-release rate rapidly increased for the first 15 minutes. The rate then slowly decreased and steadied off to ~100 ml/min. Ninety minutes into the test, the liquid-release rate briefly fell to 35 ml/min, sharply increased to 130 ml/min, and slowly decreased to a quasi-steady rate of 90 ml/min in the next 80 minutes.

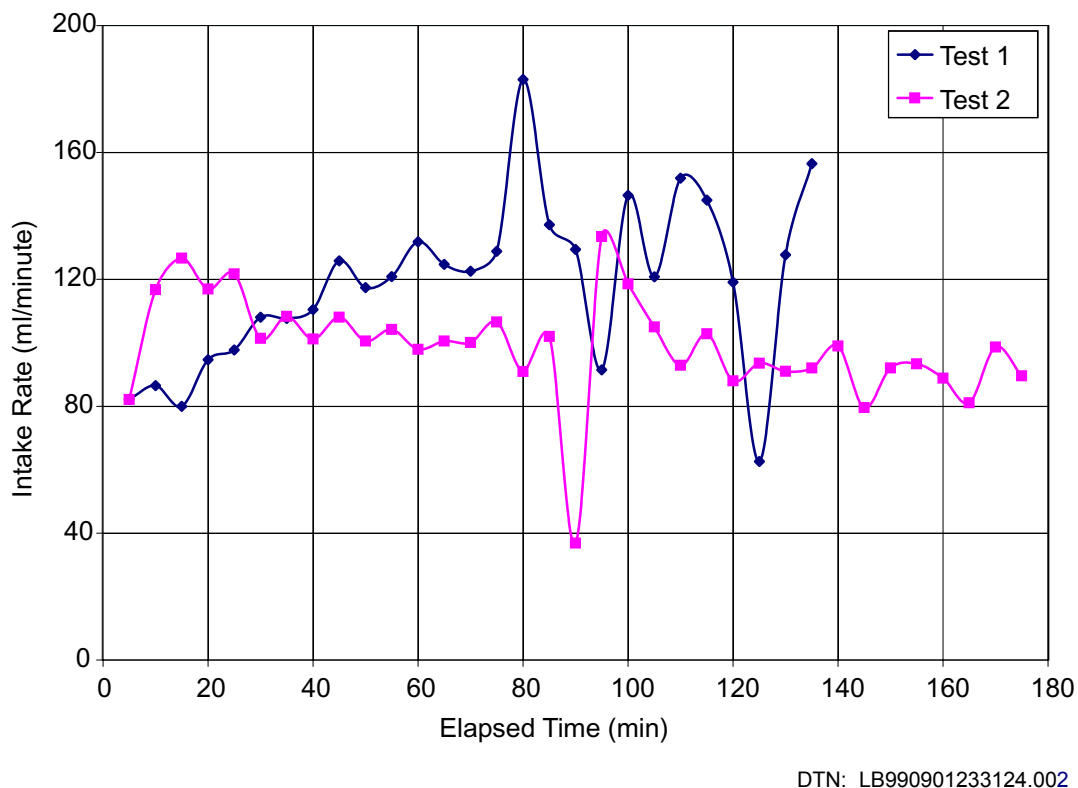


Figure 47. Water Intake Rates Observed in the High Permeability Zone.

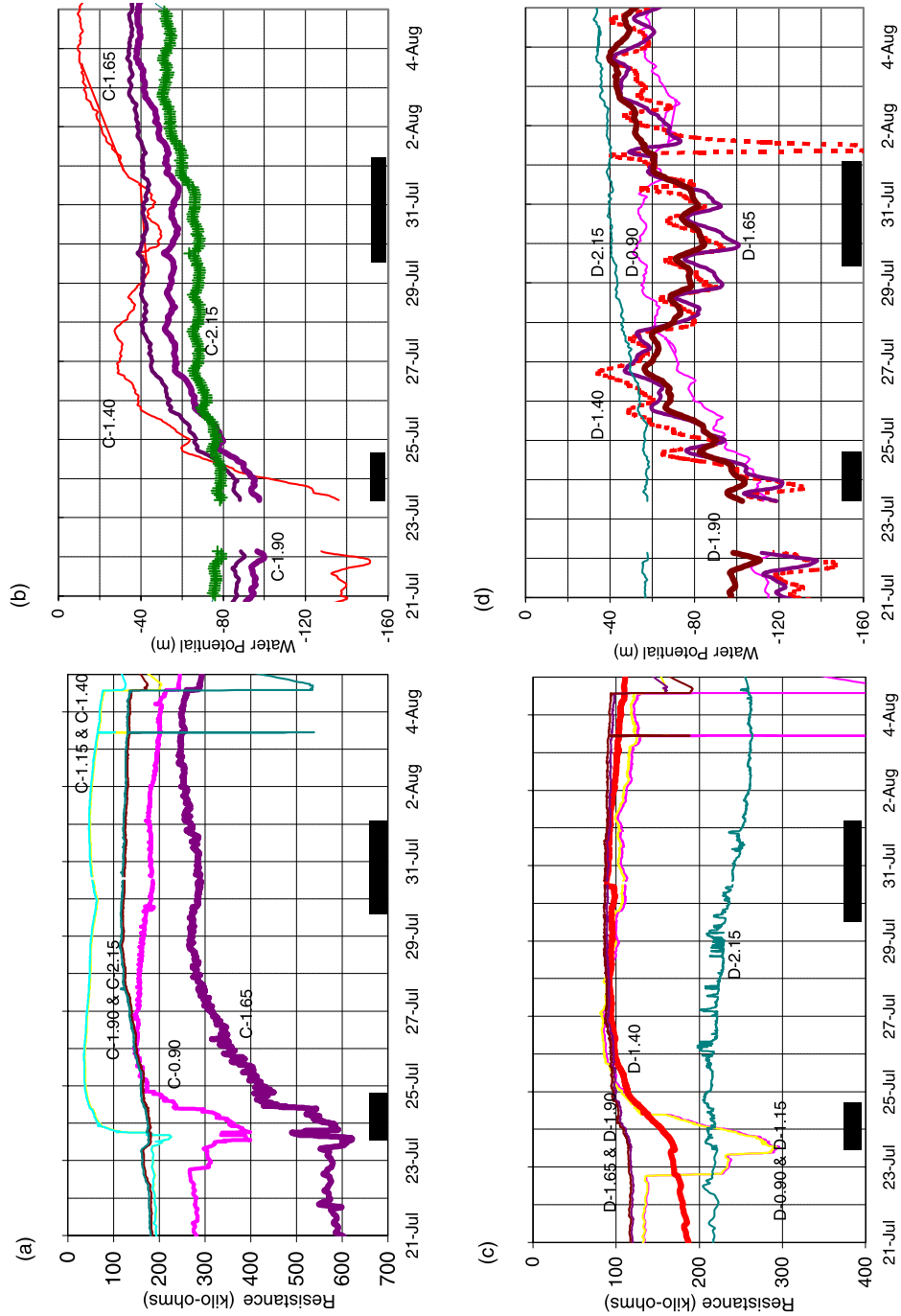
6.6.2.2 Formation Wetting and Drying

In the two monitoring boreholes (C and D, shown in [Figure 45b](#)) located below the injection borehole (A), changes in saturation were detected both by the electrical resistivity probes (ERPs) as shown in [Figure 48a](#) and [Figure 48c](#) and by the psychrometers as shown in [Figure 48b](#) and [Figure 48d](#). The ERPs consisted of two electrical leads sandwiched between pieces of filter paper. The results in [Figure 48](#) are the responses to liquid release in the LPZ located 0.75–1.05 m from the borehole collar. In both boreholes, large changes in saturation were detected by either ERPs or psychrometers or both located between 0.9 and 1.9 m from the collar. At a distance of 2.15 m from the borehole collar, the changes were much smaller.

The wetting process reduces electrical resistance and increases the water potential (making it less negative). The drying process induces opposite changes. In borehole C the first drying response was detected by the ERP located at 0.90 m from the borehole collar, as illustrated in [Figure 48a](#). A step increase in resistance was observed 30 minutes after water had been released, suggesting some initial drying with dry air preceding a wetting front. Two hours later, an abrupt increase in wetting was indicated by a stepped decrease in resistance. ERPs located at 1.15, 1.40, and 1.65 m also detected the arrival of a wetting front within 2 to 4 hours of liquid release. In borehole D ([Figure 48c](#)), the ERPs located at 0.9 and 1.15 m from the collar were first to detect increases in saturation, 30 minutes after the first release of water. At distances of 1.40 and 1.65 m, the wetting front arrived 6 hours later.

In both boreholes, the probes that had the largest and quickest responses (i.e., probes located between 1.15 and 1.65 m) were also the ones that showed some drying between the two injection events. Probes located at a distance of 0.90–1.15 m detected a continuous drying trend after the initial period of injection.

The borehole C psychrometer data in [Figure 48b](#) supported the ERP data in [Figure 48a](#) with smoother and more systematic changes induced by wetting front arrivals. The sensors closer to the release point had larger changes in water potential. At distances between 1.40 and 2.15 m from the collar, water potentials were between -140 and -75 m before the first injection. Immediately after water was introduced, water potentials began to rise steadily for the next four days, reaching values between -70 and -30 m. In response to the second injection period (i.e., July 29–August 4, 1998 in [Table 16](#)), the most noticeable increases in potentials were observed in the psychrometer located at 1.40 m, where water potentials increased from -40 to -15 m after the second injection period. In borehole D, illustrated in [Figure 48d](#), changes in water potential were observed between 0.90 and 1.90 m following the first injection. However, the extent of drying as seen in the decrease in water potentials at 1.40 and 1.65 m was greater than observed in borehole C. During the second wetting event, water potentials in this zone were similar to those observed following the first event. Oscillatory responses could be related to variations of drift conditions for sensors near the borehole collars. This is a speculative interpretation to be substantiated or refuted.

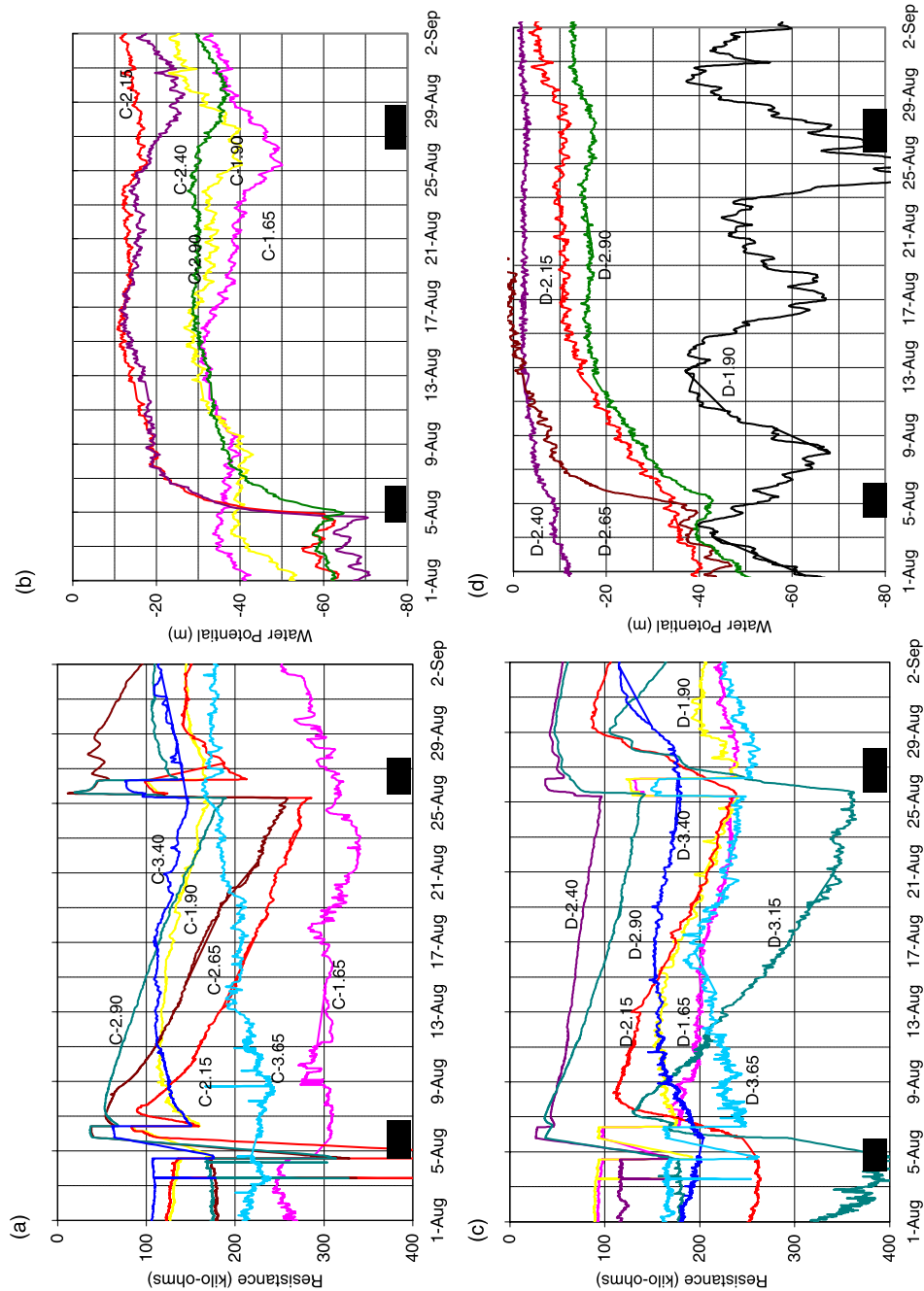


DTN: LB990901233124.002

Figure 48. Changes in Electrical Resistance and Water Potential Detected during Liquid Injection into the Low Permeability Zone. The legend identifies the sensor location in borehole (C & D) and distance of sensor from the borehole collar. Shaded zones indicate the duration of liquid-release events. Note resistance axis is inverted.

Similar to the injection response in the LPZ, changes in saturation were detected both by the ERPs and psychrometers in the monitoring boreholes (Figure 49) from liquid releases into the HPZ located 2.30–2.60 m from the borehole collar. In borehole C, changes in saturation were observed between 1.9 and 3.4 m from the borehole collar, with the largest changes observed between 2.15 and 3.15 m. Both the ERPs and the psychrometers detected the changes. The largest changes in water potentials were detected between 2.15 and 2.40 m from the borehole collar in borehole C, where pre-injection water potentials, which were between -70 to -60 m, climbed to between -20 and -10 m, after the first set of releases. These values persisted after the second set of releases. In borehole D, saturation changes were observed over a slightly wider span along the borehole (i.e., 1.65 to 3.65 m from the borehole collar), with the noticeable changes observed between 1.90 and 3.40 m from the borehole collar. After the initial release of water in the HPZ, water potentials between locations 2.15 and 2.90 m increased over a period of a week. These were between -15 to -5 m for the duration of the remaining liquid releases.

In both boreholes, the psychrometer data suggest that after the first batch of water releases (i.e., August 4–6, 1998) water potentials were significantly increased (e.g. -60 to -20 m) which then persisted until the start of the second period of injection (August 25–28, 1998). During this second set of injections, more water was retained by the formation, resulting in further increases in water potentials. The ERP and psychrometer data indicate that the zones between 2.15 and 2.40 m in borehole C, and between 2.15 and 2.65 in borehole D, showed the largest changes during active testing.



DTN: LB990901233124.002

Figure 49. Changes in Electrical Resistance and Water Potential Detected during Liquid Release into the High Permeability Zone. The HPZ is located between 2.30 to 2.60 m from the borehole collar. The legend identifies the sensor location in borehole (C & D) and distance of sensor from the borehole collar. Shaded zones indicate the duration of two groups of liquid-release events. Note resistance axis is inverted.

6.6.2.3 Seepage into the Slot

Seepage into the slot was observed during all eight tests in the HPZ (and none in the LPZ tests). The test results are summarized in Table 17. The eight tests were conducted in two groups (Table 16 and illustrated in Figures 48 and 49 as two shaded test duration zones). During the first test in the first group (Test HPZ-1), water was first observed on the slot ceiling five minutes after the start with 0.41 liters of water released under constant-head conditions. In the HPZ-2 and HPZ-3 tests, water appeared in the slot within 3 minutes after 0.17 and 0.14 liters, respectively, had been released. In the HPZ-4 test, water appeared in the slot after five hours with 1.50 liters of water injected at a rate of 5 ml/min.

In the second group of tests, travel time for the first drop of water was 3 minutes after 0.14 liters was injected at a rate of ~ 69 ml/min (Test HPZ-5). In the HPZ-6 and HPZ-7 tests, the arrival time of the wetting front was 7 minutes after 0.26 and 0.20 liters of water were injected at a rate of 38 and 29 ml/min, respectively. In the final HPZ-8 test, water first appeared in the slot after 1:08 hr, with 0.90 liters injected into the formation at a rate of 14 ml/min.

Table 17. Summary of Liquid-Injection Tests in the High Permeability Zone.

Test Number	Injection Rate (ml/min)	Duration of Injection (hh:mm)	Volume Recovered (l)	Travel Time of First Drop (hh:mm)	Volume of Water In Formation (l)		Water Retained in Formation (%)
					At First Drop	At End of Injection	
HPZ-4	5	11:54	0.36	5:00	1.51	3.03	89
HPZ-8	14	11:19	4.56	1:08	0.90	4.82	51
HPZ-7	29	10:36	13.21	0:07	0.20	5.02	28
HPZ-6	38	8:00	14.73	0:07	0.26	3.71	20
HPZ-3	53	5:25	11.14	0:03	0.14	6.31	36
HPZ-5	69	4:26	11.47	0:03	0.14	6.90	38
HPZ-2	98	2:56	12.17	0:03	0.17	5.15	30
HPZ-1	119	2:17	11.61	0:05	0.41	4.67	29

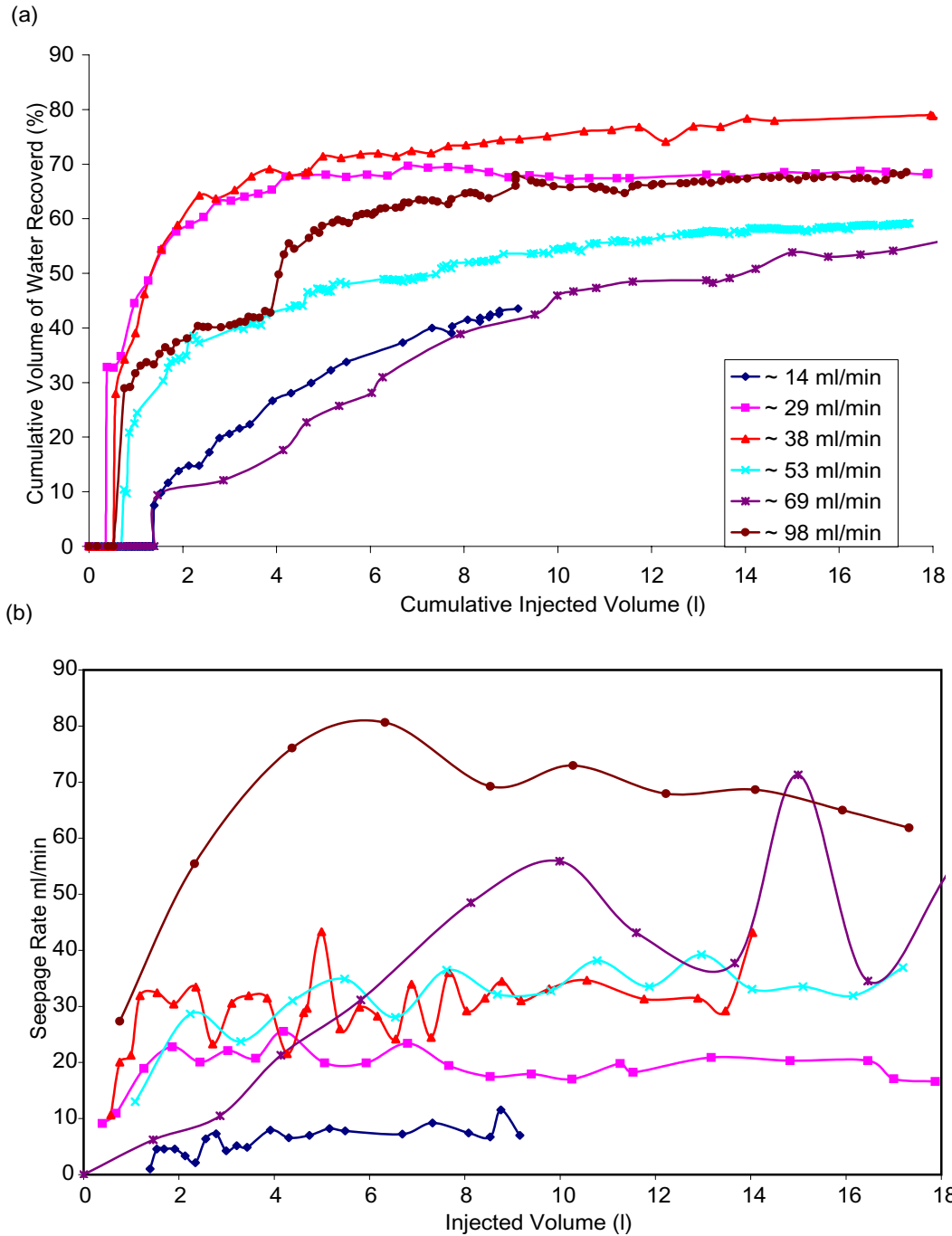
DTN: LB990901233124.002

NOTES: Volumes in liters

Time in hr:min

Injection rates in ml/min

The fraction of injected water recovered in the slot continued to increase as each test progressed. Significant variability was observed in the percentage of water recovered and the seepage rate during and between tests (Figure 50a and b). Seepage variability was related to both the amount of water injected and the rate at which water was released into the formation. Early in each test, the amount of water recovered sharply increased. The percentage of injected water recovered approached relatively constant values after approximately 10 liters of water had been injected. Intermittent seepage behavior (Figure 50b) was observed during all the tests.

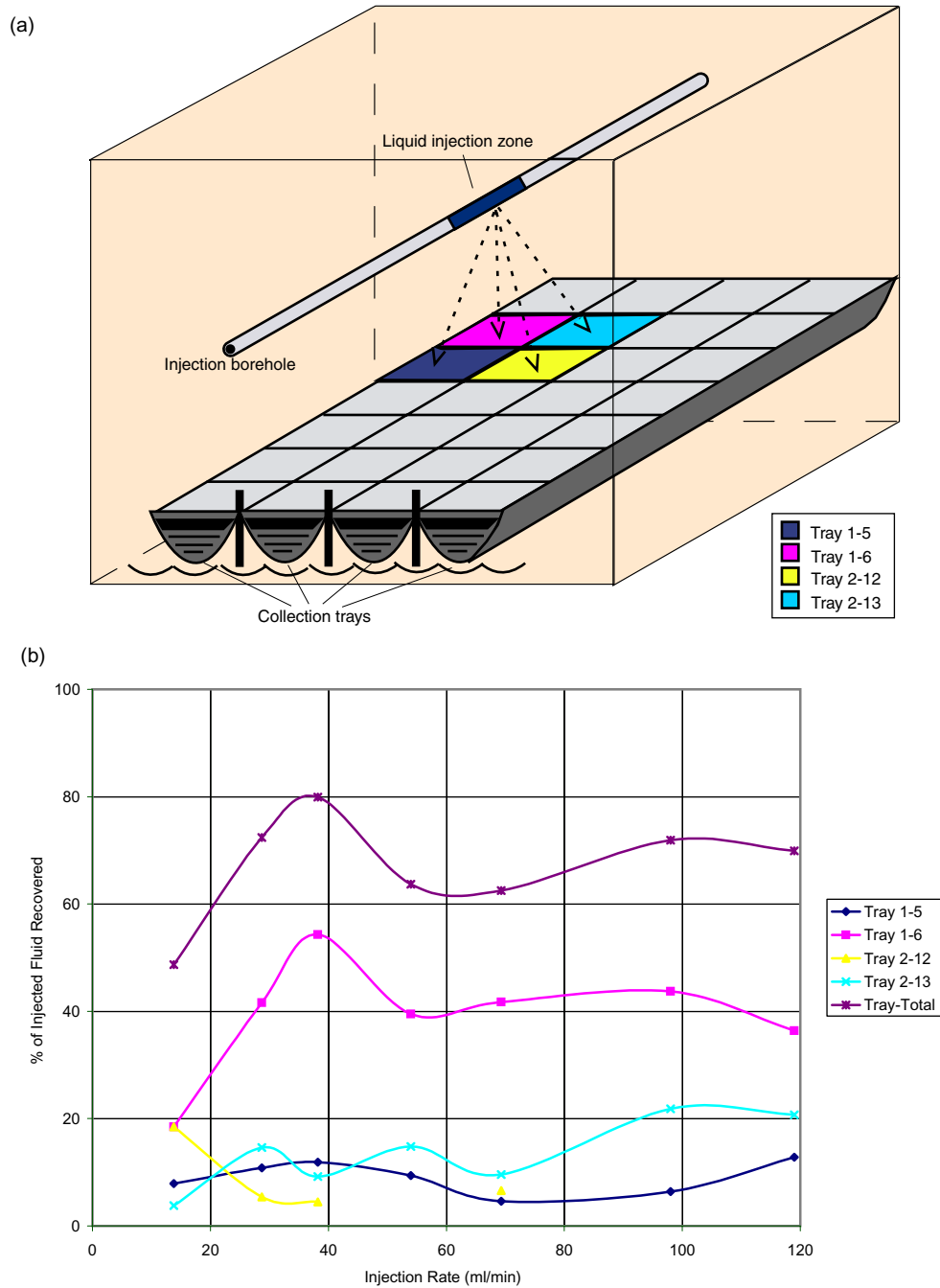


DTN: LB990901233124.002

Figure 50. Seepage into Slot: (a) Percentage of Injected Water Recovered and (b) Seepage Rates for Various Release Rates.

As illustrated in [Figure 51](#), the percentage of the amount of injected water recovered at the release rate of 38 ml/min was higher than the percentages at other injection rates. The first maximum percentage could be associated with the dominant flow path connecting the injection zone with the outflow slot boundary. With increasing injection rate, additional flow paths, either through other fractures or through other areas in the same fracture, could contribute to the storage and flow of additional water.

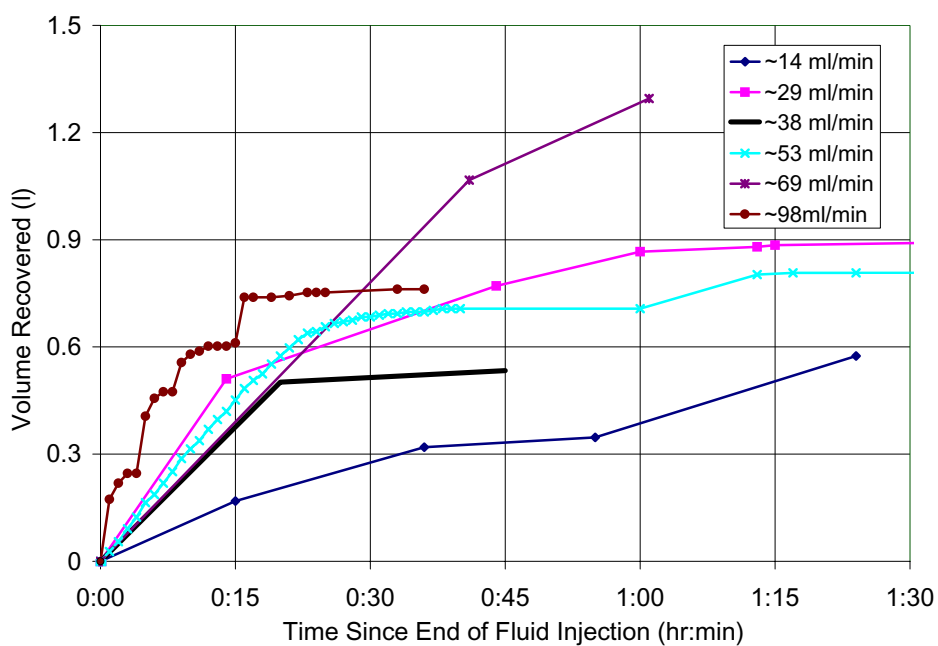
[Figure 51](#) also illustrates the distribution of seepage among the collection trays in the slot. As each test progressed, water initially appeared on the slot ceiling at one single point directly below the injection zone, and seepage water was collected from four trays located around the point of entry. During these tests, water seeping into the slot was largely concentrated in a single tray, with the three other trays collecting significantly smaller amounts of water. Slight increases at higher injection rates were noticeable in some of the secondary trays. The remaining 24 trays stayed dry during all the liquid-release tests.



DTN: LB990901233124.002

Figure 51. Seepage into Collection Trays in the Slot: (a) Tray Configuration and (b) Percentages of Injected Water Recovered for Different Trays.

In all the tests during which there was seepage, 0.5 to 1.3 liters of water entered the slot after the water supply to the formation was switched off (Figure 52). Most of this water was collected within one hour, with recovery rates being largest immediately after the test. The constant-head test with ~98 ml/min release rate had a ‘stepped’ nature to the post-injection recovery. During the first fifteen minutes, the 0.8 liters of collected water appeared in four bursts, each containing 0.10–3 liters of water. Changes of similar magnitudes were observed in the tests with injection rates of ~53 ml/min and ~14 ml/min (with one late burst each shown in Figure 52).

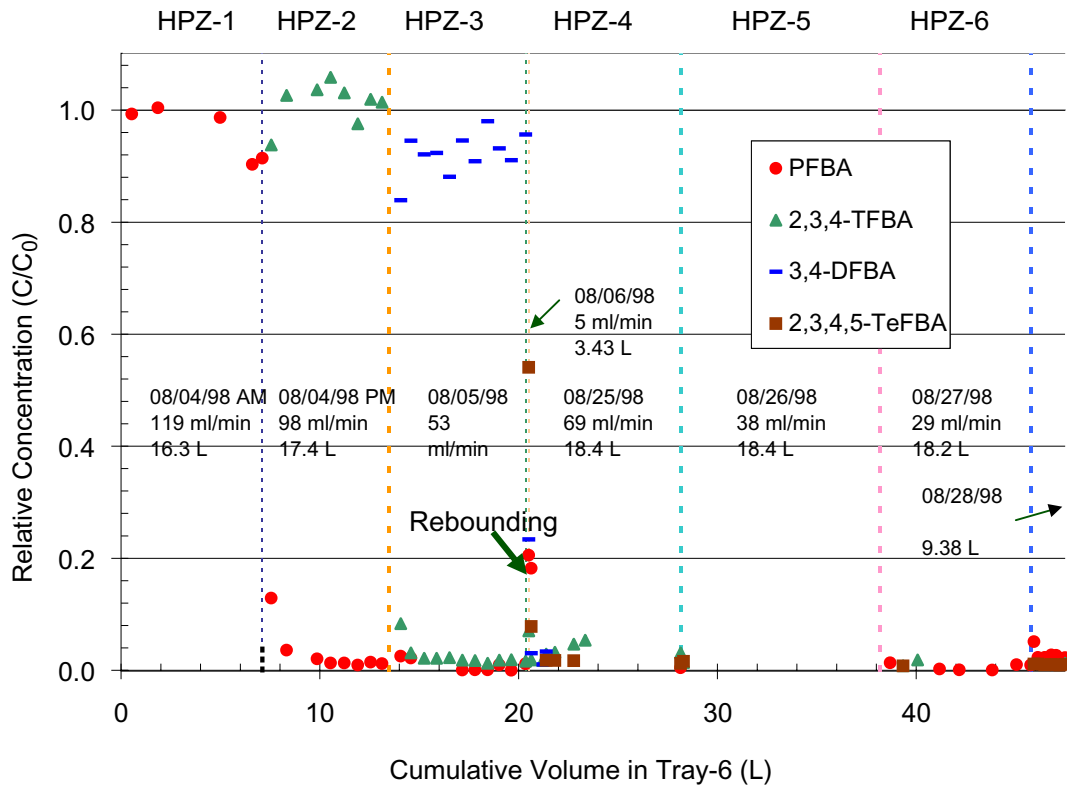


DTN: LB990901233124.002

Figure 52. Volume of Water Recovered in the Slot after Liquid Injection into the High Permeability Zone was Stopped.

6.6.2.4 Tracer Recovery

Tracers injected in the HPZ were detected in the water samples collected in the slot. (None of the traced water introduced in the LPZ was recovered.) Typically, tracers introduced in one test were rapidly flushed out of the system during the subsequent test (Figure 53). The pattern of recovered concentrations of tracers suggests that plug flow was the dominant process by which ‘new’ water replaced ‘old’ water from the previous test. Some recovery of tracers from the formation was observed during subsequent tests.



DTN: LB99091233124.001

Figure 53. Tracer Concentrations in Seepage Water Following Injection into the High Permeability Zone.

6.7 ANALYSES OF FLOW THROUGH THE FAULT AND MATRIX IN THE TEST BED AT ALCOVE 4

The evolution of a flow field and the migration of a wetting front following the release of liquid into a fault and matrix were evaluated in a test bed using a cluster of horizontal boreholes.

6.7.1 Flow Tests in Paintbrush Tuff Unit Layers and Fault

Field experiments were conducted in the PTn within the ESF at Yucca Mountain. These experiments included multiple releases of tracer-laced water in isolated zones along three horizontal boreholes. The zones into which water was released were selected based on air-permeability measurements conducted over 0.3-m sections of borehole (Section 6.5.2). The plumes that developed from these releases were monitored in six separate horizontal boreholes. During and following liquid-release events, changes in saturation and water potential along horizontal monitoring boreholes were continuously recorded by an automated data acquisition system.

6.7.1.1 The Test Bed

The test bed is located at Alcove 4 in the ESF. It is accessed through an alcove excavated (by an Alpine miner) at approximately 67 degrees to the central axis of the ESF North Ramp. Alcove 4 transects portions of the lower Pah Canyon Tuff (Tpp) and the upper pre-Pah Canyon bedded tuffs (Tpbt2) of the PTn (nomenclature of Buesch et al. 1996, p. 7). The central axis of the alcove has an azimuth of 6 degrees, which coincides with the approximate strike of the PTn units in the vicinity. The north face of the alcove, in which the test bed is located, is approximately 6 m wide and 5.3 m high (Figure 54).

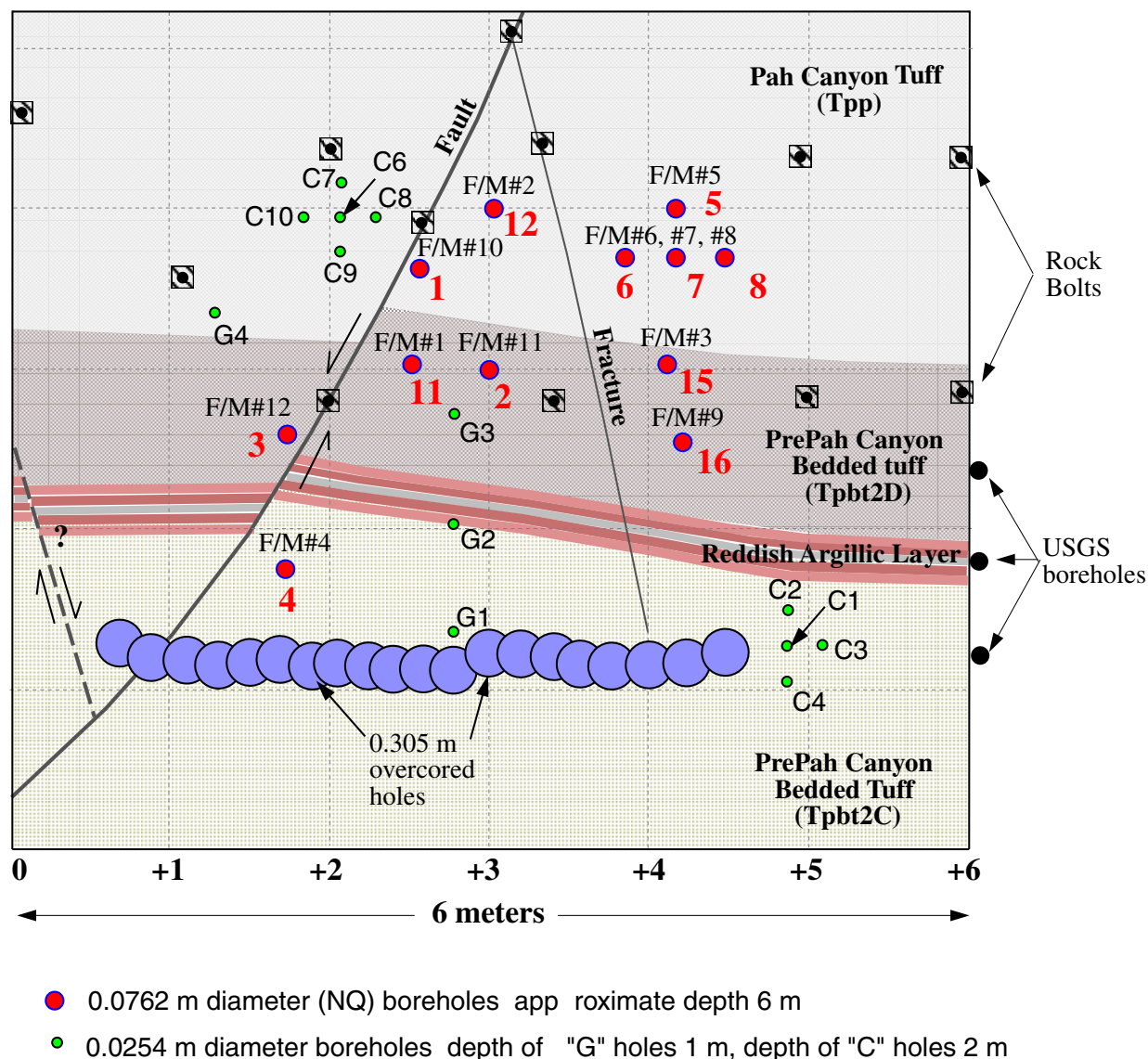


Figure 54. Geological Sketch for the North Face of Alcove 4 in the ESF at Yucca Mountain. Also included are location of boreholes and the slot.

The lower Tpp and upper Tpbt2 units D and C (units from Moyer et al. 1996, pp. 46-50) are exposed along the north face of Alcove 4. Tpp is nonwelded and pumice-rich. It exhibits a chalky-white color and is apparently zeolitically altered (based on destruction of the texture of the matrix ash and destruction of the integrity of the glass shards, Moyer et al. 1996, p. 46). Zeolitic alteration in the North Ramp of the ESF commonly follows fractures and faults that cut through the Tpp and Tpbt2 units (Barr et al. 1996, p. 44). The contact between the lower Tpp and upper Tpbt2D is sharp in Alcove 4, marked by distinct color changes. Tpbt2D is also nonwelded, possibly reworked, and has variably abundant (while zeolitically altered) pumice within a fine- to coarse-grained, medium-brown matrix.

Below Tpbt2D, lying in the upper Tpbt2C, is a thin (0.20-0.30 m), light pink to red argillically altered layer that is almost completely offset by a small, westward-dipping normal fault.

Alteration within this layer can be traced from the end of Alcove 4 out into the North Ramp. It is uncertain whether the argillic alteration seen in Alcove 4 is laterally continuous, though reddish alteration is commonly observed in several boreholes and in outcrops across Yucca Mountain at the same stratigraphic horizon (Moyer et al. 1996, pp. 54-55). The remaining Tpb2C exposed along the north face below the argillic layer is massive and nonwelded, has very pale tan coloring, and contains abundant, coarse pumice and lithic fragments.

Cutting the north face of Alcove 4 is a normal fault with a small offset (0.25 m). As mapped along the crown at the end of the alcove (Barr et al. 1996, full-periphery geologic map OA-46-289, DTN: GS960908314224.020 for the crown, but not for the end face), the fault has a strike of approximately 195 degrees and a westward dip of 58 degrees. The fault is open in the ceiling and is closed, with knife-edge thickness, near the invert on the north face. Intersecting the fault near the alcove crown along the north face is a high-angle fracture. The cause of the fracture is uncertain and could have been induced by drilling or drying, considering the location of rock bolts and the clay content of the rocks. The orientation of the fracture is unknown, though it has an apparent eastward dip of about 75 degrees. Similar to the fault, the fracture appears to have a large aperture near the ceiling and a much smaller aperture (eventually becoming undetectable) near the invert.

Two distinct features that were imposed on the formation define the layout of the field experiment, i.e., a horizontal slot and a series of horizontal boreholes. The slot, located immediately below the test bed, was designed to capture any seepage resulting from gravity drainage. It was excavated by a drilling sequence that required 0.10-m diameter pilot holes drilled parallel at 0.22-m spacing, perpendicular to the alcove wall. These pilot holes were then over-cored by a 0.3-m drill-bit to excavate a 6.0-m-wide, 4.0-m-deep and 0.3-m-high cavity located approximately 1.5 m above the alcove floor. I-beam supports were installed along the length of the slot to prevent it from collapsing during the duration of the field tests.

Twelve 6.0-m-long, 0.1-m-diameter boreholes were drilled into the alcove face, as illustrated in [Figures 54 and 55](#). Boreholes 1, 4, 11 and 12 were positioned to intersect the fault for the purpose of conducting flow tests within the fault. Borehole 2 was located to detect moisture that could migrate through the matrix below borehole 12. Borehole 12 was the injection borehole for the fault flow tests conducted. The configuration of boreholes 5, 6, 7, and 8 was designed to investigate the nature of matrix flow in the Tpp, with borehole 5 serving as the injection borehole and 6, 7, and 8 equipped with probes to detect changes in moisture conditions. Borehole 3 on the left side of the fault and Boreholes 15 and 16 away from the injection boreholes were not instrumented for the tests conducted. (Boreholes 9, 10, 13, and 14 were planned but not drilled).

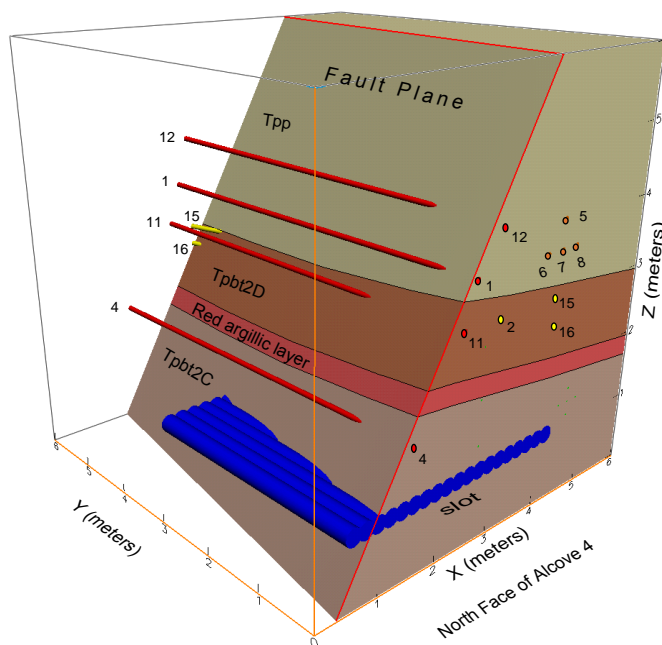


Figure 55. Schematic Illustration of Three-Dimensional View of the Boreholes, Slot, and Lithological Unit Contacts in the Alcove 4 Test Bed.

6.7.1.2 Instrumentation

The flow investigation had three distinct components: (1) controlled release of water into isolated zones, (2) borehole monitoring for changes in saturation and water potential, and (3) the monitoring of seepage from the slot ceiling. For each component, new instruments were developed, details for which are described in [Attachment VII](#). Because water did not seep into the slot, the seepage monitoring system was not used. Key features of the liquid-injection and borehole-monitoring system are presented in the following sections.

6.7.1.2.1 Fluid Injection

The liquid-release experiments required water to be injected into the formation over a 0.3-m section of borehole with a constant-head boundary condition to determine the maximum rates at which the zone could take in water. The main components of the fluid-release apparatus included an inflatable packer system used to isolate the injection zone, a pump to deliver water to a constant-head chamber from which water was introduced into the injection zone, and a reservoir to provide a continuous supply of water. To capture the temporal variability in vertical flux of water from the injection zone, we developed an automated liquid-release system to measure changing flow rates on a ponded surface. This system allowed for continuous measurement of local liquid-release rates during the entire experiment.

6.7.1.2.2 Borehole Monitoring

In six monitoring boreholes (Boreholes 1, 2, 11, 6, 7, and 8 in [Figure 55](#)) located above the slot, changes in saturation and water potential were continuously recorded during the entire investigation. Changes in saturation along boreholes were measured with ERPs located at 0.25-m intervals along a 6.0-m length of each borehole. Water potential measurements were made with psychrometers, as described in [Attachment VII](#) for Alcove 6 testing. The psychrometers and ERPs were housed in special Borehole Sensor Trays (BSTs) installed along the length of each monitoring borehole.

6.7.1.3 Liquid-Release Experiments

Air-permeability measurements were made along 0.3-m sections of all nine boreholes to determine the exact location of the fault in boreholes 4, 11 and 12, as discussed in Section 6.5.2. All water used in the ESF (for mining-related activities and scientific investigations) was spiked with the same concentration of lithium bromide. For the entire duration of the experiments, saturation and water-potential changes along the monitoring boreholes were continuously measured.

A total of 193 liters of water was released into borehole 12 during seven events, under constant-head conditions, between October 21 and November 5, 1998, as summarized in [Table 18](#). In this borehole, as in all others, water was released over a 0.30-m interval. Here, the injection interval was centered at a distance 1.4 m from the borehole collar, determined from air-permeability measurements to be the location of the fault.

Table 18. Summary of Liquid Releases into the Fault Zone in Borehole 12

Test Number	Date (mm/dd/yy)	Volume Injected (l)	Duration (hh:mm)	Average Intake rate (ml/min)
1	10/21/98	42.90	5:12	138
2	10/22/98	41.44	5:59	115
3	10/26/98	21.34	4:22	81
4	10/27/98	29.53	6:59	70
5	10/28/98	22.16	6:10	60
6	11/04/98	17.08	5:48	49
7	11/05/98	18.85	6:31	48

DTN: LB990901233124.005

In borehole 5 away from the fault, water was released into two zones. In the first zone (located 1.50 to 1.80 m from the collar) 1.37 liters of water were released to the zone on October 19, 1998, and a similar volume was released on October 20, 1998. Because a problem was detected with the constant-head system, no more water was injected into this zone. On October 27, 1998, after the injection system was repaired, water was released into borehole 5 at a distance of 2.44–2.74 m from the borehole collar. In this zone, 6.5 liters of water were released under constant head conditions over a period of 23 days.

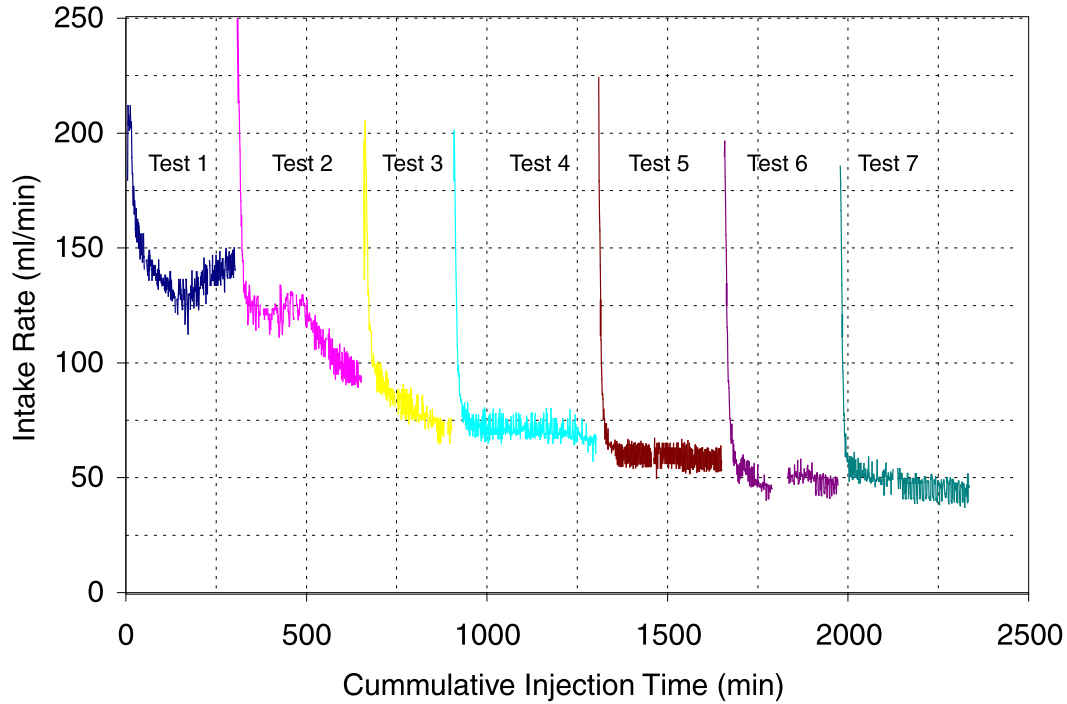
6.7.2 Observations of Fault Flow and Matrix Flow

During and following the release of water into the test bed, intake rates (rates of water moving into the formation during constant-head tests), travel times, and lateral dispersion of the plume (as seen along the length of horizontal boreholes) were continuously monitored. In the following section, the observed hydrologic responses to liquid releases in the three zones as detected by ERPs and psychrometers are presented.

6.7.2.1 Fault Responses

6.7.2.1.1 Intake Rates

Water was injected into the section of borehole 12 that intercepted the fault approximately 1.40 m from the collar. Here, 193 liters of water were released into the formation during seven events that extended over a period of two weeks as illustrated in [Figure 56](#). Each event lasted between 4 and 7 hours, during which 20–43 liters of water entered the injection zone. Each release event began with water filling the 1.37-liter injection cavity in about 3 minutes, after which the liquid-release apparatus kept the injection zone filled by maintaining a constant-head boundary for the period of injection. After water was injected into the formation, the 1.37 liters of water occupying the injection zone were released to the formation under falling head conditions.



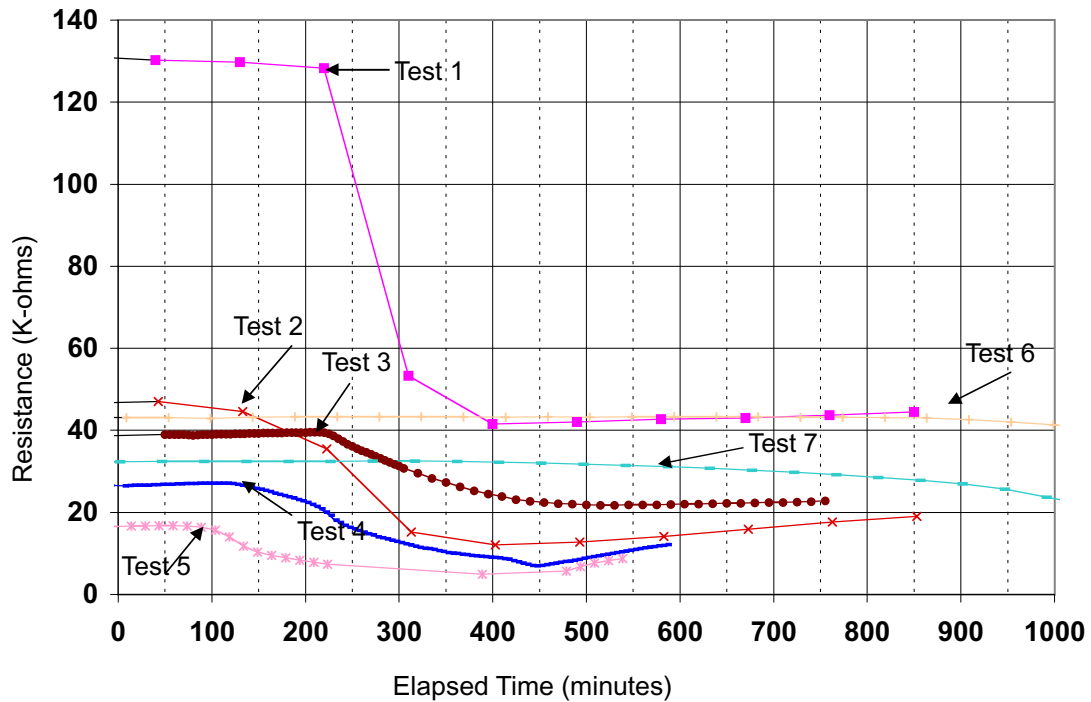
DTN: LB990901233124.005

Figure 56. Intake Rates along the 0.3-m Zone Located on the Fault in Borehole 12.

During Test 1 into the fault, the intake rate dropped from 200 ml/min to 120 ml/min over a period of 180 minutes before recovering to 145 ml/min in the next 120 minutes. In Test 2, conducted one day later, the intake rate dropped from 200 ml/min to 120 ml/min over a period of 80 minutes before remaining fairly constant for the next 100 minutes. Approximately 180 minutes after this release event started, the intake rates began to drop steadily, reaching a rate of 95 ml/min by the end of the test. In Test 3, which was initiated four days later, the intake rates rapidly dropped to 95 ml/min during the first 40 min and then continued to decrease at a more gradual rate for the next 200 minutes to a rate of 70 ml/min. During Tests 4 and 5, conducted during the next two days, the pattern of rate change was similar, with an initially high intake rate quickly dropping to a near constant value (70 to 60 ml/min, respectively). In Test 4, this constant value persisted 300 min into the test, after which there was a gradual decrease in intake rates for the remainder of the test. During Test 6, which began after a six-day hiatus, water was injected during two intervals. During this test, water was introduced under constant-head conditions for 140 and 158 minutes periods with a gap of 22 minutes, during which water imbibed into the formation under a falling head. The intake rates rapidly dropped to 50 ml/min. In Test 7 into this zone, the intake rates again dropped to 50 ml/min after 100 minutes of release. The rates gradually decreased during the 200 minutes of injection, which approached 40 ml/min after 18 liters of water had been injected.

6.7.2.1.2 Travel Times in Fault

When water was introduced into borehole 12, the time taken for the wetting front to travel 1.07 m along the fault to borehole 11 varied among the seven tests (Figure 57). In the first test, water was detected in the lower borehole ~300 minutes after the first release, while in the second test the travel time was reduced to ~200 minutes. For the third test, this travel time was ~250 min; in the fourth test, water appeared in the fault in borehole 11 within ~150 minutes. The fastest travel time was observed for the fifth test when the front arrived within ~120 minutes in borehole 11. In the last two tests, the travel times were significantly slower, with increasing saturations observed 400 and 700 minutes after the initial release of water.

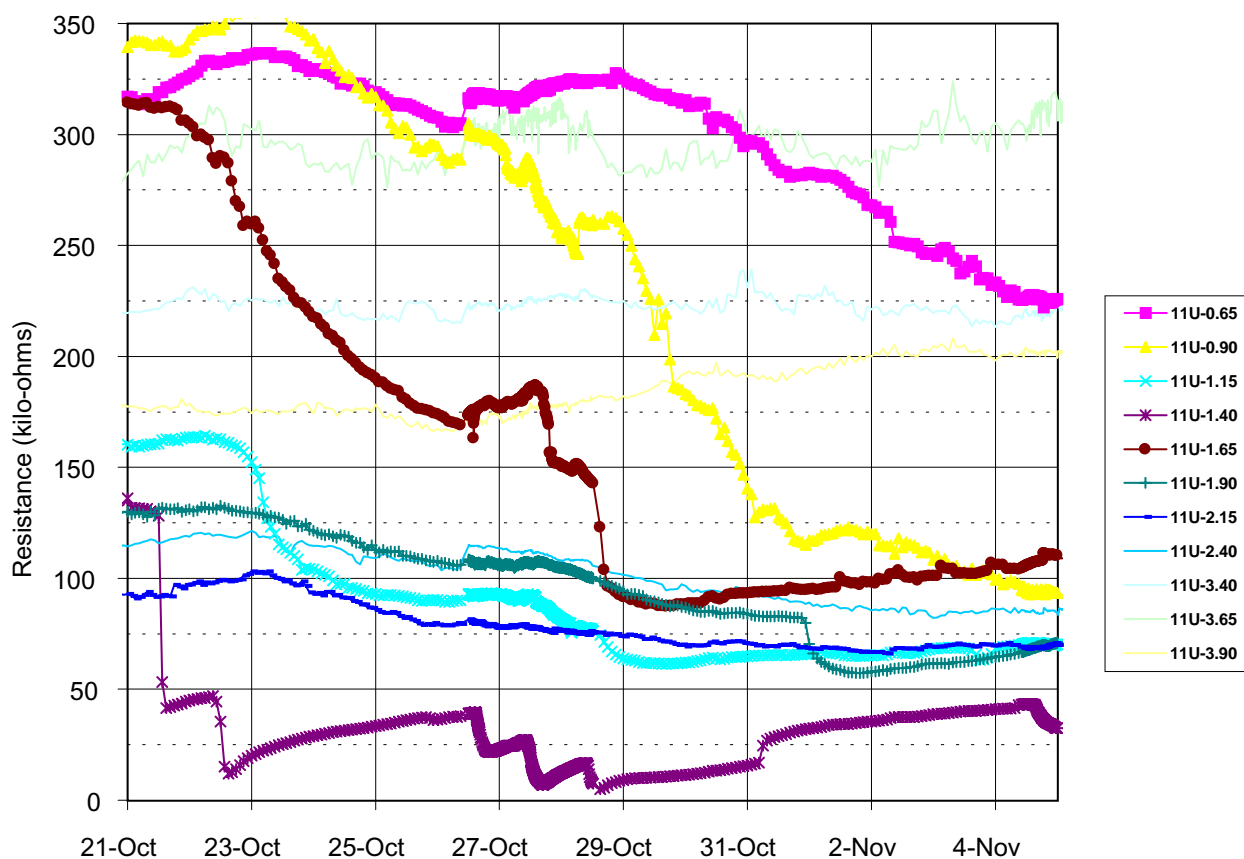


DTN: LB990901233124.005

Figure 57. Wetting Front Arrival in Borehole 11 Following Liquid Released into the Fault in Borehole 12.

6.7.2.1.3 Dispersion

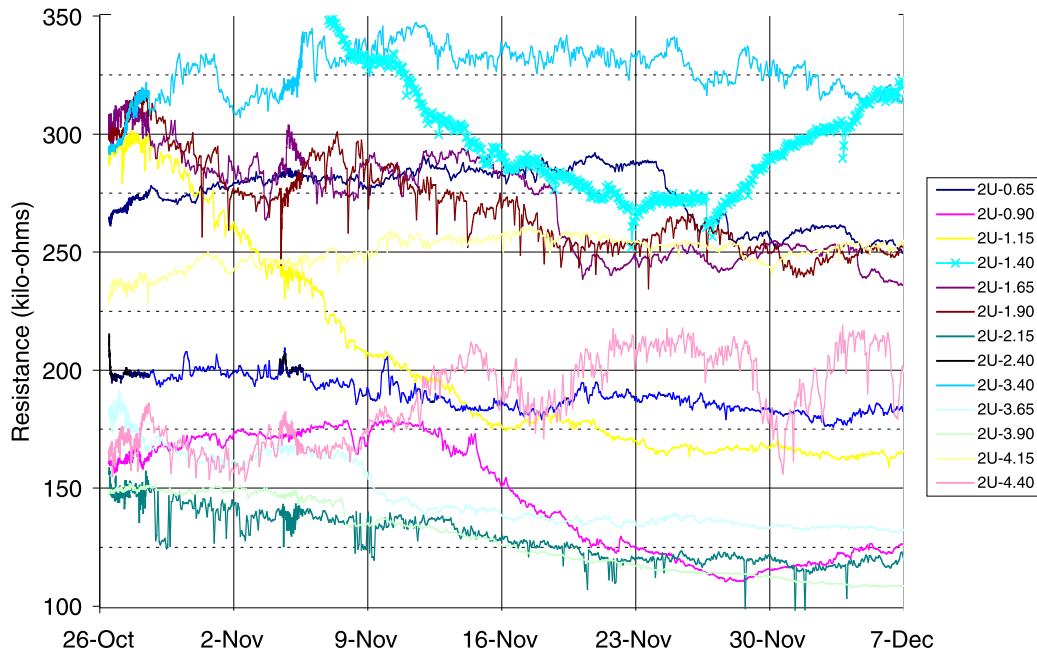
Water injected into the fault in borehole 12 was detected along the length of borehole 11 by ERPs located between 0.65 and 2.40 m (Figure 58). Unlike the ERP located on the fault (1.40 m from the collar), which showed a stepped response to individual release events, these other ERPs showed a slow, gradual decrease in resistance measurements. The first response was seen in the ERPs located on either side of the fault with the one at 1.65 m responding first. ERPs located between the alcove face and the fault appeared to be significantly drier at the start of the experiment than those located deeper in the test bed. These ERPs responded with larger decreases in resistance measurements following the start of the release water. The largest response to the injection events in borehole 12 was detected between 0.9 and 1.65 m from the collar in borehole 11.



DTN: LB990901233124.005

Figure 58. Changes in Electrical Resistance in Borehole 11 in Response to Liquid Released into the Fault in Borehole 12. The legend indicates the location of the measurement (in meters) from the collar. The 'U' indicates that these are measurements from the upper BSTs in the borehole.

In borehole 2 located 0.97 m vertically below borehole 12, the first ERPs to detect the wetting front were centered immediately below the fault (Figure 59). Here, at a distance of 1.15 to 1.65 m from the borehole collar, changes in saturation were detected almost one week after the first injection event on October 21, 1998. Over the next three weeks, ERPs at 1.15 and 1.40 m continued to detect increasing saturations, while the ERP at 1.65 m wetted for four days before maintaining a relatively constant saturation level for the next 18 days. At depths between 1.90 and 2.40 m, the response was delayed very slightly.



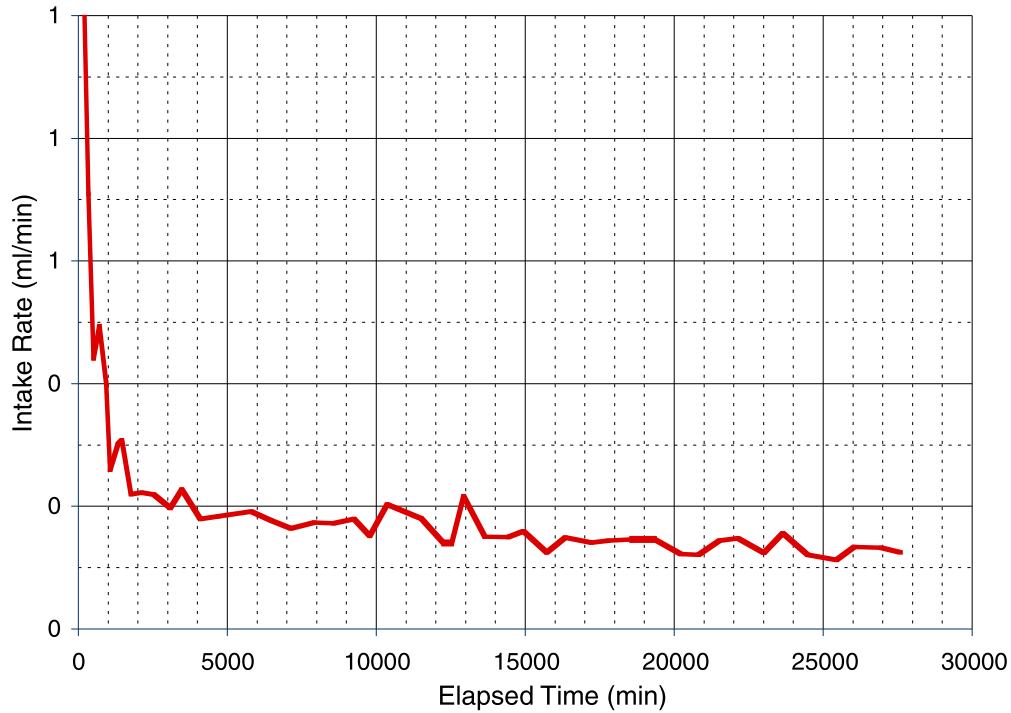
DTN: LB990901233124.005

Figure 59. Changes in Electrical Resistance in Borehole 2 in Response to Liquid Released into the Fault in Borehole 12. The legend indicates the location of the measurement (in meters) from the collar. The 'U' indicates that these are measurements from the upper BSTs in the borehole.

6.7.2.2 Matrix Responses

6.7.2.2.1 Intake Rates

When water was released into borehole 5, in the zone 2.44–2.74 m from the collar, the intake dropped steeply to 1 ml/min within 150 minutes (Figure 60). The intake rate then continued to gradually decrease over the next 2,000 minutes before reaching a constant rate of ~0.1 ml/min. This rate remained approximately constant for the entire duration of test.



DTN: LB990901233124.005

Figure 60. Intake Rates along a 0.3-m Zone in the Matrix Located 2.44–2.74 m from the Collar in Borehole 5.

6.7.2.2.2 Wetting Front Migration

Following the first release of water in borehole 5 on October 27, 1998 (at 2.44–2.74 m from the collar), the wetting front was detected in the upper section of borehole 6 (located 0.45 from borehole 5) after a period of 14 days on November 10, 1998 at a distance of 2.90 m from the collar (Figure 61). Some of the sensors near the collar had high resistance values and fluctuating changes that might represent responses to additional drying and wetting processes near the borehole collar.

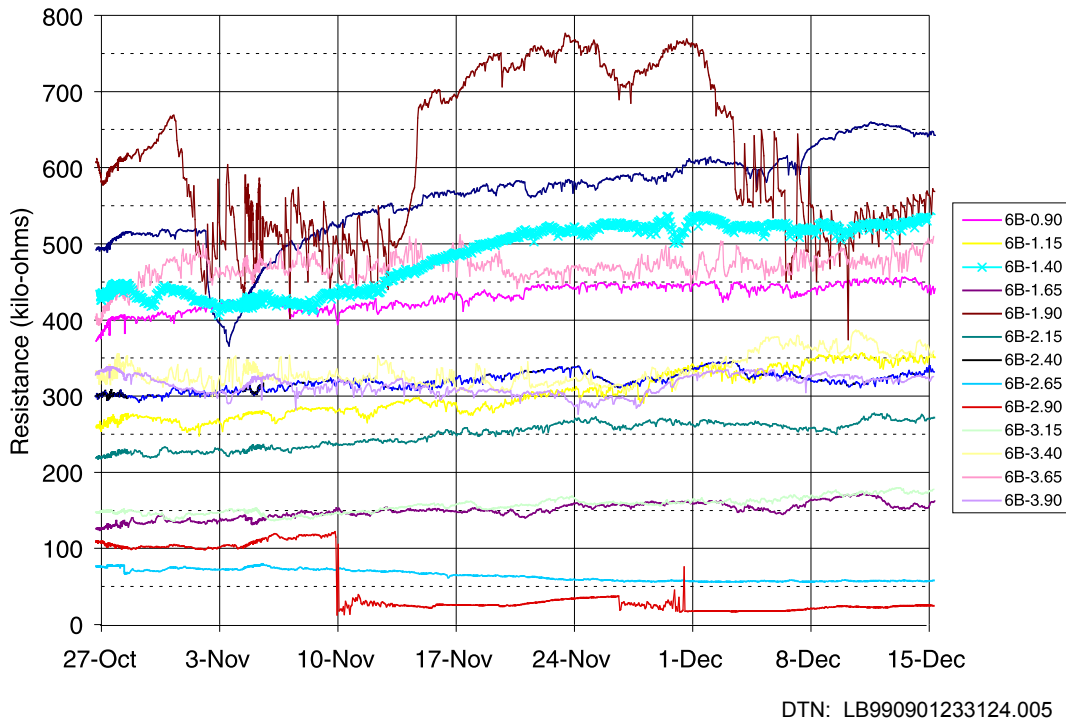


Figure 61. Changes in Electrical Resistance in Borehole 6 in Response to Liquid Released in Borehole 5. The legend indicates the location of the measurement (in meters) from the collar. The 'B' indicates that these are measurements from the lower BSTs in the borehole.

6.8 COMPILATION OF WATER-POTENTIAL MEASUREMENTS IN NICHEs

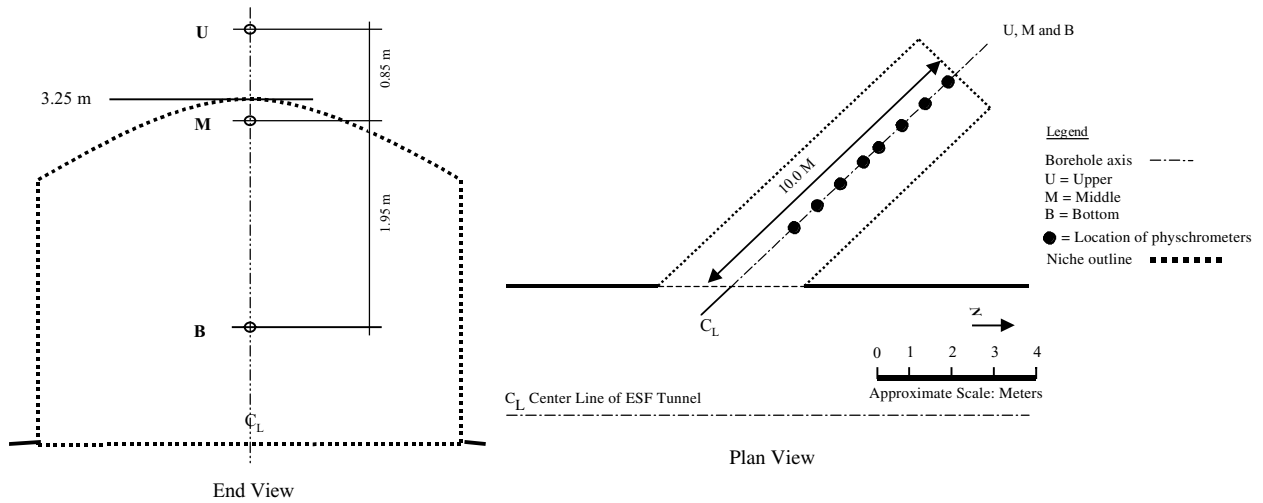
Measurements of water potentials from three niche sites in the ESF are presented. These sites are located on the west side of the ESF Main Drift at Niches 3566, 3650, and 3107. Two faults (the Ghost Dance and Sundance faults) lie within the immediate vicinity of the niches, with Niche 3566 lying between the Sundance fault and a cooling joint branching out from the fault.

The primary objective of this effort was to determine the water potential at various points within the three niche sites. To meet this objective, we adapted a common method to measure water potential, the use of psychrometers, for borehole application. The psychrometers were also used in wetting front detection, as described in Section 6.6 for Alcove 6 and Section 6.7 for Alcove 4. The sensitivity of psychrometer performance is described in [Attachment VIII](#).

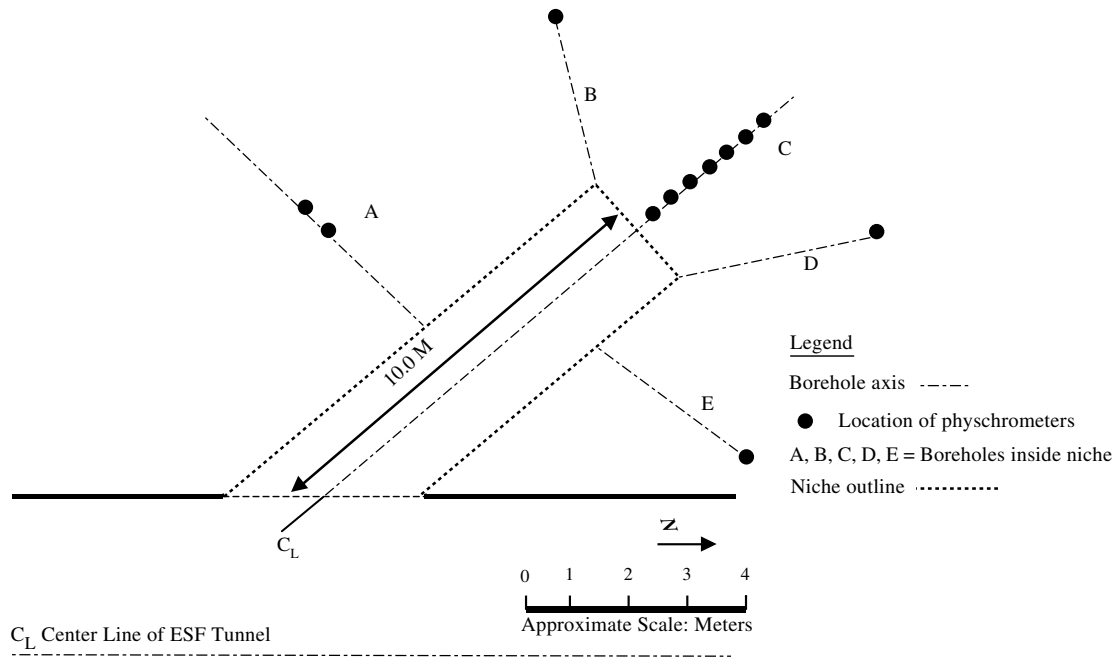
6.8.1 Location and Timing of Water-Potential Measurements at Niches

Water potentials were measured either along the length or at the ends of 0.0762-m-diameter boreholes. Three different types of housing units were used to locate psychrometers in the boreholes. The main feature of the housings was the creation of a small air chamber that allowed for quick equilibration and measurements of humidity close to the borehole wall.

At Niche 3566, two separate sets of measurements were made: i.e., before and after niche excavation. Pre-excavation measurements were made in May 1997 in three holes (U, M, and B) at a distance of 10 m from the borehole collar ([Figure 62a](#)). Between July and September 1997, two sets of measurements were made along borehole U at distances between 3.5 and 8.0 m from the collar. Post-excavation measurements of water potential were made in October 1997 in five boreholes extending radially along a horizontal plain from the niche cavity ([Figure 62b](#)).



(a)



(b)

Figure 62. Schematic Illustration of the Location of Psychrometers in Niche 3566 (a) in Pre-Excavation, (b) in Post-Excavation Conditions.

At Niche 3650, two separate sets of water-potential measurements were made in July 1997, before and after air-permeability tests were conducted in the boreholes. In three boreholes at this location (ML, BR, and BL), water potentials were measured at the end of the boreholes (10 m). In borehole UM, measurements were made close to the borehole collar, i.e., between 0.6 and 1.2 m (Figure 63).

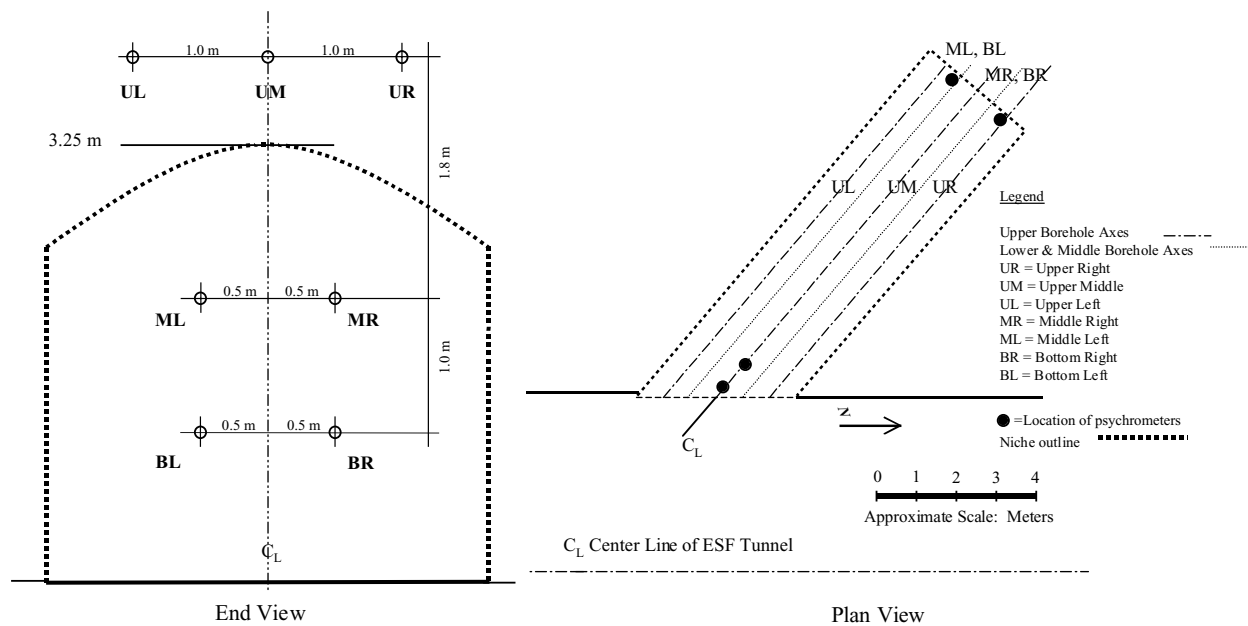


Figure 63. Schematic Illustration of Location of Psychrometers in Niche 3650.

At Niche 3107, four boreholes were instrumented with psychrometers (Figure 64). One set of potential measurements were made in December 1997 and January 1998. In the upper middle (UM) borehole, multiple measurements were made along the first 3.0 m, while in the remaining three boreholes (ML, UL, UR), single measurements were made using different lengths of borehole cavity. In the upper-right borehole (UR), sensors were located at the back of the borehole and sealed off with inflation packers such that the borehole cavity was less than 0.04 m long. In the upper-left (UL) borehole, sensors were located 5 m from the borehole collar, with the cavity sealed off with inflation packers. In this case, the sensing cavity extended over 5 m of the borehole. In the middle-lower borehole (ML), sensors were located 0.3 m from the borehole collar, with an inflation packer installed to isolate the entire 10-m length of borehole from the ESF Main Drift.

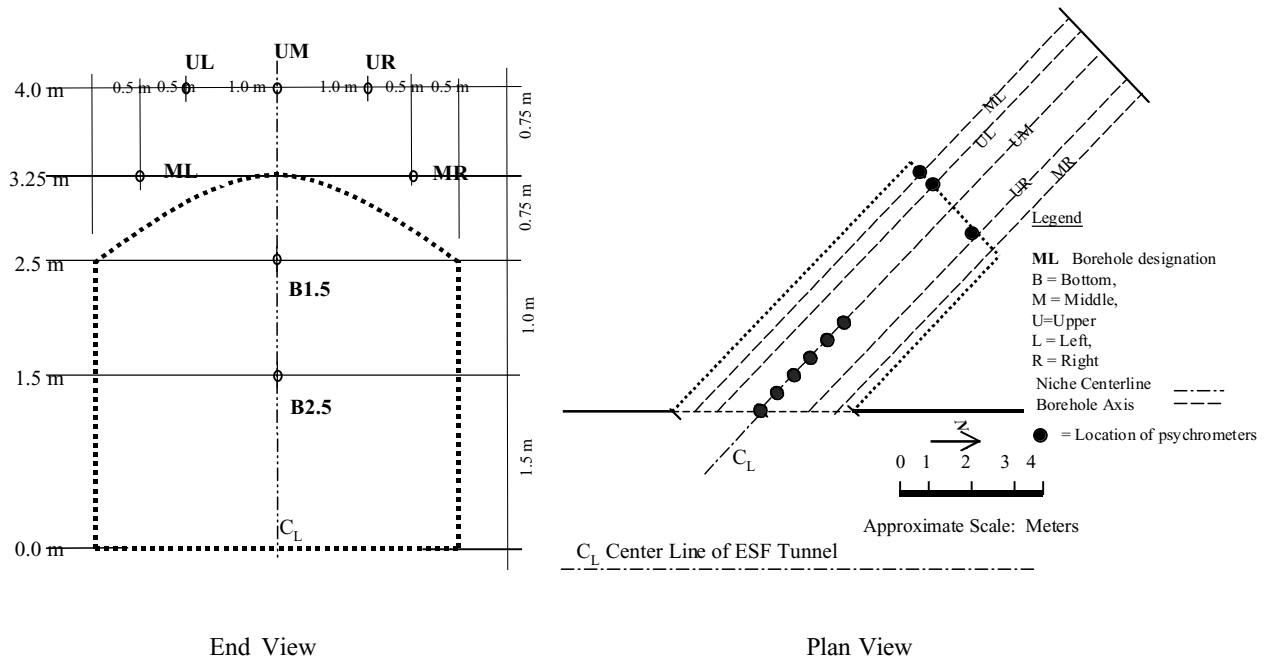


Figure 64. Schematic Illustration of Location of Psychrometers in Niche 3107 (Pre-Excavation).

6.8.2 Observations of Dryout in Niche Boreholes

Water-potential measurements obtained from the three niches are summarized in Tables 19 to 21. The time and duration of measurements are presented for each location.

Table 19. Water-Potential Measurements in Niche 3566.

Borehole ID	Dist. from collar (m)	Duration of measurement	Psych #	Water Potential (m)
Pre-Excavation				
U	10.0	5/9-16/97	Psy -51	-13
U	10.0	5/9-16/97	Psy -52	-13
M	10.0	5/9-16/97	Psy -53	-7
M	10.0	5/9-16/97	Psy -54	0.4
B	10.0	5/9-16/97	Psy -55	-12
U	6.1	7/8-14/97	Psy -42	-49
U	5.5	7/8-14/97	Psy -43	-46
U	5.5	7/8-14/97	Psy -44	-34
U	4.9	7/8-14/97	Psy -45	-46
U	4.3	7/8-14/97	Psy -48	-68
U	3.7	7/8-14/97	Psy -50	-62
U	7.9	9/16-24/97	Psy -42	-49
U	7.3	9/16-24/97	Psy -60	-46
U	6.7	9/16-24/97	Psy -45	-71
U	6.1	9/16-24/97	Psy -48	-67
U	5.5	9/16-24/97	Psy -50	-36
Post-Excavation				
A	6.25	10/18-21/97	Psy-43a	-2
A	6.75	10/18-21/97	Psy-60	-30
B	6.00	10/18-21/97	Psy-51	-43
C	0.15	10/18-21/97	Psy-49	-132
C	0.76	10/18-21/97	Psy-42	-33
C	1.98	10/18-21/97	Psy-45	-22
C	1.98	10/18-21/97	Psy-47	-47
C	1.37	10/18-21/97	Psy-48	-40
C	2.60	10/18-21/97	Psy-43	-57
D	6.00	10/18-21/97	Psy-54	-22
D	6.00	10/18-21/97	Psy-56	-32
E	6.00	10/18-21/97	Psy-57	-75
E	6.00	10/18-21/97	Psy-59	-81

DTN: LB980001233124.001

Table 20. Water-Potential Measurements in Niche 3650.

Borehole ID	Dist. from Collar (m)	Duration of Measurement	Psych #	Water Potential (m)
Pre-Air-Injection Testing				
UM	1.2	7/1-8/97	Psy -48	-127
UM	0.6	7/1-8/97	Psy -49	-139
UM	0.6	7/1-8/97	Psy -50	-165
BR	10.0	7/1-8/97	Psy -51	-37
BR	10.0	7/1-8/97	Psy -52	-39
BR	10.0	7/1-8/97	Psy -53	-32
BL	10.0	7/1-8/97	Psy -54	-24
BL	10.0	7/1-8/97	Psy -55	-36
ML	10.0	7/1-8/97	Psy -57	-1
Post-Air-Injection Testing				
ML	10.0	7/24-28/97	Psy -51	-29
ML	10.0	7/24-28/97	Psy -52	-38
ML	10.0	7/24-28/97	Psy -53	-39
BR	10.0	7/24-28/97	Psy -54	-58
BR	10.0	7/24-28/97	Psy -55	-49
BR	10.0	7/24-28/97	Psy -56	-48
BL	10.0	7/24-28/97	Psy -57	-21
BL	10.0	7/24-28/97	Psy -58	-15
BL	10.0	7/24-28/97	Psy -59	-28

DTN: LB980001233124.001

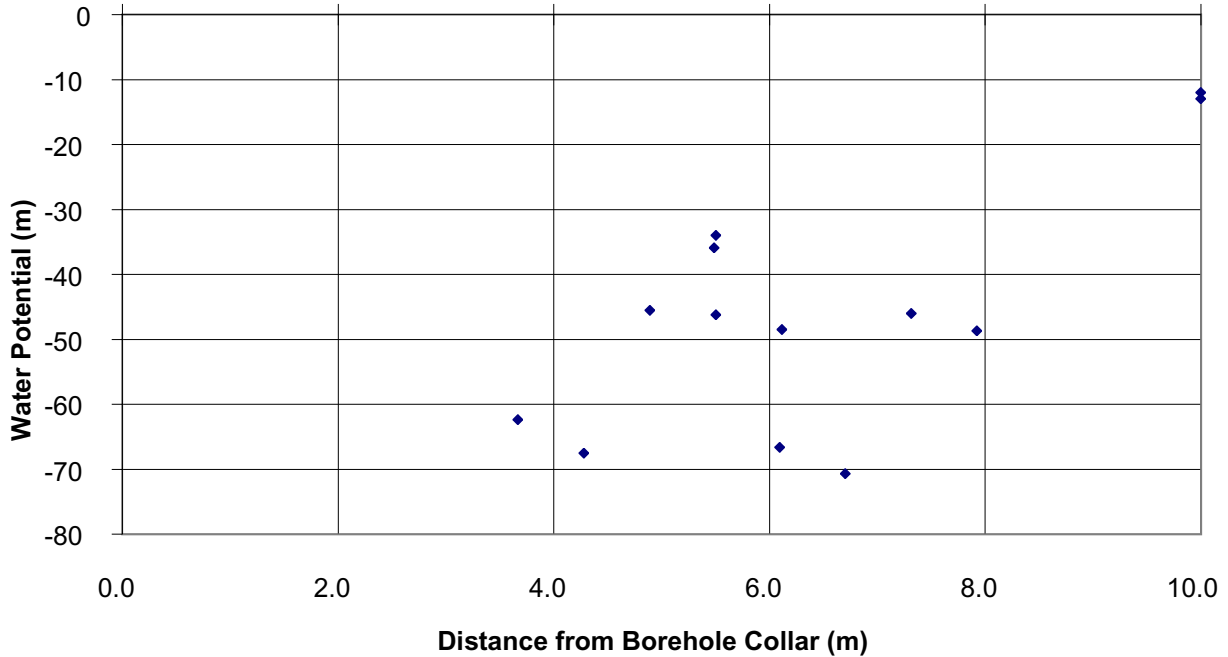
Table 21. Water-Potential Measurements in Niche 3107.

Borehole ID	Dist. from collar (m)	Duration of measurement	Psych #	Water Potential (m)
UM	0.45	12/22/97-1/8/98	Psy-86	-273
UM	1.06	12/22/97-1/8/98	Psy-83	-154
UM	1.67	12/22/97-1/8/98	Psy-75	-83
UM	2.90	12/22/97-1/8/98	Psy-68	-28
UL	10.00	12/22/97-1/8/98	Psy-64	-15
ML	10.00	12/22/97-1/8/98	Psy-66	-84

DTN: LB980001233124.001

6.8.2.1 Niche 3566 (Pre-Excavation)

The water potentials measured at the ends of the three pre-excitation boreholes (U, M, and B) in Niche 3566 were close to saturation values, indicating that approximately 10 m from the ESF, the formation is relatively wet. Of the three, the end of the middle borehole appeared to be wettest, with water potentials between 0.4 and -7 m. Measurements made along the profile of borehole U (between 3.7 and 7.9 m from the collar) ranged between -34 and -71 m (Figure 65 and Table 19).



DTN: LB980001233124.001

Figure 65. Pre-Excavation Water Potential Measured along Borehole U in Niche 3566.

6.8.2.2 Niche 3566 (Post-Excavation)

In the excavated niche cavity, water potentials were monitored in five boreholes. The monitored locations in borehole A (Figure 62b) were at 6.25 and 6.75 m from the collar. High water potentials were measured at these points (i.e., -2 and -30 m respectively). In three of the remaining boreholes (B, D, and E) water potentials measured at depths of 6.0 m varied significantly between boreholes. Borehole D (-27 m) was wettest, followed by B (-43 m), and then E (-78 m). These observations appear to be consistent with those made in the pre-excitation holes, which indicated that the formation tended to get wetter with increasing distance from the Main Drift.

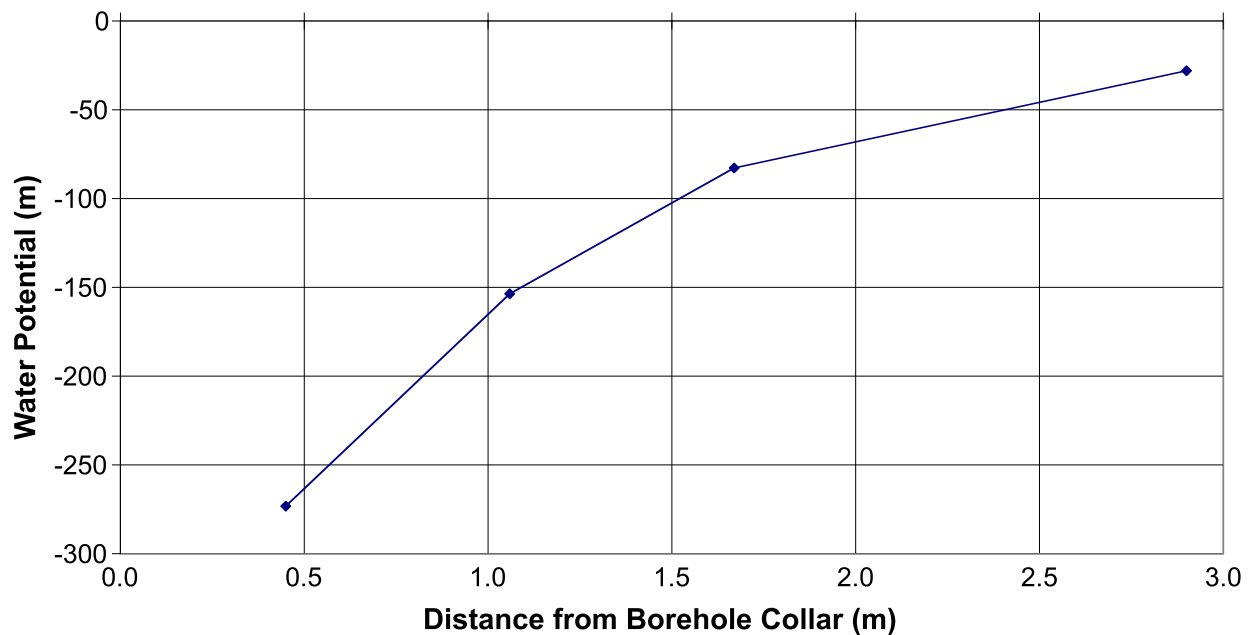
Measurements made close to the collar in borehole C suggest that there was significant dry-out in the rock surrounding the niches to a depth of at least 0.15 m, extending possibly to 2.6 m.

6.8.2.3 Niche 3650 (Pre-Excavation)

Measurements were made at the end of three boreholes BR, BL, and ML (Figure 63, Table 20), each 10 m long, before and after a series of air-permeability tests. Pre-test water-potential values ranged between -1 and -39 m. However, following the test, water potentials in one hole (BR) dropped to between -48 and -58 m, while in another hole (BL) the measurements did not show significant changes. Closer to the borehole collar of Borehole UM, readings made between 0.6 and 1.2 m indicate a relatively dry zone, with water potentials between -125 and -137 m.

6.8.2.4 Niche 3107

The observations made in Niche 3107 (Table 21) show significant variability among the boreholes in the niche. Measurements made at the ends of boreholes UL (-15 m) and ML (-84 m) indicate that at a depth of 10 m with a separation distance of 0.9 m (0.75 m vertically and 0.5 m horizontally, as illustrated in Figure 64), there is a steep potential gradient. Furthermore, from observations within borehole UM, it is clear that there is a prominent dry-out zone (Figure 66) associated with the Main Drift of the ESF.



DTN: LB980001233124.001

Figure 66. Water Potential Measured along Borehole UM in Niche 3107.

6.9 OBSERVATIONS OF CONSTRUCTION-WATER MIGRATION

During the Cross Drift excavation, sensors and water-collection trays were placed in a borehole below the Starter Tunnel and along the ESF Main Drift at the cross-over point. This section summarizes the results of monitoring the migration of water plumes from tunneling activities. A secondary objective was to evaluate the performance of ERP as a tool to detect the migration of wetting fronts in the unsaturated zone of fractured tuffs. The time domain reflectometry (TDR) was also used to monitor construction-water arrivals in drift walls. The TDR is based on electric measurement of waveguide reflection signals from changes in dielectric constant associated with water content changes.

6.9.1 Equipment Set-Up for Construction-Water Monitoring

6.9.1.1 Starter Tunnel Borehole

To monitor the migration of a water plume resulting from construction of the Cross Drift, a 30-m-long borehole (0.10 m ID) was drilled at an angle of 30 degrees (from the horizontal), along the proposed path of the Cross Drift tunnel (Figure 67). This borehole was in the Tptpul unit. The borehole originated at the end of a starter tunnel that was the launching pad for the Tunnel Boring Machine (TBM) used to excavate the Cross Drift. Changes in water saturation and potential were monitored along the entire length of borehole, using psychrometers and ERPs, as the TBM advanced through the formation above.

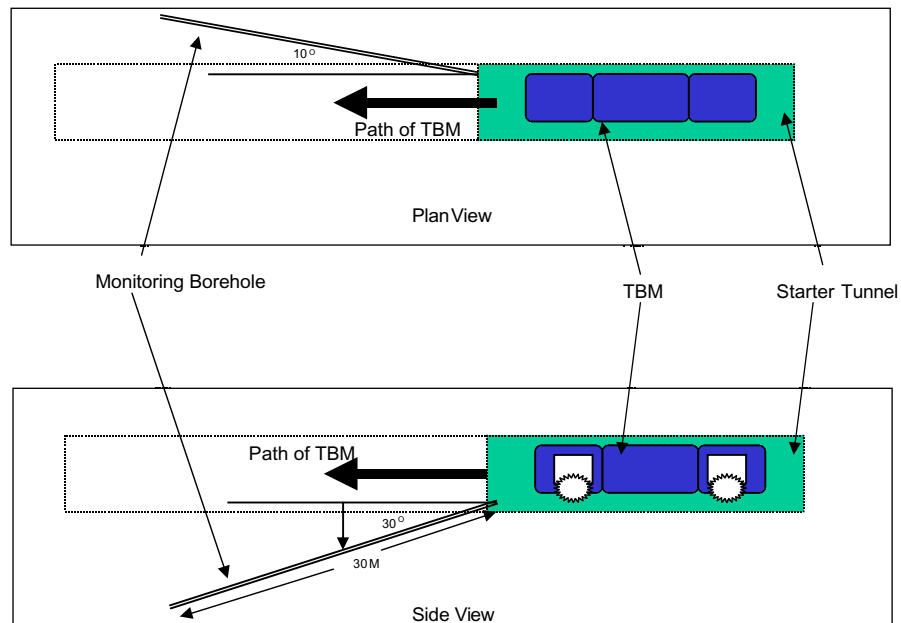


Figure 67. Schematic Illustration of the Location of Wetting Monitoring Borehole at the Starter Tunnel of the Cross Drift.

6.9.1.2 Electrical Resistivity Probes and Psychrometers

The psychrometers and ERPs were housed in PVC trays. These trays were fabricated from PVC pipes (0.10 m OD) bisected along the lengths. On each tray, psychrometers were installed at a spacing of 1.0 m along the borehole, while ERPs were located at 0.5-m intervals. To locate the psychrometers, we glued squares of PVC (0.02 m) at the 1.0-m mark and drilled small diameter holes (~0.003 m ID) through the tray. Psychrometers were then installed in these holes (Figure 68). ERPs were attached to the outer surface of the PVC trays with strips of Velcro. This housing permitted close contact between the ERPs and borehole wall, while allowing the psychrometers to contact the borehole wall through a small cavity.

A steel spoon, 3.0 m long, having the same configuration as the trays, was used to locate each PVC tray along the borehole. Typically, each tray was placed on the steel spoon and carried to the desired location where the spoon was slipped out, allowing the tray to settle snugly against the borehole wall.

Twenty-seven psychrometers and 54 electrical resistivity probes located on nine PVC trays were installed in the borehole (Figure 68) on February 26, 1998. Psychrometer data were collected at 1.5-hour intervals starting on February 28, for a period of four months. ER data collection started on March 25, 1998, and was collected at the same frequency and for the same duration as the psychrometers.

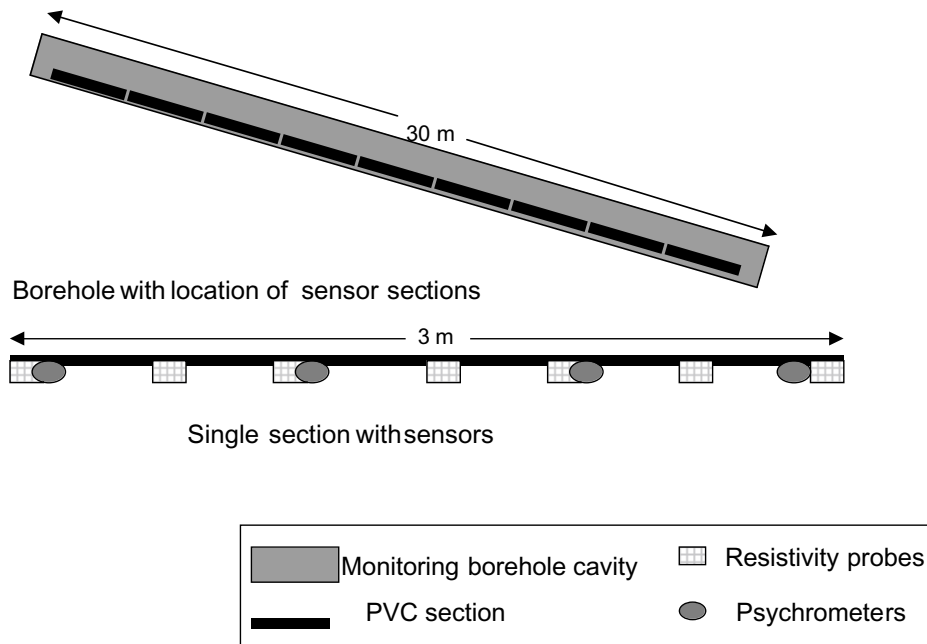


Figure 68. Schematic Illustration of the Borehole Wetting Front Monitoring System with Psychrometers and Electrical Resistivity Probes.

6.9.1.3 Drift Monitoring at the Cross-Over Point

The schematics of the seepage detection system, with fluid collection trays hanging below the ceiling of the ESF Main Drift, is illustrated in Figure 5. The schematics of the associated sensor arrays are illustrated in Figure 69. The seepage monitoring system was used to detect the wetting front in the ESF Main Drift as the result of releases of traced water in the Cross Drift above.

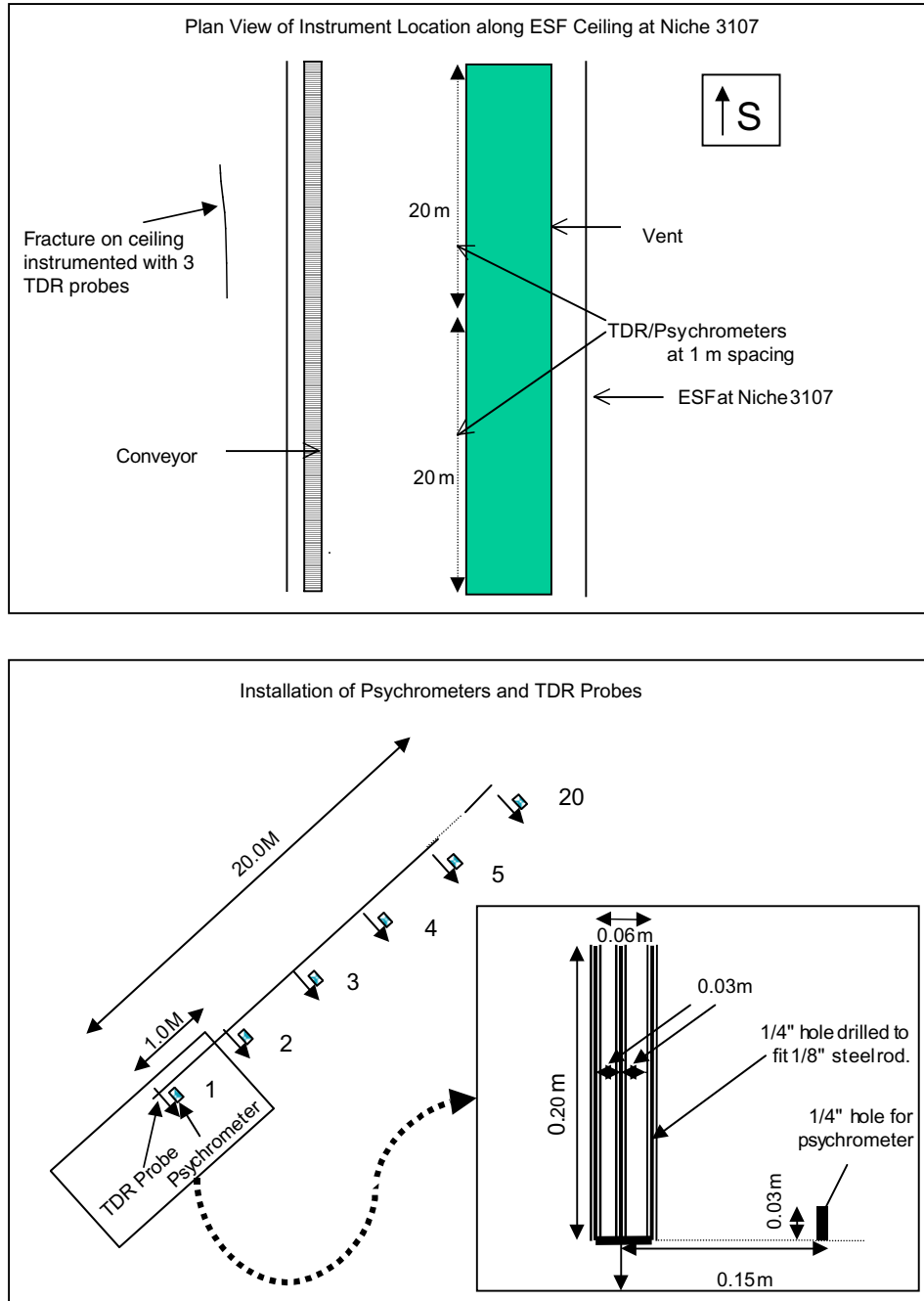


Figure 69. Schematic Illustration of Sensor Arrays for Wetting Front Monitoring.

At the cross-over monitoring station, we installed 132 collection trays, each 0.3 m wide and 1.23 m long, from station 30+40 to 30+80 m. The trays were hung below the tunnel ceiling next to the ventilation duct along the ESF Main Drift. On the drift walls above the spring line (3.18 m above the floor), psychrometers and TDR probes were installed. A horizontal sensor array with 40 psychrometer-TDR pairs at 1-m spacing was installed along the west wall (right rib). At the cross-over location, vertically along the west wall, between the spring line and the ventilation duct, three psychrometers were installed. On the east wall (left rib), three TDR probes were installed along the trace of a major fracture. In addition to the sensor on the walls, an infrared camera and a video camera periodically monitored the area around one TDR probe on the fracture trace. The infrared images are sensitive to temperature changes associated with evaporation processes.

6.9.2 Wetting Front Detection and Monitoring Below the Cross Drift

The following results are presented to show that wetting front was detected up to 12.15 m below the Cross Drift Starter Tunnel and no seepage was observed at the Cross-Over point in the Main Drift 17.5 m below the Cross Drift. The Starter Tunnel is located in the upper lithophysal TSw tuff unit and the Cross-Over point is located in the middle nonlithophysal TSw tuff unit.

6.9.2.1 Wetting Front Detection at the Starter Tunnel

The responses of all psychrometers and ERPs used in this investigation are summarized in [Tables 22 and 23](#). The last columns of both tables, all working sensors with signals in response to construction-water usage are labeled "yes" and not in response are labeled "no." With the arrival of a wetting front, the water potential measured by psychrometers and the electrical resistance measured by ERPs change to near zero values.

Table 22. Psychrometers Response to Excavation at the Starter Tunnel of the Cross Drift

PSY_ID	Dist. Collar (m)	Vertical Depth (m)	Response to Tunneling
Psy_30.3	30.3	15.15	-
Psy_29.3	29.3	14.65	-
Psy_28.3	28.3	14.15	No
Psy_27.3	27.3	13.65	-
Psy_26.3	26.3	13.15	No
Psy_25.3	25.3	12.65	No
Psy_24.3	24.3	12.15	Yes
Psy_23.3	23.3	11.65	No
Psy_22.3	22.3	11.15	Yes
Psy_21.3	21.3	10.65	No
Psy_20.3	20.3	10.15	No
Psy_19.3	19.3	9.65	-
Psy_18.3	18.3	9.15	Yes
Psy_17.3	17.3	8.65	Yes
Psy_16.3	16.3	8.15	Yes
Psy_15.3	15.3	7.65	Yes
Psy_14.3	14.3	7.15	Yes
Psy_13.3	13.3	6.65	Yes
Psy_11.4	11.4	5.7	Yes
Psy_10.4	10.4	5.2	Yes
Psy_9.4	9.4	4.7	Yes
Psy_7.2	7.2	3.6	-
Psy_6.2	6.2	3.1	Yes
Psy_5.2	5.2	2.6	Yes
Psy_3.9	3.9	1.95	-
Psy_2.6	2.6	1.3	-
Psy_1.6	1.6	0.8	Yes

Table 23. Electrical Resistivity Probe Responses to Excavation at the Starter Tunnel of the Cross Drift

ER_ID	Dist. Collar (m)	Vertical Depth (m)	Response to Tunneling
ER_30.3 m	30.3	15.2	No
ER_29.8 m	29.8	14.9	No
ER_29.3 m	29.3	14.7	No
ER_28.8 m	28.8	14.4	No
ER_28.3 m	28.3	14.2	No
ER_27.8 m	27.8	13.9	No
ER_27.3 m	27.3	13.7	Yes
ER_26.8 m	26.8	13.4	Yes
ER_26.3 m	26.3	13.2	No
ER_25.8 m	25.8	12.9	No
ER_25.3 m	25.3	12.7	No
ER_24.8 m	24.8	12.4	No
ER_24.3 m	24.3	12.2	Yes
ER_23.8 m	23.8	11.9	No
ER_23.3 m	23.3	11.7	No
ER_22.8 m	22.8	11.4	No
ER_22.3 m	22.3	11.2	Yes
ER_21.8 m	21.8	10.9	Yes
ER_21.3 m	21.3	10.7	Yes
ER_20.8 m	20.8	10.4	No
ER_20.3 m	20.3	10.2	Yes
ER_19.8 m	19.8	9.9	Yes
ER_19.3 m	19.3	9.7	Yes
ER_18.8 m	18.8	9.4	Yes
ER_18.3 m	18.3	9.2	Yes
ER_17.8 m	17.8	8.9	Yes
ER_17.3 m	17.3	8.7	Yes
ER_16.8 m	16.8	8.4	Yes
ER_16.3 m	16.3	8.2	Yes
ER_15.8 m	15.8	7.9	Yes
ER_15.3 m	15.3	7.7	Yes
ER_14.8 m	14.8	7.4	Yes
ER_14.3 m	14.3	7.2	Yes
ER_13.8 m	13.8	6.9	Yes
ER_13.3 m	13.3	6.7	Yes

Table 23. Electrical Resistivity Probe Responses to Excavation at the Starter Tunnel of the Cross Drift (cont.)

ER_ID	Dist. Collar (m)	Vertical Depth (m)	Response to Tunneling
ER_12.8 m	12.8	6.4	Yes
ER_11.4 m	11.4	5.7	Yes
ER_10.9 m	10.9	5.5	Yes
ER_10.4 m	10.4	5.2	Yes
ER_9.9 m	9.9	5.0	Yes
ER_9.4 m	9.4	4.7	Yes
ER_8.9 m	8.9	4.5	Yes
ER_7.2 m	7.2	3.6	Yes
ER_6.7 m	6.7	3.4	Yes
ER_6.2 m	6.2	3.1	Yes
ER_5.7 m	5.7	2.9	Yes
ER_5.2 m	5.2	2.6	Yes
ER_4.7 m	4.7	2.4	Yes
ER_3.9 m	3.9	2.0	Yes
ER_3.1 m	3.1	1.6	Yes
ER_2.6 m	2.6	1.3	Yes
ER_2.1 m	2.1	1.1	Yes
ER_1.6 m	1.6	0.8	Yes
ER_1.1 m	1.1	0.6	Yes

6.9.2.1.1 Psychrometers

The data from the psychrometers illustrated in [Figure 70](#) show that along the entire length of the borehole, the walls were at water potentials approximately -500 m when the sensors were installed in late February 1998. A uniform, steep increase in water-potential values over the first two weeks in March suggests the recovery of the borehole wall from drying that occurred during the dry drilling of this borehole. The following four months of data show all psychrometers approaching equilibrium values, with water potentials ranging from -70 to 0 m ([Figure 70](#)).

Superimposed on this asymptotic trend in water-potential values are periodic deviations with psychrometers nearer the borehole collar showing a larger number of such events. These events were restricted to the first two months of monitoring, and by the third week of April the last of these events had occurred. In three of the psychrometers (located at distances of 1.6, 6.2 and 9.4 m from the borehole collar), we found evidence of wetting events, which increased water potential to (near) zero. The psychrometer at 1.6 m had near-zero water potential for three distinct periods. The first extended from the start of monitoring until March 3, with the second

extended for four days beginning on March 8. A final period, significantly shorter, lasted for almost 24 hours on March 22. The psychrometer located at 6.2 m measured water potential close to zero for a three-day period starting on March 8th. The psychrometer located at 9.4 m detected water-potential values close to zero for a single event on March 13, for nearly eleven hours.

One concern that could arise from the use of a slanting borehole to measure wetting front migration is the possibility of the bore cavity short-circuiting flow paths. For this particular investigation, this short-circuiting does not appear to be happening, as indicated by the analysis of recovery responses observed at the depth of 5.2 m. Here, the response to a wetting event was negligible when compared with other psychrometers close to this location (above and below), suggesting that this zone was well isolated (hydraulically) from the adjacent zones and did not detect the wetting front. In the remaining eight psychrometers located between 9.4 m and 17.3 m from the borehole collar, we found evidence of small increases in water potential that extend beyond the projected recovery rate. Some of these increases coincided with periods when the psychrometers at distances of 1.6, 6.2 and 9.4 m along the borehole showed near-zero potentials; the rest of the psychrometer data remained uncorrelated until the end of April 1998. The psychrometers up to a distance of 10.4 meters maintained a sinusoidal response, which fluctuated around a trend of slow water-potential increase.

By early May 1998, the rates at which water potential was increasing had decreased significantly, and by mid-June all psychrometers readings appeared to have stabilized. In the case of two deep psychrometers (i.e., at 18.3 m and 22.3 m), there appears to have been individual events that for brief periods increased the rate at which water potentials were increasing. The deep psychrometers maintained nearly constant readings once they approached equilibrium, without the oscillations observed for shallow psychrometers.

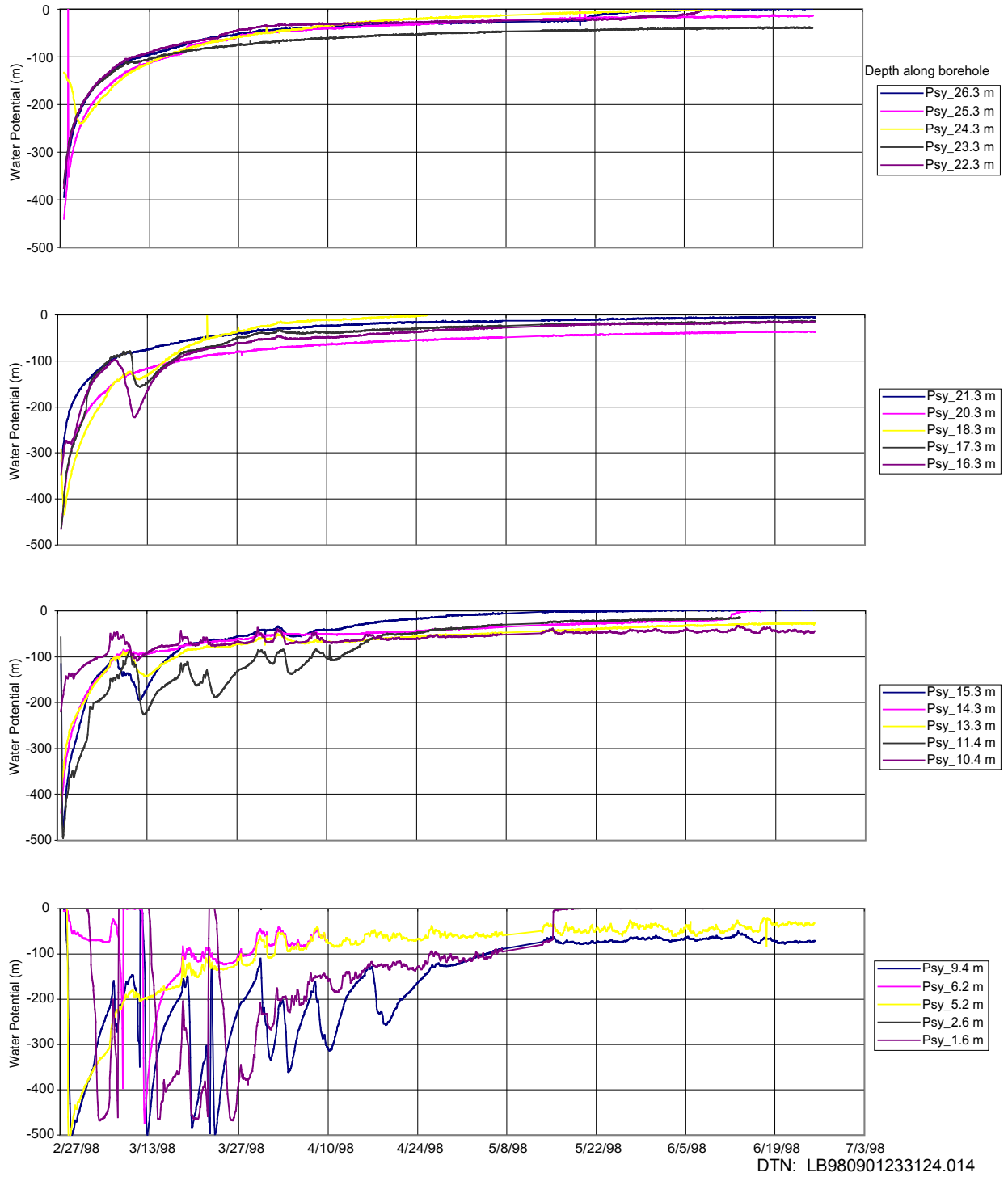
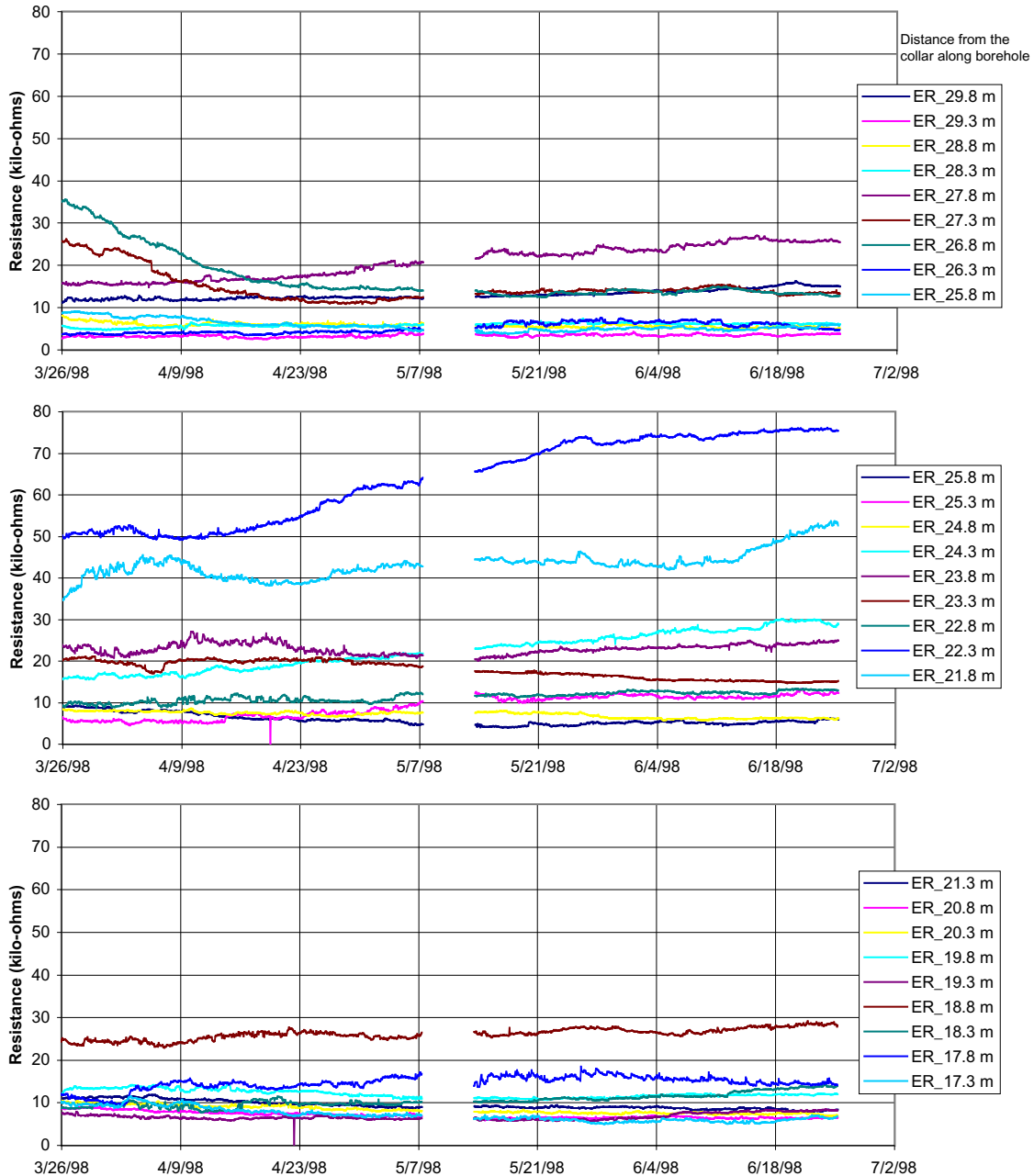


Figure 70. Changes in Water Potential Observed along the Wetting Front Monitoring Borehole at the Starter Tunnel of Cross Drift.

6.9.2.1.2 Electrical Resistivity Probe

Measurements of electrical resistance were initiated in late March and continued until late June. Figure 71 summarizes the responses observed from probes located at 0.5-m intervals along the walls of the borehole between 17.3 and 29.8 m from the borehole collar.



DTN: LB980901233124.014

Figure 71. Changes in Electrical Resistance Observed along the Wetting Front Monitoring Borehole at the Starter Tunnel of the Cross Drift.

6.9.2.1.3 Potential Sensor Comparison

As part of an effort to evaluate the performance of ERPs as a sensor to monitor the arrival and movement of a wetting front, a series of probes were installed adjacent to psychrometers along the borehole length. The performance of the ERPs were compared with those of psychrometers.

From the psychrometer data collected between late March and June, 1998, as illustrated in [Figure 72](#), the events of interest were:

- Sinusoidal responses in the shallower psychrometers (e.g., psychrometer at distance of 5.2m).
-
- The wetting and drying cycles observed in the shallower zones as the borehole walls approached equilibrium (e.g., psychrometer at distance of 9.4 m).
-
- Steady approaches to equilibrium as seen in the deeper psychrometers (i.e., at depths greater than 10.4 m).

[Figures 72a to 72c](#) summarize examples of responses of both psychrometers and ERPs for the three response patterns observed in the psychrometer data. (The y-axes for resistance were presented in decreasing scales so that wetter sensors have higher y-values.) In two of the three cases, the ERPs responded in a pattern similar to that of psychrometers located adjacent to the probes. With the exception of the sensor at 5.2 m, the sinusoidal response observed by the psychrometer was well tracked by the ERPs, with points of changing trends fairly well synchronized. However, the direction of the trends between small time intervals is not consistent, suggesting that the response times of the probes are significantly different. The ERPs at shallow depths might be sensitive to air flows through the fractures in addition to moisture conditions in the vicinity of the probes. The psychrometers measure the moisture conditions in the vicinity of the probes.

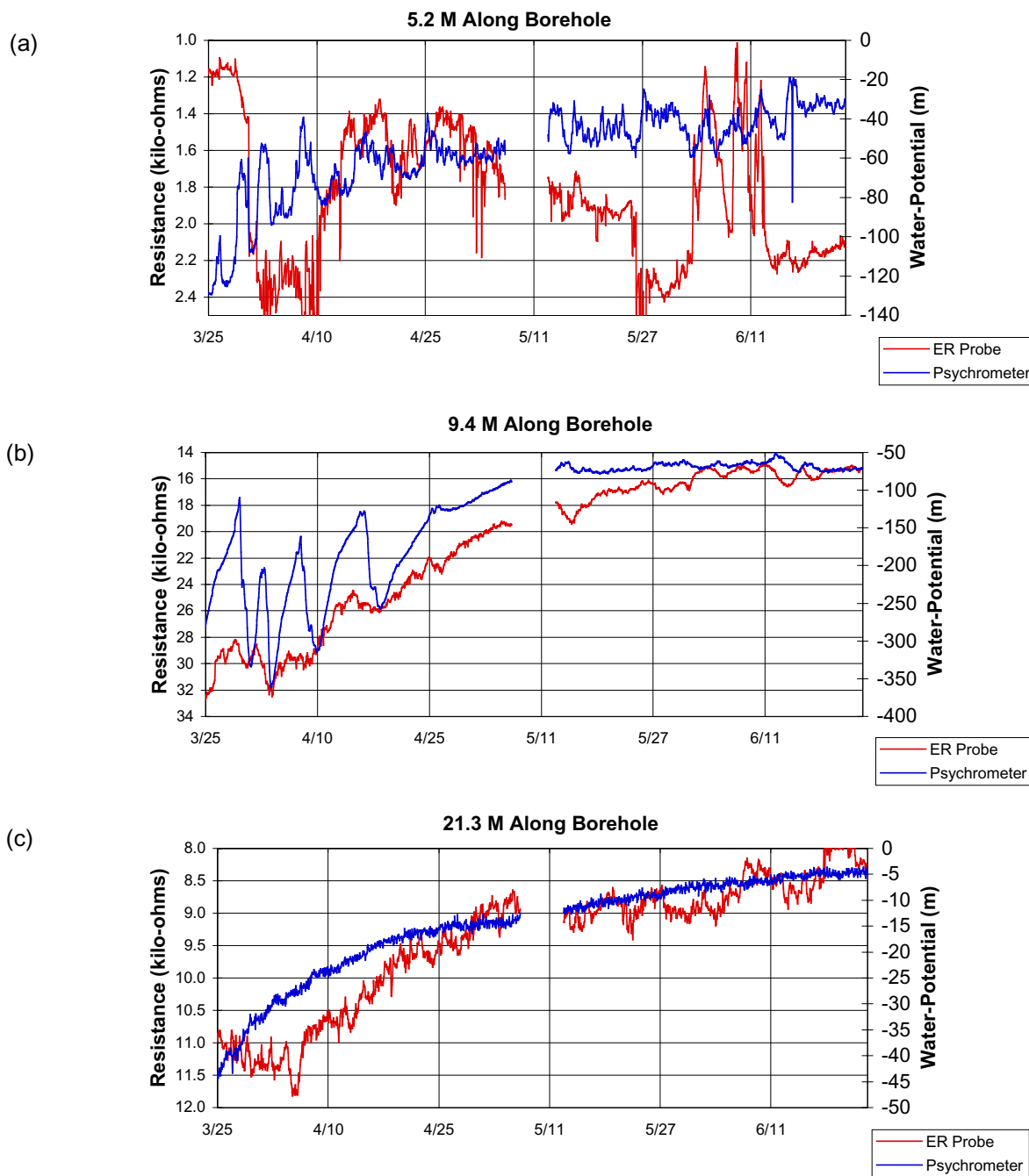


Figure 72. Comparison of Performance of Electrical Resistivity Probe and Psychrometer.

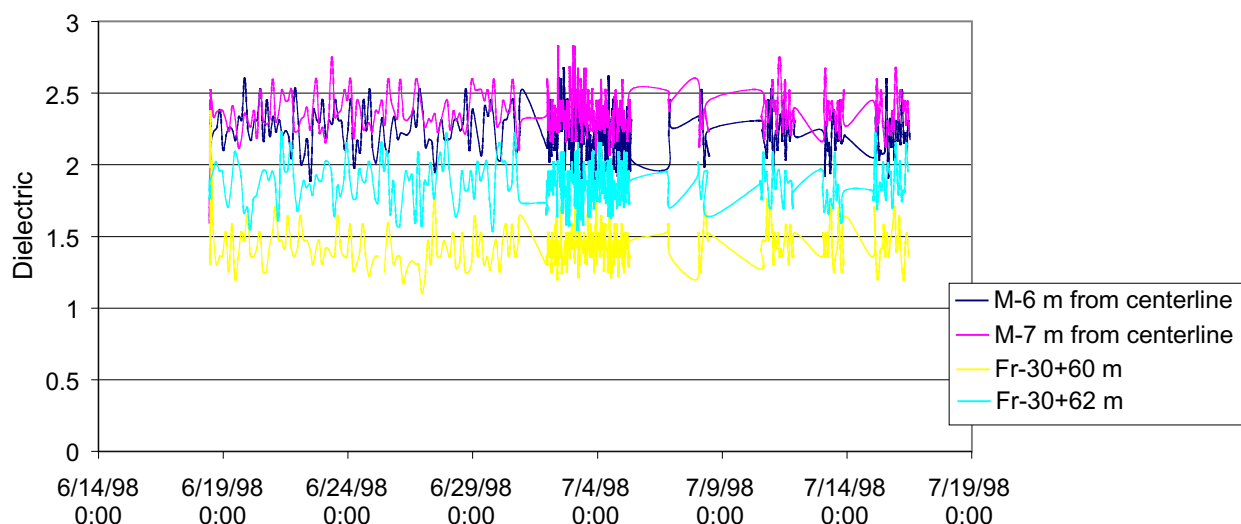
At a distance of 9.4 m, the potential increased steadily from -400 m to -70 m between late March 1998 and June 1998, and the corresponding ERP measurements followed a similar pattern. Here, large fluctuations in water potentials in relatively short periods of time (-200 m in 4 days) were comparably detected by both types of probes. The slower, more gradual recovery observed by psychrometers deeper in the formation was generally well tracked by the ERPs (e.g., at 21.3 m).

6.9.2.2 Wetting Front Monitoring at the Cross-Over Point

The Cross Drift passed over the ESF Main Drift on the second shift of July 1, 1998. No seepage was observed. The observers in the ESF Main Drift could hear rumbling noises from the TBM and feel vibrations on the railroad tracks and tunnel wall. However, no falling of loose rock was observed.

Figure 73 illustrates an example of the data collected by the TDR probes. No evident signals were associated with wetting front arrivals. These null results from the sensors substantiated the field observations of no seepage associated with TBM passing over the ESF Main Drift. The confirmation of no seepage at the cross-over point establishes the lower limit for the drift-to-drift flow and drift seepage processes associated with localized construction-water usage. It also provides a guide to the design of controlled drift-to-drift experiments planned at this unique location, with one drift above another drift.

The underground water usage in the Cross Drift is being monitored by the ESF Constructor on a shift-by-shift basis; the tunnel-water use logs are being evaluated by the M&O Determination of Importance Evaluation group.



Measurement of Dielectric in Formation Matrix (M-6, M-7) and Fracture (Fr) at Crossover Point

DTN: LB980901233124.014

Figure 73. Example of Time Domain Reflectometry Probe Data at the Cross-Over Point in the ESF Main Drift.

6.10 STATUS OF ANALYSES OF ESF CONSTRUCTION EFFECTS

The construction of the ESF introduced large-scale perturbations to the moisture conditions in the UZ at Yucca Mountain, affecting the saturation distribution and the pneumatic flow field around the drifts. Ventilation of the drifts and use of construction water are both necessary operations for the excavation and for the daily access to the underground study sites. The ESF moisture-monitoring data collection, initiated in 1995 during the excavation of the North Ramp of the main ESF tunnel, continues in the Cross Drift excavated in 1998. The ESF main loop is 8 km long and 8 m in diameter, and the Cross Drift is 2.6 km long and 5 m in diameter. Given the size, length, and spatial coverage, the moisture perturbations by the ESF is *de facto* the single largest-scale test for the site evaluation of Yucca Mountain.

6.10.1 Summary of Construction-Induced Effects

6.10.1.1 Status of the ESF Moisture-Monitoring Study

The moisture conditions in the ESF tunnels were monitored at 17 stations in the ESF main tunnel (from station 7+20 to station 73+50) and 10 stations in the Cross Drift (from station 0+25 to station 25+55), as summarized in [Table 24](#). Relative humidity, temperature, barometric pressure, and air velocity were measured at various stations. The moisture-monitoring stations were supplemented by measurements from sensors mounted on the TBM during excavations and by periodic surveys conducted along the tunnels with sensors on a mobile cart. An infrared camera was used in mobile surveys to measure the temperature changes on the tunnel walls.

Table 24. Moisture-Monitoring Stations in the Exploratory Studies Facility

Moisture-Monitoring Station Location/ ID*	Description**	DTN/Report ID***
21+00/LB20, 28+30/LB50, 35+00/LB40, 42+50/LB60, 47+00/LB70, 51+73/LB80, 57+50/LB90, 64+59, 67+00, 73+50, AOD5, BKH5	Relative Humidity, Temperature, and Pressure in ESF Monitoring Stations in Report "Evaluation of Moisture Evolution in the Exploratory Studies Facility." VA Supporting Data	LB960800831224.001
	Moisture Data Report from October, 1996 to January, 1997	LB970300831224.001
	Moisture-Monitoring Data Collected at ESF Sensor Stations, Moisture Monitoring Before and After the Completion of the ESF	LB970801233124.001
	Moisture-Monitoring Data Collected at Stationary Moisture Stations	LB970901233124.002
7+20/GS#3, 10+93/GS#4, 28+93, 51+64, 67+20, Operator-Shack/GS#1 (on TBM), Vent-Line-Intake/GS#2 (on TBM)	Moisture Monitoring in the ESF, Oct. 1, 1996 through Jan. 31, 1997	GS970208312242.001
	Moisture Monitoring in the ESF, Feb. 1, 1997 through July. 31, 1997	GS970708312242.002
	Moisture Monitoring in the ESF, August 1, 1997 through July. 31, 1998	GS980908312242.024
Cross Drift GS: 0+25, 2+37, 2+88, 3+38, 10+03, 21+07, 24+75; LB: 14+35, 21+40, 25+55	Moisture Monitoring in the ECRB, 04/08/98 to 7/31/98	GS980908312242.035 LB990901233124.006/ This AMR/Section 6.10.2.2

NOTES: * LB for stations maintained by LBNL, and GS for stations maintained by USGS in this cooperative moisture-monitoring study.
 ** From ATDT or equivalent description.
 *** The list of source data in Section 8.3 includes only DTNs used in this AMR. Other DTNs listed in this table are for information only.

The moisture data in the drifts, together with ventilation data and construction-water usage data, can be used to evaluate the amounts of moisture removed from the ESF drifts and the net quantities of construction water drained into the surrounding tuff formations. In this AMR, examples of recent moisture-monitoring data in the Cross Drift are presented. Simple observations are qualitatively discussed to highlight the importance of excavation and operation data for determining the site perturbations. Potential sources of collaborative evidence of the induced effects are presented in [Tables 24, 25, and 26](#).

6.10.1.2 Rock Drying and Moisture Transport

Moisture removals from the drift walls induce drying in the surrounding rocks, and construction water migrates through the inverts to the deep tuff media. Tables 25 and 26 list the field-testing activities on potential and saturation measurements in the ESF. A subset of the data listed in Table 25 on potential measurements was presented in Section 6.8. Borehole monitoring measurements by psychrometers to evaluate the drying processes in the rocks were carried out in niches along the ESF Main Drift. Additional measurements are in progress in boreholes along the Cross Drift. In addition to psychrometers, the heat-dissipation probes are extensively used in the ESF for wall monitoring.

Table 26 lists the saturation measurements for both monitoring of wetting fronts and for determining *in situ* conditions. Examples of construction-water monitoring along the Cross Drift with ERPs were discussed in Section 6.9. Neutron logging along boreholes are periodically conducted. Cores from boreholes were used to measure saturations of tuff matrix. TDR measurements were also deployed.

Table 25. Water-Potential Measurements in the Exploratory Studies Facility

Potential Measurement	Description*	DTN/Report ID**
Niche 3566 - psychrometer Niche 3650 - psychrometer	3 main boreholes, 5 lateral boreholes in Niche 3566, 5/9/97 - 10/21/97; 6 main boreholes in Niche 3650, 7/1/97 - 7/28/97	LB980001233124.001/ This AMR/Section 6.8.2
Niche 3566 - heat dissipation probe	21 heat dissipation probe drill holes, 11/4/97 - 7/31/98	GS980908312242.022
Niche 3107 - psychrometer	3 main boreholes, 12/22/97 - 1/8/98	LB980001233124.001/ This AMR/Section 6.8.2.4
Alcove 7 - heat dissipation probe	heat dissipation probe drill holes, 12/9/97 - 1/31/98	GS980308312242.007
Alcove 3 - filter paper Alcove 4 - filter paper	1 core hole in Alcove 3, 2 core holes in Alcove 4	GS980908312242.033, GS980908312242.032
North Ramp 7+27 to 10+70 South Ramp 69+65 to 76+33 - filter paper	18 North Ramp boreholes, 3 Alcove 4 boreholes, and 46 South Ramp boreholes, HQ, 2-m length	GS980308312242.004
South Ramp - heat dissipation probe	heat dissipation probe drill holes, 8/1/97 - 1/4/98	GS980308312242.002
Cross-Over Point 30+62 in the ESF Main Drift Below the Cross Drift - psychrometer	43 psychrometers on ESF drift walls, 6/19/98 - 7/16/98	LB980901233124.014/ This AMR/Section 6.9.2.2
Cross Drift Starter Tunnel - psychrometer & electrical resistivity probe	1 slant borehole below the invert	LB980901233124.014/ This AMR/Section 6.9.2.1
Cross Drift 0+50 to 7+75 - heat dissipation probe	6 heat dissipation probe drill holes, 4/23/98 - 7/31/98	GS980908312242.036
Surface Based Boreholes - psychrometer	USW NRG-7a, UE-25 UZ#4, UE-25 UZ#5, USW UZ-7a and USW SD-12; 1/1/97 - 6/30/97; 7/1/97 - 9/30/97; 10/1/98 - 3/31/98	GS970808312232.005, MOL.19980226.0042-0045, GS971108312232.007, MOL.19980226.0607-0614, GS980408312232.001, MOL.19980706.0269.

NOTE: * ATDT or equivalent description.

** The list of source data in Section 8.3 includes only DTNs used in this AMR. Other DTNs listed in this table are for information only.

Table 26. Saturation Measurements in the Exploratory Studies Facility

Saturation Measurement	Description*	DTN/Report ID**
Niche 3566 (#1) - core Niche 3650 (#2) - core	3 main boreholes, 6 lateral boreholes in Niche 3566 (#1) and 7 main boreholes in Niche 3650 (#2)	GS980908312242.018, GS980908312242.020
Alcove 6 - core Alcove 7 - core	3 boreholes in Alcove 6, 1 borehole in Alcove 7	GS980908312242.029, GS980908312242.028
Alcove 3 - core Alcove 4 - core	1 core hole in Alcove 3, 2 core holes in Alcove 4	GS980908312242.033, GS980908312242.032
North Ramp 7+27 to 10+70 South Ramp 59+65 to 76+33 - core	Borehole samples	GS980308312242.005, GS980308312242.003
South Ramp - time domain reflectometry	TDR measurements, 8/1/97 - 1/4/98	GS980308312242.001
Cross Drift Starter Tunnel - core	1 slant borehole core	GS980908312242.030
Cross-Over Point 30+62 in the ESF Main Drift Below the Cross Drift - time domain reflectometry	43 TDR probes on ESF drift walls, 6/19/98 - 7/16/98	LB980901233124.014/ This AMR/Section 6.9.2.2

NOTE: * From ATDT or equivalent description.

** The list of source data in Section 8.3 includes only DTNs used in this AMR. Other DTNs listed in this table are for information only.

6.10.2 Moisture Conditions and Perturbations Observed in Drifts

6.10.2.1 ESF Main Drift Observations

Preliminary evaluation of the moisture data during ESF excavation showed that the moisture conditions were sensitive to construction activities. The daily usage of water for excavation, muck transport, dust-control, and other operations introduced rapid changes in moisture conditions throughout the tunnel atmosphere and in the wall rock. During weekends in 1996 when construction activities were absent, the tunnel atmosphere generally stabilized to either high-humidity conditions if the ventilation was turned off, or to low-humidity conditions if the ventilation was left on (DTN: LB960800831224.001). After completion of the ESF main tunnel with two portals for entrance and exit, high-humidity conditions were suppressed by natural ventilation through the portals (DTN: LB970801233124.001).

The following order-of-magnitude estimate of drift capacity represents the ESF system in 1996 conditions. For a 6250-m-long tunnel with cross-sectional area of 40 m², the humid tunnel air can contain 2500 kilograms of excess water mass if we estimate that the tunnel is on average 50% more saturated than the outside air, with the corresponding vapor density difference on the order of 0.01 kg/m³. If the tunnel air is ventilated with flow rate of 47 m³/s or 100,000 ft³/min

(cubic feet per minute, or cfm), it will take 5,300 seconds or 1.5 hours to remove and replace the tunnel air. The water-removal rate of 2,500 kg over 1.5 hr corresponds to 285 m³/week (285 kiloliter/week or 75,000 gallon/week). Approximating that all the moisture in the tunnel air is from evaporation, the equivalent evaporation rate from the tunnel walls and invert (with area 6250 m x 23.7 m) is on the order of 100 mm/yr.

The vapor-density differences between different locations, together with a simple approximation of air flow in the tunnel, were used to estimate the moisture-removal rate and the equivalent evaporation rate. The weekly rates of amount of water removed by ventilation were a substantial fraction of water used in the tunnel. The estimated equivalent evaporation rates were on the order of 200 mm/yr, with standard deviation over 90 mm/yr, for both the Topopah Spring welded tuff units in a 1400-m section centered at Alcove 5 (the thermal test alcove) and the Paintbrush nonwelded units in a 380-m section between Alcove 3 and Alcove 4. The uncertainties were related to fluctuations in the moisture conditions introduced by construction activities, including air ventilation and water usage.

The equivalent evaporation rate over 100 mm/yr was an order of magnitude larger than the ambient percolation flux. The large evaporation rate could suppress the observations of active seeps and contribute to the apparent dry tunnel conditions. Rock temperatures near the TBM were observed to change spatially and temporally and could be related to evaporation from rock surfaces. Water potentials near the rock surfaces were measured with heat dissipation probes, and potential profiles along boreholes were measured by psychrometers in niches and alcoves along the ESF Main Drift and along the Cross Drift, as summarized in [Table 25](#). Field measurements in boreholes and laboratory measurements of physical and hydrologic properties of cores were conducted to measure saturation distributions, as summarized in [Table 26](#) and Section 6.8. The dry-out zones could extend nominally 1 to 3 m into the walls, with fractures and faults likely extending the depths of drying influence.

The advances of the ESF tunnel excavations were detected pneumatically by sensors in 10 surface-based boreholes within 200 m of the ESF. In comparison to the damping of barometric signals from the ground surface, less attenuation and phase lag were observed for signals from the ESF. For the borehole NRG-7a, within 30 m in horizontal distance from the ESF tunnel, the changes of water potential could also be related to the ESF dry-out (See last entry of [Table 25](#) for DTNs of surface-based boreholes.)

The main effects of ESF ventilation are the drying of rocks around the tunnel, the suppression of potential seepage into tunnels, and the perturbation of the gas flow field around the tunnel. Niche 3566, Alcove 7, and the last section of the Cross Drift, are closed for long time periods to gain additional information on the rewetting processes and potential seepage events. Both the data collected during active ventilation phases and passive nonventilation phases would contribute to the assessment of UZ responses to large-scale perturbations at Yucca Mountain.

6.10.2.2 Cross Drift Observations

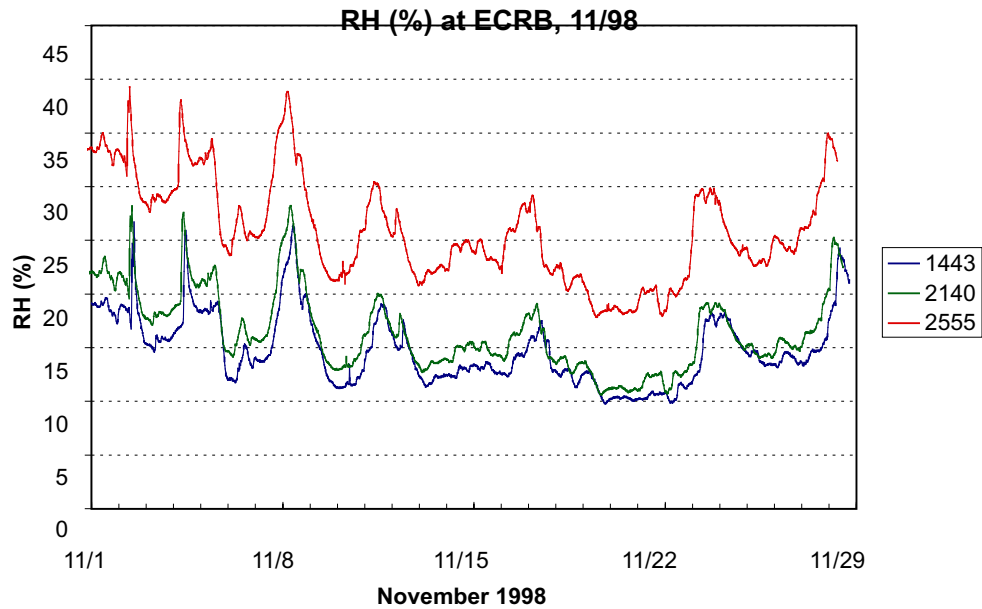
The drift conditions at the Cross Drift in 1998 were similar to the conditions of the ESF Main Drift in 1996. High-humidity conditions existed in the new sections just excavated. Relative humidity data from three moisture stations in the Cross Drift are illustrated in [Figures 74 and 75](#)

for the month of November, 1998, right after the completion of the excavation by the TBM. The moisture sensor assembly at Cross Drift Construction Station (CDCS) 25+55 (2,555 meters from the Cross Drift entrance) are located near the Solitario Canyon fault on the western boundary of the potential repository block. The other two stations, at CDCSs 14+43 and 21+40, measured the moisture conditions in the middle part of the Cross Drift within the potential repository block.

The figures illustrate the temporal fluctuations and the spatial distributions of moisture conditions along the Cross Drift. The data were collected every 15 minutes. CDCS 25+55 was much more humid than the other two stations under the control of the same ventilation system. The day shifts had more activities than the other two shifts. During the week of Thanksgiving holiday (November 26, 1998), there were increases in moisture conditions that might be correlated with ventilation shut down. The monthly averaged relative-humidity values are $15 \pm 3\%$ for CDCS 14 + 43, $18 \pm 4\%$ for CDCS 21 + 40, and $28 \pm 5\%$ for CDCS 25 + 55.

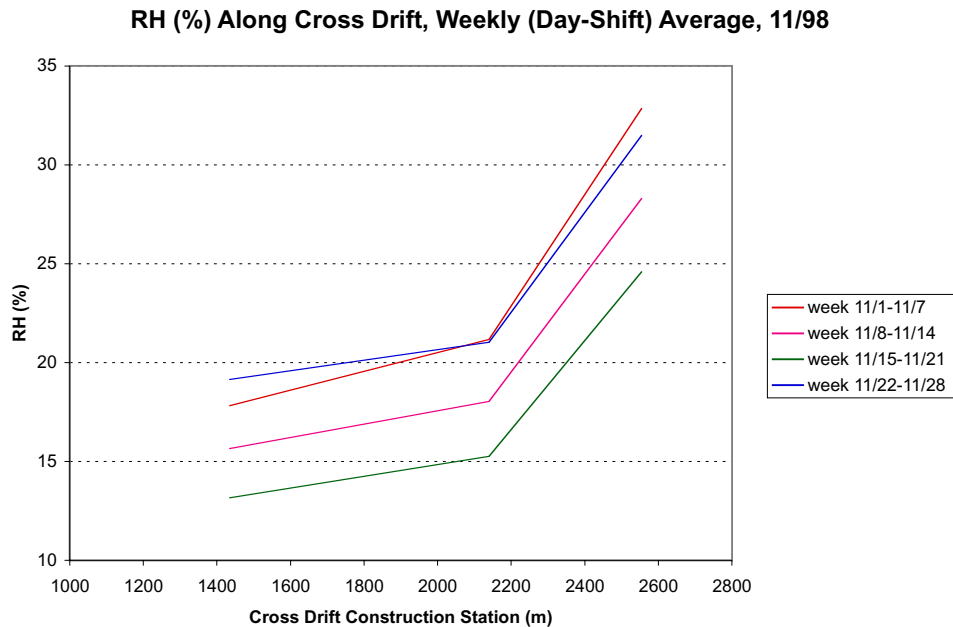
The spatial variations illustrated in [Figure 75](#) are based on weekly averaging over the day shifts. The differences in relative humidity are more clearly shown with the spatial distribution plot. While the magnitude varies from week to week, the spatial gradients were relatively constant. The average gradients for the two sections were 3.4% per kilometer between CDCSs 14+35 and 21+40, and 25.2% per kilometer between CDCSs 21+40 and 25+55. The section near the end of the tunnel apparently had more moisture removed than the section near the entrance.

The temporal and spatial distributions are presented to illustrate the characteristics of the moisture evolution in a newly excavated tunnel. Moisture gradients, together with the ventilation rates, are needed to calculate the moisture removal rates. The Cross Drift is a simple tunnel system in comparison with the ESF Main Drift. There is only one ventilation line operating along the Cross Drift, without any secondary branches separating the air flows into side alcoves and niches.



DTN: LB990901233124.006

Figure 74. Relative Humidity Temporal Variations in the Cross Drift. The data were collected in November, 1998 after completion of excavation. The legends are the distances in meters from the moisture station to the Cross Drift entrance.



DTN: LB990901233124.006

Figure 75. Relative Humidity Spatial Variations along the Cross Drift. The weekly averages of day shift data are presented for November 1998 after completion of excavation.

7. SUMMARY AND CONCLUSIONS OF AMBIENT FIELD TESTING ANALYSES

Since the inception of the ambient field testing program in 1995 during the excavation of the ESF, progress was made in drift seepage studies of four niches, fracture/fault flow testing in two alcoves, and wetting-front and moisture monitoring along the ESF drifts. This AMR U0015 focuses on *in situ* field testing of processes. The technical summary and conclusions for analyses in Sections 6.1 through 6.10 are given in Sections 7.1 through 7.10. In brief, the key findings include:

- Seepage thresholds were established, with measured values at Niche 3650 ranging from the equivalent flux of 200 mm/yr to 136,000 mm/yr for flow paths through fractures and fracture network. Fracture characteristic curves were derived from the seepage threshold data with the effective fracture porosity as high as 2.4%.
- Heterogeneity was systematically evaluated, with borehole-scale and drift-scale distributions and excavation-induced enhancements of permeability variations orders of magnitude larger than the site-to-site variations of average values along the main drift.
- Dyes and nonreactive tracers were confined locally (within 1.0 m × 1.6 m area for the last test) near the liquid-release points above the niche ceiling.
- Flow partitioning data with 92% fracture flow and 8% matrix flow were derived from independent analyses of seepage water and dye-stained rock samples. The water front moved much deeper into tuff matrix than inferred from measurements with nonreactive bromide tracer and sorbing dye tracers.
- Fracture flow paths were spatially heterogeneous and discrete in TSw. Fault zone flow paths and nonwelded tuff layers contributed to the complexity of pneumatic responses in PTn, with an argillic layer dampened the pneumatic responses effectively.
- Fracture flows in TSw were intermittent in nature even when the flow boundary conditions were stable.
- Fault and matrix flows in PTn had large capacities to accommodate damping of infiltration pulses.
- Rock dry-out zones were shown to extend approximately 3 m into the tunnel wall, construction water was detected nearly 10 m below the invert, and large changes in relative humidity conditions could be related to moisture removal by ventilation.

These findings are inputs to other AMRs and to the UZ flow and transport PMR. The AMRs are identified in the following list on the current field status of testing and monitoring activities at different sites in the ESF. The list includes many other laboratory studies on samples collected in the ESF and field studies analyzed in other AMRs.

- Extensive pneumatic air-permeability tests were conducted in borehole clusters before and after niche excavation, and in alcove test beds before liquid releases. The test results are inputs to the AMR on the seepage calibration model, the AMR on hydrologic data, and the AMR on abstraction of drift seepage.
- Niche 3566, in the vicinity of the Sundance fault, is currently sealed. The first damp feature in the potential repository horizon was observed in this niche.
- Niche 3650, in a fractured setting away from faults, had over 40 liquid-release tests conducted to quantify seepage thresholds. The core samples from the latest test were analyzed for tracer distribution. The test results are inputs to the AMR on the seepage calibration model, the AMR on hydrologic data, and the AMR on UZ flow models and submodels.
- Niche 3107 in a relatively uniform rock mass, below the cross-over point between the ESF Main Drift and Cross Drift, is the site of ongoing liquid-release tests to quantify the seepage-memory effects.
- Niche 4788, in an intensely fractured zone, has phases of pre- and post-excavation characterization completed and the seepage testing initiated.
- Alcove 6, in a fractured zone with relatively competent matrix blocks, has been used for a preliminary series of tests, with water dripped into a slot below the test bed collected. The test results can be used to compare with the fracture flow fractions predicted by the AMR on UZ flow models and submodels.
- Alcove 4, in a layered zone with a fault bounded by porous PTn, has been used for a preliminary series of tests, with a new series of tests planned to evaluate the migration of injected water. The test results can be used to evaluate the lateral diversion at the PTn addressed by the AMR on UZ flow models and submodels.
- Alcove 1, 30 m below the ground surface near the North Portal in the Tiva Canyon welded tuff unit, is the site for the largest liquid-release tests at the ESF. The test results from two series of flow and tracer tests are analyzed in the AMR on UZ flow models and submodels. Matrix diffusion is shown to be important in diluting the tracer concentration and reducing the tracer breakthrough at the Alcove 1 test site.
- Water-potential measurements with heat dissipation probes, with psychrometers, and with tensiometer are conducted in ESF boreholes at alcoves, at niches, and systematically along the ECRB Cross Drift. The recent results of potential data from ECRB are inputs to the AMR on calibrated property model.
- Construction-water migration was monitored at the starter tunnel of the Cross Drift and below the cross-over point. Early data on the distributions of lithium bromide tracers from boreholes drilled into the drift floor (invert) are inputs to the Yucca Mountain site description document.

- Chloride-36, chloride, calcite, strontium, and other geochemical analyses are reported in the AMR on geochemistry data and the AMR on transport properties data. The uses of geochemistry and transport properties data for model calibration and validation are reported in the AMR on UZ flow models and submodels and the AMR on radionuclide transport model.
- Moisture-monitoring stations continue to collect data to evaluate the impact of tunnel ventilation and moisture removal.

The ambient testing program is conducting additional tests to collect data in the lower tuff units and to confirm, validate, refine, or refute existing and alternative conceptual models for seepage into drifts, fracture flow, fracture-matrix interaction, and drainage and migration below the potential repository. With most of the potential repository horizon in the lower lithophysal unit of the TSw, it is critical to characterize this unit to determine if the presence of lithophysal cavities and friable tuff media change the seepage distributions and percolation characteristics. The seepage threshold quantification needs to be confirmed with long-term tests to address the concerns about the capillary barrier concept under steady-state conditions, the effects of evaporation, and the effects of moisture storage and flow diversion capacities. Quantification of spatial distribution of fast flow paths and assessment of temporal variations of episodic percolation events require testing and monitoring refinements for *in situ* conditions.

The following field activities are in progress:

- Niche 1620 (along the Cross Drift): Seepage testing in lower lithophysal unit, along with studies of excavation effects by pneumatic air-permeability tests, and fracture-matrix interaction tests.
- Systematic testing along the Cross Drift with pulsed air injections and liquid releases in slanted boreholes drilled into the crown along the Cross Drift.
- Drift-to-drift study with liquid released in Alcove 8 in the Cross Drift and wetting front monitored in Niche 3107 and in the ESF Main Drift at the cross-over point.
- Potential measurements along the Cross Drift and behind the bulkheads which are currently closed to induce rewetting.

The emphasis of this AMR is on active-flow testing in niches and alcoves. These activities, together with many other laboratory and field activities analyzed in other AMRs, provide data for inputs to other modeling AMRs and to the UZ flow and transport model for process evaluation, calibration, and validation. Since different activities and analyses for *in situ* field testing in processes are in different stages of progress, the summaries of test analyses presented in the following ten sections are in the different degrees of maturity. Section 7.n is the summary of data analyses in Section 6.n, with $n = 1, \dots, 10$. The data are summarized with minimal speculative interpretations. Credible interpretations can be achieved with close interactions

between testing and modeling, as documented in the AMRs cited, and on an activity-by-activity basis.

This document may be affected by technical product input information that requires confirmation. Any changes to the document that may occur as a result of completing the confirmation activities will be reflected in subsequent revisions. The status of the input information quality may be confirmed by review of the DIRS database.

7.1 SUMMARY OF AIR-PERMEABILITY DISTRIBUTION AND EXCAVATION-INDUCED ENHANCEMENT IN NICHES

Using the pneumatic packer system developed with automated controls and data acquisition, extensive series of air-permeability tests were systematically conducted in borehole clusters at four niches. Single-hole permeability data has proven its use in detecting changes in permeability (and boundary conditions) as a result of nearby excavation and in characterizing sites. Pre-excavation and post-excavation permeability profiles with 0.3-m spatial resolution are presented for boreholes used for drift-seepage and liquid-release tests. Air-permeability distributions are used as inputs for the seepage calibration model to assess the capillary barrier and seepage threshold mechanisms. Fractures immediately above the niches are important to the evaluation of seepage into drifts. The main results from air-permeability profile and distribution analyses are:

- The excavation-induced permeability enhancements in borehole intervals are large, with the average enhancements for boreholes in one to two orders of magnitude.
- Drift-scale variation of permeability values and permeability enhancement along boreholes and among different boreholes within the niches are larger than differences among different niche sites.

It is important in drift-scale assessment to characterize the permeability distributions controlling local flow path and seepage spatial variation. The relatively small difference in mean permeability values for different niches is encouraging in the reduction of uncertainties associated with site-scale spatial heterogeneity. If subsequent liquid-seepage tests in locally distinct niches result in seepage threshold values within a relatively narrow range, the uncertainties for seepage into drifts could be greatly reduced for the middle nonlithophysal unit of TSw, where all existing niches were located. The characterization effort is planned for the lower tuff units to acquire the necessary data for the majority of the potential repository horizon area.

7.2 CONCLUSIONS OF LIQUID-RELEASE AND SEEPAGE TESTS IN NICHES

7.2.1 Pre-Excavation Liquid-Release Testing and Niche Excavation Activities

Numerous liquid-release tests were conducted prior to the excavation of each niche to evaluate how far a finite pulse of water would travel through relatively undisturbed fractures located in the middle nonlithophysal zone of the Topopah Spring welded unit.

The maximum depth that the wetting front moves increases with increasing mass of fluid injected. It appears that maximum-depth data cannot discriminate the type of flow (i.e., high-angle fracture versus network flow) observed during the test. Lateral spreading and the aspect ratio (i.e., ratio of depth to lateral spreading) may be stronger measures of the type of flow that predominates. Increased lateral spreading of the wetting front appears to be typical of well-connected fracture networks containing both high- and low-angle fractures, whereas large aspect ratios appear to be typical of flow in individual vertical fractures.

7.2.2 Post-Excavation Seepage Tests at Niche 3650

The purpose of the seepage tests was to investigate the amount of water that would drip into a mined opening from a transient liquid-release event of short duration.

- Forty post-excavation liquid-release tests were conducted on 16 different test intervals located above Niche 3650 within the middle nonlithophysal zone of the Topopah Spring welded unit.
- Of the 16 zones tested, water seeped into the capture system from 10 intervals, water appeared at the niche ceiling but did not drip in 3 cases, and water did not appear at all when introduced into the three remaining zones.
- The seepage percentage, defined as the amount of water captured in the niche divided by the amount released into the rock, ranged from 0 to 56.2%.

It was determined during the early stages of testing that the memory effect, or wetting history, had a profound impact on seepage. If the liquid-release tests were performed too close together in time, then it was found that the seepage percentage increased dramatically, as one would expect. This is because the fractures contained residual moisture, and their unsaturated conductivity was higher during subsequent tests. The test with seepage percentage of 56.2%, the third test in a series of four tests in the same interval, was conducted within 2 hours after the second test with 23.2% seepage. In comparison, the first test conducted 20 days before the second test had a fairly consistent result of 22.6% seepage.

The seepage threshold flux, defined as the flux of water that when introduced into the injection borehole results in zero seepage, was evaluated for the 10 zones that seeped in Section 6.2.2.1.

- The seepage threshold fluxes measured at Niche 3650 range from 6.35E-09 to 4.31E-06 m/s or 200 to 136,000 mm/yr.

The seepage threshold data were evaluated and interpreted using analytical techniques derived for a homogenous, unsaturated porous medium derived by Philip et al. (1989) subject to the limiting assumptions discussed in Section 5.2.2. The analysis resulted in realistic values of the sorptive number (α), an exponential fitting parameter characteristic of the capillary strength of the fractures.

- Values for α^{-1} equal to 9.8 and 490 Pa were measured for representing flow through two types of *in situ* fractures, including high-angle fractures and a network of interconnected fractures, respectively.

Two types of flow paths were observed in the field during the mining operation, as described in Section 6.2.1.2. Estimates of the volumetric water content were produced in Section 6.2.2.3 using wetting front arrival times recorded during the seepage tests. The α -values resulting from the analyses performed in Section 6.2.2.2 were used to estimate the water potentials of the fractures reported in Section 6.2.2.4. Water-potential estimates and the corresponding volumetric water contents were used to construct the fracture-water retention curves presented in Section 6.2.2.5. Examination of these plots indicates that:

- Fractures appear to drain very quickly, approaching a residual water content of perhaps 0.1 to 0.2% at water potentials as high as -0.01 m.
- Saturated water content or effective fracture porosity may be as high as 2.4%.

7.2.3 Constraints, Caveats, and Limitations of the Niche Seepage Test Results

The seepage test results at Niche 3566, including the determinations of the seepage thresholds, are based on multiple liquid release tests conducted over short duration with some of the rates high enough to induce artificial seepage. The tests were conducted in open niche conditions with the humidity affected by the ventilation in the tunnel. The effects of evaporation can remove water from the rock through the vapor phase and may reduce the liquid seepage flux in determining the seepage threshold.

The ongoing tests at other niches are conducted over longer test periods, with some at lower release rates and under better control of ventilation and humidity effects. The same approaches will be used in tests at the lower lithophysal TSw unit. The constraints, caveats, and limitations of the currently available seepage test results from one niche in the middle nonlithophysal TSw unit should be carefully evaluated to assess the applicability in future use.

7.3 CONCLUSIONS OF TRACER-MIGRATION DELINATION AT NICHE 3650

Tracer distribution in cores around a liquid-release event at Niche 3650 was analyzed. The results showed that:

- The tracer migration from the latest test was localized and possibly confined within the 1.0 m \times 1.6 m area directly below the liquid-release interval, with a vertical scale of about 0.7 m. This result is based mainly on analyses of iodine as a conservative tracer.
- Spatial distributions of other dye tracers resulting from early liquid-release tests consistently point to localized flow with limited lateral spreading of tracer migration. The previous liquid release and seepage tests with dyes were conducted over six months before the latest test.

Liquid-release tests reported in Section 6.2 indicated that post-excavation seepage water was captured in most cases directly beneath the test zone or in capture cells immediately adjacent to the interval. Flow-path observations during niche excavations generally showed that the dyes did not spread laterally to great extents (also see Section 6.2 and preliminary results of Niches 3566 and 3650 reported in Wang et al. 1999, pp. 329–332). Gravity-driven flow is the primary flow

mechanism in fracture systems, either through individual fractures and/or through the fracture network connected to the release intervals. In Section 6.4 of this report, further laboratory tests of tracer sorption and fracture-matrix interactions are presented.

The absence of nonreactive tracers, especially iodine introduced only at the latest pulse release, together with the localized spatial distributions of dyes long after the liquid releases, strongly suggested that the gravity-driven component was strong. Capillary imbibition and capillary barrier effects could promote lateral spreading. Longer-term tests with sampling over larger areas than the latest pulse test, as well as early liquid-release tests, could further quantify the migration and retention of tracers. Tracer-test results could be used to investigate the occurrence and significance of localized flow and to assess the mechanisms governing contaminant transport.

7.4 SUMMARY AND CONCLUSIONS ON TRACER PENETRATION AND WATER IMBIBITION INTO WELDED TUFF MATRIX

Field and laboratory tracer experiments have been conducted to investigate the flow partitioning between fracture flow and matrix imbibition in unsaturated conditions. During niche excavation, dye-stained rock samples were collected for laboratory analyses. Additional tuff samples collected from the potential repository horizon were machined as rock cores for laboratory studies of tracer penetration into the rock matrix under two initial water saturations. In the drift seepage tests using dye tracers, seepage-water samples were collected. A rock-drilling and sampling technique was developed to profile the tracer concentration in the rock matrix over distance.

- For rock samples, the sorbing dye-tracer penetration depths are on the order of several millimeters from the flowing fractures.
- In well-controlled laboratory tracer-imbibition tests under both high and low initial water saturations, the concentration profiles of sorbing dyes lag behind the nonreactive bromide front, with the travel distance for dyes being a few millimeters over the contact time of about 18 hours.
- The bromide front lags significantly behind the moisture front at high initial water saturation of 75.8%. On the contrary, the front is comparable to the moisture front in the rock core at the initial water saturation of 12.5%.
- Retardation of sorbing tracers increases with a decrease in saturation, as measured in the dry core and in the wet core, verifying the functional relationship between retardation and water content.
- Core measurements can be used to measure retardation factors in *in situ* conditions to check the results of batch experiments using crushed tuff in saturated conditions.
- The flow partitioning data with 92% fracture flow and 8% matrix imbibition were derived independently from seepage water sampled in drift seepage tests conducted after niche excavation and laboratory analyses of dye-stained samples collected during niche excavation.

Data presented in Section 6.4 revealed interesting processes, especially at the interface boundary region between the core bottom and the water reservoir, simulating the contact of flowing fracture with adjoining tuff matrix. Data of flow partitioning, front separation, and tracer retardation can be used for validation of fracture-matrix interaction and fracture flow models.

7.5 SUMMARY OF SINGLE-HOLE PERMEABILITY DISTRIBUTIONS AND CROSS-HOLE CONNECTIVITY ANALYSES

Cross-hole analyses of pneumatic air-permeability test data are presented for Niche 4788, Alcove 6, and Alcove 4. Cross-hole connectivity analyses for Niche 4788 are used in the seepage tests in this intensely fractured zone. The pneumatic air-permeability test results were used for interval selection and test interpretation in the series of tests conducted for fracture flows and fracture-matrix interactions in TSw at Alcove 6 and for fault and matrix flows in PTn in Alcove 4. The main results from permeability distribution and cross-hole analyses are:

- Welded-tuff test sites have distinct flow paths clearly identified by cross-hole analyses from isolated injection intervals to observation intervals.
- The fracture flow connections are predominately one-way, with an injection interval inducing response in an observation interval, but the interval not necessarily detecting injection into the original observation interval.
- The PTn test bed in Alcove 4 has many more connections than the corresponding TSw sites in niches and in Alcove 6. Weaker connections were trimmed out to reveal the stronger connections.
- The argillic layer in the test bed was shown from cross-hole analyses to be a nearly impermeable barrier.
- Stronger connections were associated with a fault in the test bed at Alcove 4. A high-permeability zone near the end of the test block was identified by the air-permeability results and cross-hole analyses.

7.6 CONCLUSIONS OF FRACTURE FLOW IN FRACTURE-MATRIX TEST BED AT ALCOVE 6

Fracture flow data were collected in a slotted test bed located at Alcove 6 of ESF within the TSw. With a slot below injection zones, it was possible to quantify both the inflow into the system and outflow at the lower boundary, and to better evaluate the flow field in underground test conditions.

In this field study, techniques developed to investigate flow in fractured welded tuffs were evaluated. Results from field tests suggest that *in situ* characterization of certain fundamental flow parameters (such as travel times, percolation and seepage rates, etc.) can be achieved with this approach.

The test results revealed aspects of flow in unsaturated, fractured systems and provided insight towards the conceptualization of flow through unsaturated and fractured rock formations. The Alcove 6 test is the first and only test conducted in the ESF on unsaturated fractured tuff with attempts to take liquid mass conservation explicitly into account. In field tests, it is frequently difficult to control the boundaries and liquid can flow to unknown domains. Transient data collected at Alcove 6 also contribute to the evaluation of unsaturated flow in fractured tuffs. Some of the test result interpretations require additional analyses and modeling. The main focus currently is to present the data and to stimulate credible, not speculative, interpretations.

Several series of liquid-release tests were conducted with localized injections of liquid into a low permeability zone and into a high permeability zone along a borehole. The major test results were:

- For all injections into both LPZ and HPZ, changes in electrical resistance and psychrometer readings were detected in two monitoring boreholes ~0.6 m below the point of injection.
- For the LPZ tests, water did not seep into the slot located 1.65 m below.
- Liquid-release rate into the LPZ was observed to steadily decrease by two orders of magnitude (from >30 to < 0.1 ml/minute) over a period of 24 hours.
- In the HPZ, liquid-release rates under constant-head conditions were significantly higher (~100 ml/minute), with intermittent changes observed in the intake rate.
- For injection tests in HPZ, water was observed to drip into the slot in 3 to 7 minutes at high injection rates of ~28 to ~100 ml/min, in 1 hour at the low injection rate of 14 ml/min, and in 5 hours at the lowest rate of 5 ml/min.
- During the course of each test, seepage rates measured in the slot showed intermittent responses despite constant-head or constant-rate conditions imposed at the input boundary.
- The percentage of cumulative volume of water recovered in the slot was observed to increase in most tests, approaching steady-state values after ~10 liters of water had been injected.
- A maximum of 80% of the injected water was recovered for high-rate injection tests.
- The saturated volumes of fracture flow paths were estimated for each test from measurements of fluid volume before wetting front arrivals and from measurements of drainage volume into the slot after termination of injection. The flow path volumes were found to increase from <0.2 liter initially to ~1.0 liter during recovery, with some stepped increments of 0.1 to 0.3 liter observed.
- Plug flow process was observed with tracer analyses. "New" water replaced "old" water from the previous test.

The stepped and intermittent changes could be associated with heterogeneous distribution of storage volumes in the connected fracture flow paths, in the dead-end fractures, and in the rock matrix blocks. The test results from Alcove 6 could be used to evaluate fracture flows and fracture-matrix interactions.

7.7 CONCLUSIONS OF FLOW THROUGH THE FAULT AND MATRIX IN THE TEST BED AT ALCOVE 4

Fault and matrix flow data were collected in a test bed located in the PTn at Alcove 4 in the ESF. Using a series of horizontal boreholes, the intake rates and plume travel times in various locations within the test bed were determined.

These test results revealed aspects of flow in a fault located within the nonwelded tuffs and provided insights into the flow properties of the PTn. A series of localized liquid-release tests helped determine that:

- Intake rates within a fault located in the PTn decreased as more water was introduced into the release zone (i.e., from an initial value of ~200 ml/min to ~50 ml/min after 193 liters of water entered the injection zone).
- The travel time of the wetting front resulting from water released in the fault decreased when the fault was wet (i.e., in closely timed tests, the plume traveled faster in subsequent releases).
- Over time, the hydrologic properties of the fault appear to be altered, with water traveling along the fault at significantly slower rates.
- The matrix adjacent to the fault imbibed water that was introduced into the fault. Changes in saturation were seen more than 1.0 m from the point of release.
- The intake rates and wetting front travel times in the matrix were significantly slower than in the fault. Water released into the matrix was observed to travel 0.45 m in 14 days.

7.8 CONCLUSIONS OF WATER-POTENTIAL MEASUREMENTS IN THE NICHES

Psychrometer measurements in the ESF suggest that significant variability in water potentials between and within the three niches. The main observations are:

- The extent to which ventilation effects may have penetrated the rock is possibly greater than 3 m.
- Two possible zones were observed to have significantly high water potentials in Niche 3566. The first was observed at the end of the middle borehole. The second was detected 6.25 m along borehole A in Niche 3566. Borehole A was drilled from the niche toward the Sundance fault.

- There was large variability (-15 and -84 m) in the short distance of 0.9 m between two boreholes at Niche 3107.
- In the zone beyond where ventilation effects of the ESF were observed (i.e., at 10 m depths), Niche 3566 (with potential 0.4 to -13 m) appeared to be wetter than Niche 3650 (with potential -1 to -39 m).

These potential measurements were conducted before the bulkhead closed in Niche 3566 and before seepage measurements in Niches 3650 and 3107. The data are presented for future comparisons with potential measurements elsewhere in the ESF, including the Cross Drift.

7.9 CONCLUSIONS OF MONITORING THE CONSTRUCTION-WATER MIGRATION

While no seepage was observed in the ESF Main Drift at the cross-over point, the sensors in a borehole below the starter tunnel of the Cross Drift detected signals associated with wetting-front migration.

7.9.1 Starter Tunnel

- Three events were observed along the borehole below the starter tunnel at depths close to 10 m. The ponding event that occurred on March 8, 1998 increased water-potential values up to a depth of 8.65 m (17.3 m along the borehole). During this event, the magnitude of the disturbance decreased further into the borehole, with an interesting aberration observed at a depth of 9.4 m: the change in water potentials was significantly larger than the expected trend.
- At different times during the monitoring period, the impact on changes in water-potential values occurred at different locations along the borehole. Early in March 1998, the large impacts were restricted to close to the borehole collar, while by early April, 1998 these impacts were relatively larger — between 9.4 and 11.4 m.
- One concern that could arise from the use of a slanting borehole to measure wetting front migration is the possibility of the bore cavity short-circuiting flow paths. For this particular investigation, this short-circuiting does not appear to be happening, as indicated by the analysis of recovery responses observed at the depth of 5.2 m. Here, the response to a wetting event was negligible when compared with other psychrometers close to this location (above and below), suggesting that this zone was well isolated (hydraulically) from the adjacent zones and did not detect the wetting front.
- The response of the electrical resistivity probes when compared with the performance of psychrometers suggests that these probes (with their current design) can be effectively used as a qualitative tool to detect the arrival (or departure) of wetting fronts. Unlike psychrometers, these probes are relatively inexpensive, easy to maintain, and have a low failure rate. These advantages make them particularly useful for extensive down-hole monitoring applications in fractured-rock environments found at Yucca Mountain.

7.9.2 Monitoring of Cross-Over Point

- No seepage was observed nor were wetting-front signals detected at the cross-over point when the Cross Drift TBM passed over the ESF Main Drift. The TBM apparently did not use enough water to induce dripping into the Main Drift, 17.5 m below. The confirmation of no seepage at the cross-over point establishes the lower limit for the drift-to-drift flow and drift seepage processes associated with construction-water usage.

In the potential repository at Yucca Mountain, performance-confirmation drifts are planned to be located above (or below) the waste emplacement drifts to monitor the waste-induced impacts. It is therefore important to evaluate the drift-to-drift migration, drift seepage, and wetting-front detection to assess the potential impacts. The experience in the integrated monitoring station at the cross-over point (with seepage collection trays, water-potential and wetting-front sensors, and thermal/visual imaging devices) can be applied to future testing and monitoring tasks.

7.10 CONCLUSIONS OF ANALYSES OF CONSTRUCTION EFFECTS

Some observations of ESF moisture conditions are presented. From the observations:

- The newly excavated drift has high humidity conditions detected near the TBM.
- The relative humidity gradient near the end of the tunnel was greater than the gradient close to the entrance in the month after the excavation.

8. INPUTS AND REFERENCES

8.1 DOCUMENTS CITED

- Andreini, M.S. and Steenhuis, T.S. 1990. "Preferential Paths of Flow under Conventional and Conservation Tillage." *Geoderma*, 46, 85–102. Amsterdam, Netherlands: Elsevier Science. TIC: 245381.
- Barr, D.L.; Moyer, T.C.; Singleton, W.L.; Albin, A.L.; Lung, R.C.; Lee, A.C.; Beason, S.C.; and Eatman, G.L.W. 1996. *Geology of the North Ramp—Stations 4+00 to 28+00, Exploratory Studies Facility, Yucca Mountain Project, Yucca Mountain, Nevada*. Denver, Colorado: Bureau of Reclamation. ACC: MOL.19970106.0496.
- Braester, C. 1973. "Moisture Variation at the Soil Surface and the Advance of the Wetting Front During Infiltration at Constant Flux." *Water Resources Research*, 9 (3), 687–694. Washington, D.C.: American Geophysical Union. TIC: 242383.
- Buesch, D.C. and Spengler, R.W. 1998. "Character of the Middle Nonlithophysal Zone of the Topopah Spring Tuff at Yucca Mountain." *High-Level Radioactive Waste Management, Proceedings of the 8th International Conference, Las Vegas, Nevada, May 11–14, 1998*. La Grange Park, Illinois: American Nuclear Society. TIC: 237082.
- Buesch, D.C.; Spengler, R.W.; Moyer, T.C.; and Geslin, J.K. 1996. *Proposed Stratigraphic Nomenclature and Macroscopic Identification of Lithostratigraphic Units of the Paintbrush Group Exposed at Yucca Mountain, Nevada*. Open-File Report 94–469. Denver, Colorado: U.S. Geological Survey. ACC: MOL.19970205.0061.
- CRWMS M&O (Civilian Radioactive Waste Management System Management and Operating Contractor) 1999a. *Analysis & Modeling Development Plan (DP) for U0015 In Situ Field Testing of Processes, Rev 00*. TDP-NBS-HS-000006. Las Vegas, Nevada: CRWMS M&O. ACC: MOL.19990830.0377.
- CRWMS M&O 1999b. *M&O Site Investigations. Activity Evaluation*. Las Vegas, Nevada: CRWMS M&O. ACC: MOL.19990317.0330.
- CRWMS M&O 1999c. *M&O Site Investigations. Activity Evaluation*. Las Vegas, Nevada: CRWMS M&O. ACC: MOL.19990928.0224.
- DOE (U.S. Department of Energy) 1998a. "Total System Performance Assessment." Volume 3 of *Viability Assessment of a Repository at Yucca Mountain*. DOE/RW-0508. Washington, D.C.: U.S. Department of Energy, Office of Civilian Radioactive Waste Management. ACC: MOL.19981007.0030.
- DOE 1998b. "License Application Plan and Costs." Volume 4 of *Viability Assessment of a Repository at Yucca Mountain*. DOE/RW-0508. Washington, D.C.: U.S. Department of Energy, Office of Civilian Radioactive Waste Management. ACC: MOL.19981007.0031.

Dyer, J.R. 1999. "Revised Interim Guidance Pending Issuance of New U.S. Nuclear Regulatory Commission (NRC) Regulations (Revision 01, July 22, 1999), for Yucca Mountain, Nevada." Letter from J.R. Dyer (DOE) to D.R. Wilkins (CRWMS M&O), September 9, 1999, OL&RC:SB-1714, with enclosure, "Interim Guidance Pending Issuance of New U.S. Nuclear Regulatory Commission (NRC) Regulations (Revision 01)." ACC: MOL.19990910.0079.

Freeze, R.A. and Cherry, J.A. 1979. *Groundwater*. Englewood Cliffs, New Jersey: Prentice-Hall. TIC: 3476.

Ghuman, B.S. and Prihar, S.S. 1980. "Chloride Displacement by Water in Homogeneous Column of Three Soils." *Soil Science Society of America Journal*, 44 (1), 17–21. Madison, Wisconsin: Soil Science Society of America. TIC: 246698.

Klinkenberg, L.J. 1941. "The Permeability of Porous Media to Liquids and Gases." *API Drilling and Production Practice*, 200-213. Washington, DC: American Petroleum Institute. TIC: 217454.

LeCain, G.D. 1995. *Pneumatic Testing in 45-Degree-Inclined Boreholes in Ash-Flow Tuff near Superior, Arizona*. Water-Resources Investigations Report 95–4073. Denver, Colorado: U.S. Geological Survey. ACC: MOL.19960715.0083.

Moyer, T.C.; Geslin, J. K.; and Flint, L E. 1996. *Stratigraphic Relations and Hydrologic Properties of the Paintbrush Tuff Nonwelded (PTn) Hydrologic Unit, Yucca Mountain, Nevada*. Open-File Report 95–397. Denver, Colorado: U.S. Geological Survey TIC: 226213.

Muskat, M. 1982. *The Flow of Homogeneous Fluids Through Porous Media*. Boston, Massachusetts: International Human Resources Development. TIC: 208295.

Philip, J.R. 1985. "Reply to 'Comments on Steady Infiltration from Spherical Cavities.'" *Soil Science Society of America Journal*, 49, 788–789. Madison, Wisconsin: Soil Science Society of America. TIC: 240255.

Philip, J.R. 1986. "Linearized Unsteady Multidimensional Infiltration." *Water Resources Research*, 22 (12), 1717–1727. Washington, D.C.: American Geophysical Union. TIC: 239826.

Philip, J.R.; Knight, J.H.; and Waechter, R.T. 1989. "Unsaturated Seepage and Subterranean Holes: Conspectus, and Exclusion Problem for Circular Cylindrical Cavities." *Water Resources Research*, 25 (1), 16–28. Washington, D.C.: American Geophysical Union. TIC: 239117.

Porro, I. and Wierenga, P.J. 1993. "Transient and Steady-State Transport through a Large Unsaturated Soil Column." *Ground Water*, 31 (2), 193–200. Westerville, Ohio: National Ground Water Association. TIC: 246899.

Pullan, A.J. 1990. "The Quasilinear Approximation for Unsaturated Porous Media Flow." *Water Resources Research*, 26 (6), 1219–1234. Washington, D.C.: American Geophysical Union. TIC: 239824.

Selby, S.M., ed. 1975. *CRC Standard Mathematical Tables, 23rd edition*. Cleveland, Ohio: CRC Press. TIC: 247118.

Wang, J.S.Y. and Elsworth, D. 1999. "Permeability Changes Induced by Excavation in Fractured Tuff." *Rock Mechanics for Industry, Proceedings of the 37th U.S. Rock Mechanics Symposium, Vail, Colorado, June 6–9, 1999*, 2, 751–757. Alexandria, Virginia: The American Rock Mechanics Association. TIC: 245246.

Wang, J.S.Y.; Trautz, R.C.; Cook, P.J.; Finsterle, S.; James, A.L.; and Birkholzer, J. 1999. "Field Tests and Model Analyses of Seepage into Drift." *Journal Of Contaminant Hydrology*, 38 (1–3), 323–347. Amsterdam, Netherlands: Elsevier Science. TIC: 244160.

Warrick, A.W.; Biggar, J.W. and Nielsen, D.R. 1971. "Simultaneous Solute and Water Transfer for an Unsaturated Soil." *Water Resources Research* 7 (5), 1216–1225. Washington, D.C.: American Geophysical Union. TIC: 245674.

Wemheuer, R.F. 1999. "First Issue of FY00 NEPO QAP-2-0 Activity Evaluations." Interoffice correspondence from R.F. Wemheuer (CRWMS M&O) to R.A. Morgan (CRWMS M&O), October 1, 1999, LV.NEPO.RTPS.TAG.10/99-155, with attachments, Activity Evaluation for Work Package #1401213UM1. ACC: MOL.19991028.0162.

White, I. and Sully, M.J. 1987. "Macroscopic and Microscopic Capillary Length and Time Scales from Field Infiltration." *Water Resources Research*, 23 (8), 1514–1522. Washington, D.C.: American Geophysical Union. TIC: 239821.

SOFTWARE CITED

Macro/Routine: Perm Formula 1 ft Zone.vi V1.0. ACC: MOL.19991018.0188.

Macro/Routine: Mettler Double Scale 1.vi V1.0. ACC: MOL.19991018.0189.

Plotting Program: Earthvision V4.0. STN: 30035-2 V4.0.

8.2 CODES, STANDARDS, REGULATIONS, AND PROCEDURES

64 FR (Federal Register) 8640. Disposal of High-Level Radioactive Waste in a Proposed Geologic Repository at Yucca Mountain. Proposed rule 10 CFR (Code of Federal Regulations) 63. Readily available.

AP-SI.1Q, Rev. 1, ICN 0. *Software Management*. Washington, D.C.: U.S. Department of Energy, Office of Civilian Radioactive Waste Management. ACC: MOL.19990630.0395.

AP-3.10Q, Rev. 1, ICN 0. *Analyses and Models*. Washington, D.C.: U.S. Department of Energy, Office of Civilian Radioactive Waste Management. ACC: MOL.19990702.0314.

DOE 1998c. *Quality Assurance Requirements and Description*. DOE/RW-0333P, REV 8. Washington D.C.: DOE OCRWM. ACC: MOL.19980601.0022.

QAP-2-0, Rev. 5. *Conduct of Activities*. Las Vegas, Nevada: CRWMS M&O. ACC: MOL.19980826.0209

YAP-12.3Q, Rev. 0. *Control of Measuring and Test Equipment and Calibration Standards*. Las Vegas, Nevada: Yucca Mountain Site Characterization Office. ACC: MOL.19990729.0230

8.3 SOURCE DATA, LISTED BY DATA TRACKING NUMBER

GS960908314224.020. Analysis Report: Geology of the North Ramp - Stations 4+00 to 28+00 and Data: Detailed Line Survey and Full-Periphery Geotechnical Map - Alcoves 3 (UPCA) and 4 (LPCA), and Comparative Geologic Cross Section - Stations 0+60 to 28+00. Submittal date: 09/09/1996.

LB960800831224.001. Relative Humidity, Temperature, and Pressure in ESF Monitoring Stations. Submittal date: 08/23/1996.

LB970300831224.001. Moisture Data Report from October, 1996 to January, 1997. Submittal date: 03/13/1997.

LB970801233124.001. Moisture Monitoring Data Collected at ESF Sensor Stations. Submittal date: 08/27/1997.

LB970901233124.002. Moisture Monitoring Data Collected at Stationary Moisture Stations. Submittal date: 09/30/1997.

LB980001233124.001. Water Potential Measurements in Niches 3566, 3650, and 3107 of the ESF. Submittal date: 04/23/1998.

LB980001233124.002. Air Permeability Testing in Niches 3566 and 3650. Submittal date: 04/23/1998.

LB980001233124.004. Liquid Release Test Data From Niche 3566 and Niche 3650 of the ESF in Milestone Report, "Drift Seepage Test and Niche Moisture Study: Phase I Report on Flux Threshold Determination, Air Permeability Distribution, and Water Potential Measurement.". Submittal date: 11/23/1999.

LB980101233124.001. Data collected from Niche at Construction Station 3650. Submittal date: 01/30/1998.

LB980101233124.002. Post-Excavation Permeability Data Collected from Niche 3650 of the ESF. Submittal date: 11/04/1998.

LB980901233124.002. Laboratory Imbibition, Tracer, and Seepage Tests in Niches 3566, 3650, 3107, and 4788 in the ESF. Submittal date: 09/14/1998.

LB980901233124.003. Liquid Release and Tracer Tests in Niches 3566, 3650, 3107, and 4788. Submittal date: 09/14/1998.

LB980901233124.004. Pneumatic Pressure and Air Permeability Data from Alcove 6 in the ESF. Submittal date: 09/14/1998.

LB980901233124.009. Pneumatic Pressure and Air Permeability Data from Alcove 4 in the ESF. Submittal date: 09/14/1998.

LB980901233124.014. Borehole Monitoring at the Single Borehole in the ECRB and ECRB Crossover Point in the ESF. Submittal date: 09/14/1998.

LB980901233124.101. Pneumatic Pressure and Air Permeability Data from Niche 3107 and Niche 4788 in the ESF from Chapter 2 of Report SP33PBM4: Fracture Flow and Seepage Testing in the ESF, FY98. Submittal date: 11/23/1999.

LB980912332245.001. Air Injection Data from Niche 3107 of the ESF. Submittal date: 09/30/1998.

LB990601233124.001. Seepage Data Feed to UZ Drift-Scale Flow Model for TSPA-SR. (Pneumatic pressure and air permeability data.) Submittal date: 06/18/1999.

LB990601233124.002. Seepage Data Feed to UZ Drift-Scale Flow Model for TSPA-SR. (Drift seepage testing.) Submittal date: 06/18/1999.

LB990601233124.003. Seepage Data Feed to UZ Drift-Scale Flow Model for TSPA-SR. (Tracer detection data.) Submittal date: 06/18/1999.

8.4 OUTPUT DATA, LISTED BY DATA TRACKING NUMBER

LB990901233124.001. Alcove 6 Tracer Tests for AMR U0015, "In Situ Field Testing of Processes." Submittal date: 11/01/1999.

LB990901233124.002. Alcove 6 Flow Data for AMR U0015, "In Situ Field Testing of Processes." Submittal date: 11/01/1999.

LB990901233124.003. Tracer Lab Analyses of Dye Penetration in Niches 3650 and 4788 of the ESF for AMR U0015, "In Situ Field Testing of Processes." Submittal date: 11/01/1999.

LB990901233124.004. Air Permeability Cross-Hole Connectivity in Alcove 6, Alcove 4, and Niche 4 of the ESF for AMR U0015, "In Situ Testing of Field Processes." Submittal date: 11/01/1999.

LB990901233124.005. Alcove 4 Flow Data for AMR U0015, "In Situ Field Testing of Processes." Submittal date: 11/01/1999.

LB990901233124.006. Moisture Data from the ECRB Cross Drift for AMR U0015, "In Situ Testing of Field Processes." Submittal date: 11/01/1999.

8.5 SUPPORTING DOCUMENTS

Finsterle, S.; James, A.L.; Ritcey, A.C. and Wang, J.S.Y. 1998. *Model Prediction of Cross-Drift Impact on Moisture*. Yucca Mountain Project Level 4 Milestone SP33T1M4. Berkeley, California: Lawrence Berkeley National Laboratory. ACC: MOL.19980507.0177.

Finsterle, S.; James, A.L.; Wang, J.S.Y.; Fabryka-Martin, J.T.; Wolfsberg, L.E.; Flint, A.; and Guertal, W.R. 1998. *Model Prediction of Local Plume Migration From the Cross Drift*. Yucca Mountain Project Level 4 Milestone SP33S3M4. Berkeley, California: Lawrence Berkeley National Laboratory. ACC: MOL.19980507.0177.

Wang, J.S.Y.; Flint, A.L.; Nitao, J.J.; Chesnut, D.A.; Cook, P.; Cook, N.W.G.; Birkholzer, J.; Freifeld, B.; Flint, L.E.; Ellet, K.; Mitchell, A.J.; Homuth, E.F.; Griego, G.J.; Cerny, J.A.; and Johnson, C.L. 1996. *Evaluation of Moisture Evolution in the Exploratory Studies Facility*. Yucca Mountain Project Level 3 Milestone TR31K6M. Berkeley, California: Lawrence Berkeley National Laboratory. ACC: MOL.19961231.0089. DTN: LB960800831224.001 (Q).

Wang, J.S.Y. 1996. *Moisture Data Report for July to September 1996*. Yucca Mountain Project Level 4 Milestone M4-TR31K7M. Berkeley, California: Lawrence Berkeley National Laboratory. ACC: MOL.19980501.0479.

Wang, J.S.Y., Cook, P.J.; Trautz, R.C.; James, A.; Finsterle, S. Sonnenthal, E.; Salve, R.; Hesler, G.; and Flint, A.L. 1997. *Drift Seepage Test and Niche Moisture Study: Phase 1 Progress Report on Data Interpretation and Model Prediction*. Yucca Mountain Project Level 4 Milestone SPC31DM4. Berkeley, California: Lawrence Berkeley National Laboratory. ACC: MOL.19980501.0484. DTNs: LB970601233124.001 (Q). LB980001233124.001 (Q). LB980901233124.002 (Q).

Wang, J.S.Y. 1997. *Moisture Data Report for October 1996 to January 1997*. Yucca Mountain Project Level 4 Milestone SP331FM4. Berkeley, California: Lawrence Berkeley National Laboratory. DTN: LB970300831224.001 (Q).

Wang, J.S.Y., Cook, P.J.; Trautz, R.C.; Salve, R.; James, A.L.; Finsterle, S.; Tokunaga, T.K.; Solbau, R.; Clyde, J.; Flint, A.L. and Flint, L.E. 1997. *Field Testing and Observation of Flow Paths in Niches, Phase 1 Status Report of the Drift Seepage Test and Niche Moisture Study*. Yucca Mountain Project Level 4 Milestone SPC314M4. Berkeley, California: Lawrence Berkeley National Laboratory. ACC: MOL.19980121.0078.

Wang, J.S.Y.; Trautz, R.C.; Cook, P.J.; Finsterle, S.; James, A.L.; Birkholzer J.; and Ahlers, C.F. 1998. *Testing and Modeling of Seepage into Drift: Input of Exploratory Study of Facility Seepage Test Results to Unsaturated Zone Models*, Yucca Mountain Project Level 4 Milestone SP33PLM4. Berkeley, California: Lawrence Berkeley National Laboratory. ACC: MOL.19980508.0004.

Wang, J.S.Y.; Trautz, R.C.; Cook, P.J.; and Salve, R. 1998. *Drift Seepage Test and Niche Moisture Study: Phase 1 Report on Flux Threshold Determination, Air Permeability Distribution, and Water Potential Measurement*. Yucca Mountain Project Level 4 Milestone SPC315M4. Berkeley, California: Lawrence Berkeley National Laboratory. ACC:

MOL.19980806.0713. DTNs: LB980001233124.001 (Q), LB980001233124.002 (Q), and LB980001233124.004(Q).

INTENTIONALLY LEFT BLANK

9. ATTACHMENTS

Attachment I – Document Input Reference Sheet

Attachment II – Automated Air Injection System

Attachment III – Comparison of Liquid and Air-Derived Saturated Hydraulic Conductivities

Attachment IV – Water Content Profile Evaluation

Attachment V – Tracer Measurements of Niche Cores

Attachment VI – Laboratory Measurements of Retardation and Front Separation

Attachment VII – Field Equipment for Controlled Water Release, Wetting Front Detection and Seepage Collection

Attachment VIII – Measurement of Water Potentials Using Psychrometers

INTENTIONALLY LEFT BLANK

ATTACHMENT I -DOCUMENT INPUT REFERENCE SHEET

DIRS as of the issue date of this AMR. Refer to the DIRS database for the current status of these inputs.

OFFICE OF CIVILIAN RADIOACTIVE WASTE MANAGEMENT DOCUMENT INPUT REFERENCE SHEET									
1. Document Identifier No./Rev.: ANL-NBS-HS-000005/Rev. 00		Change:		Title: <i>In Situ</i> Field Testing of Processes					
Input Document		3. Section	4. Input Status	5. Section Used in	6. Input Description	7. TBV/TBD Priority	8. TBV Due To		
2. Technical Product Input Source Title and Identifier(s) with Version	2a						Unqual.	From Uncontrolled Source	Un-confirmed
1.	DTN: GS960908314224.020. Analysis Report: Geology of the North Ramp - Stations 4+00 to 28+00 and Data: Detailed Line Survey and Full-Periphery Geotechnical Map - Alcoves 3 (UPCA) and 4 (LPCA), and Comparative Geologic Cross Section - Stations 0+60 to 28+00. Submittal date: 09/09/1996.	Entire	N/A- Qualified- Verificati on Level 2	6.7.1.1	Geologic map of Alcove 4	N/A	N/A	N/A	N/A
2.	DTN: LB960800831224.001. Relative Humidity, Temperature, and Pressure in ESF Monitoring Stations. Submittal date: 08/23/1996.	Entire	N/A- Qualified- Verificati on Level 2	6.10.1.1 6.10.2.1	Moisture condition in ESF.	N/A	N/A	N/A	N/A

OFFICE OF CIVILIAN RADIOACTIVE WASTE MANAGEMENT DOCUMENT INPUT REFERENCE SHEET									
1. Document Identifier No./Rev.: ANL-NBS-HS-000005/Rev. 00			Change:	Title: <i>In Situ</i> Field Testing of Processes					
Input Document		3. Section	4. Input Status	5. Section Used in	6. Input Description	7. TBV/TBD Priority	8. TBV Due To		
2. Technical Product Input Source Title and Identifier(s) with Version							Unqual.	From Uncontrolled Source	Un-confirmed
3.	DTN: LB970300831224.001. Moisture Data Report from October, 1996 to January, 1997. Submittal date: 03/13/1997.	Entire	N/A- Qualified- Verificati on Level 2	6.10.1.1	Moisture condition in ESF.	N/A	N/A	N/A	N/A
4.	DTN: LB970801233124.001. Moisture Monitoring Data Collected at ESF Sensor Stations. Submittal date: 08/27/1997.	Entire	N/A- Qualified- Verificati on Level 2	6.10.1.1 6.10.2.1	Moisture condition in ESF.	N/A	N/A	N/A	N/A
5.	DTN: LB970901233124.002. Moisture Monitoring Data Collected at Stationary Moisture Stations. Submittal date: 09/30/1997.	Entire	N/A- Qualified- Verificati on Level 2	6.10.1.1	Moisture condition in ESF.	N/A	N/A	N/A	N/A
6.	DTN: LB980001233124.001. Water Potential Measurements in Niches 3566, 3650, and 3107 of the ESF. Submittal date: 04/23/1998.	Entire	TBV- 3280	6.8.2 6.8.2.1 6.8.2.4 6.10.1.2 Att. VIII	Water potential measurements in niches 3566 and 3650.	1	N/A	N/A	✓

OFFICE OF CIVILIAN RADIOACTIVE WASTE MANAGEMENT DOCUMENT INPUT REFERENCE SHEET									
1. Document Identifier No./Rev.: ANL-NBS-HS-000005/Rev. 00			Change:	Title: <i>In Situ</i> Field Testing of Processes					
Input Document		3. Section	4. Input Status	5. Section Used in	6. Input Description	7. TBV/TBD Priority	8. TBV Due To		
2. Technical Product Input Source Title and Identifier(s) with Version	Unqual.						From Uncontrolled Source	Un-confirmed	
7.	DTN: LB980001233124.002. Air Permeability Testing in Niches 3566 and 3650. Submittal date: 04/23/1998.	Entire	N/A- Qualified- Verificati on Level 2	6.1.2.2 6.1.2.3 6.2.2.1 Att. III	Pre- and Post-Excavation Permeability Profiles. Statistical Comparison of Air-Permeability Distributions. Post-Excavation Liquid-Release and Seepage Threshold Fluxes. Comparison of Liquid and Air-Derived Saturated Hydraulic Conductivities.	N/A	N/A	N/A	N/A

OFFICE OF CIVILIAN RADIOACTIVE WASTE MANAGEMENT DOCUMENT INPUT REFERENCE SHEET									
1. Document Identifier No./Rev.: ANL-NBS-HS-000005/Rev. 00			Change:	Title: <i>In Situ</i> Field Testing of Processes					
Input Document		3. Section	4. Input Status	5. Section Used in	6. Input Description	7. TBV/TBD Priority	8. TBV Due To		
2. Technical Product Input Source Title and Identifier(s) with Version							Unqual.	From Uncontrolled Source	Un-confirmed
8.	DTN: LB980001233124.004. Liquid Release Test Data From Niche 3566 and Niche 3650 of the ESF in Milestone Report, "Drift Seepage Test and Niche Moisture Study: Phase 1 Report on Flux Threshold Determination, Air Permeability Distribution, and Water Potential Measurement." Submittal date: 11/23/1999.	Entire	TBV-	6.2.1.1 6.2.1.2 6.2.1.3.1 6.2.2.1 6.2.2.3 6.2.2.4 6.4.1.2 Att. III	Pre-Excavation Liquid-Release Test Data Dye Penetrations into Rocks Post-Excavation Liquid-Release and Seepage Threshold Fluxes Estimated Volumetric Water Content (θ) of the Fractures Estimated Water Potentials (ψ) of the Fractures Dye Penetrations into Rocks liquid-release rate, Q_o , measured	1	N/A	N/A	✓
9.	DTN: LB980101233124.001. Data collected from Niche at Construction Station 3650. Submittal date: 01/30/1998.	Entire	TBV-0897	6.2.2.1	Seepage threshold analyses.	1	N/A	N/A	✓

OFFICE OF CIVILIAN RADIOACTIVE WASTE MANAGEMENT DOCUMENT INPUT REFERENCE SHEET									
1. Document Identifier No./Rev.: ANL-NBS-HS-000005/Rev. 00			Change:	Title: <i>In Situ</i> Field Testing of Processes					
Input Document		3. Section	4. Input Status	5. Section Used in	6. Input Description	7. TBV/TBD Priority	8. TBV Due To		
2. Technical Product Input Source Title and Identifier(s) with Version	Unqual.						From Uncontrolled Source	Un-confirmed	
10.	DTN: LB980101233124.002. Post-Excavation Permeability Data Collected from Niche 3650 of the ESF. Submittal date: 11/04/1998.	Entire	N/A-Reference only	6.1.2.3	Air-permeability distribution analyses.	N/A	N/A	N/A	N/A
11.	DTN: LB980901233124.002. Laboratory Imbibition, Tracer, and Seepage Tests in Niches 3566, 3650, 3107, and 4788 in the ESF. Submittal date: 09/14/1998.	Entire	N/A-Reference only	6.4.1	Tracer penetration analyses.	N/A	N/A	N/A	N/A

OFFICE OF CIVILIAN RADIOACTIVE WASTE MANAGEMENT DOCUMENT INPUT REFERENCE SHEET									
1. Document Identifier No./Rev.: ANL-NBS-HS-000005/Rev. 00			Change:	Title: <i>In Situ</i> Field Testing of Processes					
Input Document		3. Section	4. Input Status	5. Section Used in	6. Input Description	7. TBV/TBD Priority	8. TBV Due To		
2. Technical Product Input Source Title and Identifier(s) with Version							Unqual.	From Uncontrolled Source	Un-confirmed
12.	DTN: LB980901233124.003. Liquid Release and Tracer Tests in Niches 3566, 3650, 3107, and 4788 in the ESF. Submittal date: 09/14/1998.	Entire	N/A- Qualified- Verificati on Level 2	6.2.1.1 6.2.1.2 6.2.2.1 6.2.2.2 6.2.2.3 6.2.2.4 6.2.2.3 6.2.2.5 6.4.1.2 Att. III Att. IV-2	Pre-Excavation Liquid-Release Test Data Post-Excavation Liquid-Release and Seepage Threshold Fluxes Capillary Strength (α^{-1}) of the Fractures Estimate of water content Estimate Water Potentials (ψ) of the Fractures Estimate Water Content Fracture-Water Characteristic Curves Dye Penetrations into Rocks Liquid-release rate, Q_s , measured Water Content Profile	N/A	N/A	N/A	N/A

OFFICE OF CIVILIAN RADIOACTIVE WASTE MANAGEMENT DOCUMENT INPUT REFERENCE SHEET									
1. Document Identifier No./Rev.: ANL-NBS-HS-000005/Rev. 00			Change:	Title: <i>In Situ</i> Field Testing of Processes					
Input Document		3. Section	4. Input Status	5. Section Used in	6. Input Description	7. TBV/TBD Priority	8. TBV Due To		
2. Technical Product Input Source Title and Identifier(s) with Version							Unqual.	From Uncontrolled Source	Un-confirmed
13.	DTN: LB980901233124.004. Pneumatic Pressure and Air Permeability Data from Alcove 6 in the ESF. Submittal date: 09/14/1998.	Entire	N/A- Qualified- Verificati on Level 2	6.1.2.3 6.5.1	Statistical Comparison of Air-Permeability Distributions Cross-Hole Responses in Welded Tuff	N/A	N/A	N/A	N/A
14.	DTN: LB980901233124.009. Pneumatic Pressure and Air Permeability Data from Alcove 4 in the ESF. Submittal date: 09/14/1998.	Entire	N/A- Qualified- Verificati on Level 2	6.1.2.3	Statistical Comparison of Air-Permeability Distributions	N/A	N/A	N/A	N/A
15.	DTN: LB980901233124.014. Borehole Monitoring at the Single Borehole in the ECRB and ECRB Crossover Point in the ESF. Submittal date: 09/14/1998.	Entire	N/A- Qualified- Verificati on Level 2	6.9.2.1.1 6.9.2.1.2 6.9.2.1.3 6.9.2.2 6.10.1.2	Wetting front detection at the Starter Tunnel. Water potential measurements in starter tunnel. Electrical resistance measurements in starter tunnel. TDR measurements at crossover point in the ESF. Changes in water potential. Changes in electrical resistance. Time domain reflectometry.	N/A	N/A	N/A	N/A

OFFICE OF CIVILIAN RADIOACTIVE WASTE MANAGEMENT DOCUMENT INPUT REFERENCE SHEET										
1. Document Identifier No./Rev.: ANL-NBS-HS-000005/Rev. 00			Change:	Title: <i>In Situ</i> Field Testing of Processes						
Input Document		3. Section	4. Input Status	5. Section Used in	6. Input Description	7. TBV/TBD Priority	8. TBV Due To			
2. Technical Product Input Source Title and Identifier(s) with Version							Unqual.	From Uncontrolled Source	Un-confirmed	
16.	DTN: LB980901233124.101. Pneumatic Pressure and Air Permeability Data from Niche 3107 and Niche 4788 in the ESF From Chapter 2 of Report SP33PBM4: Fracture Flow and Seepage Testing in the ESF, FY98. Submittal date: 11/23/1999.		Entire	N/A- Qualified- Verificati on Level 2	6.1.2.2 6.1.2.3	Pre- and post-excavation permeability profiles.	N/A	N/A	N/A	N/A
17.	DTN: LB980912332245.001. Air Injection Data from Niche 3107 of the ESF. Submittal date: 09/30/1998.		Entire	TBV-3704	6.1.2.3	Pre- and Post-Excavation Permeability Profiles	1	N/A	N/A	✓
18.	DTN: LB990601233124.001. Seepage Data Feed to UZ Drift-Scale Flow Model for TSPA-SR. (Pneumatic pressure and air permeability data.) Submittal date: 06/18/1999.		Entire	N/A- Qualified- Verificati on Level 2	1 6.1.2.2 6.1.2.3	Pre- and post-excavation permeability profiles. Tracer distribution delineation.	N/A	N/A	N/A	N/A

OFFICE OF CIVILIAN RADIOACTIVE WASTE MANAGEMENT DOCUMENT INPUT REFERENCE SHEET									
1. Document Identifier No./Rev.: ANL-NBS-HS-000005/Rev. 00			Change:	Title: <i>In Situ</i> Field Testing of Processes					
Input Document		3. Section	4. Input Status	5. Section Used in	6. Input Description	7. TBV/TBD Priority	8. TBV Due To		
2. Technical Product Input Source Title and Identifier(s) with Version							Unqual.	From Uncontrolled Source	Un-confirmed
19.	DTN: LB990601233124.002. Seepage Data Feed to UZ Drift-Scale Flow Model for TSPA-SR. (Drift seepage testing.) Submittal date: 06/18/1999.	Entire	N/A- Qualified- Verificati on Level 2	1 6.2.1.3.2	Measurement of water potential, electrical resistance, water intake rates, seepage at the alcove 6 test bed.	N/A	N/A	N/A	N/A
20.	DTN: LB990601233124.003. Seepage Data Feed to UZ Drift-Scale Flow Model for TSPA-SR. (Tracer detection data.) Submittal date: 06/18/1999.	Entire	N/A- Qualified- Verificati on Level 2	1 6.3.2.1 6.3.2.2 Att. V-2.2	Aqueous tracer measurement.	N/A	N/A	N/A	N/A
21.	Andreini, M.S. and Steenhuis, T.S. 1990. "Preferential Paths of Flow under Conventional and Conservation Tillage." <i>Geoderma</i> , 46, 85-102. Amsterdam, Netherlands: Elsevier Science. TIC: 245381.	p. 85 p. 98	N/A- Reference only	6.4.2.1	Retardation factor for FD&C Blue No. 1.	N/A	N/A	N/A	N/A

OFFICE OF CIVILIAN RADIOACTIVE WASTE MANAGEMENT DOCUMENT INPUT REFERENCE SHEET									
1. Document Identifier No./Rev.: ANL-NBS-HS-000005/Rev. 00			Change:	Title: <i>In Situ</i> Field Testing of Processes					
Input Document		3. Section	4. Input Status	5. Section Used in	6. Input Description	7. TBV/TBD Priority	8. TBV Due To		
2. Technical Product Input Source Title and Identifier(s) with Version							Unqual.	From Uncontrolled Source	Un-confirmed
22.	Barr, D.L.; Moyer, T.C.; Singleton, W.L.; Albin, A.L.; Lung, R.C.; Lee, A.C.; Beason, S.C.; and Eatman, G.L.W. 1996. <i>Geology of the North Ramp—Stations 4+00 to 28+00, Exploratory Studies Facility, Yucca Mountain Project, Yucca Mountain, Nevada.</i> Denver, Colorado: Bureau of Reclamation. ACC: MOL.19970106.0496.	p. 44	N/A-Reference only	6.7.1.1	Alcove 4 geological map.	N/A	N/A	N/A	N/A
23.	Braester, C. 1973. "Moisture Variation at the Soil Surface and the Advance of the Wetting Front During Infiltration at Constant Flux." <i>Water Resources Research</i> , 9 (3), 687–694. Washington, D.C.: American Geophysical Union. TIC: 242383.	p. 688	N/A-Reference only	5.2.3 6.2.2.2 6.2.2.3	A time-dependent solution for the average volumetric water content distribution.	N/A	N/A	N/A	NA

OFFICE OF CIVILIAN RADIOACTIVE WASTE MANAGEMENT DOCUMENT INPUT REFERENCE SHEET									
1. Document Identifier No./Rev.: ANL-NBS-HS-000005/Rev. 00			Change:	Title: <i>In Situ</i> Field Testing of Processes					
Input Document		3. Section	4. Input Status	5. Section Used in	6. Input Description	7. TBV/TBD Priority	8. TBV Due To		
2. Technical Product Input Source Title and Identifier(s) with Version							Unqual.	From Uncontrolled Source	Un-confirmed
24.	Buesch, D.C. and Spengler, R.W. 1998. "Character of the Middle Nonlithophysal Zone of the Topopah Spring Tuff at Yucca Mountain." <i>High-Level Radioactive Waste Management, Proceedings of the 8th International Conference, Las Vegas, Nevada, May 11-14, 1998.</i> La Grange Park, Illinois: American Nuclear Society. TIC: 237082.	p. 19	N/A-Reference only	6.1.1.1	Description of intensely fractured zone.	N/A	N/A	N/A	N/A

OFFICE OF CIVILIAN RADIOACTIVE WASTE MANAGEMENT DOCUMENT INPUT REFERENCE SHEET									
1. Document Identifier No./Rev.: ANL-NBS-HS-000005/Rev. 00			Change:		Title: <i>In Situ</i> Field Testing of Processes				
Input Document		3. Section	4. Input Status	5. Section Used in	6. Input Description	7. TBV/TBD Priority	8. TBV Due To		
2. Technical Product Input Source Title and Identifier(s) with Version							Unqual.	From Uncontrolled Source	Un-confirmed
25.	Buesch, D.C.; Spengler, R.W.; Moyer, T.C.; and Geslin, J.K. 1996. <i>Proposed Stratigraphic Nomenclature and Macroscopic Identification of Lithostratigraphic Units of the Paintbrush Group Exposed at Yucca Mountain, Nevada</i> . Open-File Report 94-469. Denver, Colorado: U.S. Geological Survey. ACC: MOL.19970205.0061.	pp. 5-8	N/A - Reference only	1 6.7.1.1	Lithographic tuff unit symbols.	N/A	N/A	N/A	N/A

OFFICE OF CIVILIAN RADIOACTIVE WASTE MANAGEMENT DOCUMENT INPUT REFERENCE SHEET									
1. Document Identifier No./Rev.: ANL-NBS-HS-000005/Rev. 00			Change:	Title: <i>In Situ</i> Field Testing of Processes					
Input Document		3. Section	4. Input Status	5. Section Used in	6. Input Description	7. TBV/TBD Priority	8. TBV Due To		
2. Technical Product Input Source Title and Identifier(s) with Version							Unqual.	From Uncontrolled Source	Un-confirmed
26.	CRWMS M&O (Civilian Radioactive Waste Management System Management and Operating Contractor) 1999a. <i>Analysis & Modeling Development Plan (DP) for U0015 In Situ Field Testing of Processes, Rev 00</i> . TDP-NBS-HS-000006. Las Vegas, Nevada: CRWMS M&O. ACC: MOL.19990830.0377.	Entire	N/A-Reference only	1 2	AMR plan.	N/A	N/A	N/A	N/A
27.	CRWMS M&O 1999b. <i>M&O Site Investigations. Activity Evaluation</i> . Las Vegas, Nevada: CRWMS M&O. ACC: MOL.19990317.0330.	Entire	N/A - Reference only	2	Activity evaluation.	N/A	N/A	N/A	N/A
28.	CRWMS M&O 1999c. <i>M&O Site Investigations. Activity Evaluation</i> . Las Vegas, Nevada: CRWMS M&O. ACC: MOL.19990928.0224.	Entire	N/A - Reference only	2	Activity evaluation.	N/A	N/A	N/A	N/A

OFFICE OF CIVILIAN RADIOACTIVE WASTE MANAGEMENT DOCUMENT INPUT REFERENCE SHEET									
1. Document Identifier No./Rev.: ANL-NBS-HS-000005/Rev. 00			Change:	Title: <i>In Situ</i> Field Testing of Processes					
Input Document		3. Section	4. Input Status	5. Section Used in	6. Input Description	7. TBV/TBD Priority	8. TBV Due To		
2. Technical Product Input Source Title and Identifier(s) with Version							Unqual.	From Uncontrolled Source	Un-confirmed
29.	DOE (U.S. Department of Energy) 1998a. "Total System Performance Assessment." Volume 3 of <i>Viability Assessment of a Repository at Yucca Mountain</i> . DOE/RW-0508. Washington, D.C.: U.S. Department of Energy, Office of Civilian Radioactive Waste Management. ACC: MOL.19981007.0030.	4.3.2 6 6.4	N/A - Reference only	1 6	Principal factors for safety strategy and TSPA issues.	N/A	N/A	N/A	N/A
30.	DOE 1998b. "License Application Plan and Costs." Volume 4 of <i>Viability Assessment of a Repository at Yucca Mountain</i> . DOE/RW-0508. Washington, D.C.: U.S. Department of Energy, Office of Civilian Radioactive Waste Management. ACC: MOL.19981007.0031.	2.2.4.1	N/A - Reference only	1	Priority of seepage as a principal factor.	N/A	N/A	N/A	N/A

OFFICE OF CIVILIAN RADIOACTIVE WASTE MANAGEMENT DOCUMENT INPUT REFERENCE SHEET									
1. Document Identifier No./Rev.: ANL-NBS-HS-000005/Rev. 00			Change:	Title: <i>In Situ</i> Field Testing of Processes					
Input Document		3. Section	4. Input Status	5. Section Used in	6. Input Description	7. TBV/TBD Priority	8. TBV Due To		
2. Technical Product Input Source Title and Identifier(s) with Version							Unqual.	From Uncontrolled Source	Un-confirmed
31.	Dyer, J.R. 1999. "Revised Interim Guidance Pending Issuance of New U.S. Nuclear Regulatory Commission (NRC) Regulations (Revision 01, July 22, 1999), for Yucca Mountain, Nevada." Letter from J.R. Dyer (DOE) to D.R. Wilkins (CRWMS M&O), September 9, 1999, OL&RC:SB-1714, with enclosure, "Interim Guidance Pending Issuance of New U.S. Nuclear Regulatory Commission (NRC) Regulations (Revision 01)." ACC: MOL.19990910.0079.	Entire	N/A-Reference only	4.2	Interim Guidance	N/A	N/A	N/A	N/As
32.	Freeze, R.A. and Cherry, J.A. 1979. <i>Groundwater</i> . Englewood Cliffs, New Jersey: Prentice-Hall. TIC: 3476.	p. 27	N/A-Reference only	Att. III	Hydraulic conductivity and permeability	N/A	N/A	N/A	N/A

OFFICE OF CIVILIAN RADIOACTIVE WASTE MANAGEMENT DOCUMENT INPUT REFERENCE SHEET									
1. Document Identifier No./Rev.: ANL-NBS-HS-000005/Rev. 00			Change:	Title: <i>In Situ</i> Field Testing of Processes					
Input Document		3. Section	4. Input Status	5. Section Used in	6. Input Description	7. TBV/TBD Priority	8. TBV Due To		
2. Technical Product Input Source Title and Identifier(s) with Version	Unqual.						From Uncontrolled Source	Un-confirmed	
33.	Ghuman, B.S. and Prihar, S.S. 1980. "Chloride Displacement by Water in Homogeneous Column of Three Soils." <i>Soil Science Society of America Journal</i> , 44 (1), 17-21. Madison, Wisconsin: Soil Science Society of America. TIC: 246698.	p. 17 p. 19	N/A - Reference only	6.4.2.4	Observation of nonreactive solute front lagging behind the moisture front.	N/A	N/A	N/A	N/A
34.	Klinkenberg, L.J. 1941. "The Permeability of Porous Media to Liquids and Gases." <i>API Drilling and Production Practice</i> , 200-213. Washington, DC: American Petroleum Institute. TIC: 217454.	Entire	N/A-Reference only	5.1	Gas-slip phenomenon.	N/A	N/A	N/A	N/A

OFFICE OF CIVILIAN RADIOACTIVE WASTE MANAGEMENT DOCUMENT INPUT REFERENCE SHEET									
1. Document Identifier No./Rev.: ANL-NBS-HS-000005/Rev. 00			Change:	Title: <i>In Situ</i> Field Testing of Processes					
Input Document		3. Section	4. Input Status	5. Section Used in	6. Input Description	7. TBV/TBD Priority	8. TBV Due To		
2. Technical Product Input Source Title and Identifier(s) with Version							Unqual.	From Uncontrolled Source	Un-confirmed
35.	LeCain, G.D. 1995. <i>Pneumatic Testing in 45-Degree-Inclined Boreholes in Ash-Flow Tuff near Superior, Arizona</i> . Water-Resources Investigations Report 95-4073. Denver, Colorado: U.S. Geological Survey. ACC: MOL.19960715.0083.	p. 10	N/A-Reference only	6.1.2.1	Air-permeability equation.	N/A	N/A	N/A	N/A
36.	Moyer, T.C.; Geslin, J. K.; and Flint, L E. 1996. <i>Stratigraphic Relations and Hydrologic Properties of the Paintbrush Tuff Nonwelded (PTn) Hydrologic Unit, Yucca Mountain, Nevada</i> . Open-File Report 95-397. Denver, Colorado: U.S. Geological Survey. TIC: 226213.	pp. 46-50 pp. 54-55	N/A-Reference only	6.7.1.1	Stratigraphic units.	N/A	N/A	N/A	N/A

OFFICE OF CIVILIAN RADIOACTIVE WASTE MANAGEMENT DOCUMENT INPUT REFERENCE SHEET									
1. Document Identifier No./Rev.: ANL-NBS-HS-000005/Rev. 00			Change:	Title: <i>In Situ</i> Field Testing of Processes					
Input Document		3. Section	4. Input Status	5. Section Used in	6. Input Description	7. TBV/TBD Priority	8. TBV Due To		
2. Technical Product Input Source Title and Identifier(s) with Version							Unqual.	From Uncontrolled Source	Un-confirmed
37.	Muskat, M. 1982. <i>The Flow of Homogeneous Fluids Through Porous Media</i> . Boston, Massachusetts: International Human Resources Development. TIC: 208295.	p. 734	N/A-Reference only	6.1.2.1	Cylindrical flow solution	N/A	N/A	N/A	N/A
38.	Philip, J.R. 1985. "Reply to 'Comments on Steady Infiltration from Spherical Cavities.'" <i>Soil Science Society of America Journal</i> , 49, 788-789. Madison, Wisconsin: Soil Science Society of America. TIC: 240255.	Entire	N/A-Reference only	6.2.2.2	Capillary barrier.	N/A	N/A	N/A	N/A
39.	Philip, J.R. 1986. "Linearized Unsteady Multidimensional Infiltration." <i>Water Resources Research</i> , 22 (12), 1717-1727. Washington, D.C.: American Geophysical Union. TIC: 239826.	p. 1728-1719 p. 1725 Sec. 4 Sec. 8	N/A-Reference only	Att. V-2	Analytic solution for unsteady infiltration.	N/A	N/A	N/A	N/A

OFFICE OF CIVILIAN RADIOACTIVE WASTE MANAGEMENT DOCUMENT INPUT REFERENCE SHEET									
1. Document Identifier No./Rev.: ANL-NBS-HS-000005/Rev. 00			Change:	Title: <i>In Situ</i> Field Testing of Processes					
Input Document		3. Section	4. Input Status	5. Section Used in	6. Input Description	7. TBV/TBD Priority	8. TBV Due To		
2. Technical Product Input Source Title and Identifier(s) with Version							Unqual.	From Uncontrolled Source	Un-confirmed
40.	Philip, J.R.; Knight, J.H.; and Waechter, R.T. 1989. "Unsaturated Seepage and Subterranean Holes: Conspectus, and Exclusion Problem for Circular Cylindrical Cavities." <i>Water Resources Research</i> , 25 (1), 16–28. Washington, D.C.: American Geophysical Union. TIC: 239117.	pp. 16-20, 23-25	N/A-Reference only	5.2.2 6.2.2.2 7.2.2	Analytical solution for capillary barrier in homogenous, unsaturated porous medium.	N/A	N/A	N/A	N/A
41.	Porro, I. and Wierenga, P.J. 1993. "Transient and Steady-State Transport through a Large Unsaturated Soil Column." <i>Ground Water</i> , 31 (2), 193–200. Westerville, Ohio: National Ground Water Association. TIC: 246899.	p. 193 p. 196	N/A-Reference only	6.4.2.1 6.4.2.4	Retardation factor. Observation of nonreactive solute front lagging behind the moisture front.	N/A	N/A	N/A	N/A

OFFICE OF CIVILIAN RADIOACTIVE WASTE MANAGEMENT DOCUMENT INPUT REFERENCE SHEET									
1. Document Identifier No./Rev.: ANL-NBS-HS-000005/Rev. 00			Change:	Title: <i>In Situ</i> Field Testing of Processes					
Input Document		3. Section	4. Input Status	5. Section Used in	6. Input Description	7. TBV/TBD Priority	8. TBV Due To		
2. Technical Product Input Source Title and Identifier(s) with Version							Unqual.	From Uncontrolled Source	Un- confirmed
42.	Pullan, A.J. 1990. "The Quasilinear Approximation for Unsaturated Porous Media Flow." <i>Water Resources Research</i> , 26 (6), 1219–1234. Washington, D.C.: American Geophysical Union. TIC: 239824.	p. 1221	N/A- Reference only	6.2.2.2	Saturated conductivity.	N/A	N/A	N/A	N/A
43.	Selby, S.M., ed. 1975. <i>CRC Standard Mathematical Tables, 23rd edition</i> . Cleveland, Ohio: CRC Press. TIC: 247118.	p. 12 p. 16	Reference only	Att. III	Borehole area.	N/A	N/A	N/A	N/A

OFFICE OF CIVILIAN RADIOACTIVE WASTE MANAGEMENT DOCUMENT INPUT REFERENCE SHEET										
1. Document Identifier No./Rev.: ANL-NBS-HS-000005/Rev. 00			Change:		Title: <i>In Situ</i> Field Testing of Processes					
Input Document		3. Section	4. Input Status	5. Section Used in	6. Input Description	7. TBV/TBD Priority	8. TBV Due To			
2. Technical Product Input Source Title and Identifier(s) with Version							Unqual.	From Uncontrolled Source	Un-confirmed	
44.	Wang, J.S.Y. and Elsworth, D. 1999. "Permeability Changes Induced by Excavation in Fractured Tuff." <i>Rock Mechanics for Industry, Proceedings of the 37th U.S. Rock Mechanics Symposium, Vail, Colorado, June 6-9, 1999, 2, 751-757</i> . Alexandria, Virginia: The American Rock Mechanics Association. TIC: 245246.		pp. 752-756	N/A-Reference only	6.1.2.2	Excavation-induced permeability increases.	N/A	N/A	N/A	N/A
45.	Wang, J.S.Y.; Trautz, R.C.; Cook, P.J.; Finsterle, S.; James, A.L.; and Birkholzer, J. 1999. "Field Tests and Model Analyses of Seepage into Drift." <i>Journal Of Contaminant Hydrology, 38</i> (1-3), 323-347. Amsterdam, Netherlands: Elsevier Science. TIC: 244160.		p. 331 pp. 329-332	N/A-Reference only	6.1.2.2 6.3.1.1 7.3	Observation of a wet feature after dry excavation of Niche 3566. Distribution of fractures and dye within the welded tuff observed during niche excavations.	N/A	N/A	N/A	N/A

OFFICE OF CIVILIAN RADIOACTIVE WASTE MANAGEMENT DOCUMENT INPUT REFERENCE SHEET									
1. Document Identifier No./Rev.: ANL-NBS-HS-000005/Rev. 00		Change:		Title: <i>In Situ</i> Field Testing of Processes					
Input Document		3. Section	4. Input Status	5. Section Used in	6. Input Description	7. TBV/TBD Priority	8. TBV Due To		
2. Technical Product Input Source Title and Identifier(s) with Version							Unqual.	From Uncontrolled Source	Un-confirmed
46.	Warrick, A.W.; Biggar, J.W. and Nielsen, D.R. 1971. "Simultaneous Solute and Water Transfer for an Unsaturated Soil." <i>Water Resources Research</i> 7 (5), 1216-1225. Washington, D.C.: American Geophysical Union. TIC: 245674.	Entire	N/A-Reference only	6.4.2.4	Observation of nonreactive solute front lagging behind the moisture front.	N/A	N/A	N/A	N/A
47.	Wemheuer, R.F. 1999. "First Issue of FY00 NEPO QAP-2-0 Activity Evaluations." Interoffice correspondence from R.F. Wemheuer (CRWMS M&O) to R.A. Morgan (CRWMS M&O), October 1, 1999, LV.NEPO.RTPS.TAG.10/99-155, with attachments, Activity Evaluation for Work Package #1401213UM1. ACC: MOL.19991028.0162.	Entire	N/A-Reference only	2	Activity planning	N/A	N/A	N/A	N/A

OFFICE OF CIVILIAN RADIOACTIVE WASTE MANAGEMENT DOCUMENT INPUT REFERENCE SHEET									
1. Document Identifier No./Rev.: ANL-NBS-HS-000005/Rev. 00			Change:	Title: <i>In Situ</i> Field Testing of Processes					
Input Document		3. Section	4. Input Status	5. Section Used in	6. Input Description	7. TBV/TBD Priority	8. TBV Due To		
2. Technical Product Input Source Title and Identifier(s) with Version							Unqual.	From Uncontrolled Source	Un-confirmed
48.	White, I. and Sully, M.J. 1987. "Macroscopic and Microscopic Capillary Length and Time Scales from Field Infiltration." <i>Water Resources Research</i> , 23 (8), 1514-1522. Washington, D.C.: American Geophysical Union. TIC: 239821.	p. 1514 p. 1521	N/A-Reference only	6.2.2.2 Att. IV-2	Downward translation of wetting profile at constant velocity.	N/A	N/A	N/A	N/A
49.	Macro/Routine: Perm Formula 1 ft Zone.vi V1.0. ACC: MOL.19991018.0188.	Entire	N/A-Q	6.1 6.5	Air-permeability profiles. Cross-hole analyses.	N/A	N/A	N/A	N/A
50.	Macro/Routine: Mettler Double Scale 1.vi V1.0. ACC: MOL.19991018.0189.	Entire	N/A-Q	6.2	Liquid-release seepage tests.	N/A	N/A	N/A	N/A
51.	Plotting Software: Earthvision V4.0. STN: 30035 V4.0.	Entire	N/A-Q	6.3	Dye tracer distribution plots.	N/A	N/A	N/A	N/A

AP-3.15Q.1

Rev. 06/30/1999

ATTACHMENT II—AUTOMATED AIR INJECTION SYSTEM

The pneumatic-testing equipment is a specially designed packer system fabricated to take specific testing needs into account. Many boreholes at several sites need to be tested in a controlled fashion to allow site-to-site and borehole-to-borehole comparisons to be meaningful. For determination of connectivity between boreholes, all permutations of injection and response zones at a site need to be examined, so the boreholes must be instrumented for simultaneous measurements. In heterogeneous rock, such as that at the ESF, it is difficult to compensate for variations in results caused by different test configurations such as test interval length or test scale. It is therefore important to keep the testing as consistent as possible by varying only one parameter when performing the tests, namely the location of the test zones. These needs were accommodated not only in the design and operation of the packer system, but also in planning the borehole patterns and drilling. To ensure that the air permeability of unaltered rock would be measured, boreholes were drilled dry and at low speed, a process that minimizes damage to the formation and thereby allows the packer systems to be placed along the entire length of each borehole.

II-1 AUTOMATIC PNEUMATIC INJECTION PACKERS

In light of the need for consistency, the same packer design is used for injection and observation. This approach is amenable to the automation and remote control necessary for establishing consistent testing regimens and accommodating the large number of tests. Inflatable rubber sealing bladders on a packer string can be manipulated independently and divide a borehole into 14 different possible zones over the length of the string. Zone resolution is 0.3 meter, and the bladders cover the entire length of the string. This configuration allows 4.8 meters of borehole to be covered by one string. One 3.2-mm-diameter port for pressure measurement and one 6.4-mm-diameter port for air injection service each zone. Up to seven boreholes can be instrumented at one time. The packer inflation and air-injection lines can all be controlled automatically. A modular design allows partial dismantling of the packer strings in the field for repair or work in tight quarters. Figure II-1 shows a diagram of part of a packer assembly.

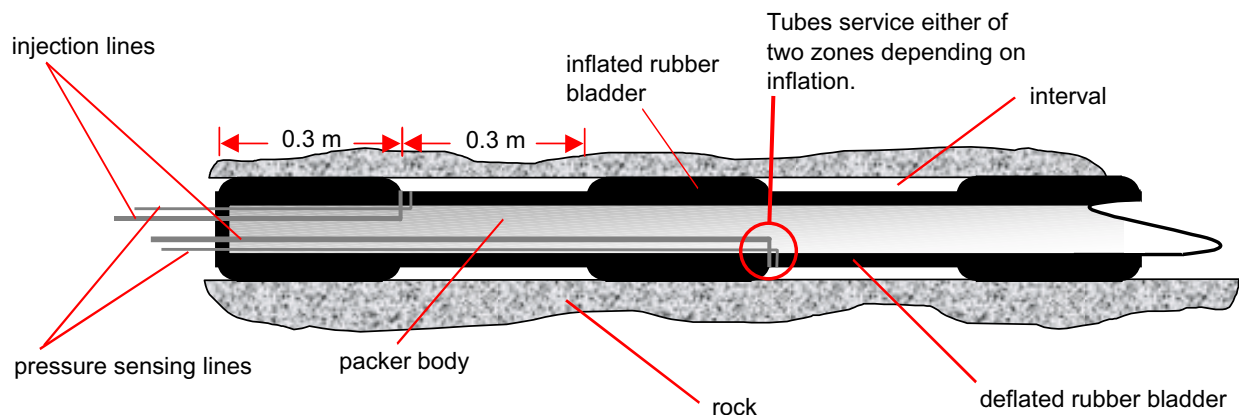


Figure II-1. Schematic Sketch of Automatic Packer Design.

If the bladders are all inflated at once, then the packer string would seal the entire section of borehole occupied by the string. However, by inflating every other bladder and allowing the remainder to remain deflated, an alternating sequence of open and closed (sealed) intervals is produced. Depending on the injection control valves, an open interval becomes either an observation zone used to monitor pressure, or it becomes the injection zone where air is introduced under pressure during a test. Once tests have been performed with these open zones, the inflated bladders are deflated, and deflated bladders are inflated, causing those zones that were once closed to become open and those that were originally open to become closed. In this manner, close to the entire length of the packer string is usable for testing every 0.3 meters without having to move the string. By changing the zones on the injection packer independently from those on the observation packers, there are four possible zone configurations available during a given packer installation. All permutations of these injection and observation positions are used to ensure that all positions within each observation borehole are allowed a chance to respond to a given injection zone. Figure II-2 shows schematically how this process is implemented. The observation packer zones are usually changed in unison because the locations of the observation zones are thought not to perturb the flow field significantly. Permutations between them would cause only second-order effects in the response system.

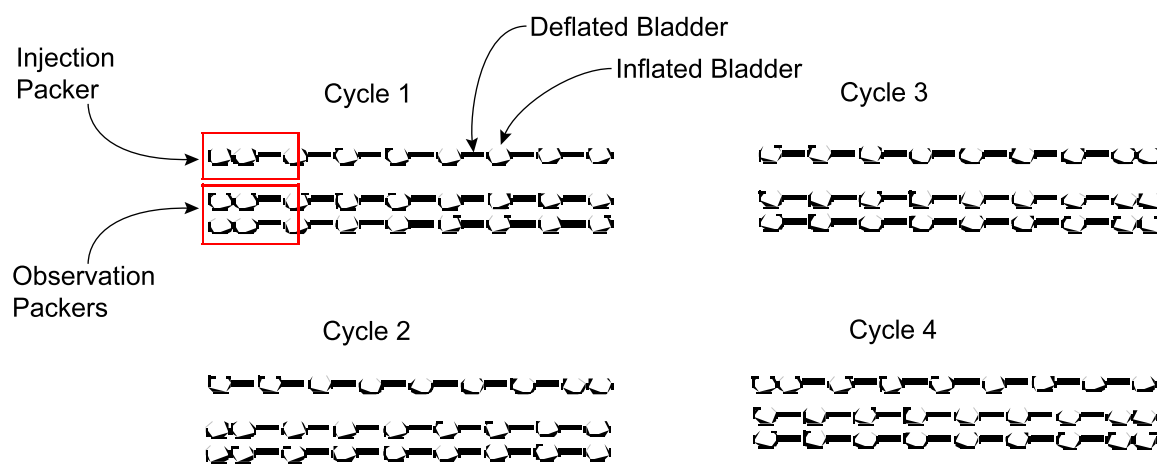


Figure II-2. Schematic Illustration of the Permutation Scheme for Automatic Packers.

II-2 AIR-INJECTION FLOW INSTRUMENTATION

Pressure monitoring for each zone was accomplished using pressure transducers accurate to a resolution of 0.3 kilopascals (kPa). Mass flow controllers (MFCs) with voltage control and output were used to inject a constant mass-flow rate of air during each permeability test. Four sizes of these controllers, from 1 to 500 standard liters per minute (SLPM), were employed to span the anticipated flow-rate ranges. The pressure transducer and MFC outputs were continually monitored and digitally recorded throughout testing, using a 27-bit voltmeter and an accompanying computer. Time resolution for the data from all sources was set nominally at five seconds.

II-3 INITIAL SETUP IN TESTING REGIMEN

Initially, by performing some manually operated tests for a given site, the operator determined under what conditions steady-state was reached and at what injection pressure packer leak-by could occur. (Leak-by is the condition of injected air forcing its way past the packer and breaking its seal with the rock.) The information from these initial tests was used to plan the automatic controls. The operator determined packer leak-by pressure by observing the pressure response in the observation zones axially adjacent to the injection zone. When leak-by occurs, a distinct and sudden pressure response occurs in the guard zone as the packer seal with the borehole is broken. The packer inflation pressure was set at roughly 240 kPa above the ambient pressure to ensure adequate contact with the borehole without risk of damage to the rubber bladders. The leak-by pressure at this inflation was usually about 138 kPa above the ambient pressure, depending on rock conditions, and the limit for any injection pressure was typically set to 80 kPa above the ambient pressure

II-4 AUTOMATION

Utilization of the automatic controls ensured that the tests would reach steady state yet allow them to be completed in minimal time. In addition, automation enabled testing to be run 24 hours a day. The automation scheme allotted a minimum time to every individual injection test. This time period allowed enough data points to be collected to determine the slope of the injection pressure response. Steady state was defined in the automation routine as when the slope of pressure change over time is less than a certain set point for the recent readings. If, after the minimum time, the criterion of steady state had not been met, the test was allowed to continue until it had been met. Pauses between tests left time to monitor recovery pressure. Any excess pressure was bled off from all zones for sufficient time to allow residual pressure in the formation to reach ambient conditions at the site before further testing. Confirmation of this bleed-off was seen in all cases.

The automation routine allowed multiple flow rates at each test interval and also ensured that injection pressure did not exceed the packer leak-by pressure. The test would be shut off if the injection pressure came within about 60% of the packer leak-by pressure and the data automatically annotated to note that steady state had not been attained. To save time, injections at higher rates would not be attempted in a zone with this situation. Conversely, if pressure in an injection zone did not rise above a certain threshold value after a short time, then the test at this rate was cut short and a higher flow rate test attempted. The multi-rate strategy ensured that, by utilizing higher flow rates, highly permeable injection intervals would more likely have sufficient pressure to generate a measurable response in the observation intervals. It also ensured that, by using low flow rates, the very tight intervals could be measured without possible interference of packer leak-by. Theoretically, the same permeability value should result for a given interval location, regardless of the flow rate used. Small differences in permeability may result at different flow rates and between repeat tests, possibly caused by movement of residual water within the fractures. In the case of water redistribution, permeability will be seen to go up slightly for higher rates as testing progresses, with injection pressures overcoming the capillary forces holding the water in the formation. A small decrease of apparent permeability with increasing flow rate can be seen in areas that are drier on account of turbulence at higher air

injection rate. Any large discrepancy between permeabilities at different flow rates and in repeat tests for a given zone can be attributed to compromised packer sealing. The maximum flow rate that did not cause the zone pressure to exceed the packer leak-by pressure during a test was chosen for the purposes of single-hole permeability calculation and for cross-hole response detection.

ATTACHMENT III—COMPARISON OF LIQUID AND AIR-DERIVED SATURATED HYDRAULIC CONDUCTIVITIES

The liquid-release rate, Q_s , measured during each test (Section 6.2.1.3.1) was converted to a liquid-release flux, q_s , using the following equation:

$$q_s = \frac{Q_s}{A \rho_w} \quad (\text{Eq. III-1})$$

where A is the cross-sectional area of flow and ρ_w is the density of water (set at 1.0E+6 g/m³). The q_s data are tabulated in DTN: LB980001233124.004 s99468_010 for the seepage tests conducted at Niche 3650.

The cross-sectional area was derived by the water level that could rise to a maximum elevation of 0.0635 m in the borehole, equal to the maximum ponding depth within the borehole. The ponding depth is controlled by the elevation of the liquid-return line, which prevents the buildup of excess pressure in the test interval by allowing water to flow from the test interval back to the surface. If water rises to the level of the return line, then wetted area A is less than the surface area of the entire test interval and equal to that portion of the curved surface area of a right circular cylinder lying below the water line as follows (Selby 1975, pp. 12 and 16):

$$A = [2\pi - (2\text{Arccosine}(d/r))]hr \quad (\text{Eq. III-2})$$

where d is equal to the vertical distance from the center of the cylinder to the water line (0.0254 m), r is equal to radius of the borehole (0.0381 m), and h is equal to the test interval length (0.3048 m). With these parameters, the cross-sectional area of flow A is equal to 5.343E-02 m².

With Assumptions 4 and 5 described in Section 5.2.1, we estimate the saturated hydraulic conductivity for liquid flow through the fractured porous medium by equating the air permeability (k) derived from the air-injection tests to the water permeability (k_l) of the porous medium. In turn, k_l is related to the saturated hydraulic conductivity (K_l) of a porous medium through the functional relation defined by Darcy's law (Freeze and Cherry 1979, Equation (2.28), p. 27):

$$K_l = \frac{k_l \rho_w g}{\mu} \quad (\text{Eq. III-3})$$

where g is the acceleration of gravity and μ is the viscosity of water. Air-permeability values reported in DTN: LB980001233124.002 s98131_002 were converted to the equivalent saturated hydraulic conductivity values ($K_l \approx K_{air-sat}$) reported in DTN: LB980901233124.003 s98293_006 as shown in Scientific Notebook YMP-LBNL-JSW-6c (p. 38). This conversion allows us to compare the $K_{air-sat}$ values to the q_s values, which are also summarized in

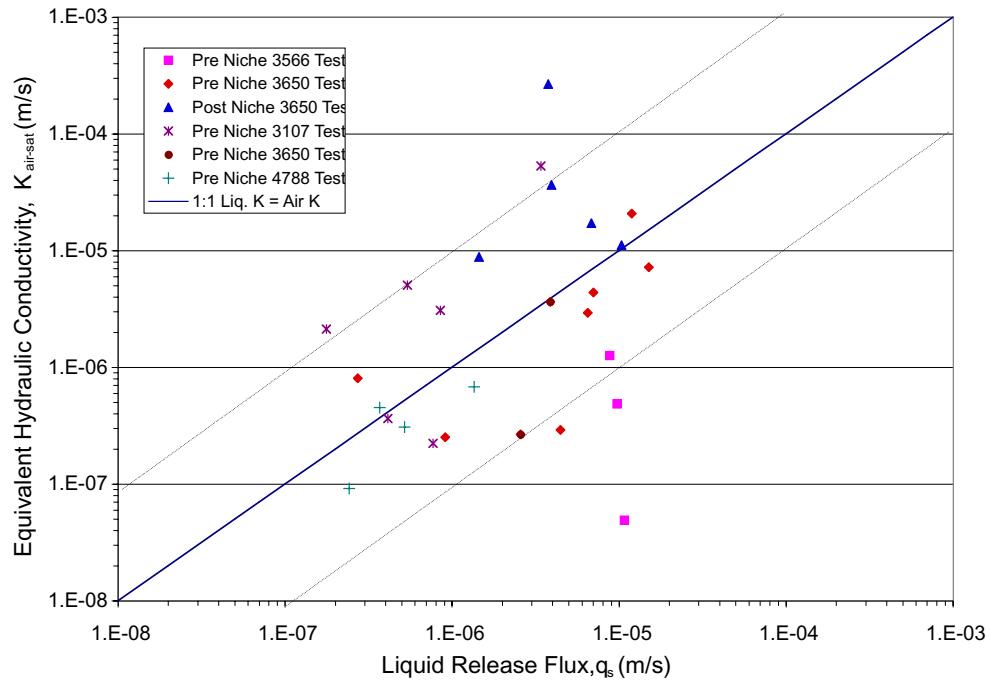
DTN: LB980901233124.003 s98293_006. The q_s values were computed using Equation III-1 and the liquid-release rates (Q_s) from the pre-excavation tests performed at Niches 3566 and 3650 (DTN: LB980001233124.004, s99468_001), the pre-excavation tests performed at Niches 3107 and 4788 (DTN: LB980901233124.003 s98293_008), and the post-excavation seepage tests from Niche 3650 (DTN: LB980001233124.004 s98132_007).¹

Under slightly ponded conditions in the borehole (i.e., saturated conditions), q_s may initially exceed the saturated hydraulic conductivity of the test interval during the early stages of the test when capillary forces predominate. During the later stages of the test, gravity-driven flow will dominate, a unit hydraulic gradient will be established near the borehole wall in the porous material, and q_s will approach K_l for the interval. Based on Assumption 5 in Section 5.2.1, gravity-driven flow is assumed to be the primary flow mechanism operating in fracture systems tested at Niche 3650. Therefore, one would expect capillary effects to be short lived, and for all practical purposes the q_s for a given interval should be equal to K_l . Theoretically, q_s can exceed K_l if water ponds to a significant depth or is injected under high pressure, creating a steep hydraulic gradient within the porous material near the borehole wall. However, the packer system used in the seepage tests was designed so that water could not pond more than 0.0635 m; otherwise return flow to the surface would occur.

Return flow provides direct evidence that the liquid pumping rate exceeded the infiltration capacity of the test interval, implying that $q_s = K_l$, which in turn should equal $K_{air-sat}$, using the approximation that $K_{air-sat}$ is a reasonable estimate of K_l . The $K_{air-sat}$ and q_s values from DTN: LB980901233124.003 s98293_006 for those tests that exhibited return flow are plotted in Figure III-1, along with a solid line that represents the relation $K_{air-sat} = K_l = q_s$. A data point located above the solid line indicates that $K_{air-sat} > K_l$, and a data point below the solid line indicates that $K_{air-sat} < K_l$. One would expect the data values to fall on the $K_{air-sat} = q_s$ line if air-permeability and liquid-release tests are directly correlated.

Figure III-1 indicates that the data points are equally distributed above and below the $K_{air-sat} = q_s$ line, with the majority of points falling within a factor of 10 of $K_{air-sat} = q_s$. Therefore, on average, or taken as a group, the equivalent saturated hydraulic conductivity derived from the air-injection tests appears to adequately characterize the true saturated hydraulic conductivity represented by q_s . The scattering of the individual data points around the line is a measure of the simplifying estimations, assumptions, and experimental uncertainties in relating air-flow processes with liquid-flow processes.

¹ The entire cross-sectional area of the borehole was used to compute the air-permeability values reported in LB980001233124.002 s98131_002 because gravitational effects on air are negligible and, thus, the entire cross-sectional area of the borehole is typically available for airflow. A smaller wetted area, as calculated by Equation III-2, was used to compute the liquid-release flux values.



DTN: LB980901233124.003

Figure III-1. Comparison of Liquid and Air-Derived Saturated Hydraulic Conductivities.

ATTACHMENT IV–WATER CONTENT PROFILE EVALUATION

IV-1 EVALUATION OF ASSUMPTION OF ONE-DIMENSIONAL (1-D) FLOW

Large α -values calculated in Section 6.2.2.2 indicate that gravity-driven flow predominates in the fractures tested at Niche 3650. Although the large α -values of themselves do not collectively imply that flow is strictly 1-D, they do imply that limited lateral spreading of the wetting front in the fractures because of capillary forces will probably be negligible during the early stages of liquid release. Once the wetting front arrives at the niche ceiling, however, capillary forces become very important as water saturations begin to increase because of the capillary barrier, resulting in water being diverted laterally around the cavity. Therefore, flow will change from 1-D to 2-D or 3-D once the wetting front arrives at the ceiling. This implies that the θ_{ave} values calculated using Braester's model are no longer valid after the wetting front arrives at the niche ceiling.

Field observations made during the pre-excavation liquid release and post-excavation seepage tests provide stronger evidence that flow is roughly 1-D. Examination of Figure 17 described in Section 6.2.1.2 for the pre-excavation liquid-release tests shows that the average aspect ratio (i.e., depth to lateral distance traveled by the wetting front) is slightly less than 2 for the tests representing fracture networks and about 4.5 for the high-angle fracture data. This implies that for a 0.65-m travel distance, we would expect lateral spreading to be on average within 0.32 m of the borehole for the fractured network case and within 0.15 m for the near-vertical fracture case. The mean angle of wetting front migration is only 26° from the vertical ($\text{Arctan}(0.32/0.65)$). This analysis is supported further by two field observations made during the post-excavation seepage tests as described in Section 6.2.1.3.1: (1) the majority of water was typically captured in only one or two 0.305×0.305 -m cells located directly beneath the test interval; (2) the wetting front typically arrived at the niche ceiling directly below the test zone.

IV-2 EVALUATION OF ASSUMPTION OF DOWNWARD TRANSLATION OF THE WETTED PROFILE AT CONSTANT VELOCITY

Earth scientists and engineers have recognized for a number of years that during infiltration tests the liquid-release rate approaches an asymptotic value equal to the hydraulic conductivity as time progresses. And in fact, steady moisture conditions are obtained rather rapidly in the vicinity of the source, typically with geometric mean of 1.7 hr when water is introduced at a water potential that is equal to or greater than zero (White and Sully 1987, p. 1514, p. 1521). In our case, water is introduced at a flux that is often times much lower than the saturated hydraulic conductivity of the fractured interval and, therefore, reliance on generalities such as those in the preceding sentence may not be appropriate. Instead, the solution developed for unsteady multidimensional infiltration by Philip (1986, p. 1725) and summarized by White and Sully (1987, p. 1521) is used herein to determine the time to steady moisture conditions. In this manner we will check the validity of Assumption 8 in Section 5.2.3 on downward translation of wetting profile at constant velocity and determine whether the volumetric water contents presented in Section 6.2.2.3 are derived using an appropriate model.

Philip (1986) developed an analytical solution for unsteady 2-D unsaturated flow from a buried horizontal cylinder into an infinite porous medium with uniform initial water content θ_n . We assume that this solution is also valid for flow through unsaturated, fractured media. Once again, Richard's equation was linearized with a constant D and the exponential relation between hydraulic conductivity and water potential, given by Equation 4 in Section 6.2.2.2. Philip (1986, p. 1719) found that regardless of the cavity shape and dimensionality of the flow field, the solution is approximately reducible to the product of the steady solution (ϑ_∞) and a function of dimensionless time (t_D) and radial coordinates (r_D dimensionless radius, $0 \leq \varphi \leq \pi$ polar angle) as follows:

$$\vartheta(r_D, \varphi; s; t_D) \approx G(r_D; s; t_D) \vartheta_\infty(r_D, \varphi; s; \infty) = G(r_D; s; t_D) \vartheta_\infty \quad (\text{Eq. IV-1})$$

Philip (1986) defines ϑ , r_D , and t_D , by Equation (15), G by Equation (29), ϑ_∞ by Equation (62), and φ in Section 4 in his paper for flow from a buried horizontal cylinder. Equation IV-1 is valid for large s (the dimensionless characteristic cavity length defined by Equation 5 in Section 6.2.2.2) and for any value of t_D .

The significance of Equation IV-1 is that the function G ranges in value from 0 to 1. This implies that at large dimensional times (corresponding to large t_D) the unsteady solution approaches the steady solution ($G \rightarrow 1$). Using the same approach employed by Philip (1986, Section 8, p. 1725) for a spherical source, we computed the time to obtain 95% of the steady-state moisture conditions ($t_{D\ 95\%}$) for flow from a buried horizontal cylinder at a radial distance that is slightly larger than the borehole ($r_D = 1.1$) and at radial distance to the niche ceiling ($r_D = 17.1 = 0.65 \text{ m} / 0.0381 \text{ m}$). The details of the analysis can be found in Scientific Notebook YMP-LBNL-JSW-6c (pp. 85-91) and the $t_{D\ 95\%}$ values are tabulated in DTN: LB980901233124.003 s98293_004 for each group of tests where seepage was observed.

The dimensional time ($t_{95\%}$) at which the moisture profile reaches 95% of its steady value can be calculated using $t_{D\ 95\%}$ (Philip 1986, Equation (15), p. 1718). Again, the details of the analysis can be found in Scientific Notebook YMP-LBNL-JSW-6c (pp. 91-92) and the $t_{95\%}$ values are tabulated in Table IV-1 and DTN: LB980901233124.003 s98293_005, along with the time of arrival of the wetting front at the niche ceiling.

Examination of the $t_{95\%}$ values in Table IV-1 indicates that for all the tests, steady-state moisture conditions (i.e., constant θ) are reached near the borehole wall within 6 minutes (344 s) of starting the test and before pumping ceased (pumping times are tabulated in DTN: LB980001233124.004 s99468_005). This demonstrates the original point of this discussion, that Assumption 8 in Section 5.2.3 on downward translation of wetting profile at constant velocity is valid. That is, q_s approached the unsaturated hydraulic conductivity of the porous media, resulting in the downward migration of the wetted profile at a constant velocity within the time limit of each test. In addition, it is important to note that in all cases, steady-state moisture conditions are obtained near the borehole prior to the arrival of the wetting front. After the wetting front arrives at the ceiling, the moisture conditions will begin to change again near the release borehole as the water saturation increases because of the capillary barrier. Based on this analysis, the use of Equation 11 in Section 6.2.2.3 to estimate volumetric water contents appears to be reasonable.

Table IV-1. Time to Steady-State Moisture Conditions.

Borehole	Test Name	Test Date	Test Interval (m)	Time to Steady State ¹		Wetting Front ² Arrival Time (hr)
				r _D = 1.1 (hr)	r _D = 17.1 (hr)	
Fracture Networks						
UR	Test #1 1-15-98	1/15/98	4.88-5.18	0.0129	0.691	0.497
	Test #1 2-6-98	2/6/98	4.88-5.18	0.0317	1.696	1.221
UL	Test #1 12-10-97	12/10/97	7.01-7.32	0.0012	0.127	0.067
	Test #1 1-6-98	1/6/98	7.01-7.32	0.0160	1.740	0.914
UR	Test #1 1-14-98	1/14/98	4.27-4.57	0.0200	1.580	0.936
	Test #1 2-5-98	2/5/98	4.27-4.57	0.0590	4.650	2.753
UM	Test 5 Niche 3650	11/13/97	4.27-4.57	0.0030	0.163	0.116
	Test 5 Niche 3650	12/3/97	4.27-4.57	0.0072	0.396	0.280
	Test #2 12-3-97	12/3/97	4.27-4.57	0.0037	0.202	0.143
	Test #1 1-7-98	1/7/98	4.27-4.57	0.0630	3.458	2.448
	Test #2 2-10-98	2/10/98	4.27-4.57	0.0957	5.249	3.715
UM	Test 4 Niche 3650	11/13/97	5.49-5.79	0.0014	0.088	0.058
	Test #2 12-4-97	12/4/97	5.49-5.79	0.0028	0.178	0.117
	Test #1 1-9-98	1/9/98	5.49-5.79	0.0186	1.164	0.764
	Test #1 2-11-98	2/11/98	5.49-5.79	0.0684	4.289	2.814
UR	Test #2 1-13-98	1/13/98	5.49-5.79	0.0005	0.527	0.150
	Test #2 2-10-98	2/10/98	5.49-5.79	0.0002	0.224	0.064
Individual or Small Groups of Vertical Fractures						
UM	Test 1 Niche 3650	11/12/97	4.88-5.18	0.0007	0.051	0.050
	Test #1 12-4-97	12/4/97	4.88-5.18	0.0011	0.085	0.083
	Test #2 12-5-97	12/5/97	4.88-5.18	0.0035	0.272	0.264
	Test #1 1-8-98	1/8/98	4.88-5.18	0.0225	1.729	1.683
	Test #1 3-6-98	3/6/98	4.88-5.18	0.0807	6.189	6.025
UR	Test #1 1-13-98	1/13/98	6.71-7.01	0.0018	0.122	0.116
	Test #1 2-3-98	2/3/98	6.71-7.01	0.0027	0.184	0.174
	Test #1 3-5-98	3/5/98	6.71-7.01	0.0195	1.307	1.238
UL	Test #2 1-6-98	1/6/98	7.62-7.92	0.0029	0.201	0.192
	Test #1 2-12-98	2/12/98	7.62-7.92	0.0024	0.166	0.158
	Test #1 3-4-98	3/4/98	7.62-7.92	0.0111	0.761	0.725
UR	Test #2 1-14-98	1/14/98	6.10-6.40	0.0030	0.267	0.267
	Test #1 2-4-98	2/4/98	6.10-6.40	0.0116	1.046	1.043

DTNs: ¹ LB980901233124.003 s98293_005, ² LB980001233124.004 s99468_014

ATTACHMENT V–TRACER MEASUREMENTS OF NICHE CORES

The core samples from the boreholes drilled above Niche 3650 ceiling were analyzed with laboratory measurements described in this section.

V-1 CORE SAMPLE PROCESSING

After the core samples were received at the laboratory, digital photographs were taken for archiving purposes. The rock samples within each packet were further subsampled for tracer analyses. The subsampling interval was nominally 10 cm. Each subsample was processed using a Jaw Crusher (Model 150, Lemaire Instruments; p. 139 of the Scientific Notebook YMP-LBNL-JSW-QH-1C) and a Micro-Mill Grinder (Scienceware[®] Model No. 372520000, Bel-Art Products; p. 139 of Scientific Notebook YMP-LBNL-JSW-QH-1C) to reduce its size so it could pass through a 2-mm sieve. Subsampling was intended to be representative of the samples within each specific subinterval. Visibly dye-stained rock was proportionally sampled together with the nondyed pieces. Depending upon the core recovery, the subsample weight ranged from 40 to 90% of the total sample weight. Note that the subsample depths were determined by the depth-interval information provided on the sample packets. It was difficult to determine the exact subsample location if the samples consisted of highly fractured pieces or rubble.

Tracer concentrations were measured on oven-dried samples, with the gravimetric moisture content individually determined by drying the samples in an oven set at 105–110°C. The background level for each tracer was measured using rock samples that had not been exposed to tracers, with identical procedure applied for dye samples. Evaluation studies, conducted by spiking rock samples with a known amount of tracer, indicated that the efficiency for this extraction procedure was $97.6 \pm 2.1\%$ (average \pm standard deviation from eight duplicated tests) for iodide, $96.9 \pm 1.9\%$ for bromide, and $78.7 \pm 2.7\%$ for FD&C Blue No.1. The sample processing procedure was not designed to be exhaustive for the tracer mass extraction; relative measurements with the identical procedure were sufficient.

Ten grams of sieved sample were weighed, in duplicates, and 20 milliliters of NANOpure water (NANOpure analytical deionization system, Barnstead; pp. 147–148 of Scientific Notebook YMP-LBNL-JSW-QH-1C) were added to the sample and mixed for tracer extraction. The paste was then filtered through a filtration system using glass vessels and a 0.45 μm Gelman Supor[®] hydrophilic polyethersulfone membrane filter (Gelman Science; p. 6 of Scientific Notebook YMP-LBNL-JSW-QH-1D). Testing with the filtration system using the standard solutions showed a negligible mass loss for tested sorbing dyes. The recovery percentages were $96.1 \pm 6.3\%$ for FD&C Blue No. 1 and $99.0 \pm 5.5\%$ for Sulpho Rhodamine B.

V-2 AQUEOUS TRACER MEASUREMENTS

V-2.1 Ionic Tracer

The filtrates were analyzed using various methods to identify the presence of tracers. Independent analyses were conducted to evaluate the potential interference between tracers present in the same sample. Analyses of iodide and bromide were conducted using Ion Specific

Electrodes (Ionplus Design, Orion), with an ion strength adjuster having a volume ratio of 50:1. Iodide measurements with the Ion Specific Electrode were highly selective and sensitive. No interferences from other tracers applied at Niche 3650 were observed.

V-2.2 Dye Tracers

Dye tracers present in sample extracts were identified and quantified using combinations of the following approaches:

- Color inspection of the extracted sample
- “Finger-printing” by Ultraviolet-Visible (UV/Vis) scanning-the sample spectra were compared and matched to those of standard solutions that exhibit the tracer characteristic wavelengths (listed as the identification peaks in [Table V-1](#))
- Concentration quantification at individual maximum/optimal wavelength for each dye

Both FD&C dyes and fluorescent dyes have colors quantifiable with the UV/Vis Spectrophotometer (Model U-2001, Hitachi). The detection limits of dyes by the UV/Vis Spectrophotometer (0.01 to 0.1 mg/l) are roughly equal to the lowest color densities in solutions that the naked eye can resolve. Fluorescent dyes can also be measured by a Fluorescence Spectrophotometer (Model RF-1501, Shimadzu). The detection limits (as well as background levels) by the Fluorescence Spectrophotometer were much lower (0.0001 to 0.002 mg/l than the limits by the UV/Vis Spectrophotometer. Refer to pp. 56–98 of Scientific Notebook YMP-LBNL-JSW-QH-1 for details on detection limits.

Table V-1. Analytical Measurement for Liquid Dye Tracers.

Dye tracer	Identification peaks in UV/Vis spectrum (nm)	Quantification peak in UV/Vis Spectrophotometer (nm)	Quantification wavelengths in fluorometric analysis (nm)
FD&C Blue No.1	307, 408, 630	630	
FD&C Yellow No. 5	257, 426	426	
FD&C Yellow No. 6	234, 313, 482	482	
FD&C Red No. 40	211, 234, 314, 504	504	
Sulpho Rhodamine B	198, 259, 284, 353, 565		Excitation: 565 Emission: 590
Pyranine	246, 289, 369, 403		Excitation: 405 Emission: 515
Acid Yellow 7	231, 275, 419		Excitation: 420 Emission: 515
Amino G Acid	219, 247, 304, 348		Excitation: 355 Emission: 445

DTN: LB990601233124.003

Figure V-1 presents results of UV/Vis wavelength scanning, which records the absorbance of a sample as a function of wavelength. The x-axis is wavelength (in nanometers) and the y-axis is instrument's response (i.e., absorbance). Figure V-1a shows the UV/Vis spectrum of the background sample, with the 975–976 nm peak present in all liquid samples, including the spectrum for the NANOpure water. The artificial spike around 340 nm is associated with the instrument's lamp change from the tungsten iodide lamp (generates visible light) to the deuterium lamp (generates UV light) during the UV/Vis scanning. This spike was also present at every UV/Vis spectrum. Figures V-1b–d show the wavelength scanning results for the standard solution of FD&C Blue No. 1, FD&C Yellow No. 6, and FD&C Yellow No. 5, respectively. The characteristic peaks were used to identify dyes present in samples by peak matching. The scanning results provided the basis for selecting the characteristic peak wavelength for dye quantification (Table V-1), avoiding as much as possible overlapped peaks to minimize ambiguity.

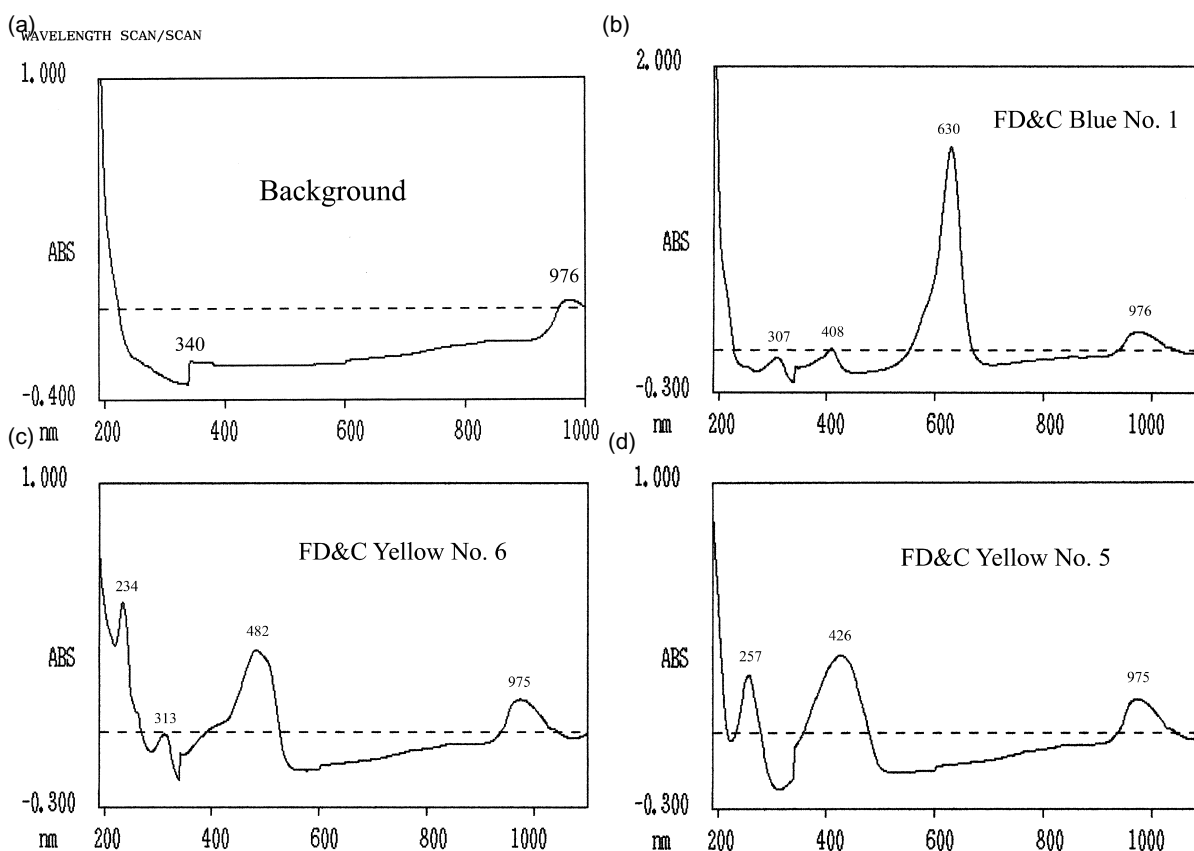


Figure V-1. UV/Vis Wavelength Scanning (Numbers in the Figures are in Nanometers). (a) The background sample. (b) FD&C Blue No. 1 standard. (c) FD&C Yellow No. 6 standard. (d) FD&C Yellow No. 5 standard. X-axis: nanometers (nm); Y-axis: absorbance (ABS). [pp. 56–98 of Scientific Notebook YMP-LBNL-JSW-QH-1].

V-2.3 An Example of Concentration Analyses

Some extracted samples from borehole 7 appeared yellowish, and several UV/Vis scans were run for these samples to compare with the spectra of standard dye solutions. Figure V-2 shows the spectra of one sample (borehole 7, 0–8 cm depth interval from the borehole collar). Peak-matching with the characteristic wavelengths of the standards (Table V-1) shows that FD&C Blue No. 1 and FD&C Yellow No. 6 are present in this sample, while FD&C Yellow 5 is not present above the background spectral level. Similarly, the yellowish color from borehole 11 extractants was found to be from pyranine rather than from FD&C Yellow No. 6 and/or FD&C Yellow No. 5 (Figures not shown; refer to pp. 69–79 of Scientific Notebook YMP-LBNL-JSW-QH-1D for more details).

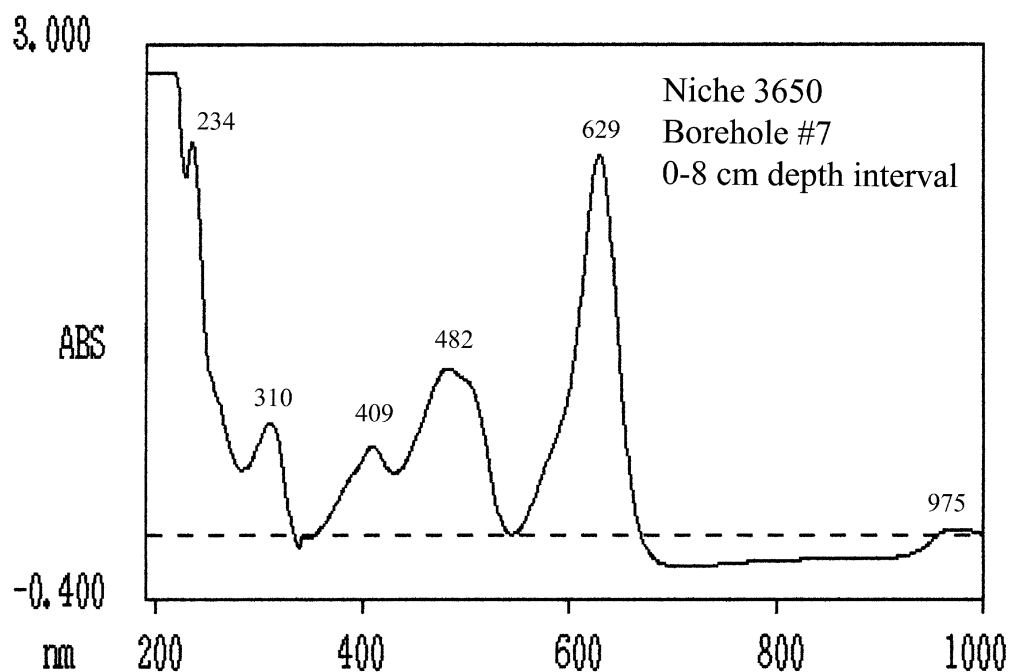


Figure V-2. UV/Vis Wavelength Scanning of a Sample (Borehole 7, 0-8 cm Depth Interval Location from the Borehole Collar). X-axis: nanometers (nm); Y-axis: absorbance (ABS). Numbers in the figures are in nm. [pp. 69–79 of Scientific Notebook YMP-LBNL-JSW-QH-1D].

ATTACHMENT VI—LABORATORY MEASUREMENTS OF RETARDATION AND FRONT SEPARATION

Laboratory analyses are described for dyed samples collected from the niches and core samples for tracer retardation and front separation measurements.

VI-1 WATER IMBIBITION

Rock cores, 5.08 cm in diameter and 2.0 cm in length, were used for the imbibition experiments to examine tracer penetration into the unsaturated rock matrix. Cores were cut and machined from a clean sample block from the same stratigraphic unit as the niche locations where tracer release tests were conducted. Porosity, bulk-density and particle-density measurements were based on the core dry weight at a temperature of 60°C.

Partial saturation of cores was obtained by equilibrating cores within relative humidity chambers controlled by different saturated brines and/or water until they reached constant weights. Cores with two different levels of initial water saturation S_w , approximately 15% and 80%, were used in this work to investigate and compare tracer penetration behavior with respect to the saturation levels.

The core was hung inside a humidity-controlled chamber, with the core bottom submerged in a water reservoir containing tracers to a depth of about 1 mm. The core weight gain was continuously recorded by a data acquisition system. This study was designed to simulate the imbibition and penetration of tracers into the matrix from a continuously flowing fracture, modeled here as the core bottom. After a predetermined period of time (about 16–20 hrs), the core was lifted out of the reservoir, and the moisture front was visually examined. Rock sampling was immediately conducted as described below. The water contained about 10 g/l LiBr, 1 g/l FD&C Blue No. 1, and 1g/l Sulpho Rhodamine B. These tracers were selected to compare the behavior of nonreactive bromide with the dyes used in the field tracer work.

VI-2 ROCK SAMPLING AND TRACER EXTRACTION

Tracer-stained rock samples were drilled, drill cuttings eluted, and the supernatant analyzed to profile tracer location and concentration. A mill (Bridgeport Series II; refer to pp. 37–38 of Scientific Notebook YMP-LBNL-JSW-QH-1A) was used for drilling, with the rock sample firmly stabilized on the working platform and the rock surface covered with tape except for the location to be drilled. A series of drills of different sizes with flat-bottom, carbide-end mill cutters were used to sample different depths from the same location. The largest drill was used for the drilling at the rock surface, and the size gradually decreased with increased drilling depth to minimize carry-over powder contamination from previous depths. A tube was placed around the carbide-end mill cutter to reduce powder loss and to maximize sample recovery. The drilling was carried out slowly and steadily in 1 mm increments as indicated by a digital caliper (Mitutoyo, precision 0.01 mm).

Drill cuttings were collected at each 1-mm interval using a stainless steel needle attached to a stainless steel filter holder, connected to a vacuum source. The vacuum intensity was tested and

adjusted before actual sample collection. Two pieces of cellulose nitrate membrane (with the membrane pore size of 0.45 μm) were used inside the filter holder to trap the sample powder. The powder was suctioned and trapped into the collection device by pointing the needle to the drilled hole and applying the vacuum. Collected cuttings were transferred to an amber-glass vial before tracer extraction. Before drilling the next interval, the drilled hole was cleaned using an air stream just strong enough to remove any powder that might be left from the collection, and the cutter was cleaned with premoistened wipes and dried with a gentle air stream.

Samples of dye-stained rocks having a flat face were selected for rock drilling. Three samples were identified to be suitable for this work. The flat surfaces with dye stains were assumed to be fracture surfaces of active flow paths induced by dye water releases. For these three samples, no visible fracture coatings were observed.

Sampling of cylinder-shaped machined cores for the laboratory studies was performed from both the top and bottom of the core, first from the cleaner top (i.e., core side not in physical contact with liquid) to 16 mm, then from the bottom to 10 mm. This sampling scheme allows a comparison and evaluation of powder contamination of the drilling method. Drilling from the two sides was conducted so that the drill holes did not intersect each other.

Dye tracers were extracted from the drill cuttings into the aqueous phase by mixing 5-ml Nanopure water with 0.1 g of powder sample, mixing nominally for 15 seconds at the speed of 1,400 rpm. The mixture was then filtered, and the concentration of the tracer in the clear aqueous phase was measured. Either Gelman Supor® hydrophilic polyethersulfone membrane filter or Whatman cellulose nitrate membrane was used for the filtration. Testing showed negligible mass loss to both membranes for FD&C Blue No. 1 and Sulpho Rhodamine B.

Extraction efficiency was evaluated by spiking a known amount of tracers into the rock powder (<104 μm) for one day. The results show the extraction efficiency of $98.0 \pm 4.6\%$ (average plus and minus standard deviation, 5 replicates) for bromide, $94.1 \pm 3.8\%$ for FD&C Blue No. 1 (6 replicates), and $55.2 \pm 0.7\%$ for Sulpho Rhodamine B (7 replicates). The extraction procedure was not designed to be exhaustive for the maximum mass extraction. Relative comparisons with identical procedures were used in this study.

VI-3 MEASUREMENT OF AQUEOUS TRACER CONCENTRATION

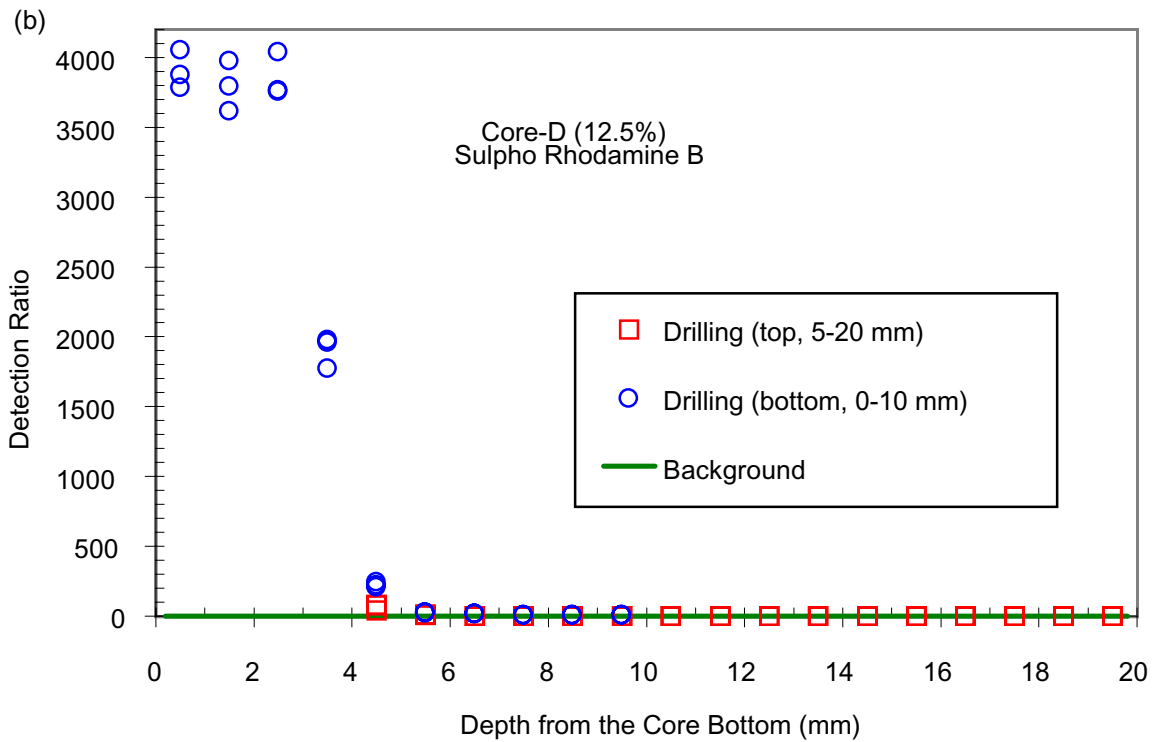
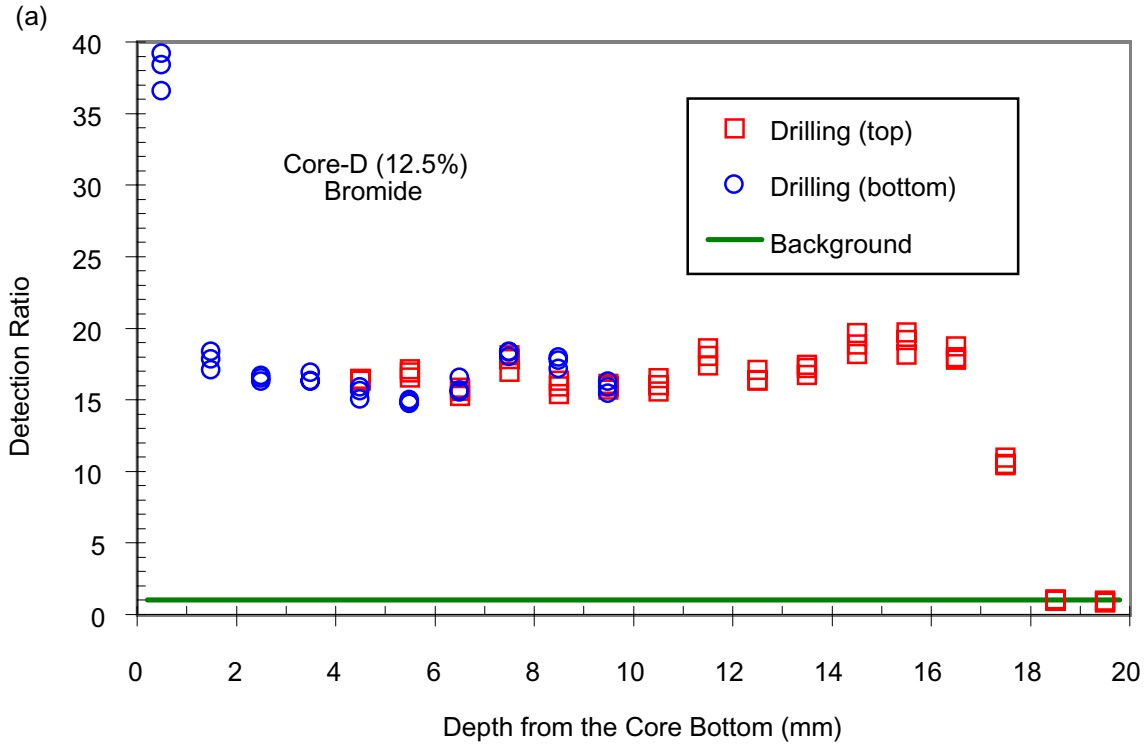
The aqueous concentration of FD&C Blue No. 1 dye was measured using a UV/Vis Spectrophotometer (Hitachi, Model U-2001) at the characteristic wavelength of 630 nm. Sulpho Rhodamine B concentration was measured using a Spectrofluorophotometer (Shimadzu, Model RF-1501) at the excitation wavelength of 565 nm and emission wavelength of 590 nm. Depending upon the tracer concentration present in the samples, samples were diluted appropriately until the final solution measurement fell into the linear range of the calibration curve. Bromide concentration was measured by Ion Specific Electrode (Orion, Ionplus design) with the addition of ion strength adjuster with a volume ratio of 50:1. Background levels for all tracers were measured with powders from clean tuff samples. The clean powder was obtained from a clean rock sample that was crushed for size reduction to pass through a 104- μm opening sieve, similar to the powder size of the drill cuttings. Refer to the associated scientific notebook

pages, listed with DTN: LB990901233124.003, for detailed entries about instrument calibration and tracer measurements.

VI-4 EVALUATION OF DRILLING TECHNIQUE:

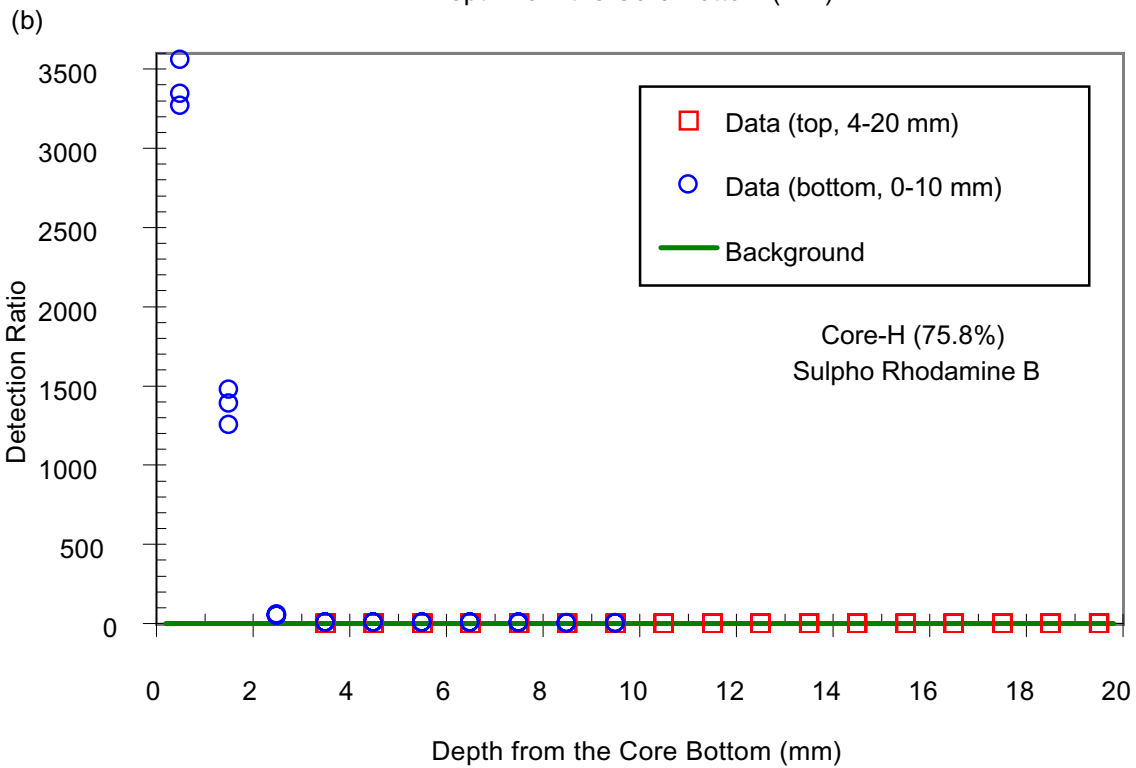
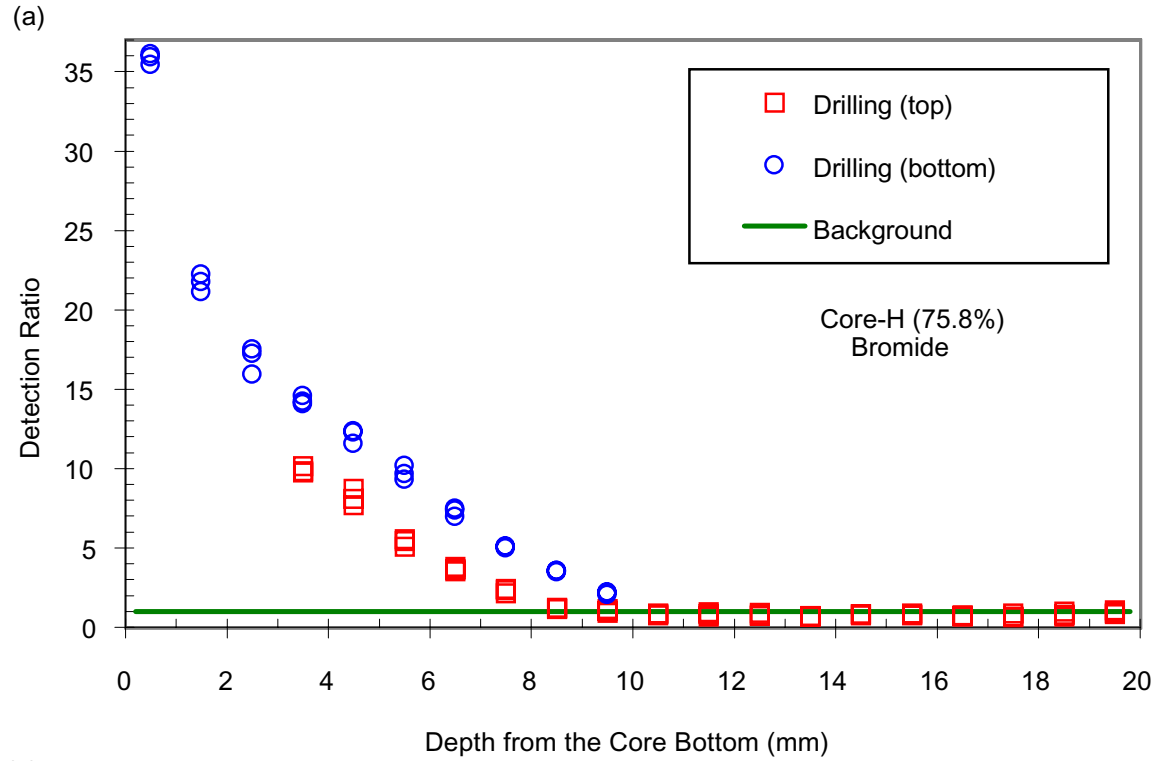
Tracer cross-contamination during drilling was evaluated by drilling from both the top and bottom for machined cores. For both drilling directions, measured tracer concentration are compared over distance in [Figure VI-1](#) for Core D with lower initial water saturation S_w and [Figure VI-2](#) for Core H with high initial S_w . Note that core bottom was the core side in physical contact with the tracer solution. For the lower S_w case, the tracer concentration is comparable for both drilling directions, showing no significant powder carry-over ([Figures VI-1a and VI-1b](#)). A slight difference at the 4–5 mm interval is observed in [Figure VI-1b](#) for Sulpho Rhodamine B. This difference could be real since the fluorometer used for measurement had a low detection limit of about 0.021 mg/kg. Overall, the drilling technique yielded reliable concentration profile results.

For the case with the higher initial S_w , the difference in measured concentration from the two drilling directions is noticeable ([Figure VI-2a](#)). After the tracer-rock contact and experiments were completed, the drilling was conducted first from the core top (cleaner side), then the core was inverted for the opposite drilling. Nominally, it took about 1 hour to finish drilling and sample collection for 10 depth intervals. The difference in concentrations shown in [Figure VI-2a](#) for the two drilling directions may result from any or a combination of (1) gravitational flow during the second drilling phase, (2) heterogeneity, (3) flow resulting from exposure to the atmosphere, (4) evaporation loss resulting from heating caused by drilling. The spreading of tracer front at the high initial S_w makes the flow redistribution effects more pronounced than the case with sharp tracer front at low initial S_w . For Sulpho Rhodamine B, the difference is less evident ([Figure VI-2b](#)). Results from the core top were utilized if the data were available.



DTN: LB990901233124.003

Figure VI-1. Comparison of Measured Detection Ratio from the Opposite Drilling Directions for Core D with Lower Initial S_w : (a) Bromide, (b) Sulpho Rhodamine B. The core ID and the initial core saturation (in parentheses) are presented in the figures.



DTN: LB990901233124.003

Figure VI-2. Comparison of Measured Detection Ratio from the Opposite Drilling Directions for Core H with Higher Initial S_w : (a) Bromide, (b) Sulpho Rhodamine B.

ATTACHMENT VII—FIELD EQUIPMENT FOR CONTROLLED WATER RELEASE, WETTING FRONT DETECTION AND SEEPAGE COLLECTION

Equipment for controlled release of water into isolated zones, borehole monitoring for changes in saturation and water potential, and collection of seepage in a excavated slot are presented for the new instruments developed for this field investigation of fracture flow and fracture matrix interaction.

VII-1 FLUID INJECTION

The liquid-release experiments required water to be injected into the formation over a 0.3-m zone in the borehole under constant-head or constant-rate conditions. The constant-head tests were conducted first to determine the maximum rates at which the zone could take in water. The subsequent set of experiments required that water be released to the formation at predetermined rates ranging from ~ 5 ml/min to ~ 100 ml/min. Both the constant-head method and the constant-rate method of injection were incorporated in the fluid-release apparatus. The main components of the fluid-release apparatus included an inflatable packer system for isolating the injection zone, a pump for delivering water, and a reservoir for providing a continuous supply of water (Figure VII-1a).

The inflation packer system consisted of two rubber packers, each 0.60 m long, connected to an inflation line (Figure VII-1b). Two stainless tubes (0.95 cm and 0.31 cm ID) passed through one of the packers to provide fluid (air and water) access into the injection zone. The 0.95-cm tube was used to deliver fluid into the injection zone, while the 0.31-cm tube was used as a siphon to remove excess water from the injection zone. Before liquid was released into the formation, the packer system was located to straddle the zone of interest (determined from air-permeability measurements) and then inflated to a pressure of ~ 200 kPa. The 0.95-cm ID stainless steel tube was then connected to a water supply line from a constant-head or a constant-rate system. During the entire period of injection, pressure in the inflation packers was continuously monitored to ensure that the injection zone remained isolated from adjacent zones of the borehole.

To capture the temporal variability in vertical flux of water from the injection zone, an automated liquid-release system was developed. This system allowed for continuous measurement of local liquid-release rates. The unit consisted of a storage tank (~ 4.5 liters) for water supply to a clear-acrylic, constant-head chamber. The chamber, 0.15 m ID and 0.30 m tall, served to maintain a constant head of water above the liquid-release surface within the injection zone (Figure VII-1c). The head maintenance was achieved with a level switch that activated the pump when the water level dropped below the control level. The control level was nominally set at or slightly above the elevation of the horizontal injection borehole. Two pressure transducers continuously recorded the height of water in each tank. A pulse damper was installed between the pump and tank to reduce any pulsating effects (caused by the pump) from migrating to the storage tank and influencing the pressure readings.

The constant-rate injection system included all the components used in the constant-head system without the constant-head chamber. To allow for easy regulation of flow rates in the field, the pump was calibrated before field deployment to relate flow rates with displayed numbers on a

10-turn speed control. In the field, the speed control was set at the desired flow rate before the pump was activated. The actual flow rate was determined from transducers located at the bottom of the water reservoir. A data acquisition system was used to record changes in head of water (water level) in the reservoir.

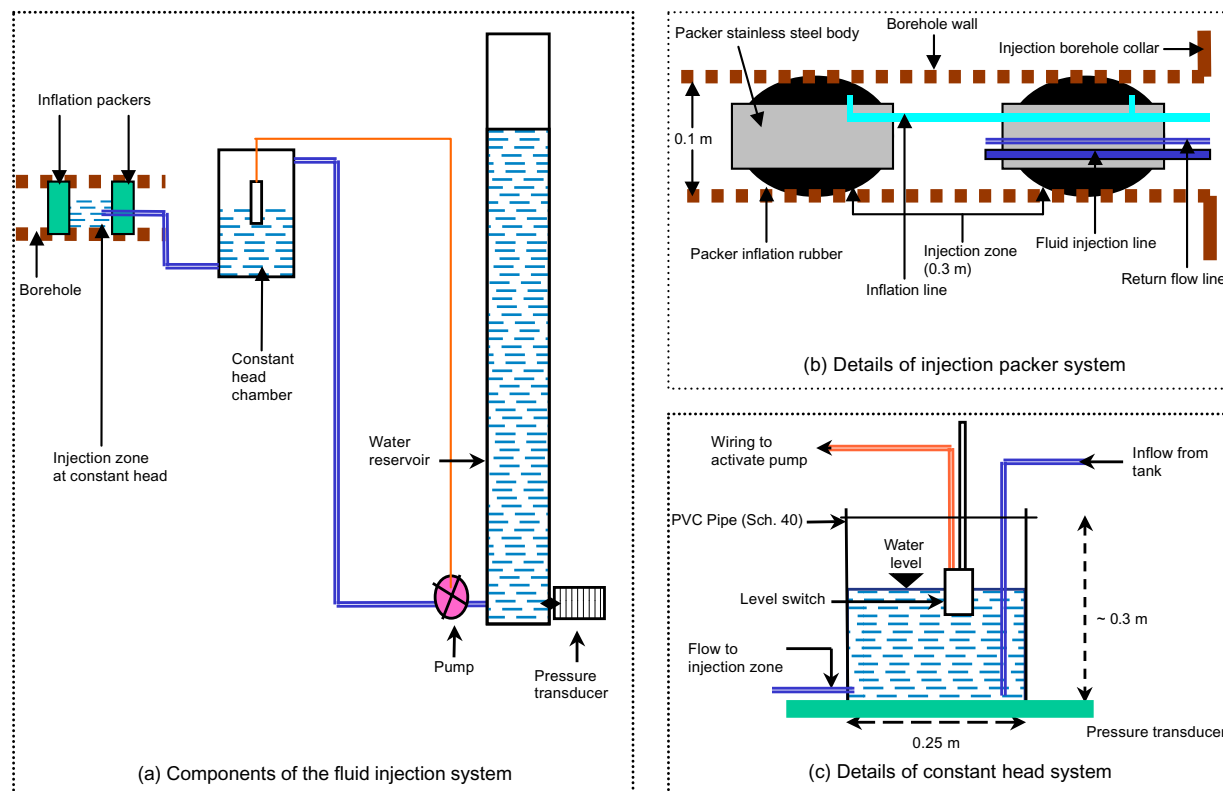


Figure VII-1. Schematic Illustration of Liquid Release System for Constant-Head and Constant-Rate Injections.

VII-2 Borehole Monitoring

In three monitoring boreholes (B, C and D in Figure 45b), changes in saturation and water potential were measured continuously during the entire field investigation. Changes in saturation were measured with electrical-resistivity probes (ERPs) located at 0.25-m intervals along the 6.0-m length of each borehole. These ERPs consisted of two electrical leads sandwiched between pieces of filter paper. Water-potential measurements were made with psychrometers. With the multiplexing capabilities of the data logger (model CR7, Campbell Scientific Inc.), hourly measurements of up to 80 psychrometers (model PST-55, Wescor Inc.) were automated. The chromel-constantan junction in the psychrometer was cooled with an electric current to a temperature below dew point to first induce condensation, followed by evaporation without electric current. Temperature depression resulting from evaporation was recorded and used to determine water potentials in the vicinity of the psychrometers.

The psychrometers and ERP were housed in Borehole Sensor Trays (BSTs), installed along the length of each monitoring borehole (Figure VII-2a). The BSTs were fabricated from 0.10-m

outside diameter (OD) PVC pipes, 3.0 m in section length. Each pipe section was cut lengthwise to produce a 0.075-m-wide curved tray (Figure VII-2b). On each tray, psychrometers were installed at 0.5-m intervals along the borehole while ERPs were located at 0.25-m intervals (Figures VII-2b and VII-2c). BST housing permitted immediate contact between ERPs and the borehole wall. The psychrometers were installed inside small cavities (0.005 m in diameter) perforated through the BST wall to measure water potentials of the rock. A steel spoon, 3.0 m long with the same configuration as the trays, was used to guide each BST to the assigned location along the borehole. Two BSTs were located along each section of borehole, one in contact with the top of the borehole and the other with the bottom. Each pair of BSTs was separated by a wedge that pressed the BSTs tight against the borehole wall. The double BST configuration improved the contacts between ERPs with the borehole wall and allowed two sensors, one on the upper BST and one on the lower BST, to detect wetting-front advances at each given location along the borehole.

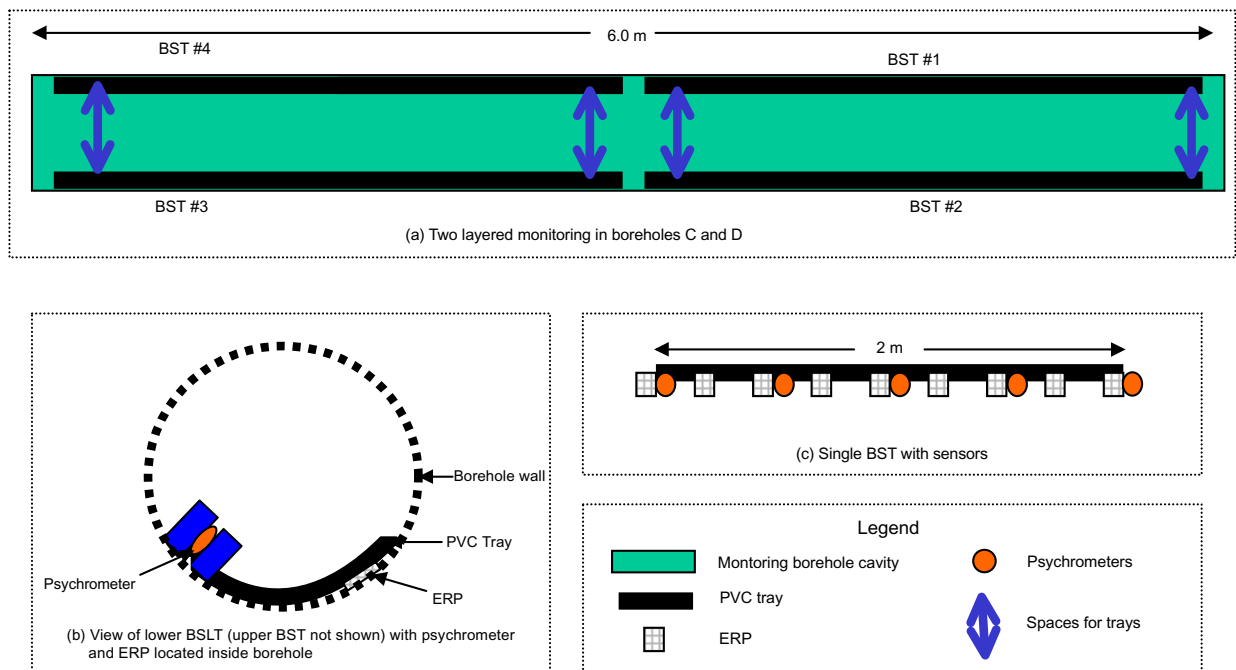


Figure VII-2. Schematic Illustration of Borehole Monitoring System.

VII-3 Seepage Collection

To measure water seeping into the slot following liquid release into the injection borehole, a water collection system was designed to capture seepage from the slot ceiling (Figure VII-3). Design of this system was dictated by the slot geometry and locations of ‘I’ beam supports. A row of stainless steel trays was fabricated for each of the four accessible compartments between the I-beams. Each tray was an inverted pyramid 0.46 m long and 0.40 m wide and tapered to a single point 0.20 m from the top. For each compartment, seven trays were assembled along a single steel frame, allowing for easy installation inside the slot. Water captured in the stainless steel trays was transferred into clear PVC collection bottles (0.076 m ID, 0.45 m tall). Water falling onto the trays was drained to the collection bottles through Teflon tubes (0.635 cm OD).

An intermittent vacuum was applied to the collection bottles such that water stored on the trays or in Teflon tubes could be sucked into the collection bottles. The amounts of seepage water in the collection bottles were periodically recorded with sampling intervals determined in the field by the rates observed.

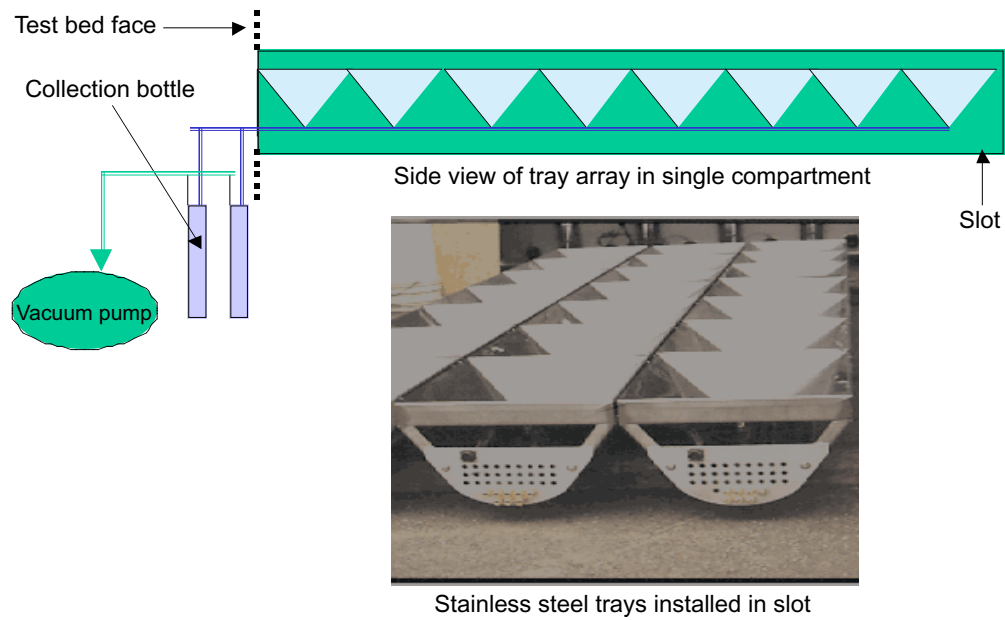
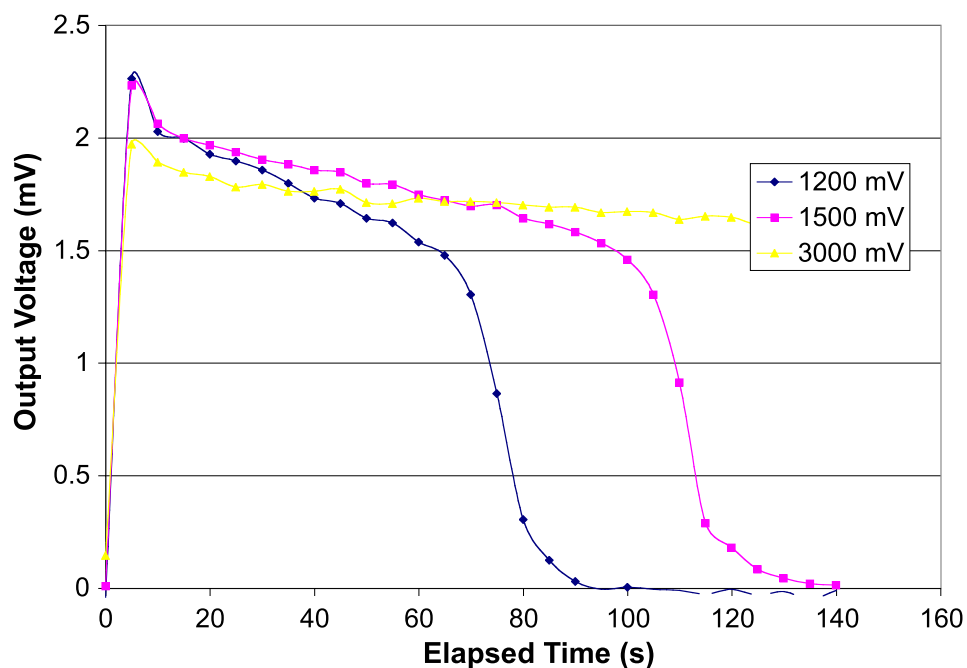


Figure VII-3. Schematic Illustration of Water Collection System Installed in Slot.

ATTACHMENT VIII—MEASUREMENT OF WATER POTENTIAL USING PSYCHROMETERS

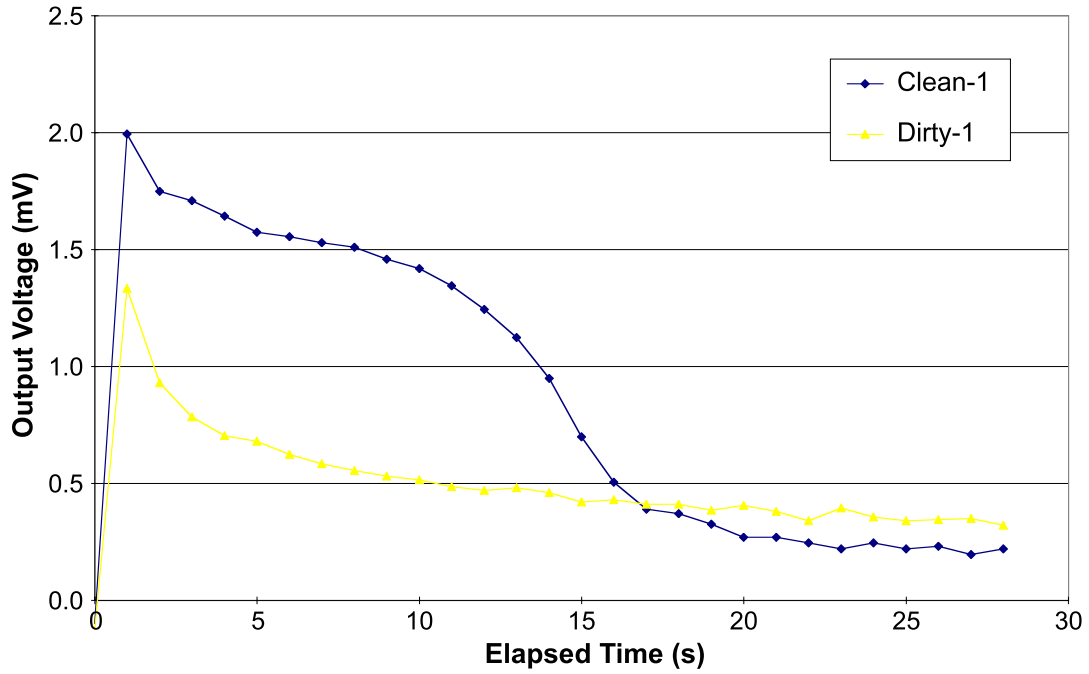
Prior to field use, all psychrometers were calibrated in the laboratory, using potassium chloride solutions (0.1-1.0 molal or mole of solute per 1000 grams of solvent). A second calibration was done in the laboratory after psychrometers had been used for field measurements, if feasible and practical. During the calibration procedure, psychrometers were isolated in an insulated box to minimize temperature fluctuations. Automated measurements were then made using the multiplexing capabilities of the CR7 data logger. When the psychrometers were observed to have reached equilibrium, they were removed from the calibration solution, washed in distilled water, air-dried, and immersed in the next solution. After calibrations were completed, all psychrometers were washed and air-dried before installation in the field.

During laboratory calibrations and preliminary field measurements, we noticed that the shape of the psychrometer output curve was significantly influenced by the size of the cooling voltage and cooling duration for a given water potential (Figure VIII-1). This curve was also dramatically altered when the psychrometers became contaminated with dust particles (Figure VIII-2). Given the high rate of failure of psychrometers in the field, it was therefore important to optimize both the cooling voltage and duration for a given water potential to help identify psychrometers that were contaminated or otherwise malfunctioning. Optimization was accomplished by increasing the cooling voltage and/or increasing the time over which the cooling voltage was applied until a well-defined plateau resulted for the psychrometer output. Data from contaminated or malfunctioning psychrometers are not for interpretation and are labeled as such in Scientific Notebook YMP-LBNL-JSW-1.2, pp. 103–152.



DTN: LB980001233124.001

Figure VIII-1. Effect of Cooling Current on Psychrometer Output Curve (PSY-732).



DTN: LB980001233124.001

Figure VIII-2. Effect of Dust Coating on Psychrometer Output Curve (PSY-731).